12-2013

Analysis, Prototyping, and Design of an Ionization Profile Monitor for the Spallation Neutron Source Accumulator Ring

Dirk A. Bartkoski
University of Tennessee - Knoxville, dirk.bartkoski@yahoo.com

To the Graduate Council:

I am submitting herewith a dissertation written by Dirk A. Bartkoski entitled "Analysis, Prototyping, and Design of an Ionization Profile Monitor for the Spallation Neutron Source Accumulator Ring." I have examined the final electronic copy of this dissertation for form and content and recommend that it be accepted in partial fulfillment of the requirements for the degree of Doctor of Philosophy, with a major in Physics.

Geoffrey Greene, Major Professor

We have read this dissertation and recommend its acceptance:

Marianne Breinig, Jeffrey A. Holmes, Takeshi Egami

Accepted for the Council:
Carolyn R. Hodges

Vice Provost and Dean of the Graduate School

(Original signatures are on file with official student records.)

Analysis, Prototyping, and Design of an Ionization Profile Monitor for the Spallation Neutron Source Accumulator Ring

A Dissertation Presented for the
Doctor of Philosophy Degree
The University of Tennessee, Knoxville

Dirk A. Bartkoski
December 2013

Dedication

This work is dedicated to my Lord and Savior Jesus Christ without whose direction I would have never pursued a deeper understanding of the universe through physics.

Acknowledgements

I would like to first thank my advisors Dr. Craig Deibele who brought the field of electromagnetics from the textbook to reality. Special thanks are also in order to Dr. Jeff Holmes without whose help I may have never passed some of my classes. Thanks are necessary to all the SNS diagnostic group technicians who taught me many useful laboratory skills and accelerator physics group members who helped me Python coding to Monte Carlo methods. I would also like to thank Kerry Ewald and Yarom Polsky who were instrumental in turning ideas into actual designs.

Thanks also go to my best friend Tim for his uncanny ability to provide the much needed occasional distraction. My mom, whose constant prayers and encouragement reminded me I wasn't alone and my dad, whose daily example of integrity, hard work, and perseverance taught me what true success required.

Finally, I can never thank enough my wife Kerri. Her constant encouragement, support, unwavering faith in me, and perpetual joy sustained me more than I can ever say. Her presence in my life for the last few years of my doctoral journey kept me sane and a constant reminder that path I was called to was the right one and the end was always in sight if you knew which direction to look.

Abstract

The Spallation Neutron Source (SNS) located in the Oak Ridge National Laboratory is comprised of a 1 GeV linear H^- [H^-] accelerator followed by an accumulator ring that delivers high intensity 1 μs [microsecond] long pulses of $1.5x10^{14}$ [1.5x10^14] protons to a liquid mercury target for neutron production by spallation reaction. With its strict 0.01% total beam loss condition, planned power upgrade, and proposed second target station, SNS ring beam-profile diagnostics capable of monitoring evolving beam conditions during high-power conditions are crucial for efficient operation and improvement. By subjecting ionized electrons created during beam interactions with the residual gas to a uniform electric field perpendicular to the beam direction, a profile may be collected based on the relation between measured ionized particle current and the beam density responsible for ionization. This form of nondestructive profile beam profile diagnostic known as an Ionization Profile Monitor (IPM). Introducing a magnetic field parallel to the electric field constrains the transverse particle motion to produce spatially accurate profiles. Presented in this work is the analysis and design of an IPM for the SNS ring capable of measuring turn-by-turn profiles with a 10% spatial accuracy for a fully accumulated high intensity proton beam. A theoretical framework is developed for the IPM operational principles and estimations for system design parameters are made based on calculations and measurement data. Detailed simulations are presented which are also used to determine design details and experimental results from a proof-of-principle IPM test chamber are reported and analyzed. Finally, a complete system design is presented based on the design criteria and simulation optimization that meets the required IPM system objectives.

Table of Contents

List of Tables

List of Figures

Chapter 1

Background and Overview

"Count what is countable, measure what is measurable, and what is not measurable, make measurable." - Galileo Galilei

The greatest discoveries in history would have remained little more than ideas and scribbles on paper without the tools used to test them. From the prism Isaac Newton used to prove the composition of light to the Hubble Space Telescope used to confirm the expansion of the universe, the advancement of physics is inextricably linked to the pursuit of better instrumentation. No better example may be found than the pursuit to understand the atom. In 1927, when Sir Ernest Rutherford began an examination of the atomic structure with α-particles, he expressed his desire for 'a copious supply' of far higher energy particles to members of the Royal Society of London, and the era of the particle accelerator was born [1].

The earliest linear accelerator built by John D. Cockcroft and Ernest Walton was 8 feet long with an energy of 800 keV and the first circular accelerator, known as a cyclotron, could fit in the palm of the hand with its 4 inch diameter. In comparison, today's largest accelerator, the Large Hadron Collider (LHC) synchrotron, has a diameter of over 5 miles and utilizes superconductors to reach energies up to 3.5 TeV. Without the instrumentation

that allows physicists to control and diagnose the particle beam, even the greatest accelerator in the world would be useless. The research presented here proposes a beam diagnostic tool known as an Ionization Profile Monitor (IPM) for the Spallation Neutron Source (SNS) that provides a non-destructive method of measuring the beam profile not yet realized in the SNS accumulator ring.

1.1 The Need for Non-Destructive Profile Measurement

While accelerator-driven spallation neutron production may be financially more expensive than neutrons created through reactor-based nuclear fission, the spallation reaction has the advantage that it can be pulsed with relative ease. Pulsed spallation neutron sources offer advantages in improved signal-to-noise ratios and also lend themselves to studies involving high energy resolution through time-of-flight techniques [2]. Spallation is the process in which a heavy nucleus emits a large number of nucleons, i.e. neutrons, as a result of bombardment by a high-energy particle, such as a proton in the case of SNS.

1.1.1 The Spallation Neutron Source

The Spallation Neutron Source is one of the world's most powerful accelerator-based pulsed neutron sources. Located at the Oak Ridge National Laboratory in Oak Ridge, Tennessee, USA, the SNS is a third generation neutron source that provides pulses of neutrons for research in neutron scattering. SNS begins with the ion source (see figure 1.1 for a layout of the SNS facility), where 1 ms long macro-pulses of H^- ions are produced in a magnetically-confined plasma at a rate of 60 Hz.

A Low Energy Beam Transport (LEBT) line transfers the ions into a 2.5 MeV Radio

Figure 1.1 Spallation Neutron Source conceptual layout. The SNS was built by a partnership of six U.S. Department of Energy laboratories. [3]

Frequency Quadrupole (RFQ) accelerator that defines the bunching structure for RF acceleration. After the RFQ, a Medium Energy Beam Transport (MEBT) section prepares the beam for the linear accelerator (linac) to accelerate the particles to approximately 88% the speed of light. An electrostatic chopper, in the LEBT, with a 50 ns rise time, along with a traveling wave chopper with a 20 ns rise time in the MEBT, cut 300 ns gaps to a level of $1x10^{-3}$ and $1x10^{-6}$ respectively, in the 1 ms macro-pulse to create a succession of mini-pulses.

The linac begins with two warm sections, a drift tube linac (DTL) and a coupled cavity linac (CCL), that accelerate the beam to 186 MeV. The latter portion of the linac is comprised of a liquid helium cooled, niobium superconducting linac (SCL) that finishes the acceleration. Upon exiting the linac, the 1 GeV H^- ions pass through a high energy beam transport line (HEBT) to a foil where they are stripped of electrons. The time structure of the resulting proton beam in the ring can be seen in figure 1.2.

The ring accumulates 1060 individual 645 ns long mini-pulses with a peak beam current of 38 mA to a full intensity of $1.5x10^{14}$ protons per pulse, as illustrated in figure 1.3. This 1 μs high intensity pulse is transported to a liquid mercury target at a rate of 60 pulses per second with an average beam power of 1.4 MW. The spallation reaction produces a range of energetic neutrons which are then moderated and sent to a variety of experiments [3], [4].

1.1.2 Beam Loss and Diagnostics

SNS is a user facility whose primary function is to provide a steady and consistent supply of neutrons for scattering experiments. As such, beam availability is a top priority. Key components to achieving maximum beam availability are the prevention of beam related damage to accelerator components and a reduction of residual radiation activation to allow for quick and safe access for maintenance personnel. While the high intensity beam of SNS

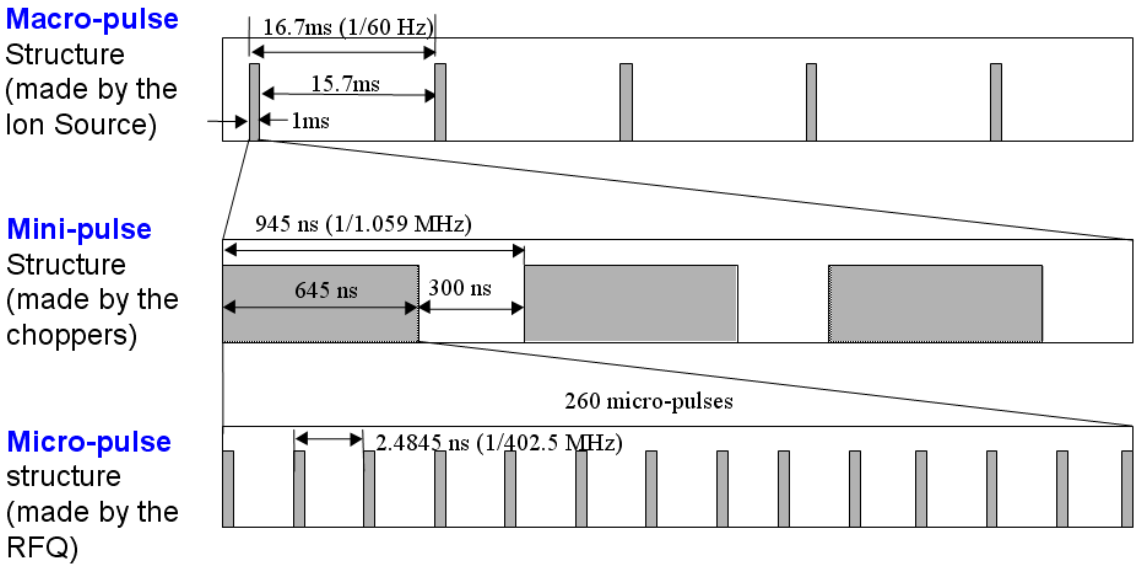

Figure 1.2 SNS beam pulse structure [5]**.**

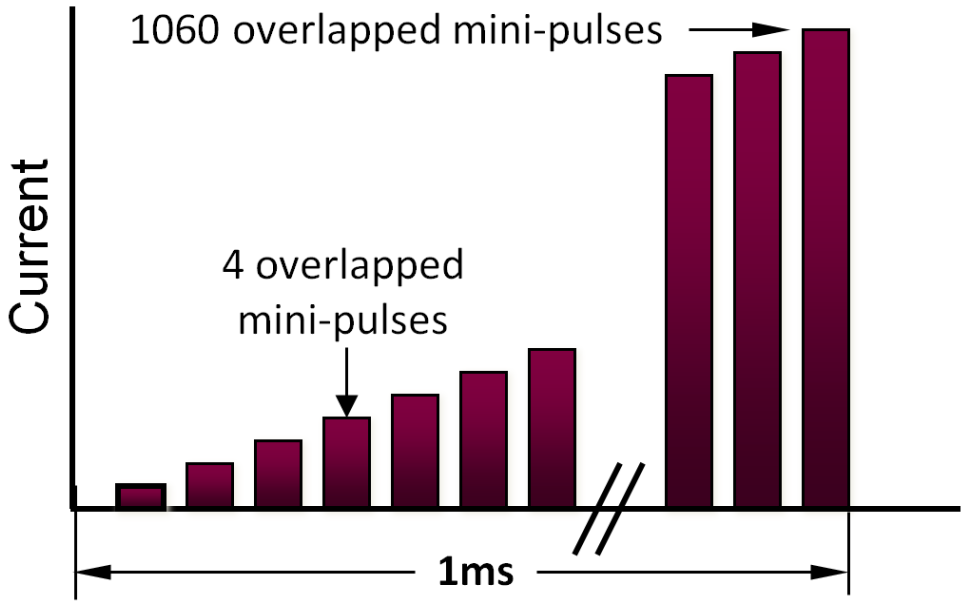

Figure 1.3 SNS accumulator ring current accumulation scheme [6]**.**

provides high fluxes of neutrons for users, it also presents unique challenges for operation. In order to achieve the required beam availability of at least 95% for SNS, a loss percentage of no more than 0.01% of the total beam is required [4]. This is an unprecedented low-loss level considering that, previously, the lowest loss high intensity machine was PSR at the Los Alamos Neutron Science Center. Fractional losses in PSR are 0.3% and 10% at ISIS in the U.K. [7]. For SNS, the 10^{-4} loss requirement translates into an uncontrolled beam loss no greater than 1 W/m and a loss current of 1 nA/m. This puts a very high importance on beam control.

Transverse beam profiles are an important diagnostic that allows physicists to characterize many beam parameters including width, emittance, halo, and position [8]. Monitoring the transverse distribution of the beam pulse during accumulation ensures the proper orbit is maintained which in turn allows for control of losses. Wirescanners provide the primary method of beam profile measurement, and this diagnostic tool works by passing a wire through the beam and measuring the current generated on the wires. The generated current is proportional to the beam density at the position of the wire. As the position of the wire is swept across the beam, the beam density profile is measured. [9].

There are 44 wirescanners installed throughout the SNS accelerator, however, they are not suitable for full beam power. It has been shown in [10] that the temperature of a conventional carbon wire would be over 2200 K for a fully accumulated 1 MW beam in the ring, while the maximum practical failure temperature for a carbon wire is 1600 K [11]. Only short pulses, on the order of 100 μs with a repetition rate of 10 Hz, could be used in the ring for a standard wirescanner profile measurement. Wirescanners are used for the full intensity beam only in the latter parts of the accelerator where the beam makes a single pass. The Ring

to Target Beam Transfer line (RTBT), for example, uses wirescanners to measure profiles because the RTBT duty factor is 0.006%, as opposed to the ring duty factor of 6%. This allows sufficient cooling between successive pulses such that the maximum wire temperature is ~400 K [10]. It is not feasible to use an interceptive form of profile measurement in the ring and therefore non-intrusive profile systems must be used.

The SNS ring lacks a complete set of profile diagnostics. Recently a prototype non-intrusive profile monitor that measures the deflection of an electron beam passing through the proton beam has been used to measure the beam profile [12]. It is desirable, however, to have a more complete set of diagnostic tools to complement the current profile monitor, especially as the SNS ring encounters higher intensity instabilities and loss corresponding to the beam power ramp from 1 MW to 1.4 MW and eventually to 3 MW.

1.1.3 Ionization Profile Monitor Overview

This research focuses on a non-destructive form of profile measurement that uses the residual gas found in the beam pipe as the medium for generating the profile signal. Ionization profile monitors work on the basic principle depicted in figure 1.4. While all accelerators require a vacuum within the beam pipe to limit disturbances to the beam by air molecules, no vacuum is perfect and highly energetic beam particles incident on residual gas molecules can ionize the gas into ion-electron pairs. The density of the residual gas ionization is proportional to the beam density distribution. By placing an electric field across the ionized gas ions or electrons, depending on the bias of the electric potential, can be accelerated toward a detector. The signal on the detector is measured as function of position and the signal level is proportional to the beam density at that location.

There are a number of variations on the basic principle that have been used

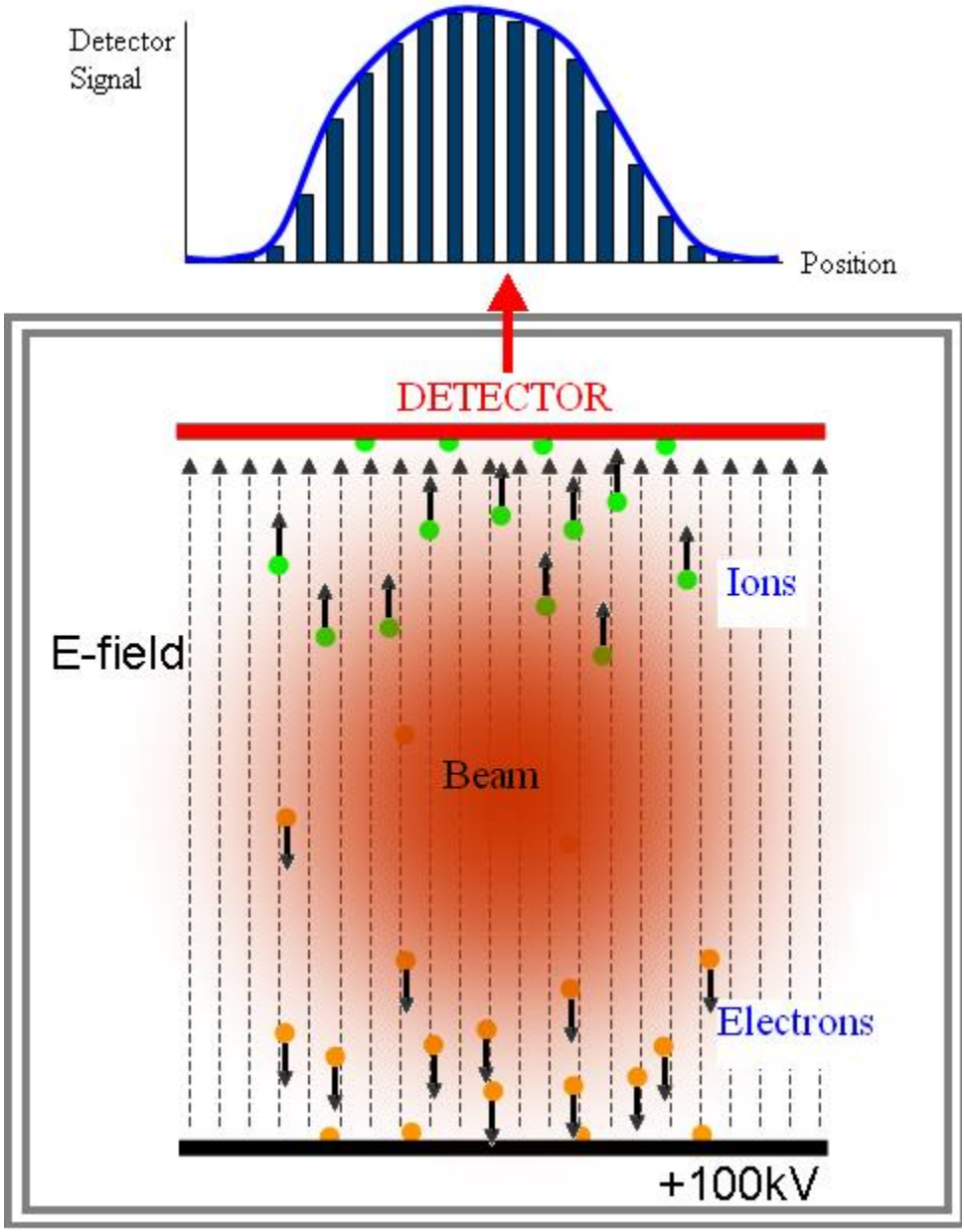

Figure 1.4 Ionization Profile Monitor basic principle illustration [13]**.**

successfully and IPMs are designed for the particular application as needed. Due to the low intensity of the profile being generated from high vacuum beam-gas interactions, the ionized gas signal must be amplified. Many IPMs use a single or multiple Multi-Channel Plates (MCP) to amplify the signal onto a detector array. Depending on the type of time resolution required, a wire array or strip electrodes can be used to deliver high time resolution ≃ 100 ns. Alternatively, a CCD camera may be used to measure light created by impinging electrons on a phosphor screen to achieve spatial resolutions around 100 μm [14]. Some accelerators with exceptionally low vacuums must create localized pressure bumps to ensure that there are enough ions to obtain a profile.

1.2 History of IPM Development

1.2.1 Early IPMs (1965 – 2002)

Ionization profile monitor technology has been in development for over forty years. Among its earliest uses was the profile measurement of intense beams at the Budker Institute of Nuclear Physics (BINP) in Russia [15]. One of the earliest publications on a residual gas based profile monitor was a paper by Fred Hornstra, Jr. and William H. Deluca [16] in the 1967 International Conference on High Energy Accelerators. They describe a novel method of measuring beam profiles by detecting ionization products created from a proton beam passing through a $1x10^{-6}$ Torr vacuum in the Zero Gradient Synchrotron (ZGS) at Argonne National Laboratory (ANL). Their system collected both ions and electrons using a 10 kV electrostatic potential and a system bandwidth of 200 kHz. It was quickly discovered that the beam space charge had a significant effect on the measured beam profile widths and the study of profile spreading has been a major issue in IPM development ever since [17]. Their

work was preceded by numerous theoretical analyses of the ionization of gases including books written by McDaniel [18] in 1954 and Massey and Burhop [19] in 1952.

After scientists at CERN heard of the ZGS IPM they designed their own version, which they called an Ionization Beam Scanner (IBS), and installed it in early 1968 in the Proton Synchrotron (CPS) [20], [21]. The IBS collected only electrons and used a single strip electrode swept over the width of the beampipe to generate profiles with a spatial resolution better than 1 mm. Other profile monitors soon followed at CERN and, by 1971, an IBS was installed [22] in the Intersecting Storage Rings. In this case, the very low residual gas pressure required the addition of a sodium vapor jet to be passed through the beam to increase the ionized electron signal [23]. The Japanese also used an IPM with a localized pressure bump to measure ions with 30 μs time resolution in their KEK Proton Synchrotron in 1977 [24].

The Fermi National Accelerator Laboratory (Fermilab) soon followed in utilizing IPM technology, beginning in 1979 in the original main ring design. Their version of an IPM incorporated micro-channel plates (MCP) with a magnesium vapor ribbon in the beam path [25]. It is significant that they were challenged by unwanted secondary emission electrons and that they used UV light for testing the MCPs. IPM's originally installed in the Fermilab Anti-Proton Source were modified and moved into the Booster. These particular IPMs had a 260 kHz bandwidth with an 8 kV potential [26]. IPMs installed in the original main ring where improved upon and installed in the Main Injector when completed in 1999. [27].

Two papers by Weisberg et al. [28], [29] published in 1981 and 1983 describe an Ionization Profile Monitor built for the Brookhaven National Laboratory (BNL) Alternating Gradient Synchrotron (AGS) that used an adjustable local gas pressure to measure ions and a

14 Gs magnet for electrons. An MCP and 64 strip detector was used to measure profiles with a time resolution of 0.1 ms. In [30], Thern provides a theoretical correction to the error due to space charge in the AGS IPM profiles; however, this theory lacked a good agreement with the Monte Carlo simulations of ionized particle trajectories and cast doubt on the validity of the correction.

By 1988 the ISIS neutron source in England had 5 non-destructive profile monitors using a single detector called a Channeltron[1] to measure electrons by sweeping across the transverse beam direction with a 50 kV/m bias field [31].

Three gas monitors were installed at the (DESY) facility and were among the first to view the beam width with a screen and camera [32], [33]. In 1988 Hornstra [34] described a "separated function feature" which allowed the most critical components of the system to be placed outside the vacuum. This work was later expanded upon by Wittenburg [32] in 1992. In a paper discussing experiences with gas ionization he went into detail about various aspects of the system, such as noise and field shaping. The system was upgraded to use MCPs, part of a migration over time away from camera detection systems [35] and toward the use of IPMs to measure the beam's transverse emittance.

A series of papers follow the development in the 1990s of residual gas profile monitors in the Tandem – ALPI accelerator at the Istituto Nazionale di Fisica Nucleare Legnaro Laboratory (INFN -LNL) . Ceci, Valentino [36], and Variale [37] authored a number of papers beginning with a preliminary study of an IPM system and outlining the version they were planning on using, which consisted of multiple MCPs and a phosphor

[1] Channeltron is a registered trademark of PHOTONIS USA.

screen with 70 µm spatial resolution. Later Bellato ,et al [38] discussed first test results and the eventual commissioning of the system .

Other IPMs in use by the 1990s were located at the Test Storage Ring (TSR) in Germany, where they were used to measure beam heating and cooling mechanisms [39], and at the French accelerator Grand Accelerator d'Ions Lourds (GANIL), in which two IPMs were designed to measure the transverse distribution and the longitudinal time distribution [40]. In [41] an IPM is described for the Brookhaven National Laboratory (BNL) Relativistic Heavy Ion Collider (RHIC) that uses a 0.14 T magnet and a 3 kV bias potential to measure averaged profiles of proton beams and single bunch gold beam profiles. Sellyey and Gilpatrick authored two papers [42], [43] that describe the design and testing of an IPM designed for future high intensity beams. Included in their research is the analysis of the radiation resistance of a number of components common to IPMs. In particular they state that the MCP is usable with a total dose of >10 Mrad, which would also apply to a Channeltron because they are made of the same materials. CERN continued to update their profile monitors when, in 1997, an IPM modified from an older Duetshes Elektron-Synchrotron (DESY) version, was used in the Super Proton Synchrotron (SPS) [22].

1.2.2 Modern IPMs (2002 – 2012)

While new IPM systems continue to be designed and installed, much of the work has focused on improving existing systems and addressing issues that affect IPM performance and accuracy. Among new profile monitors developed in recent years is an IPM designed and built for the Fermilab Tevatron to diagnose emittance blow up during the ramping of the beam energy. Beginning in 2003 a series of papers [44–46] describes a system largely based on the Fermilab Injector IPM that uses electrons to measure individual proton and antiproton

bunches. It uses a localized pressure leak and an MCP onto anode strips, and as of 2006 it had successfully used a 0.2 T magnet to measure proton bunch mismatches with 60 ns time resolution.

Other new systems include an IPM for the Japan Proton Accelerator Research Complex (J-PARC) that was designed to measure electrons with a 300 G magnetic field and -40 kV potential without the need of an MCP, due to the 1 Pa level vacuum [47], [48]. Later studies [49], [50] show the successful use of Monte Carlo simulations to determine the necessary electric and magnetic field values as well as to simulate turn-by-turn profiles using ions. Ishida in 2005 [51] showed that an IPM would not be suitable for the J-PARC neutrino beamline because the induced background was too high for the use of electrons and space-charge was too high to use ions. A paper lead by Forck in 2005 [52] and a presentation given at the 2010 International Particle Accelerator Conference (IPAC) [14] give an overview of IPM technology to date. They compare phosphor screen and MCP types of detectors as well as most current types of minimally invasive profile measurement techniques, highlighting the common practice of using ions to measure low current beams and electrons for high current beams.

Federico Roncarolo studied the accuracy of the CERN IPMs used in the SPS for eventual use in the LHC for his doctoral research. He found good agreement with wirescanners to 1%, except for beam sizes of less than 500 μm, and provided a detailed analysis of statistical errors found in profile measurements [53]. A new IPM was also developed at CERN for the Low Energy Ion Ring (LEIR) that measured profiles from a $2x10^{-12}$ Torr vacuum [54], [55]. IPM technology is also being utilized to measure non-particle-based beams as documented in the 2008 paper [56], in which an IPM is used to

collect ions created by soft laser light generated by the Free Electron Laser at the FLASH facility in DESY. A pressure bump of xenon is used to measure profiles with a 50 μm spatial resolution. An IPM prototype has been tested at the Helmholtz Centre for Heavy Ion Research (GSI) in Germany [57] for eventual use in the International Fusion Material Irradiation Facility (IFMIF), which will test suitable materials for use in future fusion reactors.

Many older IPMs have undergone upgrades as the technology has matured. The SPS at CERN, for example, was upgraded in 2003 to increase spatial resolution to lower than 0.1 mm [58]. Liakin reported improvements to the SIS heavy ion synchrotron at GSI in which higher potential end caps where used as a unique method of longitudinal field flattening [59]. Four IPMs at RHIC saw important upgrades that solved problems related to RF coupling to the beam, dynamic gain reduction of the MCPs from high signal fluxes, background from radiation spray, background form electron cloud buildup, and permanent MCP damage from high integrated signal flux [60]. In [61], [62] an interesting type of two-dimensional IPM is described that used a curved electrode to separate the velocities of the ionization products to measure vertical as well horizontal profiles simultaneously.

Recent work on IPM systems includes the upgrade of the current IPM system at the ISIS synchrotron and also fundamental EM studies of the IPM geometry and trajectory of particles in more complicated electric field configurations. It was determined that there existed a large error due the non-linearity of the drift field [63]. Later papers, including [64], [65], and recently in 2010 [66], outline major upgrades to the ISIS IPMs that include replacing the single moving Channeltron with 40 stationary ones and a method of Channeltron calibration that allows blocks of 4 gain-matched Channeltrons to be controlled

by their own power supply. The differential gain setup enables uniform profile amplification in addition to a width correction model that allows for profiles to be measured in real time.

Challenges with beam space charge have been identified since the first use of IPMs. Experience with space charge distortion led Thern (1987) [30] to publish a paper describing a model for this distortion as well as formulas for correcting it. Due to the importance of understanding this phenomenon many other groups produced work studying the calibration of ionized profiles. Amundson and colleagues (2003) [67] produced a calibration for the Fermilab Booster IPM in which they presented a formula for calibration and compared the results with real data with sufficient accuracy for their purposes.

Many modern accelerators implement IPM's in their higher energy sections. Most of these IPM's use electrons. Of the IPM's that use ions as their signal source, many are band limited and not designed for fast measurements and have low static fields that prevent fast ion collection. Table 1.1 highlights selected IPMs including those at the ISIS and J-PARC facilities, which are similar to SNS in their beam characteristics. The table shows some of the limitations of the current technology [30], [68], [69], [50]. The maximal bias potentials

Table 1.1 List of selected IPMs and their characteristics.

Accelerator	*Collection Type*	*Bias Potential*	*Time Resolution*	*Bandwidth*
AGS	Ions & Electrons	45 kV	0.1 ms	3.5 kHz
Fermilab	Ions & Electrons	30 kV	1.5 μs	300 kHz
ISIS	Ions	60 kV	35 μs	10 kHZ
J-PARC	Ions & Electrons	45 kV	35 ns	10 MHz

currently used are on the order of 50 - 60 kV. Average time resolutions for modern IPMs are ≅100 ns with the lowest being 35 ns. Profile monitors based on residual gas ionization have become a standard beam diagnostic tool in today's high current accelerators as they continue to be built and improved upon.

1.3 SNS IPM Design Criteria

It is the goal of this project to produce a complete IPM system design capable of parasitically measuring turn-by-turn transverse beam profiles in the SNS accumulator ring. The beam width accuracy must be comparable to that of currently employed profile diagnostic tools. As part of this project, a thorough analysis is presented to ensure measurement reliability. IPM system requirements are defined for a fully accumulated 1MW nominal beam consisting of $1x10^{14}$ ppp and are summarized in table 1.2. In order to measure the single turn 1 μs long bunches, the system must have sufficient bandwidth and dispersion correction to measure a bunch rise time of at least 20 ns with a dynamic range of 100 for a nominal beam. The measured beam profile width should be within ±10% of RMS beam size when compared to the profile width calculated from the beam optics at the IPM location.

For the system to be able to run parasitically during production-beam operation mode, the beam upon leaving the IPM region must be negligibly affected in its trajectory and dynamics by the IPM magnets and electrodes. Therefore, if the IPM produces multipole components in the magnetic field of greater than 1% measured at a distance of 12.78 cm from the magnet center, these will produce higher order distortions to the beam particle trajectories that cannot be compensated.

As with all ring vacuum chamber components, the same secondary electron

Table 1.2 IPM system requirements for fully accumulated $1x10^{14}$ ppp beam.

Requirement	*Value or Range*
Measured Profile Plane	Transverse Horizontal and Vertical
Longitudinal Resolution	1μs (Single Turn)
Time Resolution	20 ns
System Bandwidth	17.5 MHz
Beam Size Measurement Accuracy	±10% of RMS Beam Size
Dynamic Range	100
Maximum Beam Trajectory Deflection	0.5 mrad
Maximum Allowed Magnet Multipole Component	< 1% at 12.78 cm Radius
Radiation Resistance	$1x10^{7}$ rad

mitigation treatment must be applied to the IPM in order to reduce instabilities resulting from electron build-up. While the performance requirements for the system put lower limits on many of the design aspects, budgetary concerns will place upper limits on the size of some of the larger and more expensive components. Likewise, the location in the ring tunnel will set limits on some physical dimensions, such as the 4.2 m longitudinal distance allocated for both horizontal and vertical systems and the 2.54 m ceiling height.

1.4 Overall Organization

The remainder of this work is broken into five chapters. Chapter 2 describes the theoretical basis for the IPM system. A description of the beam-gas interaction presents the principles of gas ionization and estimates for electron-ion pair production. Study of the residual gas and SNS ring pressure then allows for estimation of the expected signal. Analysis of the residual gas sensitivity and profile generation method is also presented.

Chapter 3 is a description of the simulation studies and basic system parameter determination. Also offered in this chapter is a description of the computational method used to simulated ionized particle trajectories. A large portion of chapter 3 is dedicated to the analysis of measured errors expected in the system, methods for the error reduction, as well as an estimation measured profile accuracy.

Chapter 4 summarizes the results of an IPM test chamber built and installed in the ring to test the basic IPM proof-of-principle while chapter 5 outlines the completed design in detail for each of major system components. The summary chapter, chapter 6, recapitulates the main design elements in relation to the design goals, briefly describes future work and possible system upgrades, concluding with some final remarks.

Chapter 2

Theoretical Analysis

The following chapter will present an analysis of IPMs based on first principals that will translate the measurement requirements of table 1.2 into system specifications and a foundation for their reliability. A theoretical foundation for the principle of residual gas ionization by an energetic incident particle is developed leading to an estimate of the number of ion-electron pairs created. A study of the residual gas is performed analyzing measured pressure data from the IPM location and applying vacuum physics to understand the residual gas density and characteristics. Mechanisms of ionization are examined to determine the measured signal characteristics and errors induced by low initial particle statistics are addressed. Finally, after a description of the detector to be used, estimates for the measured signals expected are given along with a method of producing complete turn-by-turn beam profiles.

Design Considerations

A number of variations of the IPM exist. One of the goals of this project was to develop a simple design that meets the necessary specifications and that extends the technological state-of-the-art. Of the two types of IPM detection methods, use of a phosphor screen or direct

collection of ionized particles as discussed in section 1.1.3, the method of measuring ionization products directly eliminates the need for a camera and thus will be the method considered here.

A beam's passage through residual gas produces ions and electrons; both of which can be used to measure profiles. It will be shown in the following analysis that both of the particle types involve their own challenges. While ion collection is a simpler method of measurement, profiles acquired through this method present challenges that make it difficult to fulfill the system requirements as stated in table 1.2. Therefore, electron collection will be the primary design focus. However, even though electron collection will provide the required profile accuracy, it is desirable to design the system with the capability of measuring ions or electrons. This will allow for the comparison of the two profile methods and provide a test bed for the development of ion-based IPM profiles in high intensity accelerators. Additionally, it is advantageous because the design of an ion collection system requires only straightforward modifications to a system developed for electrons.

2.1 Beam-Gas Interaction

A detailed analysis of the physics involved in the implementation of a residual-gas-based beam profile monitor is necessary in order to design a system capable of measuring reliable and accurate profiles. An understanding of the interaction between the beam and the residual gas is fundamental toward the design of a non-destructive profile monitor.

2.1.1 Interaction Model

It is first necessary to develop a model for the beam-gas interaction. A complete quantum mechanical model would not only be extremely complex, but unnecessary as a number of

simplifications may be made that allow for easier analysis without loss of solution integrity.

Beam Properties

The requirements on the particle beam for the nuclear spallation process are such that incoming protons must have wavelengths ~1.3 fm, the range of the strong force, or the proton will interact with the nucleus as a whole and not individual nucleons. The de Broglie wavelength is

$$\lambda = \frac{h}{p} \tag{2.1}$$

where h is Planck's constant. For protons with mass $m_p = 938.2\ \mathrm{MeV}/c^2$, energy K = 100 MeV, and momentum $p = \sqrt{(K/c)^2 + 2m_pK}$ the wavelength is 2.7 fm. The lower energy limit for a proton to produce spallation reactions is approximately 100 MeV and optimal energies are in the GeV range [70], which can be seen from the probability for nuclear collisions by an incident proton, $P_{nuclear\ collision} = 1 - \exp(-R/\lambda_{collision})$. Here, R, the range of the proton, is a monotonically increasing function of proton energy and $\lambda_{collision}$ is the proton nuclear collision length [71]. The probability for a spallation reaction is significant only when the proton range is large compared to the collision mean free path, which happens with energies of 1-2 GeV.

Protons incident on the Hg target in the SNS have been accelerated to a kinetic energy K of 1 GeV, and when combined with their rest energy E_0 = 938 MeV, give a total energy $E = K + E_0$ of 1.938 GeV. We define the Lorentz factor by

$$\frac{E}{E_0} = \gamma = \frac{1}{\sqrt{1 - \beta^2}} \tag{2.2}$$

where

$$\beta = \frac{v}{c} \tag{2.3}$$

and c is the speed of light in vacuum. Thus, a proton having 1 GeV kinetic energy has $\gamma = 2.07$, $\beta = 0.88$, and a relativistic velocity of 88% the speed of light or 2.62×10^8 m/s.

Beam-Gas Model Assumptions

Although an energetic charged particle will interact with matter in the surrounding region, not all possible interaction processes need to be considered given the IPM conditions. A detailed analysis of the various forces and interaction mechanisms experienced by a beam particle passing through a gas has been done and may be found in Appendix A. The following summary of the results therein will form the basis for further study of the ionization process:

1) Of the four fundamental forces through which the incident proton may interact with the gas, gravity and the weak force, whose strengths, relative to the strong nuclear interaction, are 10^{-6} and 10^{-39} respectively, may be ignored due to their weakness.
2) The low gas density associated with a 10^{-8} Torr vacuum means that nuclear collisions governed by the strong force, with a range 10^{-15} m, are highly improbable.
3) In the laboratory frame, the electric force given by Coulomb's law is primarily responsible for energetic collisions, considering that the magnetic field is much smaller than the electric field for orbital electrons and may be ignored.
4) The small size of the nucleus in comparison to the atomic size and the low gas density make nuclear excitations through proton-nucleus Coulomb interactions negligible.

5) Energy loss by bremsstrahlung from beam particles interacting with the residual gas may be considered negligible due to the small momentum change experienced by the 1 GeV protons.
6) Charge exchange during beam-gas collisions is negligible due to the small collision cross-section for the process for energetic incident particles.
7) Coherent scattering may be ignored considering the diffuse nature of the gas compared to the proton wavelength.
8) The wavelength of the 1 GeV proton, $\lambda = 7.3 \times 10^{-16}$ m (see Appendix A for calculation), is sufficiently small compared to the electron wavelength ~10^{-9} m and atomic dimensions ~10^{-10} m that collisions may be treated classically.
9) The energetic proton interacts with gas molecules through the most weakly bound electrons and thus Coulomb collisions with complex gas molecules may be characterized as proton collisions with valence electrons.
10) The velocity of the proton is sufficiently high compared to the gas thermal velocity and the electron velocity that gas molecules and atomic electrons may be considered at rest. Incident proton-atom interactions may be calculated as proton-electron interactions in the proton rest frame
11) Within the limits of maximum and minimum energy transfers, proton-gas collisions may be considered elastic.

The complex behavior of beam-gas interactions leading to ionization may be simplified to classical incoherent elastic and inelastic Coulomb interactions between energetic protons and stationary orbital electrons. With this model, an analysis of the

collision process leads to an expression for the energy loss of an energetic particle in a medium. The energy loss expression provides a quantitative method for studying the ionization in the IPM.

2.1.2 Relativistic Energy Transfer

Beam-gas collisions of interest, namely inelastic collisions with valence electrons, may be separated into two categories based on the impact parameter *b* between the incident and target particles, as illustrated in figure 2.1. Hard collisions are those in which the incident particle passes within close proximity to the atomic electron and are characterized by large energy transfers that result mostly in ionizations. Roughly 50% of the energy lost by a particle passing through matter is due to a small number of hard collisions. The other 50% is the result of large numbers of small energy transfers. With *a* being the orbital electron radius, transfers where $b >> a$ are known as soft collisions and can result in ionization, excitation, or

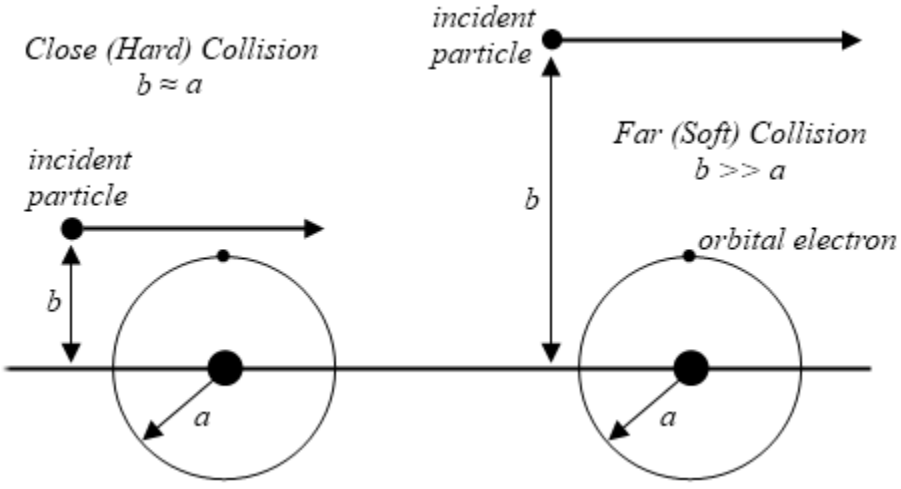

Figure 2.1 Two types of collisions defined by impact parameter and the orbital electron radius *a*. Close or Hard collisions are those where $b \approx a$ and Far or Soft collisions are those in which $b >> a$.

atomic polarization.

The probability of particular interaction processes is given by a Landau distribution [72], [73] and may be seen qualitatively in figure 2.2. While figure 2.2 shows a general case, it does elucidate some of the basic principles of the inelastic energy transfer processes due to soft collisions. There is a relatively high probability of excitation up to the ionization energy after which ionization dominates. The probability then decreases with increasing energy to a maximum allowed energy transfer.

Energy Transfer

The minimum and maximum energy transferred may be derived through elastic Coulomb collisions also known as Rutherford scattering. For energy transfers significantly larger than the binding energy required to remove an electron from its atomic orbit, the electron may be considered free (see figure 2.3 (a) for the lab frame illustration). Therefore, proton-molecular collisions may be viewed as an incident proton elastically colliding with a free stationary electron. Collision analysis is simplified when viewed in the center-of-mass frame and a complete explanation of transformation to the center of mass may be found in Appendix B.

Figure 2.3 (b) is a depiction of the collision in the center-of-mass frame with equal scattering angles θ. When transforming to the center-of-mass frame from the lab, position and velocity become that of the proton since $m_p >> m_e$ (see Appendix B for derivation). In the proton rest frame shown in figure 2.3 (c) where the electron now has momentum $p = \gamma\beta m_e c$, the collision is identical to Rutherford scattering for an energetic particle by an attractive force. In the lab frame the electron undergoes large energy transfers corresponding to large scattering angle, but the massive protons scatter through small angles and travel in

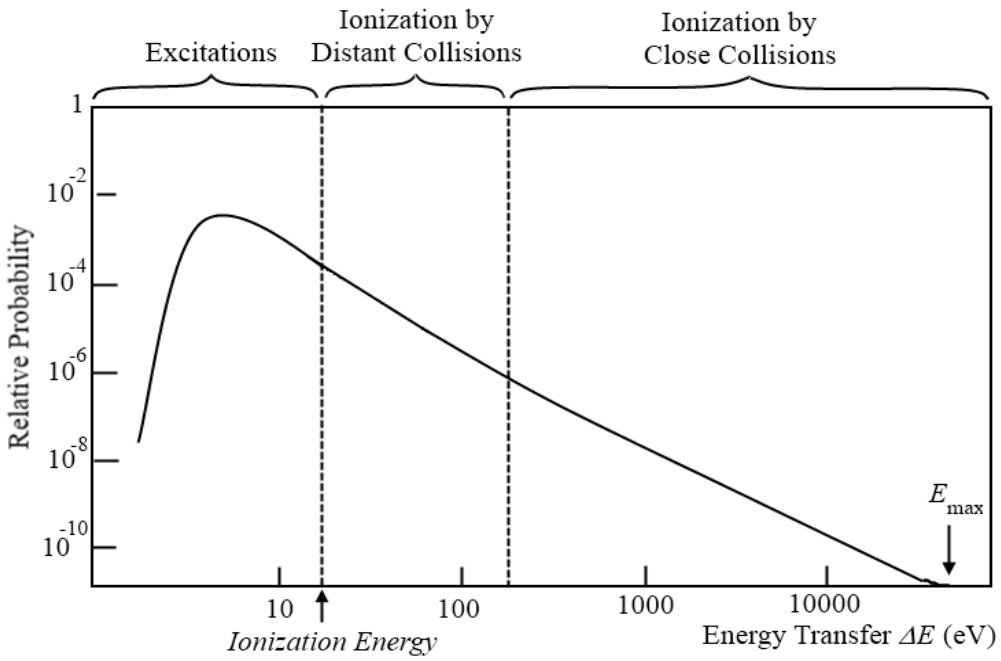

Figure 2.2 An example of the relative probability of the different processes responsible for energy transfer as a function of the energy transfer. E_{max} is the maximum kinematically allowed energy transfer.

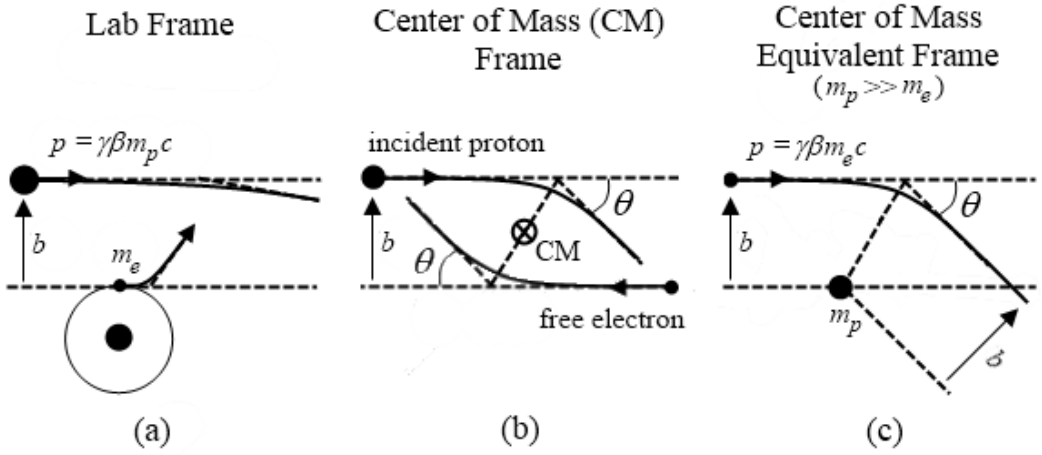

Figure 2.3 (a) Lab frame showing an incident proton with momentum *p* scattering off of an orbital electron with impact parameter *b.* (b) Collision as seen in the center-of-mass (CM) frame. (c) Center-of-mass equivalent frame when $m_p >> m_e$ where CM becomes the rest frame of the proton.

relatively straight lines.

For the general case of a massive particle *M* with charge *ze* and velocity βc incident upon a target particle with mass *m* and charge *–Ze* such that *M >> m*, the target has an initial momentum $p = \gamma\beta mc$ in the center-of-mass frame, as seen in figure 2.3. The Lorentz-invariant 4-momentum transfer squared, $Q^2 = -\left(p_i - p_f\right)^2$, where $p = (E/c, \vec{p})$ defined by the initial and final 4-momentum of a particle with energy *E* and momentum $\vec{p}$, can be shown to equal

$$Q^2 = 2\left[\frac{E_i E_f}{c^2} - m^2c^2 - |\vec{p}_i||\vec{p}_f|\cos\theta\right] \tag{2.4}$$

where θ is the scattering angle in the appropriate reference frame. In the lab frame where the mass *m* is at rest with energy mc^2

$$Q^2_{Lab} = 2\left[\frac{mc^2}{c^2}E_f - m^2c^2 - (0)|\vec{p}_f|\cos\theta\right] = 2m\left[E_f - mc^2\right] = 2mK_f \tag{2.5}$$

where K_f is the final kinetic energy of the light mass *m*. In the center-of-mass frame, elastic scattering leads to $E_i = E_f$ and $|\vec{p}_{i_{CM}}| = |\vec{p}_{f_{CM}}|$. Substituting this into (2.4) gives

$$Q^2_{CM} = 2\left[\frac{E_i^2}{c^2} - m^2c^2 - |\vec{p}_{i_{CM}}|^2\cos\theta\right] = 4p^2_{CM}\sin^2\frac{\theta}{2} = 4p^2_{CM}\frac{1}{1+\cot^2\frac{\theta}{2}}. \tag{2.6}$$

For Rutherford scattering in the heavy particle frame, the scattering parameter is related to the scattering angle by

$$b = -\frac{1}{4\pi\varepsilon_0}\frac{zZe^2}{pv}\cot\frac{\theta}{2} \tag{2.7}$$

where θ is negative for unlike charges and $p = \gamma\beta mc$ is the relativistic momentum in the center-of-mass frame (dropping the center-of-mass label CM), see Appendix B for

derivation. Solving for the cotangent in (2.7) and substituting into (2.6) gives

$$Q_{CM}^2 = 4p^2 \frac{1}{1 + \left(4\pi\varepsilon_0 \frac{bpv}{zZe^2}\right)^2} = \left(\frac{1}{4\pi\varepsilon_0}\frac{2zZe^2}{v}\right)^2 \frac{1}{b^2 + {b_{min}^c}^2}. \tag{2.8}$$

where $b_{min}^c = zZe^2/4\pi\varepsilon_0 pv$ is the classical minimum impact parameter found by setting $\theta = \pi$ in equation (2.7) for the case where the particle makes a head-on collision and reverses direction. Since the momentum transfer is the same in all reference frames, $Q_{Lab} = Q_{CM} = \sqrt{2mK_f}$, the energy transfer ΔE is equal to the final kinetic energy of the electron in the lab frame $\Delta E = K_f$ such that

$$\Delta E = \frac{2}{mv^2}\left(\frac{zZe^2}{4\pi\varepsilon_0}\right)^2 \frac{1}{b^2 + {b_{min}^c}^2}. \tag{2.9}$$

Equation (2.9) may be used to demonstrate why orbital electrons are more efficient at absorbing energy than an atomic nucleus. For an atom with Z electrons and a mass number A, the energy transfer by a singly charged incident particle such as a proton $z = 1$ to a nucleus as opposed to an electron from equation (2.9) would be $\Delta E \propto Z^2/Am_p$ with m_p being the proton mass while the energy transfer to an orbital electron with mass m_e is proportional to $1/m_e$. Considering that $A \sim 2Z$ and $m_p/m_e \cong 1836$, the energy transfer to the nucleus of a target atom is smaller by $\sim Z/3672$ showing that, due to their lighter mass, orbital electrons absorb the majority of Coulomb interaction collisions where $b \gg b_{min}$, which is the majority of collisions. This supports the assumption that only interactions between energetic particles and target nuclei may be neglected.

Maximum Energy Transfer

The energy transfer has a maximum value allowed by kinematics at the minimum impact parameter b_{min}^{c}. This classical minimum impact parameter varies inversely as the velocity squared, v^{-2} , so that the impact parameter becomes very small for large velocities. However, the uncertainty principle requires that the impact parameter can be no less than the uncertainty in the incident particle's position. By setting the minimum parameter equal to the de Broglie wavelength of the incident particle, having mass *m* with momentum $p = \gamma\beta mc$ in the heavy particle rest frame, and utilizing the de Broglie wavelength equation, $\lambda = h/p$, the quantum-mechanical minimum impact parameter[2] becomes

$$b_{min}^{q} = \frac{h}{\gamma\beta mc}. \tag{2.10}$$

For the case of 1 GeV protons, $b_{min}^{q} \approx 10^{3} b_{min}^{c}$, which justifies use of the quantum-mechanical minimum impact parameter in the derivation of the total energy loss cross section.

The maximum allowed energy transfer in a relativistic elastic head-on collision is found through kinematics to be

$$\Delta E_{max} = \frac{2\gamma^{2}\beta^{2}mc^{2}}{1 + 2\gamma\left(\frac{m}{M}\right) + \left(\frac{m}{M}\right)^{2}}. \tag{2.11}$$

In the event $M \gg m$, $\Delta E_{max} \cong 2\gamma^{2}\beta^{2}mc^{2}$ is a sufficient approximation for protons with kinetic energies < 340 GeV. The maximum energy transfer given by equation (2.11) for a 1 GeV proton is 2.9 MeV or 0.3% of the proton kinetic energy. This result gives credence to

[2] Alternative derivations in the literature [75], [85], [89] use the Heisenberg uncertainty principle to derive the minimum quantum impact parameter b_{min}^{q} with the same result expect replacing *h* with $\hbar$.

the assumption that the change of momentum to the proton is very small and that the proton trajectory undergoes very small deviations.

Minimum Energy Transfer

Examining the energy transfer equation (2.9), it would seem that as $b \to \infty,\ \Delta E \to 0$. Again, this is an erroneous conclusion due to the classically based collision analysis and the fact that we neglected binding energy and assumed a free electron. From quantum mechanics it is known that bound systems may only absorb energy in quantized amounts. For the case of energy transfer due to relativistic Coulomb fields, the field of a relativistic charged particle with velocity βc varies in time as $\Delta t \approx b/\gamma\beta c$ where b is the impact parameter (see Appendix C for a derivation of relativistic electromagnetic fields).

The ground state target electron may be approximated as a harmonic oscillator with frequency f_0. If the time the incident particle interacts with the electron Δt is long compared to the electron orbital period $1/f_0$, then the electron will respond adiabatically. It will absorb energy slowly over many oscillations, transitioning to lower excited states and returning to the ground state without appreciable energy transfer. However, if the characteristic frequency of the incident field, $1/\Delta t$, is close to the resonance frequency of the electron there will be a large energy transfer. The limiting condition is $\Delta t \cong 1/f_0$, which means $b_{max} \cong \gamma\beta c/f_0$.

Now for the real case of an atom with Z elections, each electron may act as a set of oscillators with frequencies corresponding to the transition energies, where f_i is related to the ith energy $E_i = hf_i$. The energy transfer to a single electron is $\propto \ln f_i$ [74]. By summing all the contributions from all Z electrons, the electronic binding energy for an atom may then be characterized by a weighted geometric mean of frequencies f_i with weights w_i such that

$$Z \ln\langle f \rangle = \sum_i w_i \ln f_i \tag{2.12}$$

[75], [76]. The sum rule $Z = \sum_i w_i$ has been used to group Z electrons into sets of electrons w_i being represented by the resonant frequency f_i.

The mean ionization/excitation energy I defined as the average minimum allowed energy transfer that includes excitation processes and ionization may be set equal to the characteristic minimum energy transfer as

$$I = h\langle f \rangle. \tag{2.13}$$

Since I accounts for all possible atomic ionizations as well as excitations, it is proportional to the number of electrons Z of the absorbing material and larger than the energy required to remove the least bound electron from the atom. While the mean ionization/excitation energy may, in principal, be calculated from the transition frequencies and related strengths, this task can be very difficult, and the standard method of progression is to utilize empirical values for I [77],[78]. From experimental data, a useful approximation for the mean excitation/ionization energy, in eV, is given in [79] as

$$I = 9.1Z\left(1 + 1.9Z^{-2/3}\right). \tag{2.14}$$

I is also often estimated as (10 eV)Z for Z >15. For an absorber other than a monatomic medium, Z should be replaced with

$$Z_{eff} = \frac{\sum_i \left(\frac{w_i}{A_i}\right) Z_i^2}{\sum_i \left(\frac{w_i}{A_i}\right) Z_i} \tag{2.15}$$

where w_i is weight fraction defined as the weight of the ith molecular component divided by the total molecular weight, A_i is the atomic weight, and Z_i the atomic number of the ith

element of the molecule.

Values of I have been compiled in table 2.1 for various gases relevant to the IPM system, each with corresponding atomic number Z, mass number A, and density ρ. E_{ex} and E_I are the energies required to produce the first excited stated and to remove the first electron, respectively. The W-value W_I in table 2.1, to be defined shortly, is a measure of the amount of energy actually required to form an ion-electron pair. As a general rule, about half the energy from an incident particle transferred to an absorbing atom or molecule is spent on excitation, and so the energy to form an ion pair W_I is always larger than the ionization energy and roughly twice E_I [80]. From empirical observations, such as W_I in table 2.1, the energy to create ion-electron pairs is ~30 eV and is fairly constant for most gases and types of incident particles [81].

2.1.3 Energy Loss

An energetic particle loses energy to the surrounding medium through excitations and ionizations. The number of ion-electron pairs created as the incident particle traverses a thickness of the target material may be calculated from the energy lost by the particle and the energy required for ionization W_I. Continuing with the same model as before, where an incident heavy particle interacts with an atomic electron such that the electron may be considered free and at rest, the total energy lost by the energetic particle with charge number z, charge ze , and momentum γMv is the energy loss per electron collision times the number of electrons in the surrounding medium.

By using the expression for the energy transfer due to a single collision at an impact parameter b, $\Delta E(b)$ from equation (2.9) and the illustration in figure 2.4 showing the infinitesimal interaction volume dV at b, the differential total energy loss is given by

Table 2.1 IPM gas values of density ρ at NTP (NTP: 20° C, 1 atm), first excitation energy E_{ex} and ionization energy E_I, mean ionization/excitation energy I, and effective energy to produce an ion-electron pair W_I.[3]

Gas	*Name*	*Z*	*A*	ρ (g/cm^3)	E_{ex} (eV)	E_I (eV)	I (eV)	W_I (eV)
H_2	Hydrogen	2	2	8.38×10^{-5}	10.8	15.4	19.2	37
H_2O	Water (Vapor)	10	18	7.56×10^{-4}		12.6	71.6	38
N_2	Nitrogen	14	28	1.17×10^{-3}	8.1	16.7	85.0	35
C_2H_6	Ethane	14	30	1.26×10^{-3}	8.2	11.5	45.4	26
O_2	Oxygen	16	32	1.33×10^{-3}	7.9	12.8	95.0	31
Ar	Argon	18	40	1.66×10^{-3}	11.6	15.7	188	26
CO_2	Carbon Dioxide	22	44	1.86×10^{-3}	7.0	13.8	85.9	34

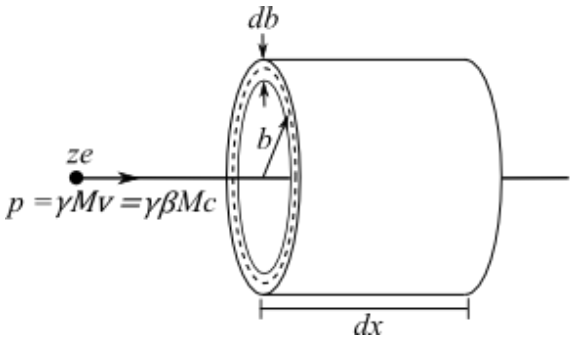

Figure 2.4 Graphical representation of the infinitesimal interaction volume of an incident particle with mass *M* at an impact parameter *b*.

[3] Data compiled from [71], [77], [80], [86], [119], [248–252][86], [119], [248–252].

$$-dE(b) = \Delta E(b)\, N_e\, dV = \Delta E(b)\, N_e\, 2\pi b\, db\, dx \tag{2.16}$$

where N_e depends on the absorber atomic number Z, weight A, density ρ, and Avogadro's number N_A as $N_e = \rho Z N_A / A$.

The total differential energy loss per unit length may be found by integrating (2.16) over all impact parameters up to the limit b_{max} established by the minimum allowed energy transfers

$$-\frac{dE}{dx} = 4\pi N_e \left(\frac{ze^2}{4\pi\varepsilon_0}\right)^2 \frac{1}{m_e v^2} \int_0^{b_{max}} \frac{b}{b_{min}^2 + b^2}\, db. \tag{2.17}$$

The solution to the integral in (2.17) gives $\frac{1}{2}\ln(b_{max}^2/b_{min}^2 + 1)$ but since $b_{max} \gg b_{min}$ the integral is approximately $\ln(b_{max}/b_{min})$ making the energy loss

$$-\frac{dE}{dx} = 4\pi N_e \left(\frac{ze^2}{4\pi\varepsilon_0}\right)^2 \frac{1}{m_e v^2} \ln\frac{b_{max}}{b_{min}}. \tag{2.18}$$

Inserting the expressions for the maximum and minimum impact parameters found in found in section 2.1.2 into equation (2.18) and using the minimum ionization/excitation energy $I = h\langle f \rangle$, the energy loss becomes

$$-\frac{dE}{dx} = 4\pi \left(\frac{ze^2}{4\pi\varepsilon_0}\right)^2 N_A \frac{Z}{A} \rho \frac{1}{m_e c^2} \frac{1}{\beta^2} \ln\frac{\gamma^2 \beta^2 m_e c^2}{I}. \tag{2.19}$$

The semi-classical semi-relativistic equation for the energy loss shown in (2.19) is similar to the original result Neils Bohr derived in 1915 [82] and illustrates many of the fundamental principles of energy loss. However, a more complete theory was given by Bethe in [83].

Bethe Formula

Bethe used quantum mechanics to solve the hard and soft collision cases separately and then combined them to form a fully quantum mechanical and relativistic theory of energy loss by

moving charged particles.[4]

$$-\frac{dE}{dx} = 4\pi\left(\frac{e^2}{4\pi\varepsilon_0}\right)^2 N_A \frac{Z}{A}\rho\frac{z^2}{m_e c^2}\frac{1}{\beta^2}\left[\ln\frac{2\gamma^2\beta^2 m_e c^2}{I} - \beta^2 - \frac{\delta}{2} - \frac{C}{Z}\right] \qquad (2.20)$$

is the Bethe formula for energy loss, where $\delta/2$ and *C/Z* are density and shell corrections, respectively. The second term, $-\beta^2$, in (2.20) is a relativistic correction that arises when taking into consideration the spin of the incident particle. The $\delta/2$ term is a density effect that results from the polarization of the medium by the incident particle and is more pronounced for condensed targets. At large γ, the energetic particles' transverse electric fields expand (as discussed in Appendix C) causing absorber polarization to produce a screening effect that reduces the energy due to soft collisions [84].

The shell correction, *C/Z* where *C* depends on β and the atomic number *Z*, is a low energy correction, significant when $\beta \lesssim 0.4$, under the assumption that the energetic particle velocity is much larger than the target electron velocity. If the incoming particle energy is not much larger than the orbital electron velocity, then there will be no significant energy transfer. Thus, for low energy particles, the most tightly bound and fastest electrons, K shell electrons being foremost, will no longer contribute to energy loss [85]. The shell and density corrections are negligible for 1 GeV protons.

Equation (2.20) is valid for $0.05 < \beta\gamma < 1000$ to within a few percent [86] for heavy particles. For $0.01 < \beta < 0.05$ there is not a satisfactory theory and values of energy loss are found through fits to empirical data. For $\beta < 0.01$ the energy loss has been found to be $\propto \beta$

[4] For a full quantum mechanical derivation of the Bethe formula see [85]. See also[74] and [253] for additional treatment. For a full review of the correction terms in the Bethe equation see [93] and the references therein.

[87]. The energy loss $-dE/dx$ is often referred to as the linear stopping power and generally given in units of $\mathrm{MeV} \cdot \mathrm{cm}^{-1}$, while the mass stopping power is defined as

$$S = -\frac{1}{\rho}\frac{dE}{dx} \tag{2.21}$$

It describes the energy loss per g/cm^2 of absorbing medium traversed and is given in $\mathrm{MeV} \cdot \mathrm{cm}^2 \cdot \mathrm{g}^{-1}$ with ρ being the density. It can be seen from equation (2.20) that, for a given incident particle, the mass stopping power varies little for various materials because the ratio of the atomic weight to the atomic number *Z/A* is approximately 2 for most elements. This means that energy loss depends more on the material thickness in units of mass/area than on the specific material traversed.

The stopping power for a mixture may be evaluated by using Bragg's additivity rule. This rule states that the energy loss due to the traversal of a combination of absorbers is equivalent to that obtained from traversing pure layers of each absorber in the right proportions [88]. The total stopping power is then

$$S = \sum_i w_i S_i \tag{2.22}$$

where w_i is the same weight defined in equation (2.15), the ith component is the ith compound in the absorber mixture, and S_i is the stopping power of said component (see [84] and [86] for further discussion on mixture stopping power calculations). In reality the total stopping power is a sum of the energy loss due to collisions expressed by (2.20) plus that of loss due to radiation, such as bremsstrahlung. However, as discussed earlier, since radiation losses are negligible in the IPM all energy loss will be considered collisional loss.

Furthermore, it is worth noting that the Bethe formula should be viewed as a

statistical average over many discrete interactions. The energy loss distribution, shown in figure 2.2, shows that a single energetic particle will undergo many small energy transfers and a few large energy transfers. Thus, individual particle energy losses may have large fluctuations. It is important to remember that the energy loss by an energetic particle is a stochastic process of hard and soft collisions that may result in an average energy loss less than the ionization energy of the absorber [74].

2.1.4 Ionization

Secondary Ionization

As an energetic particle passes through a medium it transfers energy to orbital electrons. When the energy transfer is larger than the ionization energy of the atom or molecule, the electron will be ejected from its orbit. Ejected electrons with energies larger than the ionization energy of the material may produce further ionization and these electrons are often referred to as δ rays. Their energies may assume any value from the minimum cut off energy, ~15 eV for most gases, as seen by E_I in table 2.1, to the kinetically allowed maximum kinetic energy, which is 2.9 MeV for 1 GeV protons.

The probability of a δ electron receiving an energy between E and $E+dE$ has been shown in [89] to be $\propto 1/E^2$, meaning that the majority of electrons with the ability to cause secondary ionization occur with lower energies. In addition, through kinematics it may be shown that the emission angle θ of δ rays relative to the path of the incident particle as a function of δ ray energy E is given by

$$\cos^2\theta = \frac{E}{E_{max}} \tag{2.23}$$

where E_{max} is the maximum allowed kinetic energy. Because most δ electrons have low

energies, up to a few keV, equation (2.23) shows that the distribution of δ electrons peaks in the directions perpendicular to the 1 GeV proton trajectory.

Primary Ionization

In each interaction between an energetic particle and the particles in the surrounding medium in which a larger transfer of energy occurs than is required for ionization, an ion-electron pair is created. Of these, some of the electrons have enough energy to induce further ionization. The total number of pairs created is defined by

$$n_T = \frac{\Delta E_T}{W_I} \tag{2.24}$$

where ΔE_T is the total energy lost in the medium and W_I is the average energy required to create one ion-electron pair, as reported in table 2.1. The total energy loss may be found by multiplying the average energy loss per unit length given by (2.20) by the length of the gas volume or, alternatively, by multiplying the stopping power S in equation (2.21) by the density and material thickness. W values are often found with (2.24) by calculating or measuring the total energy loss by an energetic particle and the total number of particles created [90].

The total number ion pairs is the sum of pairs created due to primary ionizing events by the incident particle and pairs created through secondary ionization by δ rays. A detector does not measure the energy loss of the incident particle directly, but the information carriers produced by the energy loss such as ions or photons in the event of excitation. Since there are multiple modes by which a particle may lose energy in a detector chamber but not all modes leading to ion pair formation, the number of ion-electron pairs created will exhibit statistical fluctuations. The number of pairs formed will follow a Poisson distribution since there are a

given number of pairs formed within a fixed distance independently of one another with an average n_T and a standard deviation given by $\sqrt{n_T}$. However, the measured standard deviation is often smaller than given by $\sqrt{n_T}$ due to the inefficiency of some detectors at converting energy loss into measurable particles. As such, the Fano factor *F* is introduced into the standard deviation as $\sigma_{n_T} = \sqrt{F n_T}$ to account for this deviation from a pure Poisson process [91] with values of *F* being 0.2 – 0.4 for most molecular gases [92].

For a detector measuring single particles, this would place a limit on the detector resolution, Since the incident beam is composed *N* particles, each creating an average of n_T pairs with standard deviation σ_{n_T}, the total number of ion pairs n_{total} created is then $N n_T$ while the standard deviations add in quadrature resulting in $\sigma_{total} = \sqrt{N \sigma_{n_T}^2}$. The relative uncertainty σ_{total}/n_{total} of the mean number of particles collected for a beam is $1/\sqrt{N}$ times the relative uncertainty for measuring the ion pairs due to a single incident particle. This, coupled with the reduction of the standard deviation by the Fano factor, reduces the effect stochastic measurement uncertainty. The influence of measurement fluctuations will be taken into consideration during the analysis of profile accuracy presented later.

Due to the statistical nature of secondary ionization, it is difficult to separate primary and secondary ionization contributions. Newer methods of calculation based on the work in [93] (see also the references in [94] for further information on the history of ionization modeling) have allowed models such as the photoabsorption ionization and relaxation (PAIR) model which relates the amount of ionization to the cross section for photoabsorption of the medium [94]. Calculations of the number of primary ionizations have shown good agreement with experiments and an approximation for the primary ionization as a function of

the total molecular charge Z_m and the mean atomic charge of the constituent atoms $\bar{Z}$ is given in [94] as

$$n_p = 3.996 \frac{Z_m}{\bar{Z}^{0.4}} - 0.025 \left(\frac{Z_m}{\bar{Z}^{0.4}} \right)^2 . \tag{2.25}$$

Values of the total and primary ionizations are reported for selected gases in table 2.2 and have been normalized by gas pressure. Multiplying quantities in table 2.2 by the gas pressure and length of the detector gives the number of ion pairs created over the detector region.

A full qualitative view of a proton-gas interaction is shown in figure 2.5 and for an energetic proton with negligible trajectory deviation. It includes both soft and hard collisions resulting in primary ionization events as well as excitations clustered around the proton trajectory. Also shown are a number of primary ionized δ electrons producing secondary ionization trails perpendicular to the incident particle path. With an understanding of the beam-gas interaction mechanisms and knowledge of the gas composition in the SNS ring, it is possible to estimate the number of ion-electron pairs and, subsequently the expected signal size.

2.2 IPM Ionization Estimation

The process of estimating the ionization signal consists of characterizing the residual gas present, applying the general principles of ionizing interactions set forth in the previous section, and identifying mechanisms of primary signal loss. In addition, it is important to quantify the gas pressure characteristics which allow for the analysis of possible errors introduced by uncontrollable environmental conditions.

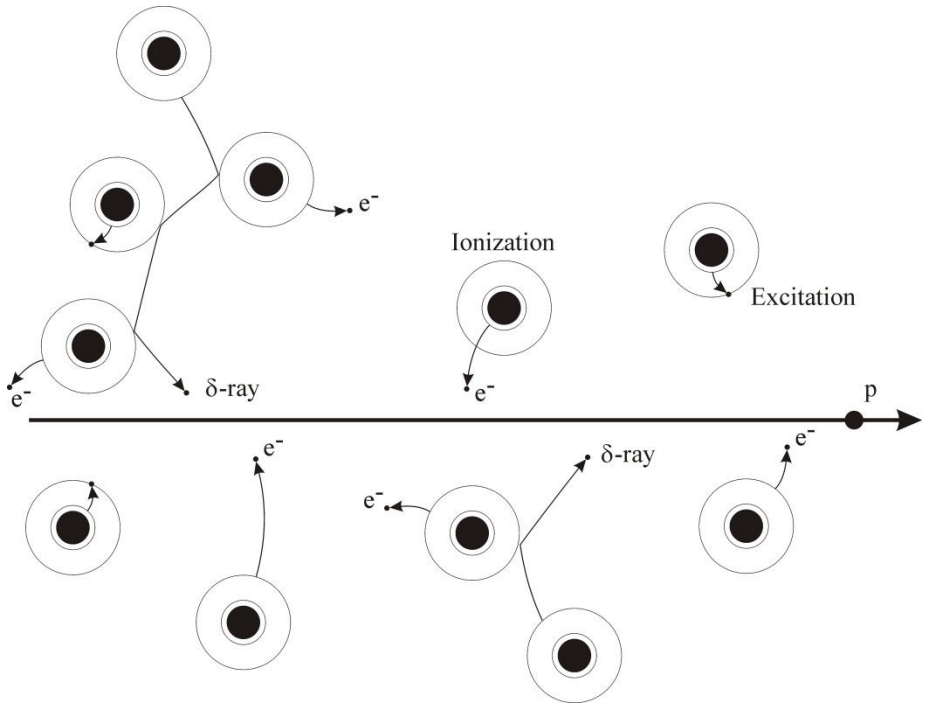

Figure 2.5 Pictorial representation of the ionization of gas molecules by an energetic proton p showing ionized electrons and secondary ionizing δ rays .

Table 2.2 Values of the total number of ionized particles n_T and primary ionized particles n_p for selected gases. Values of n_T and n_p are given in ion pairs·cm^{-1}·atm^{-1} and where the values are at NTP.[5]

	H_2	H_2O	N_2	C_2H_6	O_2	Ar	CO_2
n_T	9.2	~19	56	112	73	97	100
n_p	5.2	6.2	10	48	22	29.4	34

[5] Values are taken from [86][86] and [119]. The value for primary ionization of water was calculated from equation (2.25) .and the total by multiplying the number of primary ion pairs by 3, which is the approximate factor of total pairs to primary pairs.

2.2.1 Residual Gas Composition

Considering that the number of ion pairs produced is related to the target gas as illustrated in table 2.2, identifying the individual gases and their fractional contributions is necessary for further calculations. The composition of the residual gas is determined primarily by the outgassing properties of the accelerator components, air leaks, and the pumping efficiency of the gas constituents. Vacuum chamber components in SNS are made from 316 stainless steel. Unbaked stainless steel thermal outgassing rates per square centimeter of surface area for a few common accelerator vacuum gas components such as H_2, H_2O, CO_2, and CO are $7x10^{-12}$, $3x10^{-10}$, $5x10^{-13}$, and $5x10^{-12}$, respectively, in units of Torr $\cdot\ell\cdot cm^{-2}\cdot s^{-1}$ [95].

In order to reduce instabilities caused by secondary electrons, which will be discussed in more detail later, all components installed in the SNS ring undergo interior TiN coating. It has been found that this coating acts as a partial hydrogen barrier reducing the hydrogen outgassing rate [96]. While an initial estimation would conclude that water dominates the residual gas, the Gamma TiTan 300L Ion Pumps used in the ring are inefficient at pumping hydrogen and noble gases [97].

Residual Gas Analysis

A residual gas analysis (RGA) was taken using a Stanford Research System RGA with 100 u scanning capability [98] upstream of the IPM location. The RGA is an open ion source that uses ~70 eV electrons to ionize gas molecules after which a quadrupole filter measures the currents of different ion species based on their charge-to-mass ratio. The RGA assumes that all ion species measured are singly ionized and plots the currents measured for different masses. An RGA taken on October 26, 2007 upstream of the RF section in the SNS ring D Straight is shown in figure 2.6. Each pure gas has a specific fragmentation pattern known as a

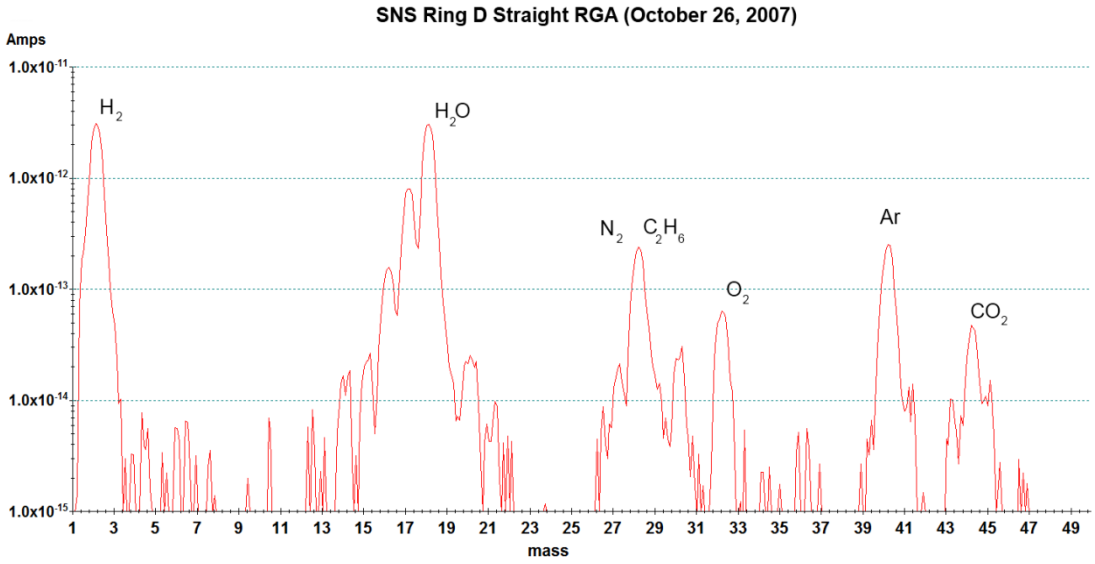

Figure 2.6 Residual gas analysis taken upstream of the RF cavities in the SNS ring D straight on October 26, 2007. Molecule/atom names for the main gas components are labeled above their respective peaks

cracking pattern, e.g., $H_2O \rightarrow H_2O^+ + HO^+ O^+ + H_2^+ + H^+$ where H_2O^+ has the largest ionization cross section [99]. The largest peaks in figure 2.6 have been analyzed and labeled with their respective gases.

The RGA used in this study is to be taken more as a qualitative tool since the analyzer used cannot distinguish between doubly ionized particles and singly ionized species with the same charge to mass ratio. In addition, it is difficult to differentiate between species with the same mass, such as nitrogen and carbon monoxide molecules, which both have a peak at mass 28. For the case in figure 2.6, nitrogen has a peak at 14 about one tenth that of nitrogen 28 while carbon monoxide would have a peak at mass 12 one twentieth that of mass 28 [100]. The small relative size of the mass 12 peak indicates the residual gas contains nitrogen as opposed to carbon monoxide and the contribution of CO may be considered negligible.

Partial Pressure Calculation

The currents measured with an RGA are not a straightforward superposition from the fractional composition of the pure gases. The actual amount of a pure gas found with an RGA depends on a number of factors including the probability of ionizing a particular mass fragment, the probability that the resulting ion will enter and pass through the quadrupole, the fact that RGAs differ in sensitivity to different ionization products, and most RGAs, including the one used, are calibrated to be sensitive to mass 28, or nitrogen.

The equation relating RGA current peak at mass *B* from gas *A*, I_{AB}, to the partial pressure of gas *A* is

$$PP_A = \frac{I_{AB} \cdot FF_{N_2 28}}{FF_{AB} \cdot XF_A \cdot TF_B \cdot DF_B \cdot S} \tag{2.26}$$

where $FF_{N_2 28}$ is the mass 28, or nitrogen, fragmentation factor, XF_A is the ionization probability for gas *A*, and TF_B is the transmission factor, which is a measure of how many ions of mass *B* make it through the detector. DF_B is a relative current detection factor for mass *B*, and *S* is an instrument-specific sensitivity factor to mass 28 in Amps/Torr [101]. For example, the partial pressure of hydrogen with a main peak at mass 2 is $PP_{H_2} = I_{H_2 2} \cdot FF_{N_2 28} \cdot FF_{H_2 2}^{-1} \cdot XF_{H_2}^{-1} \cdot TF_2^{-1} \cdot DF_2^{-1} \cdot S^{-1}$ where the detection factor *DF* is usually set to 1 [101]. The current $I_{H_2 2}$ taken from figure 2.6 is $3.2\text{x}10^{-11}$ amps and the fragmentation factor and ionization probability are found in commonly used tables such as in [101] with $FF_{H_2 2} = 0.95$, $XF_{H_2} = 0.44$. The quadrupole transmission factor relative to nitrogen is 28/*B* [102], therefore, $PP_{H_2} = 5.47\text{x}10^{-9}$ Torr.

While the RGA is not a reliable source for absolute pressure measurements, equation (2.26) may be used to calculate the fractional pressure composition. Table 2.3 shows

Table 2.3 Calculated pressure fractions for constituent pure gases in the IPM residual gas

	H_2	H_2O	N_2	C_2H_6	O_2	Ar	CO_2
PP/P_{Total}	0.113	0.739	0.029	0.032	0.010	0.069	0.007

calculated pressure fractions based on the RGA in figure 2.6. For estimations, the residual gas may be simplified as 11% hydrogen, 74% water, and 15% other, where other has a weighted mass of ~34 u. It can be seen that the IPM residual gas is primarily composed of water vapor and therefore the larger mass of water will place limitations on the IPM ion collection mode. The IPM will be designed with a vacuum port capable of affixing a residual gas analyzer in order to allow for vacuum studies of the system and comparison with theoretical calculations.

2.2.2 IPM Pressure

In order to achieve the 1 W/m beam loss requirement, the SNS ring was designed to limit the beam lost through residual gas interactions such as nuclear scattering, multi-Coulomb scattering, and residual gas ionization. Of the beam-loss mechanisms, the residual gas density is a limiting source [103] as it contributes to an instability, referred to as the e-p instability, which arises from the coupling of electrons freed through residual gas ionizations, beam loss, or ionized residual gas particles releasing secondary electrons after contacting the beam pipe. The secondary electrons are then accelerated by the beam-wall potential and receive enough energy to release tertiary electrons, leading to an electron cloud accumulation known as multipacting [104].

To mitigate the aforementioned gas-related instabilities, in addition to the TiN coating

that reduces secondary electron emission, the SNS ring was designed to operate with a 10^{-9} Torr scale vacuum [103].

Residual-Gas Temperature

In the ultra-high vacuum (UHV) regime, ~10^{-9} Torr, the mean free path of gas molecules is much larger than the dimensions of the volume. For gas particles with an abundance-weighted average diameter of 2.8 Å, the mean free path, defined in Appendix A eq. (A.6) for a pressure range P of 10^{-8} to 10^{-9} Torr and temperature of 70 °F is ~50 km, while the beam pipe diameter is 25.4 cm. In this vacuum regime, known as molecular flow, collisions between gas molecules are rare and collective fluid behavior may be ignored. Gas properties are characterized by collisions with the chamber walls and consequently, the temperature is determined by the chamber walls.

In addition to ambient temperature, the beam image current is a possible heat source. The positively charged proton beam's electric fields induce currents in the surrounding pipe wall. The 300 series stainless steel used for the accelerator structure has a finite conductivity σ of ~1.3 S/m. This results ([74] and [105]) in exponentially decaying fields and currents that depend on distance d within the conductor as $e^{-d/\delta}$. The decay constant δ is the skin depth defined by

$$\delta = \frac{1}{\sqrt{\pi\mu\sigma f}} \tag{2.27}$$

where μ is the magnetic permeability and f is the frequency of the electromagnetic field. Furthermore, the electric fields drop off much more rapidly leaving the image current generated by the more deeply penetrating magnetic field as the dominant contributor to resistive wall heating [105].

A simple calculation shows that beam-induced resistive wall heating is not a significant factor in residual gas temperature. The average power $\langle P \rangle$ dissipated due to a peak beam current I_{peak} is $\langle P \rangle = DF \cdot I_{peak}^2 \cdot R$, where *DF* is the macro-pulse duty factor of 0.06 and the resistance of the pipe *R* is the length ℓ divided by the conductivity times the cross-sectional area *A* of the conducting region. The cross-sectional area may be approximated as $2\pi r\delta$ where r is the pipe inner radius of 12.7 cm.

For a peak ring beam current of 90 A, ring length of 248 m, and skin depth (for a 1 MHz ring frequency) of 4 mm, the average power dissipated is 276 W for the whole ring during a 16.7 ms accumulation cycle. The conservation of energy requires the internal energy change of the beam pipe be equal to the net energy flow in and out of the pipe walls. In the absence of work, the internal energy change per unit time $\Delta\dot{U} = mc\, dT/dt$, where m is mass and c the specific heat, is equal to the power going in P_{beam} minus the heat transfer out through convection $\dot{Q}_{conv} = hA_s(T - T_s)$ and radiation $\dot{Q}_{rad} = \varepsilon\sigma A_s(T^4 - T_s^4)$ with A_S being the surface area, ε the emissivity, σ the Stefan-Boltzmann constant, T_s the surrounding ambient temperature, and h the convection heat transfer coefficient.

The equation for the temperature within the pipe walls

$$mc\frac{dT}{dt} = P_{beam} - hA(T - T_s) - \varepsilon\sigma A(T^4 - T_s^4) \tag{2.28}$$

may be solved numerically. The results are shown in figure 2.7 for an input beam-induced heat load of 276 W, emissivity of polished stainless steel of 0.17 [106], the mass found from the density of 8000 kg·m^{-3} and the volume of the 4 mm thick pipe wall, and a specific heat capacity of stainless steel of 502 J·kg^{-1}·K^{-1}. The surface area was assumed to be that of the outer surface since the vacuum inside the chamber precludes heat loss due to air flow, and

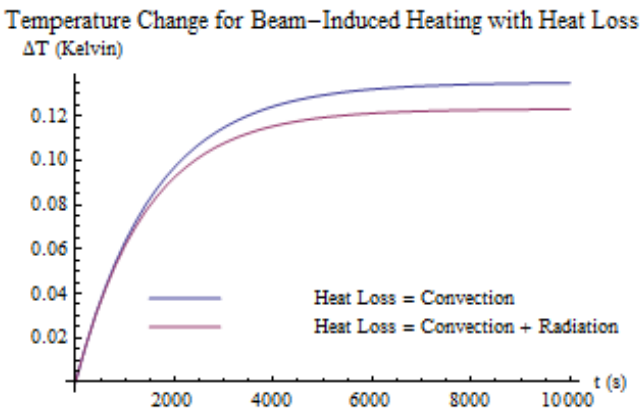

Figure 2.7 Temperature change in the beam pipe wall with heat loss due to convection and radiation for a convection heat transfer coefficient of 10 W/m^2 K.

net radiation emitted by the interior is assumed to be small. The heat transfer coefficient *h* is an experimentally determined parameter which is generally in the range of 5-25 W·m^{-2}·K^{-1} for free gas [106] and has been chosen here to be an intermediate value of 10. Heat transfer by conduction is considered to be negligible due to the much larger surface area available for convection and radiation than the area occupied by connecting support structures.

Figure 2.7 illustrates that, while the maximum temperature change is ~0.15°C or 0.3°F, the thermodynamic processes involved in the heat transfer occur on time scales of 10^3 s, which are much longer than accelerator times, 10^{-3} s. As such, the beam-induced pipe heating may be considered negligible. The residual gas temperature is assumed to be the ambient ring tunnel enclosure temperature of 68°F, or 20°C, and is taken to be constant as measurements of the temperature during run periods vary by no more than 1°F.

Pressure Profile

Since IPM functionality depends heavily on the residual gas density it is necessary to characterize the gas pressure in the IPM region. The SNS ring pressure is not constant with respect to longitudinal position. Vacuum pumps are placed periodically along the

accelerating structure at irregular intervals and, consequently, the gas pressure is at a minimum at the pump locations with maxima in between. The proposed location for the IPM, shown in figure 2.8, is downstream of the RF section in the ring D straight. Figure 2.8 also shows the locations of vacuum ion pumps (IP) and cold cathode gauges (CCG) used for pressure measurements.

The most probable speed of ideal gas molecules with molecular mass *m* and temperature *T* based on a Maxwell-Boltzmann distribution is

$$v_p = \sqrt{\frac{2k_B T}{\pi m}}. \tag{2.29}$$

For a temperature of 68°F and an average mass of 18.7 u, the average velocity of the residual gas is 288 m/s. Gas particles will travel 0.3 mm during the 1 μs ring pulses and 30 cm during an accumulation period of 1 ms. Consequently, the time it takes molecules to reach a pump is long compared to the events of interest. Therefore, global pressure may be considered constant with respect to time. There are processes that may affect local pressure. A simple analytical model may be used to calculate the pressure profile between the vacuum pumps on either side of the IPM location. The gas flow rate, or throughput, is defined through the pressure *P* in Torr and volume flow rate *S* in liter/s as

$$Q = PS. \tag{2.30}$$

Additionally, the throughput between two points may be defined [107] by

$$Q = C\Delta P. \tag{2.31}$$

where *C* is the conductance in liter/s of the structure between those two points and ΔP is the change in pressure. In the molecular flow regime, the conductance does not depend on

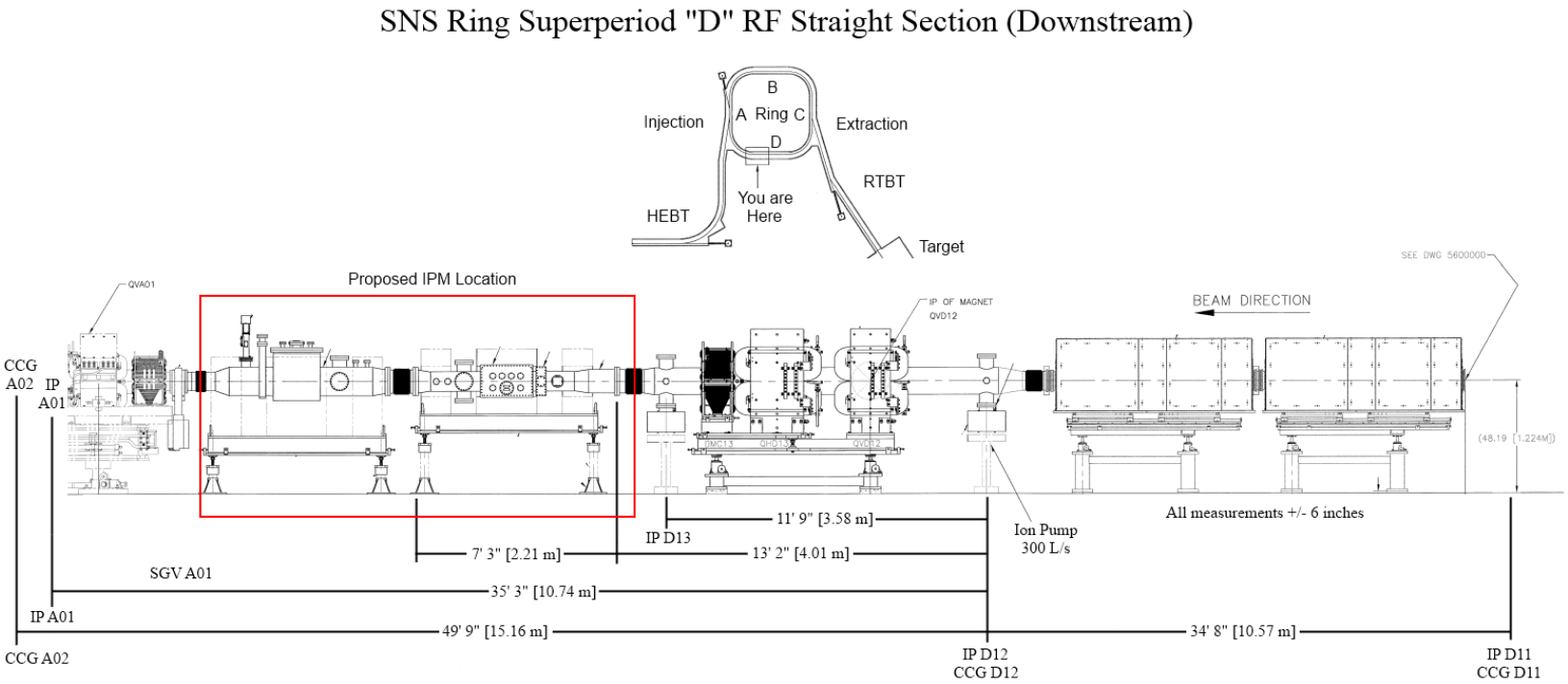

Figure 2.8 Drawing showing SNS ring D straight downstream of the RF cavities. The proposed IPM location is shown in the box. Cold cathode vacuum gauges (CCG), ion pumps (IP), and sector gate valves (SGV) are shown along with their respective longitudinal distances.

pressure and has been calculated in [108]. For a long circular tube of radius *r* for gas molecules of mass *M* at temperature *T*, the molecular flow specific conductance c_m, which is the conductance C_m multiplied by the length *L* as $c_m = C_m L$, is [109]

$$c_m = 97\pi r^3 \sqrt{\frac{T}{M}}. \tag{2.32}$$

A 1 cm long section of pipe with a 12.7 cm radius has a specific conductance of 2.5×10^5 liter $\cdot$ cm $\cdot$ s^{-1} for a gas with a temperature of 293.15 K and average mass of 18.6 u.

The flow rate is equal to the outgassing from the walls and for uniform outgassing the specific outgassing $q_0 = d\,Q(x)/dx$ is constant. From eq. (2.31) for the model shown in figure 2.9, the specific conductance and the pressure gradient in a length *dx* are related by $dP(x)/dx = -Q(x)/c_m$, where the minus sign denotes the direction of the gas flow. By taking the derivative of the rate of pressure change with respect to length *dx* and using the uniform specific outgassing rate *q*, the equation for the pressure becomes $d^2P/dx^2 = -q_0/c_m$. Integration of this equation uses the pressure at *x* = 0 and the pump with speed 2*S* from figure 2.9 as boundary conditions. For one side this gives $P = Q(0)/S = -q_0 L/-S =$

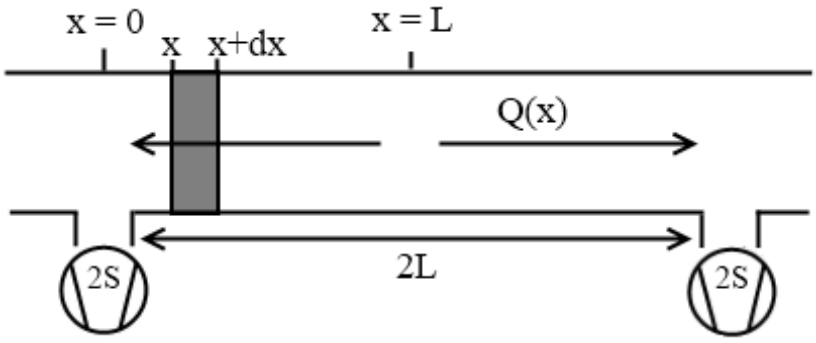

Figure 2.9 Graphical representation of a periodic vacuum chamber model with period of 2L and pumping speed S.

$q_0 L/S$ and, due to symmetry, the flow at the middle of the tube is $Q(L) = 0$. The pressure at a position x from the pump is [110]

$$P(x) = q_0 \left(\frac{2Lx - x^2}{2c_m} + \frac{L}{S} \right). \tag{2.33}$$

The result is a parabolic pressure profile between the pumps. The matter is complicated by the presence of the beam.

Ion-Induced Desorption

A uniform cylindrical beam of length L and charge eN where e is the elementary charge and N is the number of accumulated particles, has a potential inside the beam radius a of

$$V(r) = \frac{eN}{2\pi\varepsilon_0 L} \left[\frac{1}{2} - \frac{r^2}{2a^2} + \ln\left(\frac{b}{a}\right) \right] \tag{2.34}$$

where b is the vacuum chamber radius. Ions created by a fully accumulated beam of 1.5×10^{14} particles will accelerate through potentials from ~ 5 kV to ~15 kV depending on location [111]. Energetic residual gas ions can desorb gas from the pipe walls. The molecular desorption yield η, defined as the number of molecules desorbed per incident ion, is a function of the incident particle energy as well as the surface and surface condition. SNS vacuum chambers are unbaked due to the risk of leaking by large aperture flanges caused by the relative thermal motion induced by *in-situ* baking [112]. As such, the unbaked ion desorption yield for stainless steel ranges from ~5 to ~10 for incident particle energies above a few keV [113].

The ionization cross section, derived using the Bethe theory [114], [115], is given by

$$\sigma_i = 4\pi \left(\frac{\hbar}{m_e c}\right)^2 \left[\frac{M^2}{\beta^2} \ln\left(\frac{\beta^2}{1-\beta^2}\right) + \frac{C}{\beta^2} - M^2\right] \tag{2.35}$$

where M and C are related to the oscillator strengths of different molecular transitions. Using tabulated data for M^2 and C found in [116] the ionization cross sections due to a 1 GeV proton for the main residual gas constituents of H_2 and H_2O are found to be 2.09×10^{-19} cm^2 and 8.43×10^{-19} cm^2, while 1×10^{-18} cm^2 is used for the combined cross section for the remaining molecules. The additional linear gas load due to the beam is

$$q_{desorb} = \eta \sigma_i N_b P(x) \tag{2.36}$$

where N_b is the proton intensity averaged over a 16.7 ms cycle and $P(x)$ is the location dependent pressure. For the same case as shown in figure 2.9, with additional beam-induced desorption, solution of the pressure equation

$$\frac{d^2P}{dx^2} + \frac{b}{c_m} P + \frac{q_0}{c_m} = 0 \tag{2.37}$$

subject to the boundary condition $c_m \, dP/dx|_{x=0} = SP(0)$ and $c_m \, dP/dx|_{x=2L} = -SP(2L)$ results in a pressure of

$$P(x) = \frac{q_0}{b}\left[\frac{\cos\left(\sqrt{\frac{b}{c_m}}(x-L)\right)}{\cos\left(\sqrt{\frac{b}{c_m}}L\right) - \frac{\sqrt{bc_m}}{S}\sin\left(\sqrt{\frac{b}{c_m}}L\right)} - 1\right]. \tag{2.38}$$

The pressure profiles with beam, equation (2.38), and without, equation (2.33), are shown in figure 2.10 for ion desorption coefficients of 5 and 10. These were used with an SNS ion pump speed of $2S$ = 300 liter/s, gas percentages of 11% H_2, 74% H_2O, and 15% other, as well as thermal desorption rates taken from [95] for H_2, H_2O, and CO_2 of 7×10^{-12}, 3×10^{-10}, and 5×10^{-13} respectively in Torr · liter · cm^{-2} · s^{-1} for unbaked stainless steel. From

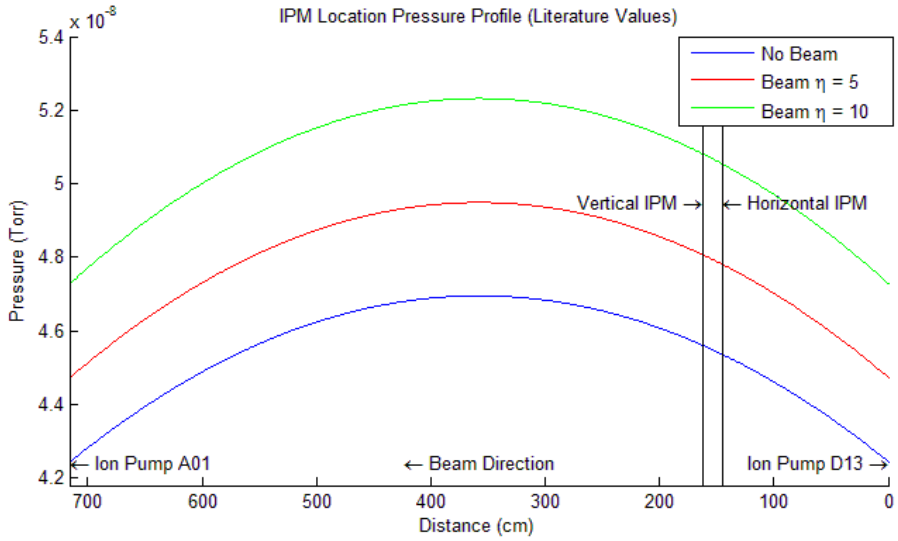

Figure 2.10 Pressure profile between identical lumped pumps using IPM location parameters with gas desorption rates taken from literature [95] **for a fully accumulated beam.**

figure 2.10 it may be seen that the pressure rise to the beam is small and accounts for ~2.5x10^{-9} Torr for the extreme case of η = 10.

Furthermore, the pressure difference between the pressure gauges and the IPM locations is no larger than 7% and the pressure difference between the pumps is ~0.5%. Emission of ions due to beam induced desorption is at least a factor of 10 less than for neutral molecules [117] and therefore makes a negligible contribution to the pressure rise. At a rate 0.1 [112], the desorption of neutral gas molecules by residual-gas electrons is small compared to that of ions. Additionally, electron-induced desorption of ions is even smaller as the fraction of ions desorbed for a species is 10^{-2} to 10^{-4} [118].

Data taken from cold cathode gauges surrounding the IPM location along with the measured beam in the ring is shown in figure 2.11. Pressures in CCG A02 are higher than those in CCG D12 due to the fact that CCG A02 is between ion pumps, illustrated by the pressure profile in figure 2.10, while CCG D12 sits directly over top of an ion pump.

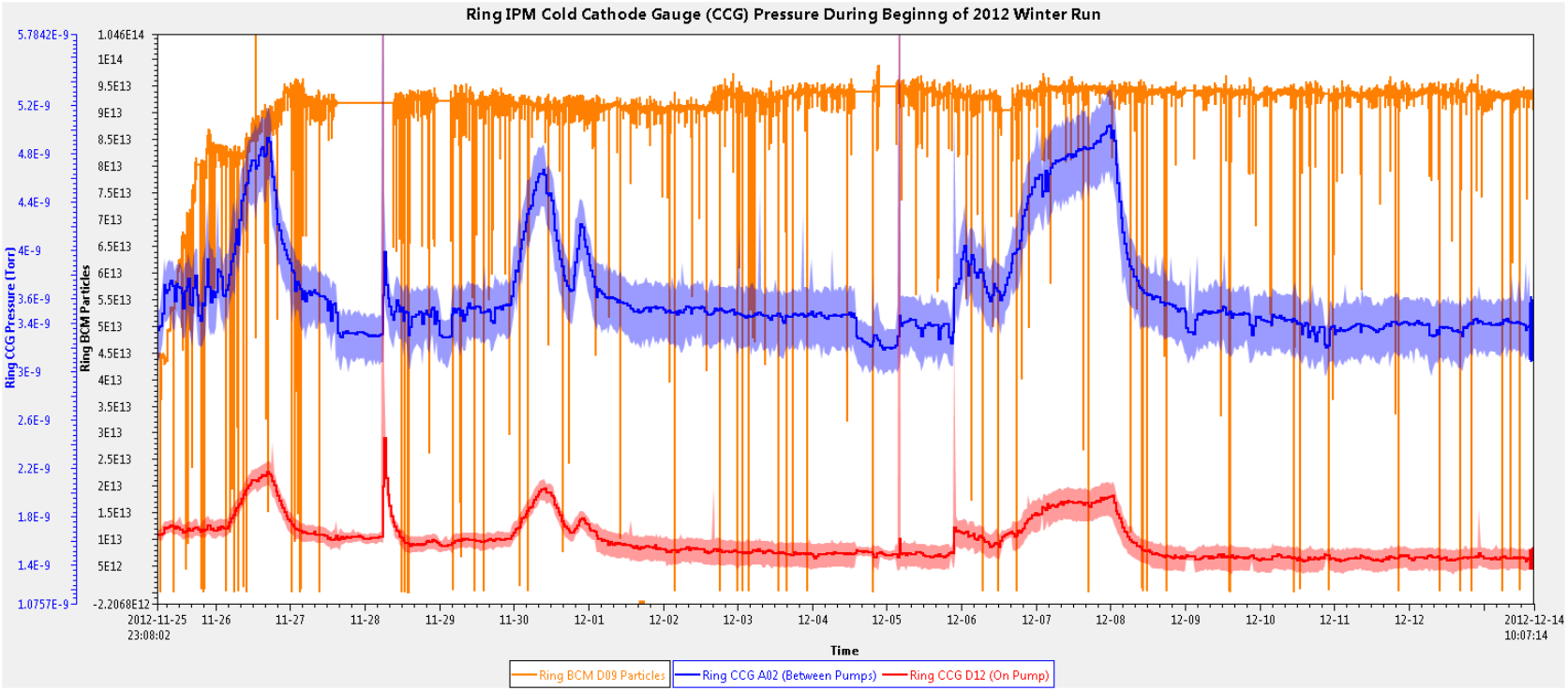

Figure 2.11 Cold cathode gauge pressures surrounding the IPM location in addition to the beam particles in the ring shown for the beginning of the 2012 winter run period starting in November 2012. CCG A02 is located downstream of the IPM and is located between ion pumps while CCG D12 is located upstream and sits directly over top of an ion pump.

Evidence for a beam induced pressure rise may be seen at the beginning of the run period during initial ramping of the beam and following periods when there is no beam in the ring for more than a few hours. After a period of approximately a day, the pressure decreases as the beam induced gas load is removed, and an equilibrium pressure is reached.

Barring any significant loss of beam, the pressure remains relatively constant at approximately $2x10^{-9}$ Torr in the IPM location but this value varies by about a factor of 2. Additionally, a long term study of multiple run cycles reveals that the overall pressure may vary by a factor of 10 depending on vacuum system maintenance. As such, it is necessary to design the IPM vacuum chamber with ports that will allow for monitoring the residual gas pressure and with a port for a residual gas analyzer. A pressure of $2x10^{-9}$ Torr corresponds to a residual gas density of $6.59x10^{7}$ gas molecules $\cdot$ cm^{-3} at 20°C.

2.2.3 Ion Estimation

As an energetic proton travels around the SNS ring, it interacts with neutral gas molecules of different species, ionizing a fraction of residual gas. The ionization products will have a certain probability to create secondary ionization products from the residual gas. Furthermore, ions accelerated by the beam toward the beam pipe wall desorb additional gas molecules, thus increasing the gas pressure. With the analysis performed in the previous sections, it is now possible to estimate the amount of ionized gas that is available for collection.

At normal atmospheric pressure, energetic incident particles passing through a gas produce primary electrons which then can produce further ionization products. However, at the UHV pressures used in the IPM, the electron scattering mean free path λ_e is very long compared to the chamber dimensions. The scattering cross sections σ_e for ~keV electrons on

gas molecules are approximately 10^{-16} cm^2 [119][120]. For example, the ionization cross section for a 1 keV electron on water molecules is $0.79\text{x}10^{-16}$ cm^2 [121]. Even with an electron number density N_e of $3\text{x}10^9$ cm^{-3}, which is representative of a relatively high IPM vacuum pressure of $1\text{x}10^{-7}$ Torr, the electron mean free path is $\lambda_e = 1/N_e\sigma_e$ = 30 km. It is highly improbable that a significant number of secondary electrons would be created.

By using the primary number of ion-electron pairs created (n_p from table 2.2) for each gas constituent together with the partial pressures from table 2.3, we obtain a weighted average $\langle n_p \rangle$ of 9.5 pairs · cm^{-1} · atm^{-1} = $1.2\text{x}10^{-2}$ pairs · cm^{-1} · Torr^{-1}. Scaling $\langle n_p \rangle$ to the IPM pressure of $2\text{x}10^{-9}$ Torr and multiplying by a detector length of 1.58 cm predicts that the number of ion-electron pairs created per incident proton is $3.9\text{x}10^{-11}$. The number of accumulated protons in the SNS ring increases linearly with each turn (~1 μs) by $1.42\text{x}10^{11}$ *protons* x *Turn Number*. The number of protons in the ring at a given time multiplied by the number of pairs created per proton gives the number particles available for collection during a single turn. The graph in figure 2.12 shows the number of ion-electron pairs created through residual-gas ionization by 1 GeV protons for each turn in an accumulation cycle for the representative gas pressures of $2\text{x}10^{-9}$ and $2\text{x}10^{-8}$ Torr. For the expected pressure of $2\text{x}10^{-9}$ Torr, the number of collectable particles at full accumulation is $5.9\text{x}10^3$, while it is 6 for the first injected turn.

Residual Gas Depletion

Since every ion-electron pair created and subsequently collected removes a gas molecule it is important to estimate the impact on the total number of molecules available to be ionized. It was just shown that a pressure of $2\text{x}10^{-9}$ Torr corresponds to a gas particle density of

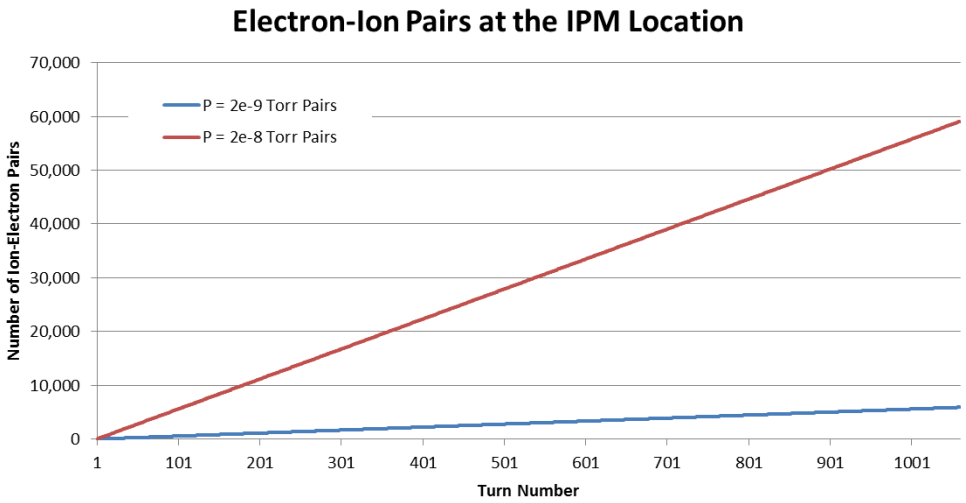

Figure 2.12 Graph of the total number ion-electron pairs created at the IPM location as a function of the number of protons present in each turn for 8 scale and 9 scale pressures.

6.59×10^{7} cm^{-3}. The detectable volume within the IPM is approximately 800 cm^3 resulting in ~5×10^{10} gas molecules capable of producing measurable particles. Based on the previous assumption that the vacuum remains unchanged during an accumulation period, the number of gas molecules is assumed to remain static during an injection cycle. The total number of protons passing through the IPM during accumulation is

$$N_{Total} = \sum_{T=1}^{Turns} \frac{N_{full}}{Turns} T \approx \frac{1}{2} N_{full} Turns \tag{2.39}$$

where N_{full} is the final proton number and *Turns* is the number of mini-pulses.

From the number of primary ion-electron pairs created, the total number of gas molecules removed from the detectable volume is $N_{pairs} = n_p N_{Total}$ where n_p is the number of primary pairs created per proton in the detector region. The total number of pairs for N_{full} = 1.5×10^{14} protons and *Turns* = 1060 is 6.3×10^{6} pairs. Only 0.013% of the original gas is ionized in one accumulation. Therefore, the depletion of the residual gas by ionization and

removal of ions and electrons is expected to be negligible.

2.2.4 Electron Estimation

The estimation of electrons is similar to that of ions but with a few additional considerations. It has been well established that an energetic proton will interact with neutral gas molecules in such a way to remove the least bound valence electrons. Ionization products consist of one ion and one electron. The probability of double ionization leading to two electrons per incident proton and possible dissociation of molecules is significantly less than that of single ionization, and can therefore be considered a negligible contribution. For example, the ratio of double ionization to single ionization cross sections for energetic protons on H_2 as measured by experimental methods in [122] is on the order of 10^{-4} and the ratio for H_2O found in [123] is 10^{-2}. While double ionization may not be an important factor in the electron signal there are additional electron production mechanisms that warrant analysis.

Electron Cloud

Electrons present in the ring arise from a few different sources. Beam-induced ionization produces the same number of electrons as ions and these electrons are useful for measuring beam profiles because their distribution is a function of the beam density. Other sources of electrons provide no information useful for profile generation and their presence is a source of profile signal contamination. Aside from ionization, one of the largest contributions of electrons relevant to the IPM is electron cloud generation by beam-induced multipacting [124].

The phenomenon of the electron cloud, briefly discussed in section 2.2.2, is shown graphically in figure 2.13. Electrons present before the arrival of the proton beam, whether they were created through residual gas ionization or due to protons striking the vacuum

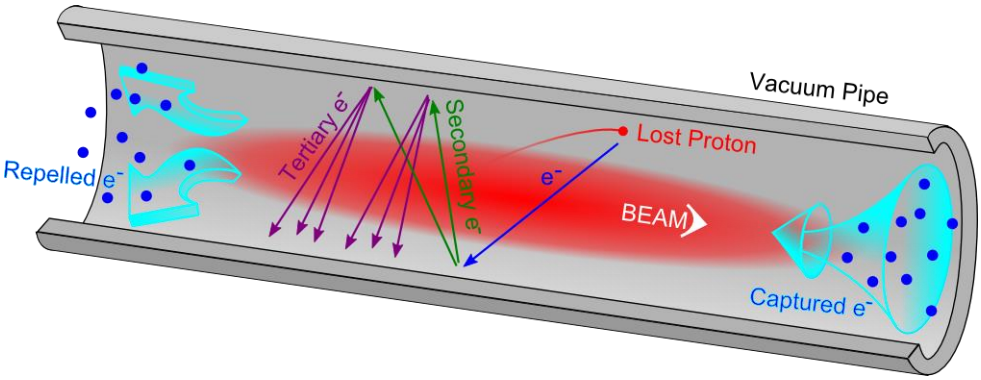

Figure 2.13 Graphical representation of electron cloud generation leading to multipacting.

chamber walls, are attracted into the proton bunch and oscillate within the beam potential well with a frequency $\omega_e \approx c\sqrt{2\pi r_e N_p}$ where c is the speed of light, r_e the classical electron radius and N_p the number of protons in the bunch [125]. These electrons are released near the trailing edge of the beam, freed from the decreasing beam potential, and contact the vacuum pipe walls with sufficient energy to create secondary electrons [126].

The secondary emission yield (SEY), defined as the number of secondary electrons created per incident electron, has a value near 2 for electrons incident on stainless steel with energies equal to the net energy gain due to the beam potential of ~100 eV [104], [125–127]. Additionally, protons lost on the pipe walls have an electron yield of ~100 [128]. These electrons may also contribute to the generation of secondary and tertiary electrons as the primary and secondary electrons are accelerated through the beam potential.

An undesirable effect of the presence of secondary electrons is that of introducing unwanted signal in the electron-based beam profile. Electrons within the beam and beam pipe have a neutralizing effect on the beam space charge [116]. Studies have shown [126], [128] that up to 10% of beam charge neutralization within the beam radius and 100% within the

beam pipe could be expected.

Electron Cloud Mitigation: TiN Coating

Experience with electron cloud related instabilities in the Proton Storage Ring (PSR) at Los Alamos [129] led to an electron cloud mitigation measure that was also designed into the SNS ring. It was found [112], [130], [131] that a ~100 μm coating of titanium nitride (TiN) lowers the peak SEY of stainless steel from 2.5 to ~1.5. It is therefore standard practice to coat all inner vacuum chamber surfaces in the SNS ring with TiN. As such, the IPM vacuum chamber will be coated using a magnetron DC sputtering method described in [112].

Electron Cloud Mitigation: Clearing Electrode

The IPM uses electrodes transverse to the beam direction to separate and accelerate the ions and electrons produced during residual gas ionization toward a detector. The electric potential produced by the electrode has the benefit of acting as a clearing field in reference to the electron cloud. Simulations, presented in figure 2.14, show the electron cloud build up due to trailing-edge multipacting during the first turn of an SNS accumulation cycle. Also shown in figure 2.14 are the electron cloud line densities for a region with a uniform electric field. It can be seen that electron cloud density decreases with increasing field strength.

An electric field of 2 kV/m lowers the peak electron cloud density by over three orders of magnitude. The actual field strength used in the IPM will be on the order of 10^2 kV/m. Once the IPM bias field is larger than a few kilovolts, the electrode potential is larger than the beam potential and therefore prevents the generation of secondary electrons. Furthermore, within the IPM chamber, any neutralization effects of the electron cloud will also be insignificant. Electron noise from the electron cloud may be considered negligible in relation to the IPM measured beam profile.

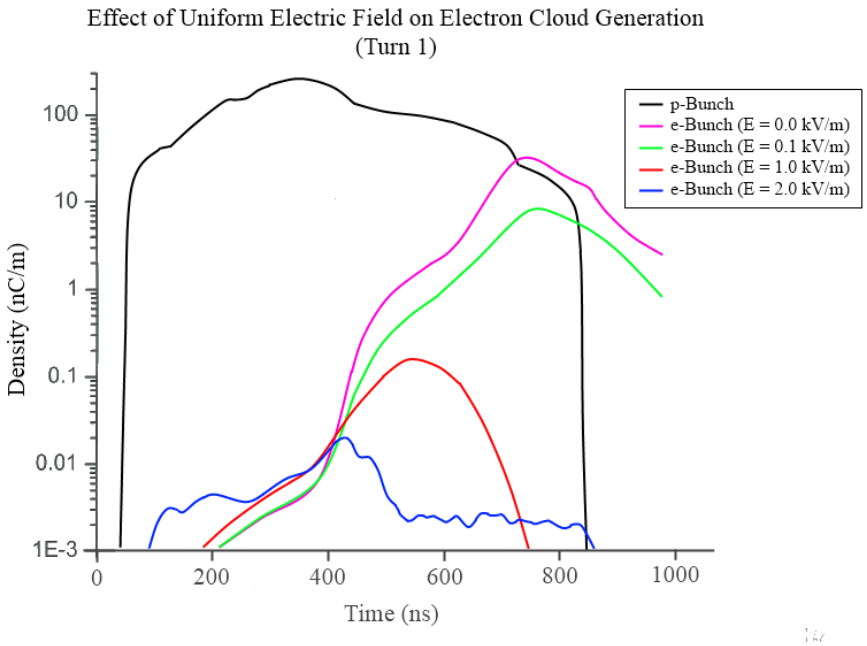

Figure 2.14 Simulation of electron cloud formation in the SNS ring for the first turn of accumulation in the presence of varying uniform electric field strengths [132]**,**[133]**.**

Field Emission Electrons

Another possible source of electron noise is electrons generated through field emission. In the high vacuum regime, large electric fields have the ability to liberate electrons from metallic surfaces by lowering the surface potential barrier to ~4.5 eV and therefore, since the electron wave function remains finite past a metal's potential wall, a metallic electron with an energy at the Fermi level will have a non-trivial probability of tunneling, known as Fowler-Nordheim tunneling, through a potential barrier of thickness ~1 nm [134]. Electric potential gradients required to induce field emission are $\gtrsim 3\text{x}10^9$ V/m, however the practical applied macroscopic fields are more on the order of 10-30 MV/m due to the enhancement of electric fields by microscopic protrusions on electrode surfaces [135].

Fields in the IPM are less than 0.5 MV/m and therefore field emitted electrons are not expected to be a source of noise in profiles found from measuring. During assembly of the

final system a precautionary technique of hand polishing the electrode with a diamond paste should be used in order to reduce microscopic protuberances [136]. This is important not only for the consideration of field emission electrons, but for reduction of possible arcing sites at higher field regions of the electrode. Furthermore, it would be informative, on completion of the IPM chamber, to pump down to high vacuum, energize the electrode, and measure the dark current present without the influence of the beam in order to ensure there is not a significant source of background electron noise.

Other Loss Mechanisms

At normal atmospheric pressures, newly created ionization products would begin to diffuse within the gas and undergo a variety of collisions that would result in signal loss. Recombination is the process in which positive ions and electrons combine to become stable, charge neutral, molecules. In the IPM, although ions are no longer guaranteed to have a Maxwellian distribution of velocities, their mean free paths may be estimated as $\lambda_{ion} = \sqrt{2}\lambda$ where λ is the ideal gas mean free path. Ions in UHV travel kilometers before interacting with a particle. Electrons, due to their light mass, have collision lengths ~4 times longer than those of ions [119]. The UHV in the IPM make recombination or any other form of post-ionization collision leading to signal loss negligible.

Furthermore, it is well known [81], [119], [137] that ionization chambers, which are gas filled detectors that collect the by-products of ionizing radiation through the use of electric potentials, prevent recombination by separating the charged particles using high electric field gradients. IPM electric fields enhance the effects of the UHV by further acting to prevent recombination.

It may be concluded that sources of electrons that would pollute the measured profile

signal are minimal during operation of the IPM. While there are still sources of electron noise, they are specific to elements of the design and will be discussed as appropriate. Furthermore, it may be concluded that natural sources of primary signal loss in the form of post-ionization collisions for both ions and electrons are negligible. Again, there are still design specific loss channels but those can only be understood within the context of design particulars and will be explored later. As it stands, the number of ions created is equal to that of electrons and the number of pairs formed is given accurately by figure 2.12 for the nominal pressure range expected in the IPM system.

2.2.5 Plasma Considerations

The passage of the beam through the residual gas leaves in its wake a partially-ionized gas that may exhibit characteristics of plasma. A plasma is a collection of charged particles in an ionized (partially or fully) gas that interact through Coulomb forces along with fields generated by their cumulative motion. Even though the assembly is roughly charge neutral, the collection shields out external electromagnetic fields and exhibits complex group behavior [138]. Using Maxwell's equations to calculate the potential of a plasma containing a slightly unbalanced mixture of ions and electrons, it may be shown [139] that the electric potential about a charge q is

$$V(r) = \frac{q}{4\pi\varepsilon_0}\frac{\exp(-r/\lambda_D)}{r}. \tag{2.40}$$

The length

$$\lambda_{D_e} = \sqrt{\frac{\varepsilon_0 k_B T_e}{N_e e^2}} \tag{2.41}$$

is known as the electron Debye length, where ε_0 is the free-space permittivity, k_B is the

Boltzmann constant, T_e is the electron temperature, N_e is the electron density, and *e* is the elementary charge. Hence, individual charges are screened from one another and collective effects dominate. The Debye length for the whole gas is related to the ion and electron lengths as $\lambda_{D_e} = \lambda_{D_i} = \sqrt{2}\lambda_D$ [18]. However, if the dimensions of the gas *d* do not greatly exceed the Debye length, $d >> \lambda_D$, then charges are no longer shielded from one another and the gas no longer exhibits plasma behavior.

For the SNS ring, N_e is 7.1 cm^{-3} at $2x10^{-9}$ Torr. From kinetic theory an electron with kinetic energy *K* = 100 eV has a temperature $T_e = 2K/3k_B = 7.7x10^5$ K, which makes the Debye length 16 m. The Debye length is 100 times larger than limiting dimension of the beam pipe width, so that the ionized gas does not satisfy the criteria to be a plasma, and any collective effects may be neglected.

2.3 IPM Signal Estimation

From estimations of the ionized particle signal it is possible to calculate the expected measured signal, given the characterization of the particle to be used. This will determine limits on the electronics required and the degree to which further signal amplification is required. Consequently, the resolution of the system may be determined and necessary design parameters set in order to optimize the IPM accuracy.

2.3.1 Channeltron Detector

Description

A Channeltron[6,7] is a single channel electron multiplier (CEM) that uses a tube made from a specially formulated lead silicate glass to create an avalanche of electrons initiated by incident radiation to amplify the incoming signal [140]. The Channeltron's basic operational principles and image are illustrated in figure 2.15. The silicate glass tubing comprising the bulk of the Channeltron has a layer of SiO_2 approximately 20 nm thick on the inner surface of the tube. Silicon dioxide has a secondary emission yield of 2.2 for 300 eV electrons [141]. Behind the SiO_2 is a highly resistive conductive layer that, when a negative potential of 1.2 to 3 kV is applied across the length of the tube, acts as a voltage divider chain producing an electric field that accelerates electrons down the glass tube in addition to replenishing the

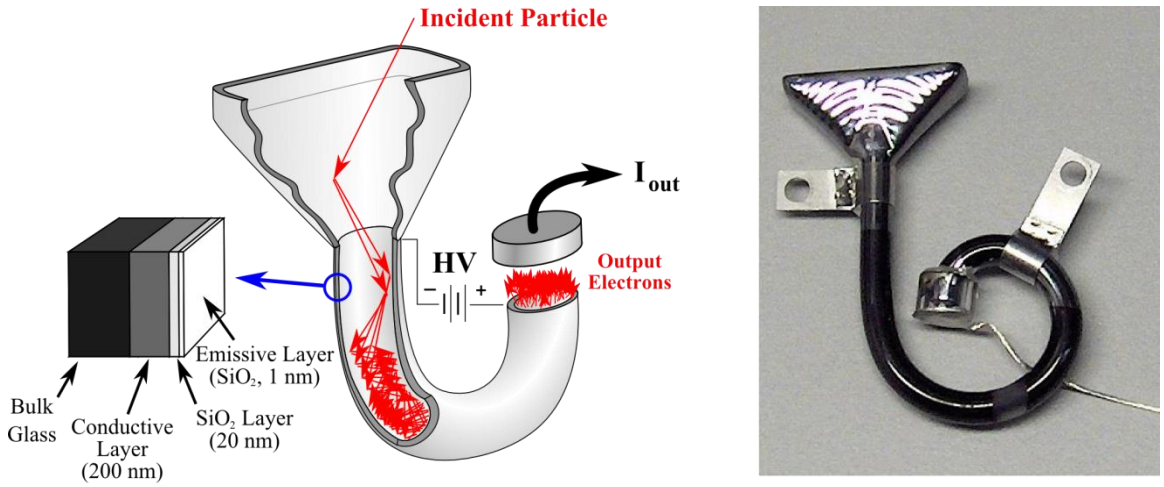

Figure 2.15 (Left) Graphical representation of a Channeltron detector showing basic principles of operation in addition to substrate structure of lead silicate glass tube walls. (Right) Actual photo of a 4800 series Channeltron with custom mounting tabs.

[6] While not an official designation, the name Channeltron will often be abbreviated as "Ctron" in this text.
[7] Detailed information on Channeltrons may be found in [140] which is made available by PHOTONIS.

supply of lost electrons from the secondary emission cascade [142].

A typical CEM gain, defined as the ratio of the output current to the input current (I_o/I_i), is 10^5 to 10^7, as shown in figure 2.16 for 4800 series Channeltrons. At a bias voltage of ~3 kV Ctrons enter a pulse mode, with a gain of 10^8, where saturation of charge within the detector causes the output signal to no longer be proportional to the input. In analogue mode, the Ctron output will be linear up to 10-20% of the bias current of 30-40 μA giving a gain linearity maximum of 5-10 μA, which is shown for a 4700 series Channeltron in figure 2.17.

Detection Efficiency

The detection efficiency is defined as the probability with which an incident particle produces an output pulse. It is a function of the particle type, mass, energy, and angle of incidence. The relative detection efficiency for ions as a function of energy is shown in figure 2.18 while figure 2.19 shows the efficiency for electron collection. From these figures it may be seen that, in the IPM ion collection mode, nearly the entirety (~90%) of ions will be transferred into measurable signal since the mean ion energy will be 60 keV, with a negligible number below 20 keV. For electrons of the same energy, the IPM electron collection mode could see only 60% of the ionized electrons detected.

For a Channeltron, dark noise is defined to be the measure of output current when there is no input signal. CEM's are known to have extremely low dark noise levels. The Channeltron used in the IPM has a maximum dark count rate of a few counts/second at 3 kV Ctron potential. For a 1 ms accumulation cycle a maximum of 0.002 counts is to be anticipated. In analog mode the dynamic range is defined as the ratio of the maximum linear output current to the dark current. The dark current is the DC current measured through the Ctron when there is no input. For a properly designed detector the dark current is typically

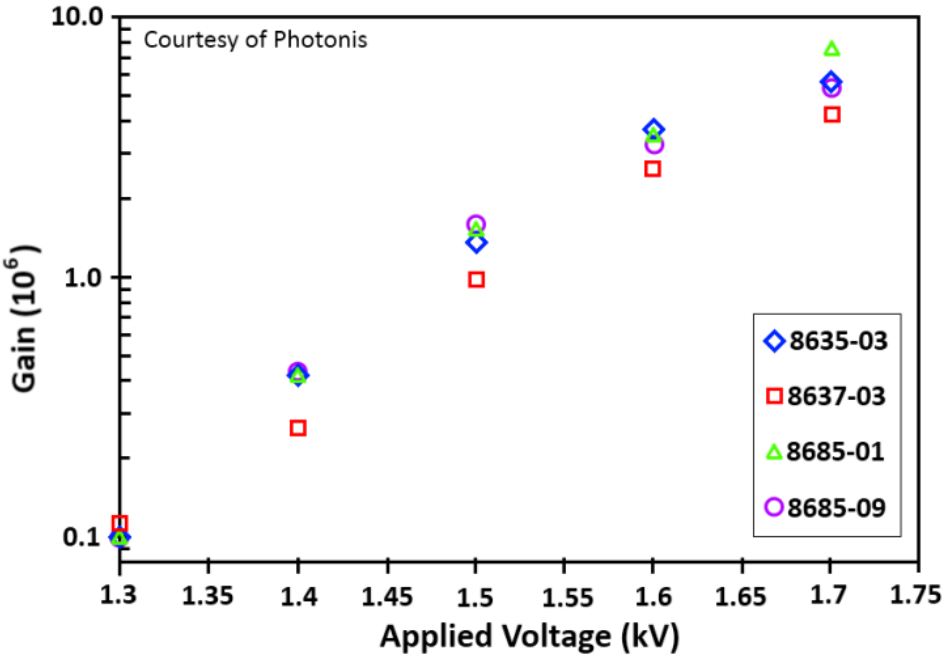

Figure 2.16 Gain of four different 4800 series Channeltrons.

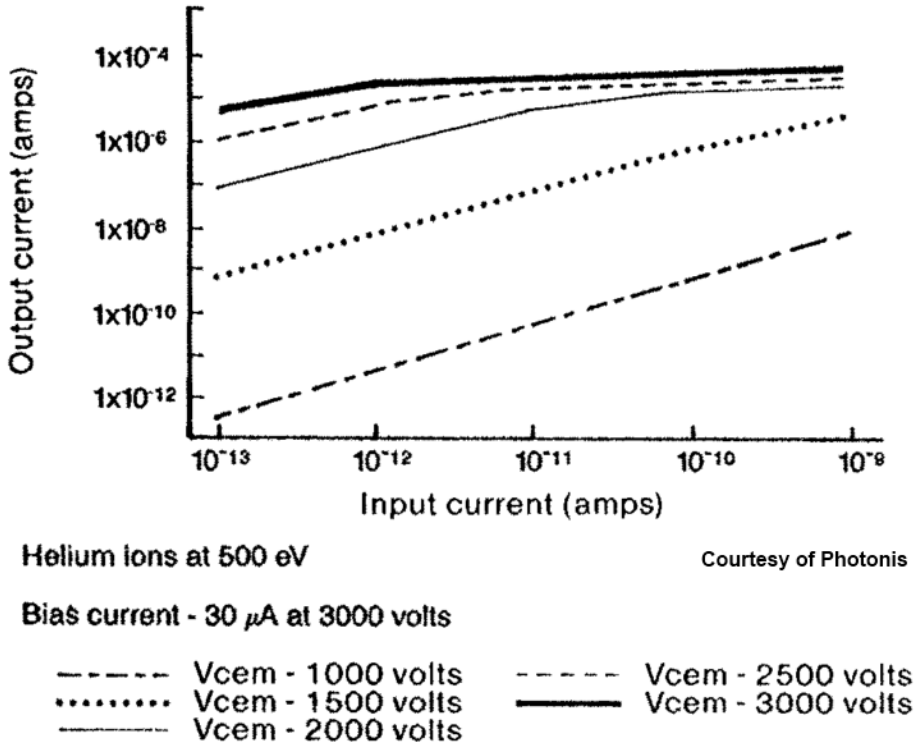

Figure 2.17 Typical 4700 series Channeltron gain linearity.

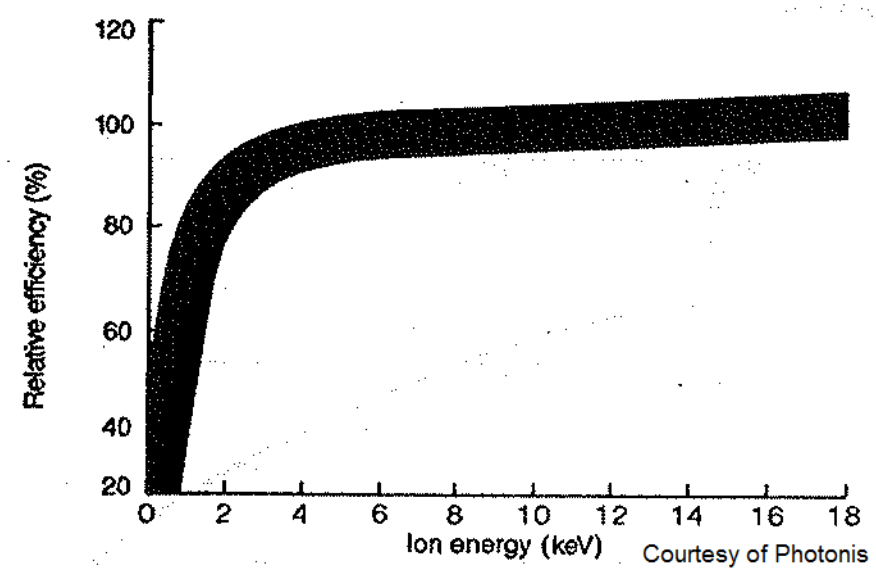

Figure 2.18 Channeltron relative ion detection efficiency. [140]

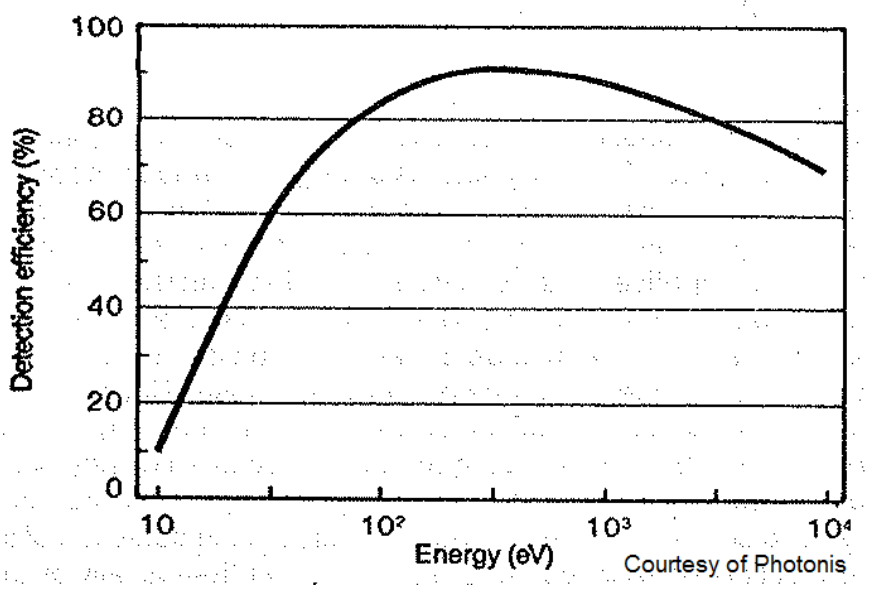

Figure 2.19 Channeltron electron detection efficiency. [140]

1 pA at a gain of 10^6. Noise generated from the detector is not expected to be a problem. While Channeltron gain is a function of incident particle mass, there is little deviation in response characteristics for the range of masses measured in the IPM.

There is experimental evidence [143],[144] that CEMs in magnetic fields have a decreased efficiency when the magnetic field strength increases to a magnitude that the cyclotron radius of the electrons inside the CEM tube becomes comparable to the radius of the tube. The electrons are curved into the opposing wall before gaining sufficient energy to generate a cascade. Upon completion of the system and before installation, it will be necessary to characterize the Ctron efficiency as a function of magnetic field strength.

Operational Considerations

It will be necessary to operate the Channeltron in the analog mode in order to distinguish between measured current amplitudes of each accumulated pulse. Consequently, prior to installation, it will be necessary to characterize each installed Ctron with a calibrated source such as an electron gun to determine the optimum operating potential which is proportional to its gain. The 4800 series Channeltron has a maximum operating pressure of $5x10^{-6}$ Torr. An operational protection limit will be included in the system electronics to turn off the detector in the event the pressure rises to 10^{-6} Torr.

Individual Channeltron gains can vary greatly. The final IPM system will have a pair of Channeltrons installed. It will be necessary to specify to the manufacturer that a set of two detectors have matching gains. The rise time is defined as the time it takes the output pulse to go from 10% to 90% of its final amplitude. This is approximately 3-5 ns for Ctrons, which is sufficiently fast to resolve the 20 ns rise time of the beam pulse, as will be shown in a later section. The Channeltron opening is 4 mm wide by 15.8 mm long as shown in the

mechanical drawing of figure 2.20.

Lifetime Considerations

The main areas of degradation within a CEM are the chamber wall input and output areas. For UHV conditions, an average Channeltron will survive ~2000 hours or 30 coulombs of extracted charge. Considering that the IPM would not be used continuously, and even during operation is run for a few minutes at a time, a single Ctron may last for many years. As a maintenance measure, the IPM chamber will be designed to allow easy access to the Channeltron to allow for replacement if the need arises.

In hadron accelerators, neutrons are the primary source of radiation produced by lost beam particles incident on the accelerating structure [145]. Neutrons, in addition to the other radioactive decay products, may have a damaging effect on materials present in the accelerator enclosure. The Channeltron, however, is designed for use in many types of radiation environments, including space, and thus is resistant to radiation damage. A study

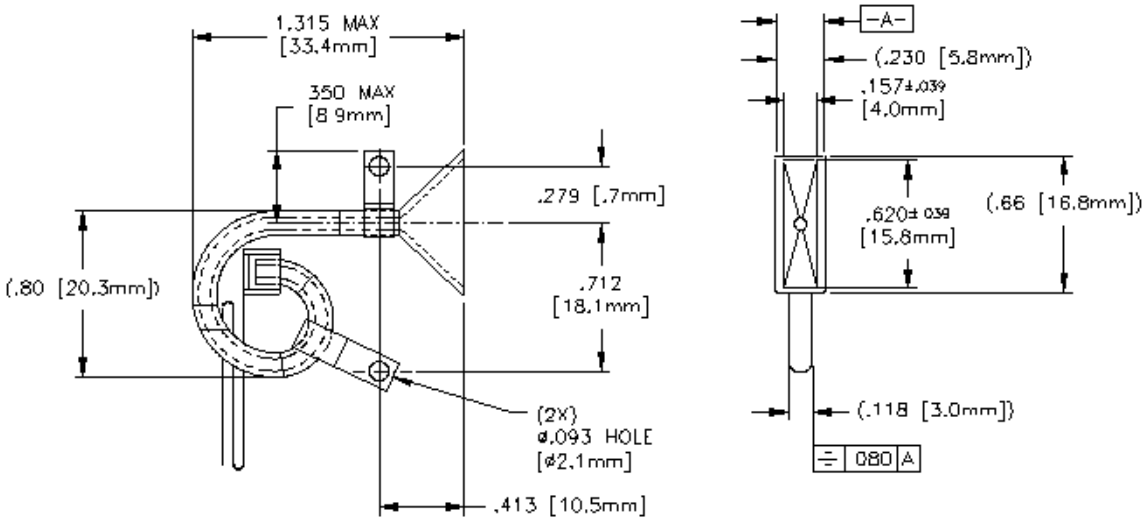

Figure 2.20 Dimensional layout of a 4800 series Channeltron. [140]

[146] was done on MCPs showing that no permanent damage was done after exposure to 10^6 rads of radiation. Beam loss monitors around the IPM location experience a measured dose rate of ~3 rad/hr. Assuming 5000 hours of beam time per year gives a dose of 15 krad/year. Assuming that the MCP radiation rate applies to Channeltrons and considering that they are constructed of the same materials, the IPM Ctron should last at least 70 years based on radiation lifetime alone.

Channeltron vs. MCP

The Channeltron is based on the same principal as the MCP and with multiple MCPs it is possible to produce gains similar to that of a single Ctron. As discussed in section 1.2, many IPMs use MCPs as their method for ionized particle collection and amplification. A brief justification is necessary for choosing the Channeltron over the MCP. It was one of the initial goals of the project to produce the simplest IPM design possible that fulfilled the measurement requirements.

MCP arrays, while having the ability to measure the entire beam region at once, suffer from a loss of uniformity in gain as the MCP ages due to the beam distribution [147]. Since the entire MCP array uses the same bias voltage, it is not possible to adjust the gain for various portions of the MCP. Furthermore, MCPs require a particle detector in the form of a phosphor screen and camera or anode strips. Additionally, Channeltron lifetimes are about 10 times longer than those of MCPs. The Channeltron provides the simplest and most robust form of particle detector for the SNS IPM system.

2.3.2 Residual Gas Sensitivity

Relative Amplitudes

There are two dominant effects that changes in the residual gas pressure have on measured beam profiles. The first occurs when comparing profiles taken at different pressures resulting in different densities of residual gas molecules. Since the number of ion-electron pairs is directly proportional to the pressure, the measured signal from the detector is directly proportional to the pressure. While characteristics such as the width and shape remain unaffected, the amplitudes of profiles will differ. In order to make relative comparisons between profiles taken under differing pressures, it will be necessary to normalize the measured profile data by the pressure coincident with the data. As mentioned earlier, the IPM chamber will include a port for a pressure gauge that may be used to normalize profile measurements.

Statistical Width Uncertainty

The second aspect of the profile affected by a change in pressure is the inherent statistical uncertainty of a measurement based on a small number of events. The number of particles available with which to construct a profile gives the first estimate of the accuracy with which the measured profile width reflects the true beam width.

Modeling the proton beam spatial distribution as a Gaussian distribution with width σ_0 and regarding the number of ionized particles N as a sample of that population, the unbiased estimate of the population standard deviation, actual beam RMS width, based on the sample is

$$\sigma_N = \sqrt{\sum_{i=1}^{N} \frac{(x_i - \mu_N)^2}{N-1}} \tag{2.42}$$

where x_i is the transverse position of the ith sample particle and μ_N is the sample mean. The concept is illustrated in figure 2.21 which shows the actual distribution with RMS width σ_0 and measured RMS width σ_N. Although ideally σ_N would equal σ_0, it will be shown later that the measured width is distorted by systematic errors, hence the larger profile of σ_N in figure 2.21. Multiple samples taken from the same population distribution will produce an ensemble of Gaussian distributions with widths whose values also satisfy a Gaussian distribution with mean σ_N and standard deviation called the standard error SE_{σ_N} (represented by σ_σ in figure 2.21). The fractional uncertainty or error in the profile using N particles is given in [148] by

$$\frac{SE_{\sigma_N}}{\sigma_N} = \frac{1}{\sqrt{2(N-1)}}. \tag{2.43}$$

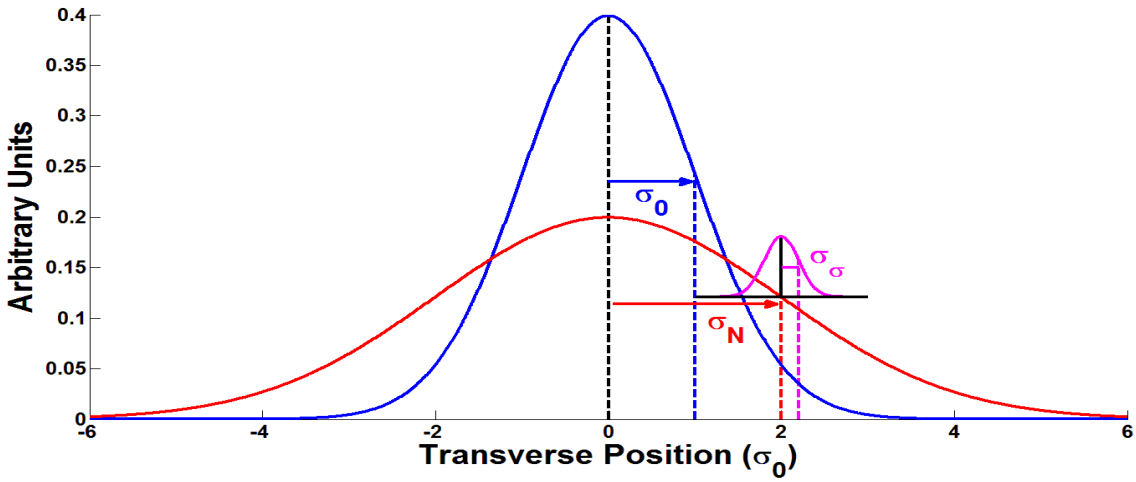

Figure 2.21 Graphical representation of the statistical error σ_σ associated with the measured profile width σ_N for the actual distribution of width σ_0.

Figure 2.22 shows the fractional error, given by equation (2.43), in percentages of the measured distribution width for each turn during the accumulation for a range of residual gas pressures. At $2x10^{-9}$ Torr, the error in the measured width decreases from 33% on the first turn to ~1% because of an increasing number of protons and a resulting increase in measurable ionization products. This means that on the first turn the measured width could not be guaranteed to be more accurate than $\sigma_N \pm 0.33\sigma_N$ at $2x10^{-9}$ Torr.

In order to reduce the statistical error, more samples are needed. Therefore, based on the assumption that the beam during each accumulation cycle is identical under the same operating conditions, it is possible to reduce the statistical error due to low detectable signal by summing the contributions at the same turn for multiple cycles. The number of measured particles scales linearly with the number of measured cycles, and the errors decrease in inverse proportion to the square root of the number of measurements, as shown in

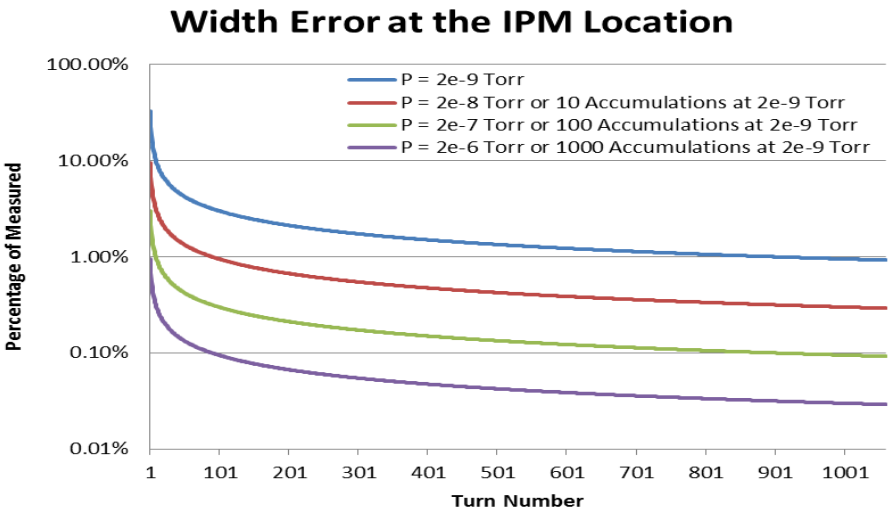

Figure 2.22 The percentage of the measured width the error assumes for each turn during an accumulation cycle is shown for varying pressures or the equivalent number of accumulation cycle repetitions.

figure 2.22. Summation over 100 macro-pulses gives a first turn error of 3% and 1000 repetitions results in a 1% error. Beyond this there is little gain in accuracy.

While a 1% accuracy is ideal, a factor of 10 increase in macro-pulse accumulations implies a factor of 10 increase in the time required to produce a profile. To achieve acceptable accuracy for the measured first turn profile will require at least 100 integrated macro-pulses. For the purposes of analysis, a 1% error in the measured RMS width will be attributed to error induced by particle number statistics.

Sensitivity to Pressure Change

In addition to the accuracy with which the measured profile represents the true profile, this technique can be used to determine the sensitivity of the width taken from separate integrated datasets from different pressures. A profile taken at a low pressure will have a much larger error in the width compared to one taken at a higher pressure. Even though both profiles represent the same beam under the same operational parameters, the measured widths could be different due to statistical considerations.

The statistical error in the measured width σ_N (see figure 2.21) is defined in relation to the actual profile width σ_0, by $\sigma_N = f_N\sigma_0$. The total measured width σ_T is the sum of the measured width plus the error σ_σ such that

$$\sigma_T = \sigma_N + \sigma_\sigma = f_N\sigma_0 + \frac{f_N\sigma_0}{\sqrt{2(N-1)}} = f_e\sigma_0 \tag{2.44}$$

where σ_σ has been replace by expression (2.43) and f_e is the total fractional error. The total fractional error then becomes

$$f_e = f_N\left(\frac{\sqrt{2(N-1)}+1}{\sqrt{2(N-1)}}\right). \tag{2.45}$$

The percent difference in the total measured profile width is

$$\frac{\sigma_{T_2} - \sigma_{T_1}}{\sigma_{T_1}} = \frac{f_{e_2} - f_{e_1}}{f_{e_1}} \tag{2.46}$$

where the subscripts 1 and 2 denote the total widths measured at two different pressures. Substituting equation (2.45) into (2.46) gives an expression for the change in width as a function of change in pressure, using $N = \epsilon N_{acc} N_{single} T n_p P = \alpha P$ where ϵ is the efficiency of the detector, N_{acc} is the number of macro-pulses being summed over, N_{single} the number of protons in a single mini-pulse, n_p the number of primary ion-electron pairs created by a single proton in the length of the detector per Torr, and *P* is the pressure. The expression is

$$\frac{\sigma_{T_2} - \sigma_{T_1}}{\sigma_{T_1}} = \frac{\sqrt{2(\alpha P_1 - 1)} - \sqrt{2(\alpha P_2 - 1)}}{\sqrt{2(\alpha P_2 - 1)}\left(\sqrt{2(\alpha P_1 - 1)} + 1\right)}. \tag{2.47}$$

For a given detector efficiency, number of accumulations, and turn, the change in the width may be compared to the change in pressure as shown in figure 2.23. Increases in pressure reduce the width due to an increase in residual gas particles. The main consequence of summing over multiple macro-pulses is to reduce the effect of a change in pressure on the width. Furthermore, figure 2.23 shows that decreases in pressure can cause very large increases in the width. Asymptotically, the width approaches a limit representing a situation in which the measured pressure has been reduced to such a degree that number of measurable particles approach one and, consequently, the width is undefined.

Figure 2.23 shows that for 10 accumulations, N_{acc} = 10, a 1% change in the width occurs at an 11% decrease in the pressure at a base pressure of 1×10^{-9} Torr, or at 1 accumulation at a pressure of 1×10^{-8} Torr. The same change in the width coincides with a change of 29% for 100 accumulations, N_{acc} = 100, and 61% for N_{acc} = 1000 all at a pressure

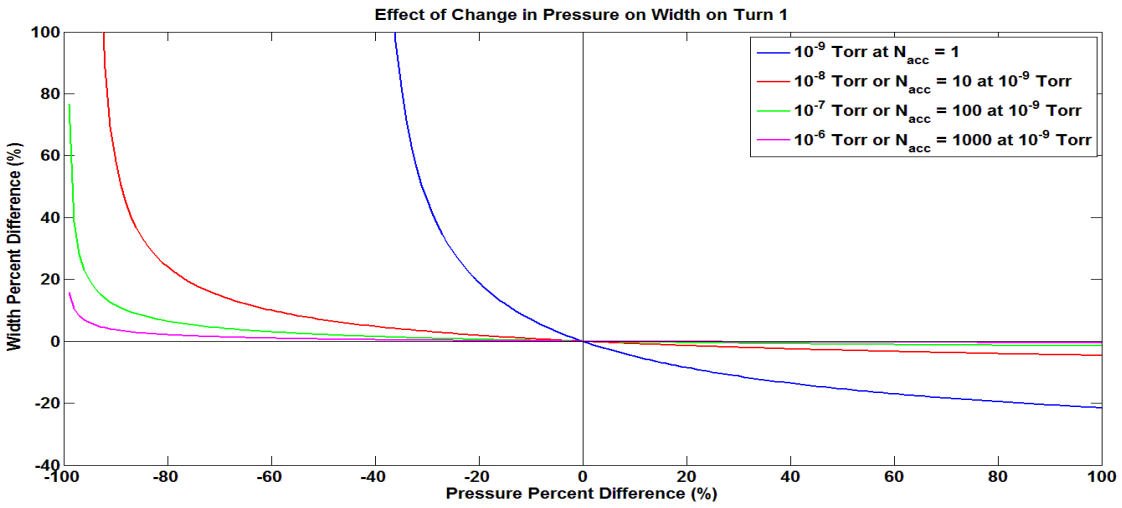

Figure 2.23 The percent change in the profile width as a function of a percent change in gas pressure for the first turn at different gas pressures or the equivalent number of aggregated accumulation cycle at 10^{-9} Torr.

of 10^{-9} Torr. From figure 2.11, which shows the measured pressures around the IPM location, it may be seen that pressure changes during ramping of ~40% may be seen while equilibrium pressures fluctuate on the order of 25%. Summing over at least 100 macro-pulses should be sufficient to significantly reduce the effect of differences in pressures between profile measurements. It should also be noted that the curves in figure 2.23 are maxima and decrease with each mini-pulse injected into the ring as illustrated by figure 2.22.

2.3.3 Profile Generation

The use of a single finite sized detector along with the need for the multiple accumulation cycles required for statistical accuracy means that turn-by-turn profiles will not be generated in real time, but by compiling multiple datasets. The process is represented graphically in figure 2.24. The Channeltron in its initial position will collect all the particles for each revolution of an accumulation cycle and continue collecting in that same position for the number of successive cycles needed to produce the desired accuracy. Then, upon moving to

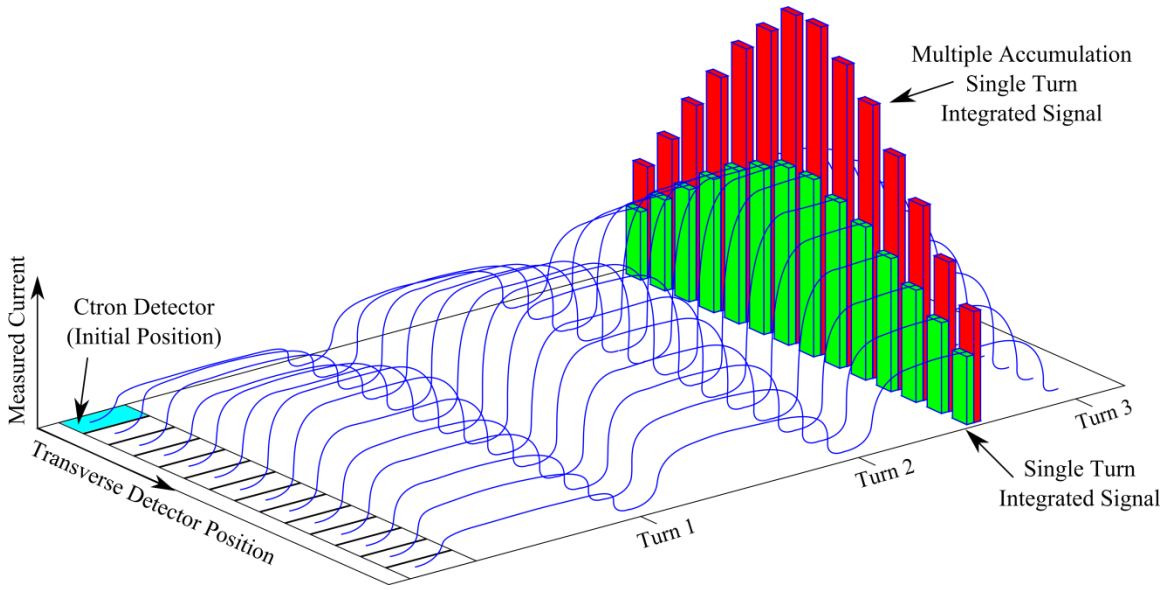

Figure 2.24 Graphical representation of the turn-by-turn profile generation process showing the collection all particles at a detector position for each turn and multiple accumulations then moving the detector transversely until the beam width has been spanned.

the adjacent transverse detector position the process is repeated until the entirety of the beam width has been scanned. After which, the current measured for each turn will be integrated, producing a single measured current representative of each turn at each detector position. The individual turn-by-turn data of each detector position is summed across the independent accumulation cycles producing a single, high particle count, dataset of histogram profiles for each turn.

The time required to produce a set of profiles is a function of the number of detector positions that are required to traverse the beam width, the speed of the actuator driving the Channeltron, and the number accumulation cycles being summed over. An estimation of measurement time will be made once all of the necessary components have been discussed in the following sections.

2.3.4 Measured Signal

Based on the estimated ionization, detector efficiency, and detector amplification it is possible to estimate signals expected to be seen by the IPM system during an accumulation cycle. A Gaussian beam is used to approximate the ring beam profile with an RMS width of 1.5 cm. Since all the ionized particles are to be summed together for each revolution during the accumulation cycle, the calculated measured currents will be averages over a 1 μs ring period.

For the first turn of an accumulation period of a nominal beam with mini-pulse average current of 22 mA, where there are expected to be ~6 collectable particles, a single Channeltron position is likely to measure only one ion or electron. This means that the minimum measurable signal for a single Channeltron is 0.16 pA. The current measured from the Channeltron with the bias voltage set to produce a 10^6 will result in a current of 0.16 μA measurable from any one Channeltron in span of the first turn. Measured currents increase linearly with the ring current, and the distribution of currents for individual Channeltrons integrated over the final turn is shown in figure 2.25.

Represented therein are three distributions: the number of ion-electron pairs and the associated average current over one turn, the current associated with the collected ions adjusted for a detector efficiency of 0.9 and the measured Channeltron current with 10^6 gain, and the collected and measured electron currents adjusted for a detector efficiency of 0.6, all at a pressure of $2x10^{-9}$ Torr. Channeltron currents of 60-90 μA would be expected on the last turn of an accumulation cycle.

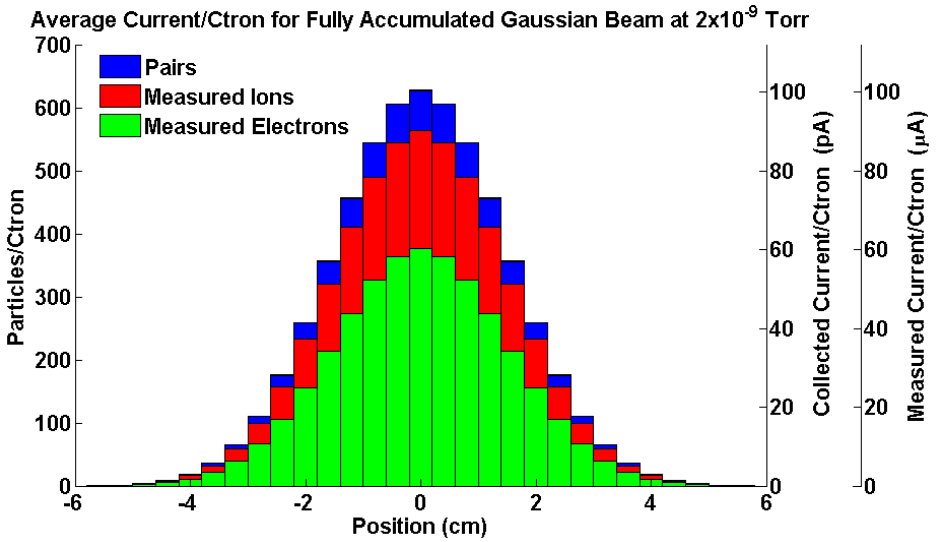

Figure 2.25 Expected IPM signals for different detector positions on the last turn of a $1.5x10^{14}$ proton beam in the SNS ring. Collected current represents the current of detected incoming ionized particles adjusted for ion and electron efficiencies. Measured current is the output current of the Channeltron with a 10^6 gain.

Signal Saturation

As discussed in section 2.3.1, there is a maximum input the Channeltron can sustain before the output is no longer a linear function of the input. This saturation limit for analog Channeltron measurements is shown in figure 2.26 along with expected Channeltron output current as a function of turn for two different gain settings. As seen in figure 2.26, at 10^6 gain, the measured signal may show saturation effects as early as turn 100. In order to prevent saturation, it may be necessary to operate the Channeltron in its lower gain region.

Since the required Channeltron bias voltage will vary from Channeltron to Channeltron, it will be necessary to experimentally determine the optimal Channeltron setting upon installation. The bias voltage is expected to be between 1.0 and 1.5 kV. Providing the detector is operated within its linear range, a dynamic range of 1000 should be obtainable from the system, allowing for profile measurements for an entire accumulation.

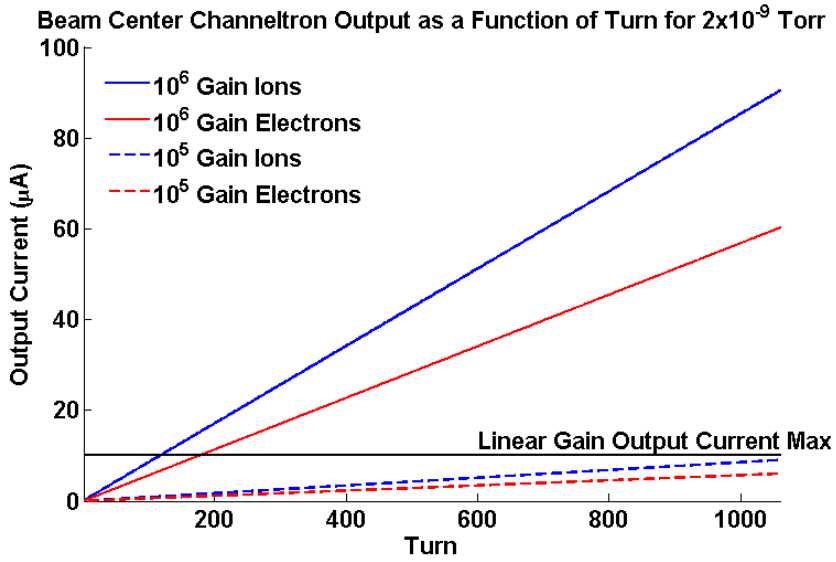

Figure 2.26 Channeltron output current for center detector position of a Gaussian beam as a function of ring accumulation turn for two different Channeltron gain settings. The approximate 4800 series linear current maximum is also shown.

2.3.5 Theoretical Summary

It has been shown that an energetic proton interacts with a residual gas primarily through electromagnetic forces with the valence electrons of gas molecules in such a way as to transfer sufficient energy to ionize a fraction of the gas. The residual gas remains constant throughout the accumulation period with a nominal pressure of $2x10^{-9}$ Torr, and is not significantly altered by the amount of ionization. There is negligible loss of the initial ionized volume and the operational aspects of the IPM design preclude signal distortions due to electron cloud effects.

Given at least 100 integrated accumulation cycles, the sensitivity to statistical inaccuracies in the profile due to limited particle count and the sensitivity to changes in the gas pressure between different data sets become negligible. The Channeltron particle detector used in the system provides a compact form of ionized particle detection and amplification

with large dynamic range. While it possible for the Channeltron to go into saturation, initial testing of the detector should prove sufficient to find the optimum detector settings.

Analysis of the fundamental theory of the IPM operational concepts has shown that it is possible to generate and collect a sufficient number of ionized residual gas particles to produce transverse beam profiles for each revolution during an accumulation cycle in the SNS ring.

Chapter 3

Simulation Analysis

With an understanding of the fundamental principles of residual gas ionization and of the use of the ionization products in the measurement of beam profiles with an Ionization Profile Monitor established in chapter 2, it is now possible to analyze the details of producing accurate profiles. The bulk of this chapter will include simulations performed to understand the effects of a variety of system parameters.

The following chapter begins with a study of ionized particle trajectories in the IPM system and describes the simulation program and techniques used. Particle trajectory analysis is used to predict the necessary fields required to produce profiles that meet the design goals. A study of the spatial accuracy is then done to analyze and estimate the possible sources of measurement error and the system requirements needed to keep the errors within the proper tolerances. Research on the time resolution and signal processing aspects of the design is presented in order to guarantee the IPM's ability to satisfy the turn-by-turn measurement requirement. Finally, a set of design parameters is presented based on the complete analysis to be used in developing the final system.

3.1 Particle Trajectory Study

The profile produced by an Ionization Profile Monitor is not a simple function of the initial positions of the ionized gas molecules. Fields used to accelerate the ions or electrons as well as the fields attributable to the beam itself have a significant impact on the measured profile. In order to understand and characterize these effects and to select design parameters to mitigate them, simulations were performed to model the trajectories of ionized particles in the IPM environment.

3.1.1 IPM Beam Range

It is first necessary to define a physical range within which the beam is expected to reside. The beam pipe diameter in the location of the IPM is 25.4 cm. Attempting to design a system that uses the entire pipe width as the measurement range would result in system dimensions that are both physically unrealistic for the ring tunnel space and prohibitively expensive. Because the beam occupies only a small fraction of the beam pipe, an estimate of the maximum expected beam size is more relevant for sizing the IPM.

Beam particles oscillate about an ideal trajectory dictated by the magnets in an accelerator lattice in such a way that the transverse beam dimensions are a function of the longitudinal position along the beam path. The beam width at a particular location is given by

$$\sigma = \sqrt{\varepsilon\beta}. \tag{3.1}$$

Where the emittance ε is a constant for a given accelerating structure and the beta function β is a longitudinal position-dependent factor describing the transverse envelope of the beam particle trajectories (see Appendix D for a complete description of the emittance and beta function as well as a detailed explanation of the beam width).

The nominal unnormalized RMS emittance for the SNS ring is equal for both transverse directions and is $\varepsilon_{rms_x} = \varepsilon_{rms_y} = 12\ \pi \cdot \text{mm} \cdot \text{mrad}$ and $\varepsilon_{99\%_x} = \varepsilon_{99\%_y} = 120\ \pi \cdot \text{mm} \cdot \text{mrad}$ for the emittance encompassing 99% of the beam particles [4] (refer to Appendix D for definitions of the 99% and RMS emittances). The beta function at the location of the IPM as calculated from the ring lattice structure is $\beta_x \cong 7$ m and $\beta_y \cong 9$ m. Allowing for a 20% error in the beta function as well as ±5 mm deviation in the beam centroid, the full beam radius including errors is

$$r_{99\%} = \sqrt{1.2\varepsilon\beta} + 5 \text{ mm}. \tag{3.2}$$

A compiled list of RMS beam sizes and full beam sizes, given in table 3.1, shows that a transverse width of 6-7 cm should be sufficient to measure the entire beam. Because the estimated beam width is only 28% of the pipe diameter, designing the system to the realistic beam size constitutes a significant savings in cost and size. One of the benefits of the chosen IPM location is that the horizontal and vertical beam sizes are very similar. This means that

Table 3.1 Calculated RMS beam sizes and full beam sizes with safety margins along with the beam pipe radius at the IPM location.

Radius	*Value*
Beam Pipe	12.7 cm
σ_{rms_x}	1.3 cm
σ_{rms_y}	1.5 cm
$r_{99\%_x}$	2.9 cm
$r_{99\%_y}$	3.3 cm

the measurement requirements of each of the transverse dimensions may be assumed to be the same. Furthermore, since the beam dimensions are comparable in the transverse dimensions, the same design for a beam width ~7 cm may be duplicated and used to measure horizontal and vertical beam profiles by rotating one system by 90° relative to the other.

3.1.2 Beam Space Charge

The beam in the SNS ring is composed of like-charged protons. The mutually repulsive force of the beam particles is what is referred to as space charge, and requires focusing accelerator components to compensate the beam's resulting divergence. Errors in the ionized particle trajectory arise from two sources; the fields in the IPM and the fields due to the beam. It will be seen that the fields related to space charge have a sizable impact on the measured profile and mitigation of space charge induced errors drives the majority of the technical requirements of the IPM system.

Positive Ionization Products

The simplest approximation of space charge is that of a uniform cylindrical distribution of N_b beam particles that has a charge per unit length, for a beam with length L, of $\lambda = eN_b/L$. Figure 3.1 shows a graphical representation of the primary electric fields present in the IPM system and a generalized trajectory for a positively charged ionized particle. Gauss's law $\vec{\nabla} \cdot \vec{E} = \rho$ gives radial electric fields

$$\vec{E}_{SC} = \frac{\lambda}{2\pi\varepsilon_0}\frac{r}{a^2}\hat{r} \qquad r < a \tag{3.3}$$

$$\vec{E}_{SC} = \frac{\lambda}{2\pi\varepsilon_0}\frac{1}{r}\hat{r} \qquad r > a \tag{3.4}$$

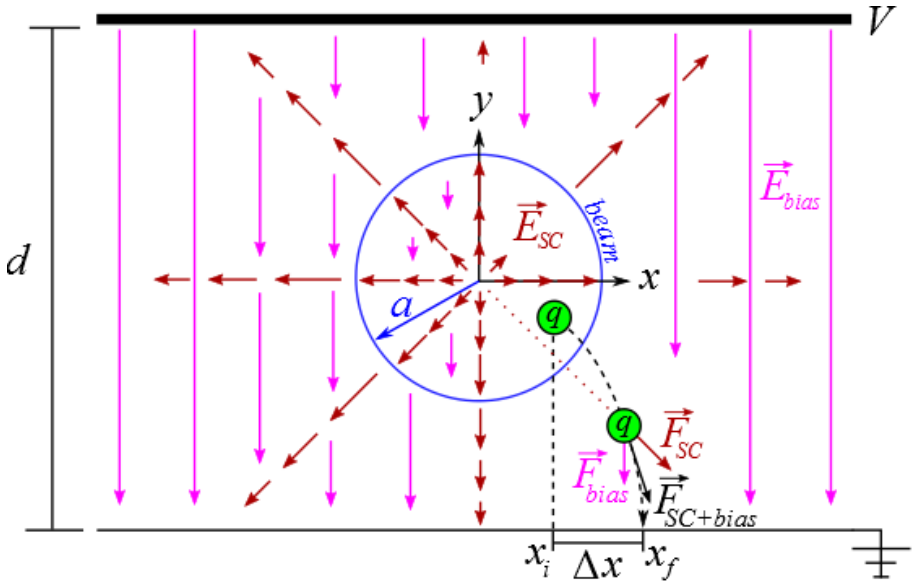

Figure 3.1 Graphical representation of the fields contributing to the distortion of particle trajectories in the IPM with an upper plate held at potential *V* creating a uniform electric field.

for a beam of radius *a*. An ionized particle with charge *q* will experience the sum of the forces from the space charge and the bias field $\vec{E}_{bias} = -\frac{V}{d}\hat{y}$ with an electric potential *V* across a gap *d*. Upon ionization, an ion or electron experiences a Lorentz force that is a superposition of the space charge and bias fields $\vec{F}_{SC+bias} = q(\vec{E}_{SC} + \vec{E}_{bias})$.

A simple calculation elucidates the influence of the beam and bias fields on the particle trajectory. Due to the *r* dependence within the beam and the 1/*r* without, the strongest beam induced forces are seen at the beam edge. Taking a single ion with charge *q* and mas *m* created at the beam edge at some height *h* above the detector, the average horizontal electric field $\langle E_{SC_x} \rangle$ over its trajectory causes a constant acceleration whose horizontal displacement is described by

$$\Delta x = \frac{q}{2m}\langle E_{SC_x} \rangle t^2 \tag{3.5}$$

assuming no initial velocity. Assuming that the vertical beam field experienced by the particle $\langle E_{bias_y} \rangle$ is negligible compared to the bias field E_{bias_y}, the collection time is found to be

$$t = \sqrt{\frac{2mh}{qE_{bias_y}}}. \tag{3.6}$$

Plugging equation (3.6) into (3.5), the beam-induced trajectory distortion is

$$\Delta x = \frac{\langle E_{SC_x} \rangle}{E_{bias_y}} h. \tag{3.7}$$

Equation (3.7) shows that the distortion of the profile trajectory, and ultimately the beam width, is directly proportional to the beam strength and increases with the number of beam particles. However, the distortion is inversely proportional to the electric bias potential V since $E_{bias_y} = V/d$ and, therefore, by increasing the IPM bias potential the distortion is mitigated. Furthermore, the direct dependence on the height of creation h in (3.7) shows that particles created at different positions above the detector will be displaced differently. This has the effect of complicating the measured profile and will be discussed later.

Expression (3.7) is illustrated in figure 3.2, which shows simulated positive ion trajectories subject to a uniform positive vertical electric bias field coupled with a space charge field produced by a fully accumulated nominal beam with a uniform circular distribution. It shows that as the electric potential increases from 10kV in figure 3.2 (a) to 30 kV in part (b) the force of the bias field begins to overpower the space charge, where the spread due to space is nearly eliminated in figure 3.2 (c). While the simulation in figure 3.2 was done for positive hydrogen ions the spread, equation (3.7), does not depend on the ion mass.

(a)

(b)

(c)

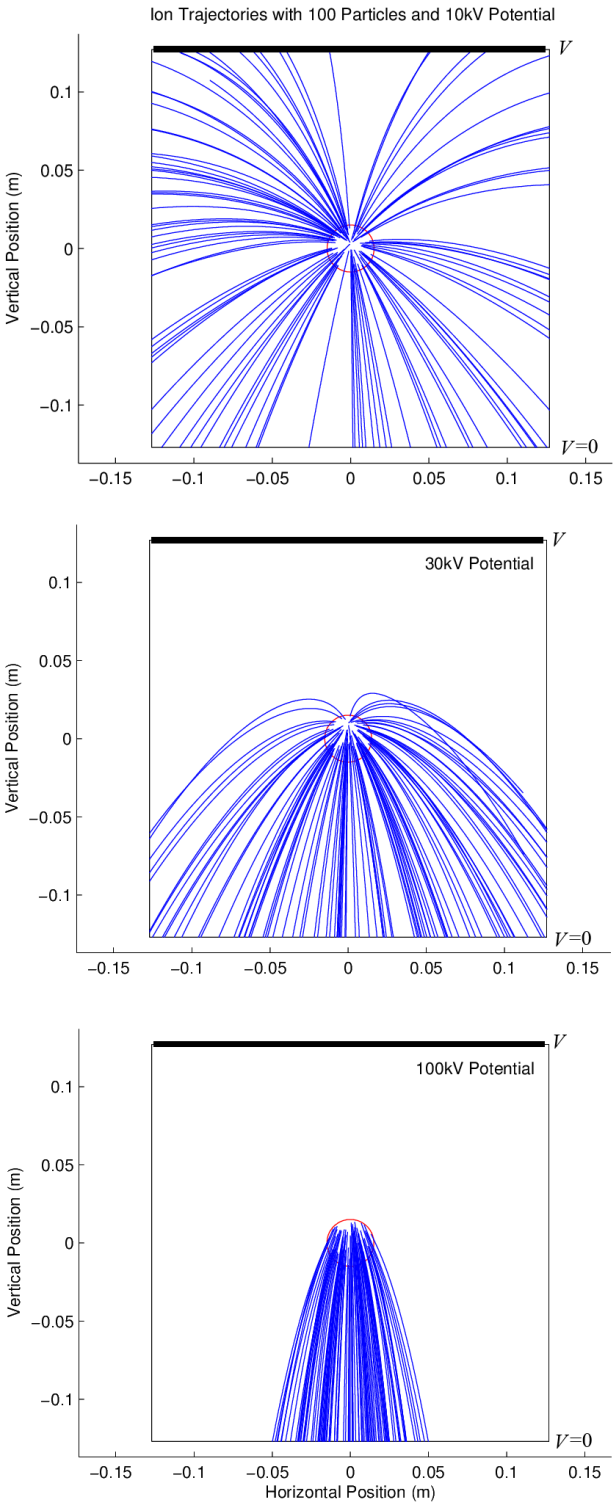

Figure 3.2 Trajectories of positive ions in uniform (a) 10kV (b) 30kV (c) 100kV positive electric potentials subject to a space charge field produced by a uniform circular distribution of charge for a fully accumulated beam.

Negative Ionization Products

Electrons created during the ionization process experience the effects of space charge in an inverse manner to that of positive ions. While ions experience a repulsive force from the beam center, electrons experience an attractive force due to the positive beam potential. An example trajectory of an electron subjected to a uniform circular space charge field with a -100 kV electric bias potential is shown in figure 3.3. The case of electron collection with only the electrical field is complicated by the fact that the majority of electrons created close to the beam center will cross the beam centerline before reaching the detector. One benefit of electron collection, provided the profile distortion can be overcome, is that the collection time is much smaller than that of ions due to the dependence of the time *t* on the particle mass *m* in equation (3.6).

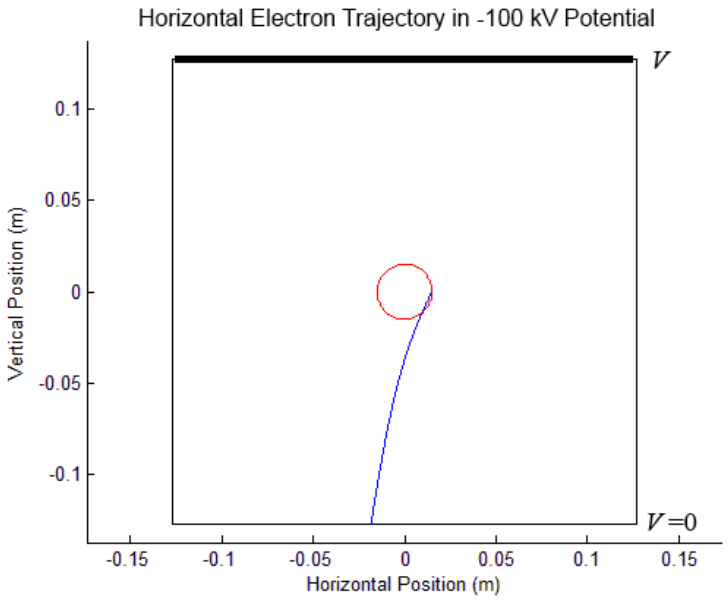

Figure 3.3 Electron trajectory in a uniform circular distribution of charge with a -100 kV uniform electric bias potential.

Electron Profile Distortion Mitigation

So far only the electric field component of the Lorentz force has been utilized to accelerate ionized gas particles toward a detector. By placing a magnetic field $\vec{B}$ transverse to the beam direction and parallel to electric bias field, a particle with mass *m* and charge *q* will experience a magnetic force given by $\vec{F}_B = q(\vec{v} \times \vec{B})$. The velocity perpendicular to the magnetic field direction $v_\perp$ will contribute to a radial force

$$F_r = ma_r = qv_\perp B. \tag{3.8}$$

The radial acceleration $a_r = v_\perp^2/r$ causes the particle to travel in a circular path with a Larmour radius

$$r_L = \frac{mv_\perp}{qB}. \tag{3.9}$$

The corresponding gyration period is

$$T = \frac{2\pi m}{qB}. \tag{3.10}$$

The cyclotron motion generated by the magnetic field coupled with the electric bias field causes the electrons to spiral around the magnetic field lines until they reach the detector. With a large enough magnetic field it is possible to confine the spiral to within the width of the Channeltron detector, thereby preventing the distortion in measured profiles. Plugging a representative transverse velocity from a 100 eV electron (the origin of this value will be given shortly) and a magnetic field of 300 G into equation (3.9) gives a radius 1.1 mm, thus making the deviation of single particle half a detector width.

The effect of an external magnetic field on electron trajectories is shown in figure 3.4, where (a) shows trajectories of 100 eV electrons with a uniform circular space charge and a -

40 kV bias potential and (b) shows the same case with an added external 300 G magnetic field. The sinusoidal motion seen in figure 3.4 (b) is a 2D projection of the cyclotron motion. With the majority of electron energies being on the order of a few eV and a beam potential on the order of 10 keV, in the absence of an electric bias field, ionized electrons lack sufficient energy to escape the beam's potential well during the beam's passage. The bias potential must be at least 20 – 30 kV in order to extract the electrons from the beam potential during accumulation.

External magnetic fields are not used with ions due to the dependence of the Larmor radius on the mass of the particle. Considering that the residual gas ions consist of light mass components such as hydrogen molecules along with much heavier molecules, such as

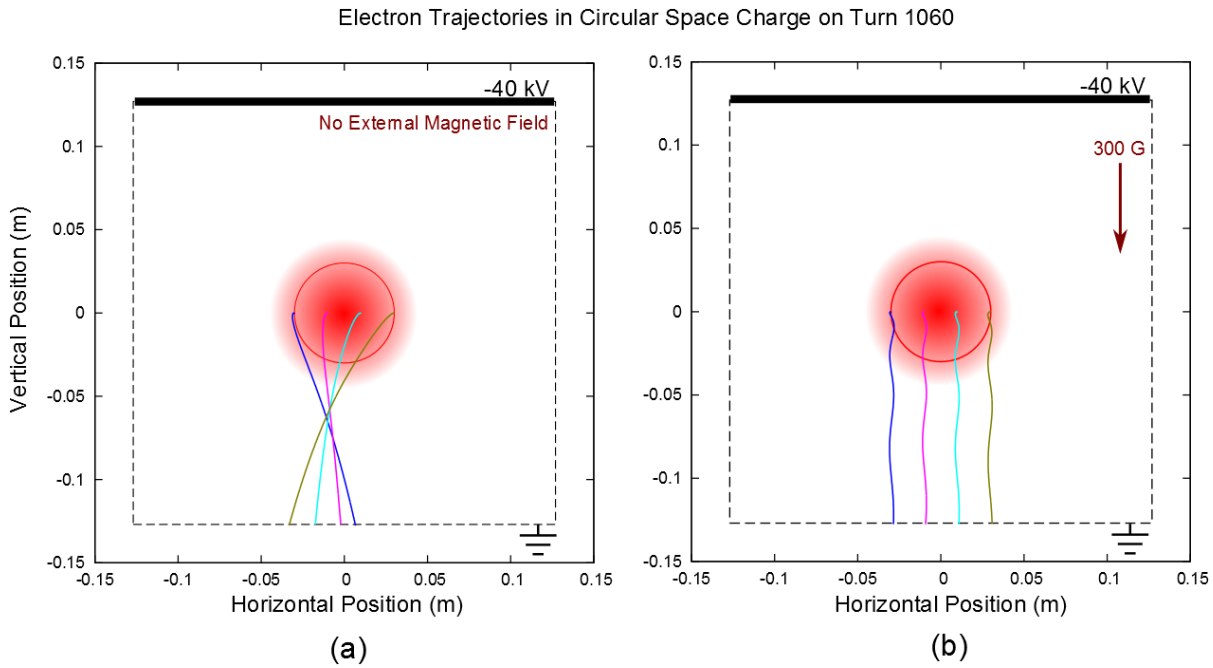

Figure 3.4 IPM simulated 100 eV electron trajectories with uniform circular space charge at the end of accumulation for (a) a -40 kV electric bias potential and no external magnetic compared to (b) with the same bias potential but including a 300 G external magnetic field.

water, the magnetic fields to produce the necessary cyclotron motion for the largest of ions are unrealistically large. For example, an ionized water molecule with a thermal initial velocity vector perpendicular to the magnetic field would require a flux density of ~600 G to produce the same radius as that of electrons. Therefore, external magnetic fields are used in electron collection only.

Beam Magnetic Field and Longitudinal Motion

The beam current produces a magnetic field that is capable of interacting with ionized gas particles. Like the beam-induced electric field, the magnetic field is directly proportional to the number of beam particles and therefore increases linearly during accumulation. Continuing with the example of a uniform cylinder of charge, the magnetic fields are

$$\vec{B}_{SC} = \frac{\lambda \beta c \mu_0}{2\pi} \frac{r}{a^2} \hat{\theta} \qquad r < a \tag{3.11}$$

$$\vec{B}_{SC} = \frac{\lambda \beta c \mu_0}{2\pi} \frac{1}{r} \hat{\theta} \qquad r > a \tag{3.12}$$

where $\hat{\theta}$ is the azimuthal direction and βc the beam velocity. The effect of magnetic field is less than that of the beam's electric field, as discussed in section 2.1.1 and shown in Appendix A. A 15 kV round beam potential has a magnetic field of ~10 G, at least an order of magnitude less than the external field required for electron collection. Due to the lack of longitudinal beam field, the ionized particle motion is primarily in the plane perpendicular to the beam path. There is, however, a mechanism by which charged particles in transverse fields may gain longitudinal motion.

Since the magnetic field produces a force that is always perpendicular to the velocity, the cyclotron motion does not change the particle's kinetic energy. For a constant external magnetic field $\vec{B}$, the helical velocity of a particle may be decomposed into components

parallel $v_\parallel$ and perpendicular $v_\perp$ to the magnetic field such that $\vec{v} = v_\parallel \hat{B} + \vec{v}_\perp$. The velocity parallel to the magnetic field $v_\parallel$ remains unchanged by the magnetic component of the Lorentz force. In the absence of electric fields, the cyclotron motion of a particle with position vector $\vec{x}$ may be reparameterized as circular motion with transverse velocity $\vec{v}_\perp$ and radius vector $\vec{r}$ traveling around a "guiding center" with velocity $v_\parallel \hat{B}$ and position vector $\vec{R}$ as illustrated in figure 3.5. The guiding center parameterization is given by

$$\vec{x} = \vec{R} + \vec{r} \tag{3.13}$$

$$\vec{r} = -\frac{m}{qB}\vec{v} \times \vec{B} \tag{3.14}$$

$$\vec{v}_\perp = \frac{d\vec{r}}{dt} = \dot{\vec{r}}. \tag{3.15}$$

With inclusion of an electric field in the Lorentz force $m\dot{\vec{v}} = q\left(\vec{E} + \vec{v} \times \vec{B}\right)$ the guiding center velocity may be found by differentiating equation (3.13) with respect to time

$$\begin{aligned} \dot{\vec{R}} &= \dot{\vec{x}} - \dot{\vec{r}} \\ &= \vec{v} + \frac{m}{qB^2}\dot{\vec{v}} \times \vec{B} \\ &= \vec{v} + \frac{1}{qB^2} q\left(\vec{E} + \vec{v} \times \vec{B}\right) \times \vec{B} \\ &= v_\parallel \hat{B} + \frac{\vec{E} \times \vec{B}}{B^2} \end{aligned} \tag{3.16}$$

where $\left(\vec{v} \times \vec{B}\right) \times \vec{B} = -\vec{v}_\perp B^2$ and $\vec{v} - \vec{v}_\perp = v_\parallel \hat{B}$ have also been used. It may be seen from the previous derivation that for uniform fields the guiding center experiences a drift, known as $E \times B$ drift, with velocity

$$\vec{v}_{E\times B} = \frac{\vec{E} \times \vec{B}}{B^2} \tag{3.17}$$

in a direction perpendicular to both the electric and magnetic fields. In the IPM, such a drift

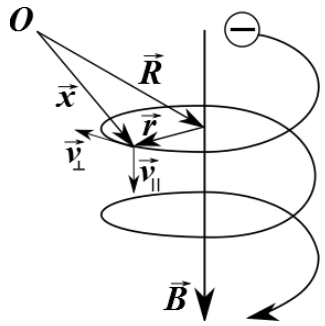

Figure 3.5 Definition of Guiding Center motion for a negatively charged particle in a uniform field.

causes motion in the longitudinal direction. For the case of $E \times B$ drift, it has shown in [74] that the equation (3.17) is only valid for $|E| < c|B|$ since the reverse case causes the particle to simply be accelerated in direction of *E*.

In the IPM, $E \times B$ drift would be the result of errors in the alignment of the external electric and magnetic fields. For example, a 300 G magnetic field with a misaligned electric field having a 10 kV perpendicular electric component results in $v_{E\times B}$ = 1.3x10^6 m/s. In 20 ns this results in a longitudinal drift of 2.6 cm. Between the permutations of the beam field and external fields there are a number of possible longitudinal drift mechanisms.

In addition to $E \times B$ drift there are guiding center velocities arising from various aspects of the beam-external field coupling. The equations for different drifts will be stated here while in-depth derivation and analysis of each may be found in [74], [149], [150] and the references therein. A guiding center drift arising from non-uniform electric and uniform magnetic fields, such as the beam's electric field and external magnetic field, takes the form

$$v_{\Delta E\times B} = \left(1 + \frac{1}{4} r_L^2 \nabla^2\right) \frac{\vec{E} \times \vec{B}}{B^2} \tag{3.18}$$

where r_L is Larmour radius. Additional drifts arise purely from nonuniformities in magnetic

field. The gradient B drift or ∇B drift is the result of the Larmour radius changing as the particle passes between regions of varying magnetic field magnitude. This longitudinal drift would be caused by a similar variation of the beam's $1/r$ magnetic field. It is

$$v_{\nabla B} = \pm \frac{1}{2} v_{\perp} r_L \frac{\vec{B} \times \vec{\nabla} B}{B^2}. \tag{3.19}$$

A form of drift occurs when the magnetic field lines curve, as they do around the beam. The curvature drift velocity is

$$v_C = \frac{m v_{\parallel}^2}{q} \frac{\vec{R}_C \times \vec{B}}{R_C^2 B} \tag{3.20}$$

where $\vec{R}_C$ is a vector from the center of the magnetic curvature to the particle position.

The cumulative motion produced by the various drifts is difficult to estimate simply. It is not necessary to find exact analytical values for the longitudinal drift as all possible drifts are accounted for during simulation of the particle trajectories, which will be discussed in the next section. Furthermore, it will be shown during analysis of particle trajectories that the electron drifts are not significant except in the most extreme of external field misalignments. While the effect of longitudinal motion would be to move individual electrons initially created above the detector region past the detector during their time of flight, since the entire mini-pulse is being summed over, the result of longitudinal drifts on the distribution as a whole would be to shift a few nanoseconds worth of pulse data at the beginning and end of a pulse.

3.1.3 Trajectory Simulation

Even the simple case of a uniform bias field E_{bias} coupled with a uniform circular beam distribution with fields given by equations (3.3) and (3.4) results in equations of motion

$$\ddot{x} = \frac{q}{m}\frac{\lambda}{2\pi\varepsilon_0 a}\frac{x}{\sqrt{x^2+y^2}} \tag{3.21}$$

$$\ddot{y} = \frac{q}{m}\frac{\lambda}{2\pi\varepsilon_0 a}\frac{y}{\sqrt{x^2+y^2}} - E_{bias} \tag{3.22}$$

outside of the beam radius *a*. The second-order coupled differential equations are best solved with numerical methods. For complex space charge fields, simulations are the only method for tracking charged particles in IPM fields such as those in figure 3.2 and figure 3.3.

Profile Benchmarking Method

A robust particle tracking program can accommodate any configuration of beam particle distribution as well as external electric and magnetic fields. Furthermore, it is desirable to be able to track ionized particles in fields produced by specific SNS ring beam configurations. Due to the lack of profile diagnostics in the ring, experimental verification of the measured IPM beam profiles will be done in the manner that ring profiles are currently measured. Wirescanners located in the RTBT measure beam profiles. These profiles are used to calculate the expected profile at different locations in the ring based on the beam optics. Upon installation, the IPM profiles will be compared to calculated beam-based profiles for benchmarking the accuracy of the system. Upon successful measurement of profiles, the IPM will provide a useful benchmark tool the SNS ring beam transport simulation code ORBIT.

ORBIT

Part of the goal of this project was to write a module for the ORBIT simulation code. ORBIT (Objective Ring Beam Injection and Tracking) is a particle tracking code developed at SNS for beam dynamics studies in the ring [151],[152]. It uses a particle-in-cell method that groups sections of beam into “macro-particles” and calculates the space charge from each macro-particle. This, together with other collective and external forces, is then used to

propagate a “herd” of macro-particles through the accelerating structure [153]. Originally written in C++, ORBIT utilizes the object-oriented language to track herds of macro-particles through nodes which describe the actions experienced by beam particles traversing different ring components. The ORBIT code is now migrating to the Python scripting language by building Python interpreters around the existing ORBIT code. During the IPM project, only portions of ORBIT have been functional in the Python version. In anticipation of the completion of PyORBIT (Python ORBIT), it was decided to do any IPM ORBIT programming in Python.

IPM Module

PyORBIT includes an electron cloud module that contains all the necessary tools to simulate the effect of the electron cloud in the ring. Included in the electron cloud module is a particle tracking class that contains methods for tracking charged particles in electric and magnetic fields, including the effects of the beam space charge. The IPM module is based on the electron cloud particle tracking module. The simulation process goes as follows:

1) Basic beam parameters such as number of beam particles and size of the beam are chosen in order to determine the space charge.
2) Electric and magnetic external bias field strengths are specified. Field distribution may also be chosen in order to study the effect of field errors on particle trajectories.
3) The beam space charge distribution is chosen.
4) Ionized particle initial conditions are set including: type of particle, random or specified initial positions, and type of initial velocities.
5) Particles are tracked subject to the Lorentz force in the prescribed fields until

each particle has contacted the IPM chamber boundary.

6) Trajectory and simulation data is collected and dumped in a series of output files.

Tracking in the IPM module is done by using a 4th Order Runge-Kutta method which is an iterative approximation for first order differential equations of the form $\dot{x} = f(x,t)$ with initial value $x(t_0) = x_0$ and $\dot{x} = dx/dt$. For a step size h, the 4th Order Runge-Kutta method [154] is

$$\begin{gathered} x_{n+1} = x_n + \frac{1}{6}(k_1 + 2k_2 + 2k_3 + k_4) + O(h^5) \\ t_{n+1} = t_n + h \\ k_1 = hf(x_n, t_n) \\ k_2 = hf\left(x_n + \tfrac{1}{2}k_1, t_n + \tfrac{1}{2}h\right) \\ k_3 = hf\left(x_n + \tfrac{1}{2}k_2, t_n + \tfrac{1}{2}h\right) \\ k_4 = hf(x_n + k_3, t_n + h) \end{gathered} \tag{3.23}$$

where $n = 0,1,2,3\ldots$ is the step number. Each step in the Runge-Kutta method gives essentially a weighted average of a point at the end of interval h estimated by the slope at the beginning, slopes in the middle based on the previous estimates, and a fourth point estimated from the slope of the third point. With greater weight placed on the middle two point estimates, the error on each step is of order $O(h^5)$.

Solving the three equations of motion $\ddot{x}, \ddot{y}$, and $\ddot{z}$ (like those in equations (3.21) and (3.22)) for the charged particle trajectories in the IPM may be done by rewriting the three second-order equations as six first order equations. For example,

$$\dot{x} = v_x$$
$$\dot{v}_x = f_x(x, y, z, v_y, v_z, t) \tag{3.24}$$

for the *x* coordinate where $f_x(x, y, z, v_y, v_z, t)$ is a function found from the Lorentz force for a charge particle subject to the superposition of bias and space charge fields. Given initial conditions (x_0, y_0, z_0) and $(v_{x_0}, v_{y_0}, v_{z_0})$, the equations in (3.24) along with the corresponding equations for the *y* and *z* components are solved with the Runge-Kutta method to give particle trajectories.

Beam Profile Approximation

While the beam in SNS linac has a Gaussian transverse distribution, the beam profile in the ring is more complex due to the nature of the requirements for the beam on the target. In order to preserve the target, while minimizing the effects of space charge in the ring to limit instabilities and beam loss, the beam must be painted over as large a phase space volume as possible [155]. While the final beam size at the target is determined by 5 quadrupoles at the end of the RTBT, the beam's density profile is determined by the injection of the beam into the ring. A set of 4 chicane dipoles along with horizontal and vertical fast kicker dipoles pass the beam from the linac through the foils for stripping and painting into the ring.

Painting is accomplished by moving the closed orbit diagonally away from the stripping foil as an increasing function of time allowing each successive injected beam pulse to fill larger and larger spatial areas [156]. The correlated painting scheme is represented in figure 3.6 (a) with the arrows showing the direction of the movement of the closed orbit. Correlated painting produces a spatial particle distribution in the ring shown in figure 3.6 (b) where the red distribution is the correlated distribution with space charge included. Transverse profiles, without (blue) and with (red) the effects of space charge, for the

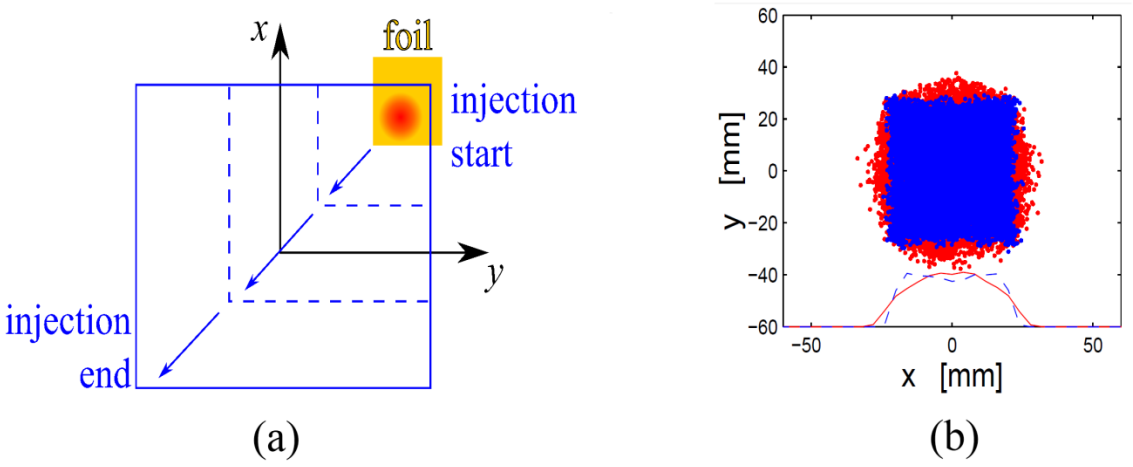

Figure 3.6 (a) Correlated SNS accumulator ring injection painting scheme. (b) Simulated beam distribution from correlated painting (blue) with space charge (red) including horizontal transverse profiles. [157]

correlated distribution are shown in figure 3.6 (b). A uniform circular distribution is a rough approximation to the case with space charge.

However, errors during passage through the ring lattice produce halo particles outside the beam core. In addition to halo, a manifestation of the central limit theorem in probability theory [158] is that the beam will tend toward a normal distribution over time [159] providing all of the errors experienced by the beam are random and uncorrelated. As such, a two-dimensional Gaussian distribution

$$f(x,y) = \frac{N}{2\pi\sigma_x\sigma_y}\exp\left(-\frac{1}{2}\left(\frac{(x-\mu_x)^2}{\sigma_x^2}+\frac{(y-\mu_y)^2}{\sigma_y^2}\right)\right) \tag{3.25}$$

can also be used to approximate the real distribution and space charge, where $\sigma_{x,y}$ are the RMS beam sizes, $\mu_{x,y}$ the beam centroids, and N is the number of beam particles.

Initial Velocities

The initial velocities of the ionized particles are determined by the energy transfer gained during the ionizing collision. As discussed in section 2.1.2, the incident proton with velocity βc primarily loses energy to orbital electrons, where the energy transfer ΔE to a free electron, with mass m_e, becomes the electron's kinetic energy. For singly charged incident particles and targets from equation (2.9), the energy transfer yields

$$\Delta E(b) = \frac{2}{m_e}\left(\frac{e^2}{4\pi\varepsilon_0}\right)^2 \frac{1}{\beta^2 c^2}\frac{1}{b^2 + b_{min}^2}. \tag{3.26}$$

The ionized electron kinetic energy is determined by the impact parameter *b*, with a range between the minimum impact parameter b_{min} and the maximum impact parameter b_{max}. The parameter b_{min} is determined by the maximum allowed energy transfer E_{max} found through relativistic kinematics, and the parameter b_{max} corresponds to the minimum energy transfer. Because the electron under consideration is the least bound electron in the absorber molecule, the minimum energy the electron can possess is that required to remove it from its neutral molecule, namely the first ionization potential E_I.

The probability of an electron gaining an energy greater than E_I is defined by the cross section of interactions with energy transfer greater than that determined by *b* relative to the total cross section for all possible energy transfers determined by b_{max} as

$$P(\Delta E > \Delta E(b)) = \bar{F}(b) = \frac{\pi b^2}{\pi b_{max}^2} = \frac{b^2}{b_{max}^2}. \tag{3.27}$$

Equation (3.27) is the definition for the Complementary Cumulative Distribution Function (CCDF) which is the probability that a random variable will be found to be than a given value [158]. Solving equation (3.27) for *b* and substituting into the equation for energy

transfer (3.26) yields the cumulative probability an ionized electron will have an energy greater than a given value E

$$\bar{F}(E) = \frac{E_I}{E} - \frac{E_I}{E_{max}}, \qquad E_I \leq E \leq E_{max}. \tag{3.28}$$

Figure 3.7 shows the CCDF for ionized electrons from water molecules where the minimum energy has been set to 12.6 eV from table 2.2 while E_{max} is 3.34 MeV for a 1 GeV proton. It may readily be seen from figure 3.7 that majority of electrons have energies under 100 eV. For example, 20% of ionized electrons for gaseous water molecules have energies less than 16 eV. While electron energies are low they are ~10^3 times larger than thermal velocities at the IPM temperature. By generating a random number for *F(E)*, equation (3.28) is used to choose random initial velocities for simulated ionized particles.

From equation (3.6) estimating the time for a particle to reach the IPM boundary under the influence of only a bias field, the time for an electron to reach a detector in a

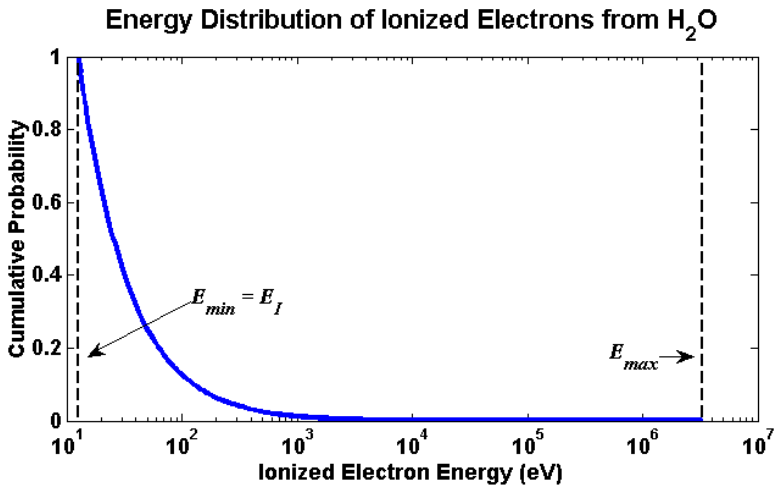

Figure 3.7 The cumulative probability distribution shown as a function of energy transfer or ionized electron kinetic energy from water molecules showing the maximum and minimum energy transfers where E_I is the ionization energy.

100 kV potential is about 2 ns. The initial velocity contribution to the distance traveled by 10 eV electrons during the collection time is ~3 mm, compared to ~11 mm due to a 10 kV bias potential. From this analysis it may be seen that the effect of electron initial velocities is more significant at lower bias potentials. For potentials on the order of 100 kV the initial velocity contribution to profile distortion is small compared to that caused by space charge effects.

Through an elastic collision analysis between the electron and incident particle, kinematics gives a relationship between the electron recoil energy *E* and the angle of electron ejection θ relative to the initial incident particle path [160]

$$\cos^2\theta = \frac{E}{E_{max}}. \tag{3.29}$$

Since it has already been shown that electron energies are typically small compared to E_{max}, electrons are ejected nearly perpendicular to the incident particle path. For IPM profile simulations, the randomly assigned electron energy is then used in equation (3.29) to produce longitudinal electron velocity directions. Transverse velocity directions are assumed to be distributed uniformly and are randomly chosen by the sphere point picking method described in [161]. Choosing direction coordinates from a unit sphere yields

$$\begin{aligned} x &= \sqrt{1-u^2}\cos\theta \\ y &= \sqrt{1-u^2}\sin\theta \\ z &= u \end{aligned} \tag{3.30}$$

where *u* and θ are uniform random variables on the ranges $u \in [-1,1]$ and $\theta \in [0,2\pi)$. Equation (3.29) is then used to find *u* in equation (3.30) instead of being randomly chosen.

The ion initial energy scales by a factor of m_e/M in the energy transfer equation

(3.26) compared to the electron energies, where *M* is the ion mass. Considering that m_e/M is never greater than $m_e/m_p \sim 10^{-4}$, the kinetic energy gained by ions during ionizing collisions is less than their thermal energies. Consequently, ions of mass *M* with a temperature *T* are given random velocities *v* determined by a Maxwellian probability distribution of speed

$$f(v) = \sqrt{\left(\frac{M}{2\pi k_B T}\right)^2} 4\pi v^2 e^{-\frac{Mv^2}{2k_B T}} \tag{3.31}$$

with directions randomly chosen using the method describe by equations (3.30). While ions are given initial velocities in simulations, the RMS velocity v_{rms} is inversely proportional to the particle mass, making $v_{rms} \cong 2$ km/s for hydrogen molecules and 640 m/s for water. During a single 1 μs pulse in the ring, hydrogen ions will drift ~2mm and water ions will drift about 0.6 mm. Therefore, ion initial velocities do not contribute significantly to the trajectory and the ions may be considered at rest for qualitative studies.

3.1.4 Ion Collection Field Analysis

Ion Collection Bias Potential

With the IPM simulation program incorporating all the applicable forces and initial conditions, it is possible to predict the magnitude of electric bias potential needed to overcome the space charge distortion. The same initial uniform circular particle distribution was used to simulate the measured IPM profiles for a range of electric bias voltages for a beam with uniform circular space charge at the end of the accumulation cycle. The results are shown in figure 3.8 along with marker lines showing the initial RMS size, RMS size plus 10%, and RMS size plus 20% of the initial distribution. The most dramatic effect of the bias

potential is seen below 200 kV above which improvements in the measured profile are only moderate. From figure 3.8 it may be seen that a measured beam size with a 10% distortion may be achieved with a 500 kV bias while a 20% increase in the measure width is reached with a 240 kV potential. Hydrogen and water molecules were also simulated, showing that the distortion is not a function of ion mass as predicted by equation (3.7).

Figure 3.8 makes clear the difficulty of collecting ions. The 500 kV potential required to meet the beam size system requirement is an exceedingly difficult technical challenge considering the limited space afforded by the IPM chamber and safety specifications needed for such a high voltage. Even a 240 kV potential provides a degree of technical challenge beyond the scope of the safety limitations delineated for this system. For ions, mitigation of beam induced profile spreading is not possible purely through hardware design within the IPM design parameters.

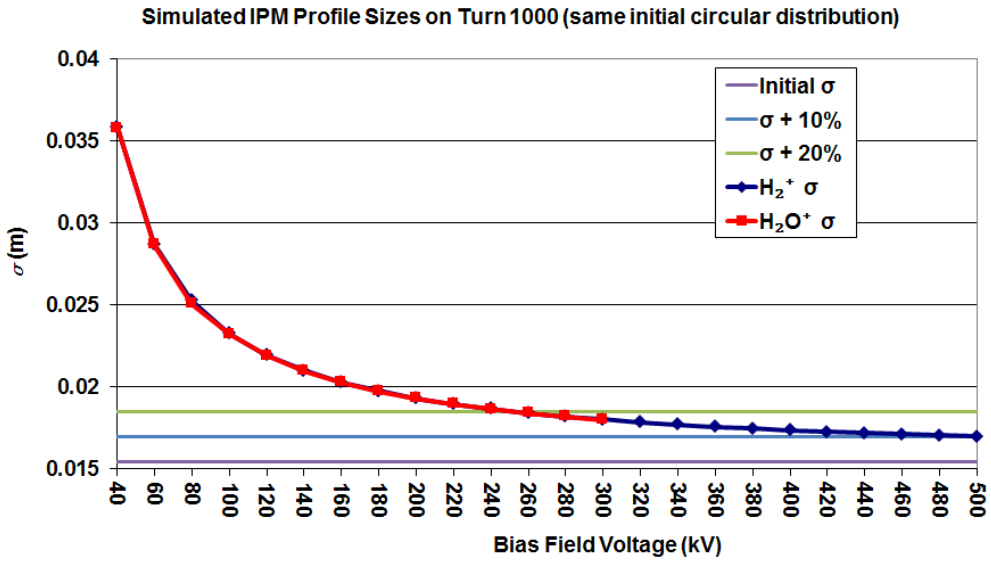

Figure 3.8 Simulated measured IPM profile RMS sizes σ as a function of electric bias potential for ions with a uniform circular distribution.

Effect of Turn Number on Ion Profile

The spreading of the beam profile is directly proportional to the space charge electric field. As the beam is injected into the SNS ring the space charge increases linearly with each injected mini-pulse. The effect of increased space charge during accumulation is shown in figure 3.9 for simulated profiles as a function of turn number for hydrogen ion collection in a 240 kV bias potential. It shows how the measured width increases with number of injected turns from almost no distortion at the first turn to a 10% size increase halfway through injection. Equation (3.7) and the case shown in figure 3.9 suggest that the profile size scales inversely with the ratio of the new potential V to 240 kV as ~240 kV/V. For smaller bias potentials the accuracy of the measured beam size fails to meet the design criteria at earlier times during the accumulation.

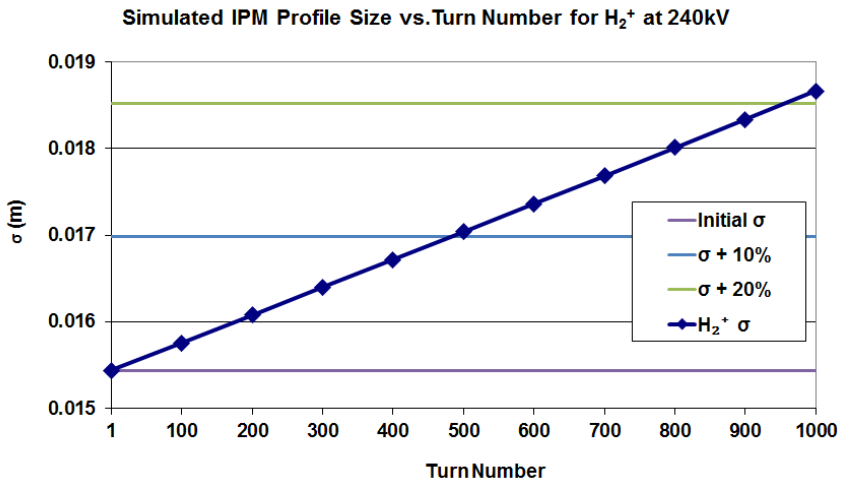

Figure 3.9 Simulated IPM profiles sizes as a function of injected turn number for hydrogen ions in a 240 kV electric bias potential.

3.1.5 Measured Ion Profile Characteristics

Width Calibration

It is possible to use a beam-based calibration to remove the distortion of the measured beam size produced by the space charge for ion generated profiles [162]. The method is fairly simple but is based on the assumption that the distortion in the width is produced by the beam and not due to nonlinear bias fields in the IPM. Assuming the previous assumption is true, the beam size is measured as the voltage on the bias potential V_{bias} is increased.

By plotting the measured beam sizes as a function of $1/V_{\text{bias}}$ the beam size is found to be nearly linear, as indicated by the expression for the distortion of particle trajectory in the presence of space charge in equation (3.7). The y-intercept represents the extrapolation of $V_{\text{bias}} \rightarrow \infty$ where an infinitely large bias potential would completely mitigate any space charge distortion, so that the measured beam size would be the true beam size. The process is illustrated in figure 3.10 for the case of H_2^+ simulated beam sizes shown in figure 3.8. In reality only the ten highest bias potential data points where used for the linear fit since the sizes exhibit nonlinear behavior attributed to the greater influence of the beam on the particle trajectories at the lower bias potentials. The fitted result reproduces the initial beam of 15.4 mm produced by a uniform density circular beam. The ions were generated at five vertical positions.

Beam Shape Distortion

The previous method for the determining the beam size is regularly used when the beam size is the primary beam parameter desired. It would be tempting to use the aforementioned beam size calibration to scale the measured profile in order to produce a profile of the correct size and then use it represent the actual beam generated with ions. However, upon further

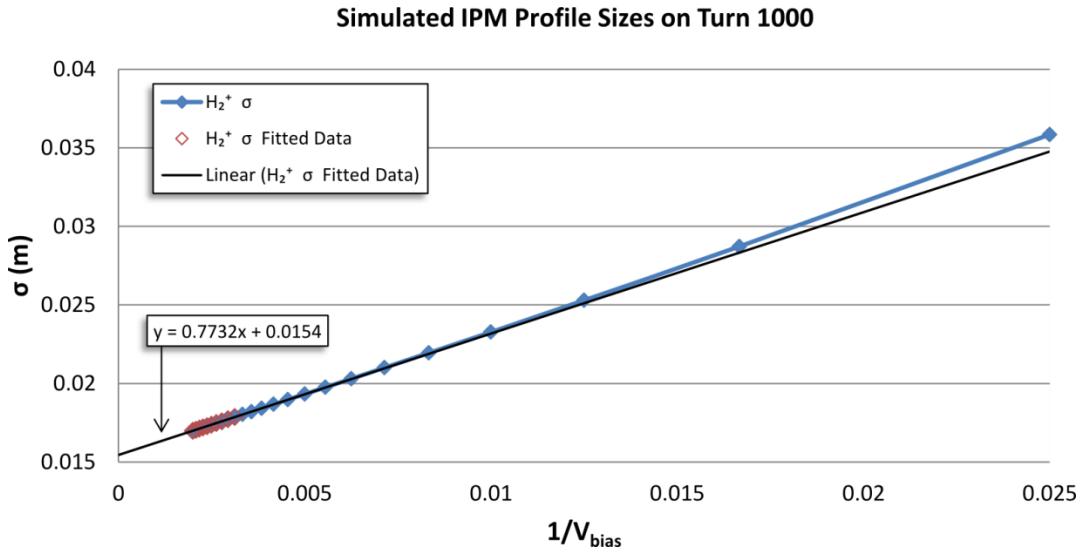

Figure 3.10 Extrapolation of simulated H_2^+ beam sizes to find the true beam. The linear fit uses only the data points representing the highest bias potentials due to the nonlinearity exhibited by strong beam coupling at lower potentials.

analysis, simply scaling an ion-generated profile is not sufficient to produce a profile that accurately represents the beam.

Figure 3.11 shows the trajectories of H_2^+ ions under the influence of space charge above the measurement plane. By following the individual trajectories from particles generated at the same horizontal position, meaning that without space charge these particles would be collected at the same final horizontal position, figure 3.11 shows that the particles reach the detector plane at different final positions. The distortion of the particles depends upon their height above the detector. The results from figure 3.11 are summarized in figure 3.12 which shows that, for a particle with an initial horizontal position falling within a given Channeltron, the final particle position and therefore the Channeltron in which it is detected increases with initial vertical position.

The effect of the dependence of the individual ion trajectories on vertical position is to cause, not only a widening of the profile, but a mixing of particles within a profile leading

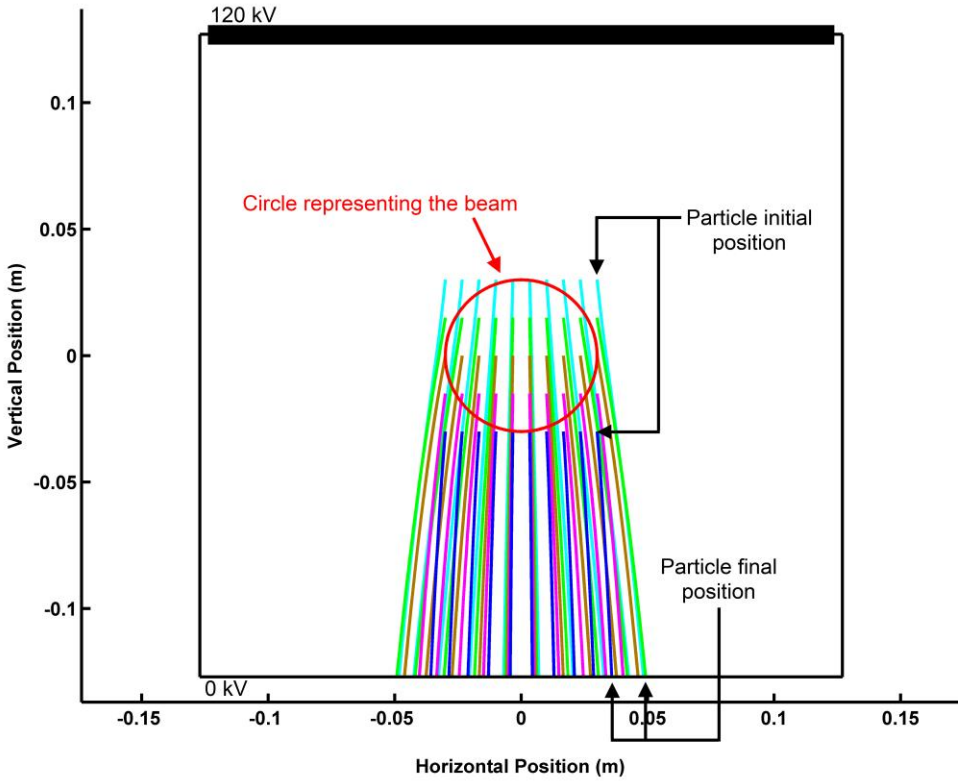

Figure 3.11 Hydrogen ion trajectories in a 120 kV bias potential with uniform circular space charge showing the mixing of particles generated at varying heights

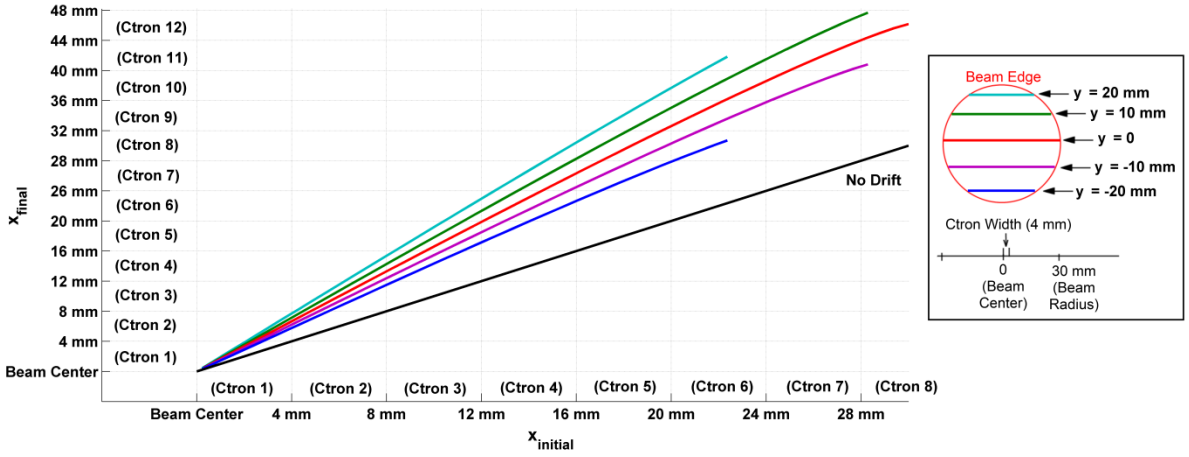

Figure 3.12 The measured particle positions as a function of initial horizontal position for selected vertical initial position. An ion experiencing no space that is produced within Channeltron 1 will be collected within the same Channeltron.

to a blurring of the characteristics of the initial ionization products. Profiles measured with ions would then have profile shapes that are not true representations of the beam that produced them. The high intensity present in the SNS ring makes the possibility of directly measuring beam profiles a formidable if not unrealistic task. It has been shown that simple calibration techniques are useful in determining basic beam parameters.

However, since the goal is to produce accurate representations of the beam, a much more complicated method of calibration is required. With an IPM installed in the SNS ring, it would be possible to research ion-profile calibration techniques. The IPM will still be designed with ion collection in mind as both a method of comparison as well as for further study and development of IPM technology.

3.1.6 Electron Collection Field Analysis

The previous analysis illustrated the difficulties associated with generating profiles with ions. There are additional issues with ion collection that will be discussed later. It is left now to analyze the fields required for the production of accurate electron-based profiles. It has been shown that electrons suffer space charge induced distortions in their trajectories and that an external magnetic field may be used to produce more accurate profiles than possible with ions.

Electron Field Optimization

Simulating a range of electric and magnetic fields for the same initial conditions and measuring the percent error, given by $\Delta\sigma\ \% = |\sigma_{measured} - \sigma_{initial}|/\sigma_{initial} \cdot 100$ gives the optimum set of field values to provide an accurate profile measurement without requiring excessive hardware requirements. The results are displayed in figure 3.13. As expected, the measured profile distortion decreases with increasing external magnetic field. The Larmor

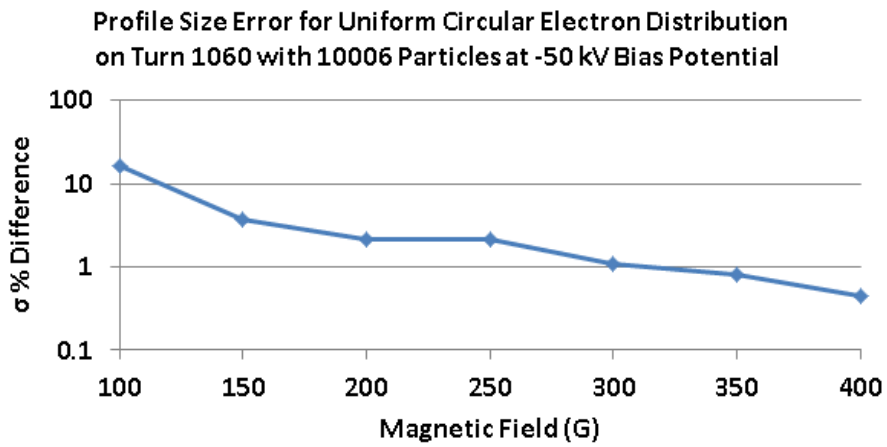

Figure 3.13 Simulated IPM profiles sizes as a function of external magnetic field from electrons with a uniform circular distribution and space charge at the end of the accumulation cycle in a -50 kV uniform bias potential.

radius is almost entirely determined by the ionized electron velocity since the external magnetic field immediately forces the particle into cyclotron motion. Any energy transferred to the particle as a result of perpendicular electric beam fields translates into longitudinal guiding center motion. The effect of increasing the electric bias field only increases the particle velocity parallel to the magnetic field lines. From figure 3.13, the profile size differs from the original by only 1% with a magnetic field of 300 G. Accuracy better than 1% provides only nominal improvement to the measured profile. The success of electron-based profiles may be seen in the individual case of initial and measured profiles in figure 3.14 for a 300 G magnetic field.

Guiding Center Drift

The longitudinal velocity induced upon the guiding center, discussed in section 3.1.2, is seen clearly in a three dimensional view of electrons in figure 3.15. The combination of guiding center motion produces asymmetric drifts about the center of the beam. For the fields used in the IPM, the drift is not expected to produce more than 1.5 cm in the longitudinal direction at

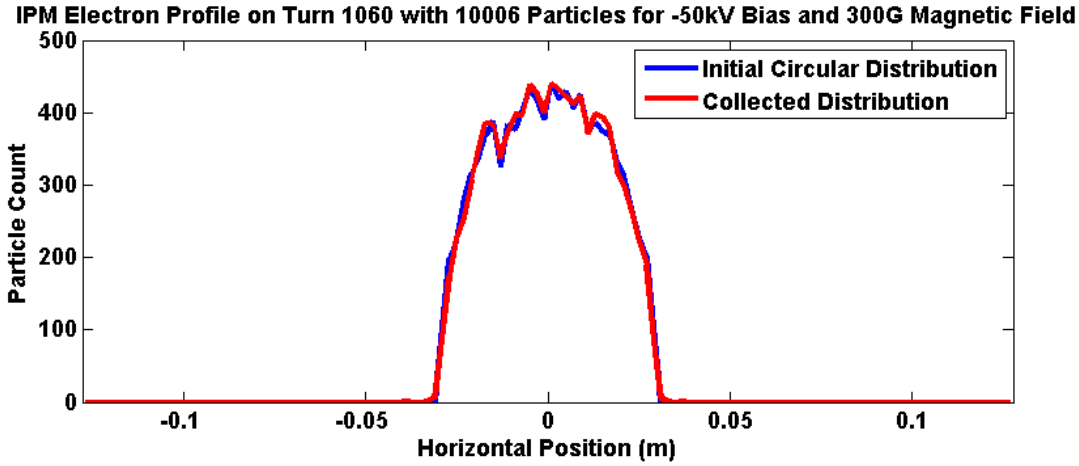

Figure 3.14 Simulated IPM profiles with uniform distributed electrons in uniform circular space charge with random initial velocities on turn 1060 in a -50 kV bias potential and 300 G magnetic field.

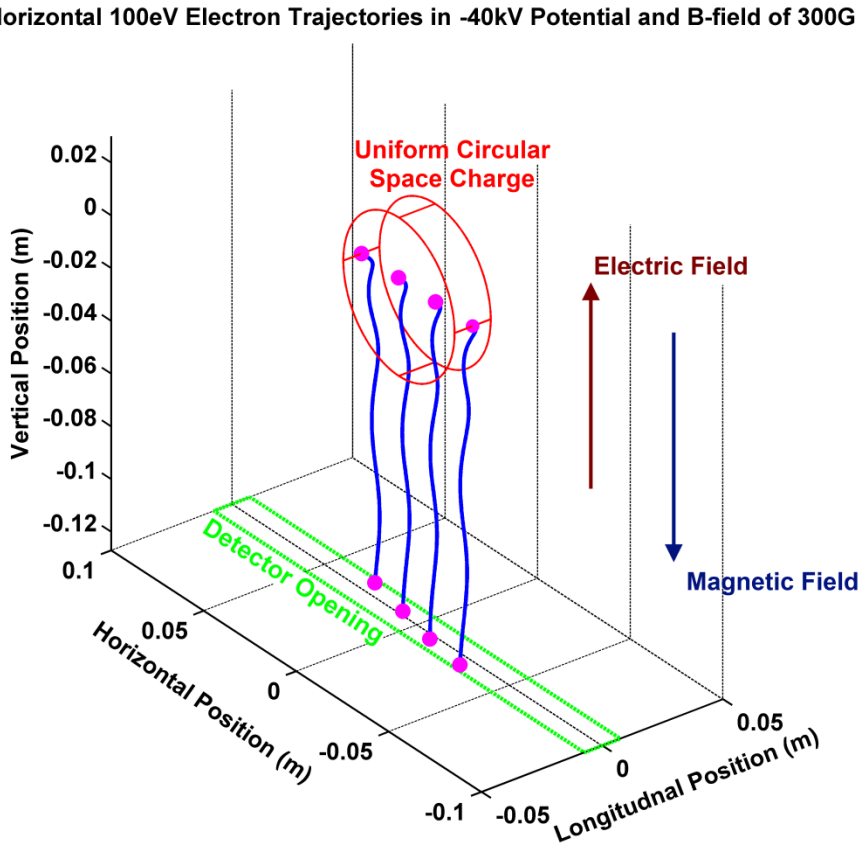

Figure 3.15 Three-dimensional 100 eV electron trajectories in a -40 kV bias potential and 300 G magnetic field showing guiding center longitudinal motion.

the detector, as shown in figure 3.15, and therefore is not expected to be an issue. Even if the external electric field were extremely misaligned to produce a perpendicular component of -20 kV to the external magnetic field, the additional drift would only be on the order of microns. Therefore, longitudinal motion due to field alignment errors will be considered negligible.

3.2 Spatial Accuracy

With an understanding of the trajectories in the IPM and a determination of the necessary field values, it is now possible to analyze more completely the accuracy of the collected measurement. Spatial accuracy defines the ability of the measured distribution to replicate the actual beam distribution and the certainty with which it is known. An accurate measurement requires not only a mitigation of beam-induced profile distortion, as previously discussed, but the counting of additional errors arising from the measurement process. Some errors may be removed from the final profile while others will be accumulated to characterize the measurement accuracy.

Error Definition

A few errors present in an IPM profile have been discussed, such as the error due to space charge distortion and the error due to small-number statistics. There are a number of other error sources that will be considered and it will be useful for further discussion to define nomenclature for the next few sections. The most useful way to categorize the effect of various profile error sources is to study their effect on the measured rms beam size σ_{meas}.

The error in measuring a beam with rms beam size σ_{beam} may be separated into a systematic component σ_{sys} and a statistical or random component σ_{rand}. A systematic error is defined to be the portion of the difference between a measured quantity and its actual

value, where this portion is consistent in all measurements as a result of the way in which the measurement is made [163]. One example is the profile distortion due to space charge. Systematic errors may be reduced with corrections or system improvements while random errors are due to stochastic variations, such as signal amplitude fluctuations from low particle numbers, and represent the uncertainty of the measurement The measured beam size is a combination of the true beam size and the error contributions such that $\sigma_{meas} = \sigma_{beam} + \sigma_{sys} \pm \sigma_{rand}$. The relative error on the beam size is defined by

$$\frac{\sigma_{meas} - \sigma_{beam}}{\sigma_{beam}} = \varepsilon = \varepsilon_{sys} \pm \varepsilon_{rand} \tag{3.32}$$

where ε_{sys} and ε_{rand} are the systematic and statistical relative errors. The percent error, found by multiplying equation (3.32) by 100, will be the primary error expression used.

3.2.2 Resolution and Statistical Errors

It is necessary to obtain an estimate of the statistical errors present in an IPM profile in order to understand how each type of error affects the measured beam size. Following an analysis found in [53] and [164], it is possible to numerically analyze errors due to stochastic processes and spatial resolution by using a Monte Carlo method. The following simulations assume a Gaussian beam distribution with rms beam size of 15 mm and center at 0 in both transverse directions. Furthermore, much of the following analysis will consider only the error on the final measured profile, meaning that any noise present is due to the entire electrical path of the signal including electronics.

Monte Carlo Simulation

Error estimation is based on a Monte Carlo approach which is uses an idealized model to generate a large ensemble of measurement possibilities due to assumed errors. The spread of

measurement results gives allows an estimation of the uncertainty. The simulation process is shown in figure 3.16. IPM profiles are produced by generating measured signals at a given number of transverse positions where the sample size at each position is a function of the detector size. In order to simulate this, a Gaussian transverse beam distribution $f(x)$ which is normalized to the number of ionized particles is used to generate measured data points $\overline{y}_i$ by integrating $f(x)$ over the detector width *w* at *k* positions $\overline{x}_i$ shown in figure 3.16 (a) as

$$\overline{y}_i = \int_{\overline{x}_i - \frac{w}{2}}^{\overline{x}_i + \frac{w}{2}} f(x)dx, \;\; i = 1, \dots, k. \tag{3.33}$$

The ensemble of measured profile points is used to generate an ideal measured IPM profile (figure 3.16 (b)) consisting of a random Gaussian distribution of *l* error points y_i, where $\overline{y}_i$ is the mean of the error distribution and σ_ε is the width characterizing the size of the error in question. Each of the *l* sets of error points represents a noisy realistic measurement where a nonlinear weighted least squares fit utilizing the Levenberg–Marquardt algorithm [165] is used to fit a Guassian distribution to each set. Three such sets and fits are shown in figure 3.16 (c).

The weights are defined such that the weight for the *j*th point in the fit is the inverse of the variance of the error distribution $1/\sigma_{\varepsilon_j}^2$. The beam sizes from all of the fitted distributions are histogrammed as illustrated in figure 3.16 (d) where *l* has been chosen as 1000 which makes the error on histogram size $1/\sqrt{2l} \approx 0.02$, which may be considered negligible. The number of histogram bins has been chosen by an algorithm described in [166] and [167] that uses an estimated Gaussian standard deviation σ and number of entries *n* to find the optimal number of bins to describe the data. The bin number is

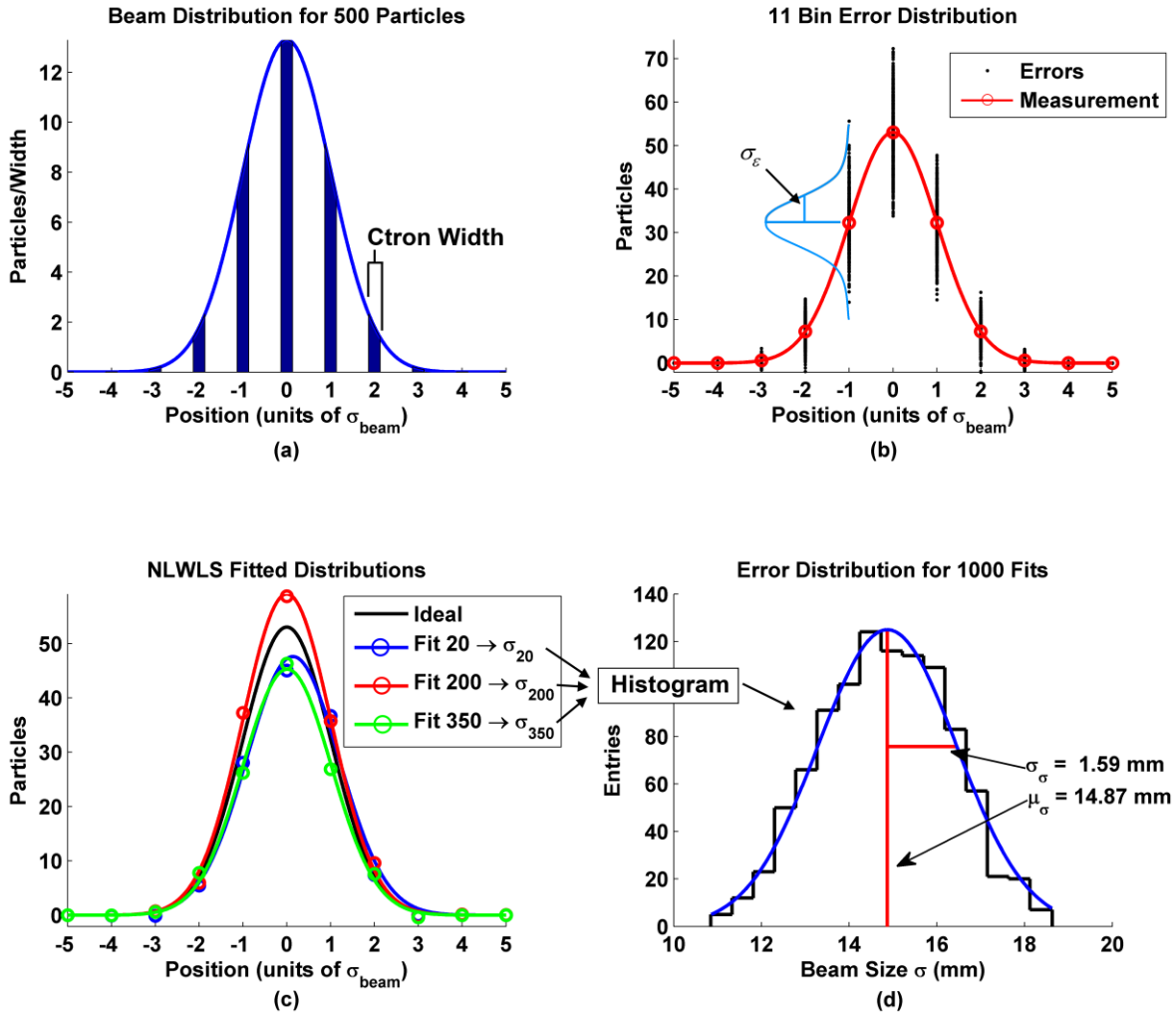

Figure 3.16 Representation of the Monte Carlo simulation method used to estimate errors. (a) Gaussian beam distribution normalized to the number of ionized particles where the dark bars show the area integrated to determine the measurement profile. (b) Red circles representing the integrated beam profile are surrounded by a random Gaussian distribution of error points where the width of the distribution σ_ε is the input error. (c) Each set of randomly chosen data points from the error distribution is fitted using a Nonlinear Weighted Least Squares (NLWLS) method. (d) The standard deviations from the fitted Gaussians are histogrammed where the μ_σ - σ_{beam} represents the systematic error and σ_σ is the statistical error.

$$Number\ of\ Bins = \frac{3.5\sigma}{\sqrt[3]{n}}. \tag{3.34}$$

The systematic error is the difference between the mean of the beam size fits $\mu_\sigma$and the true beam size σ_{beam}. The rms size of the beam sizes σ_σ characterizes the spread of the possible beam widths measured in the presence of noise and defines the statistical uncertainty of the measured IPM profile rms size.

Resolution Error

The resolution error arises from the size of the Channeltron and the fact that information within the width of a single detector is summed together and the details lost. Due to the nature of the IPM, which has a fixed width detector that can take measurements at an increasing number of locations up to the limit that one Channeltron position is immediately adjacent to the next, there is also an error due to the number of Ctron positions or bins used. The larger the number of bins used the more highly the resulting fit is constrained, which leads to a more accurate measurement of the beam size. Furthermore, it has been discussed in section 2.3.2 that the number of ionized particles can have a large influence on the measured profile, especially at low particle numbers.

The systematic error due to resolution may be analytically calculated for the case where there are no gaps between bins [53]. The measured beam size, in the absence of any distorting fields or other errors, would be the standard deviation of the random final measured particle position. Furthermore, the final particle positions are the sum of two random variables, the initial random particle positions and the random position associated uncertainty of location within a single Channeltron. The standard deviation of the sum of two uncorrelated and independent variables is $\sigma(X+Y) = \sqrt{\sigma^2(X) + \sigma^2(Y)}$ where $\sigma(X)$ and

$\sigma(Y)$ are the individual standard deviations. For the case of a Gaussian beam with standard deviation σ_{beam} and a Channeltron where all the particles entering it are uniformly distributed over a width *w*, the measured beam size is

$$\sigma_{meas} = \sqrt{\sigma_{beam}^2 + \sigma_{ctron}^2} \tag{3.35}$$

where σ_{ctron} is the standard deviation of a normalized uniform distribution of a particle $\sigma_{ctron}^2 = w^2/12$. It is useful to define the resolution as the number of Ctrons or bins that fit within one rms beam size by a single quantity *Bins per Sigma* or $Bins/\sigma_{beam}$ defined as

$$Bins/\sigma_{beam} = \frac{\sigma_{beam}}{w}. \tag{3.36}$$

By substituting equations (3.35) and (3.36) into (3.32) it has been shown [53] that

$$\varepsilon_{sys} = \sqrt{1 + \frac{1}{12(Bins/\sigma_{beam})^2}} - 1. \tag{3.37}$$

As a result of (3.37), if the bins are adjacent, increasing the number of bins or $Bins/\sigma_{beam}$ decreases the bins size and systematic error.

Two cases are presented in figure 3.17. Equation (3.37), referred to as the Bin Width Function, is plotted as a function of $Bins/\sigma_{beam}$ meaning that the bin edges touch and the bin width is changing. The Bin Width Function gives the resolution for a detector for a given bin size and, for the IPM with a maximum[8] $Bins/\sigma_{beam}$ = 15 mm/4 mm = 3.75, the systematic error is 0.3%. This is confirmed by Monte Carlo simulations, which are displayed by the other curves of Figure 3.17, for the case where $Bins/\sigma_{beam}$ represents a fixed

[8] The maximum $Bins/\sigma_{beam}$ for the IPM corresponds to the case where there a sufficient number of Channeltrons such that each Channeltron touches the next with no gaps.

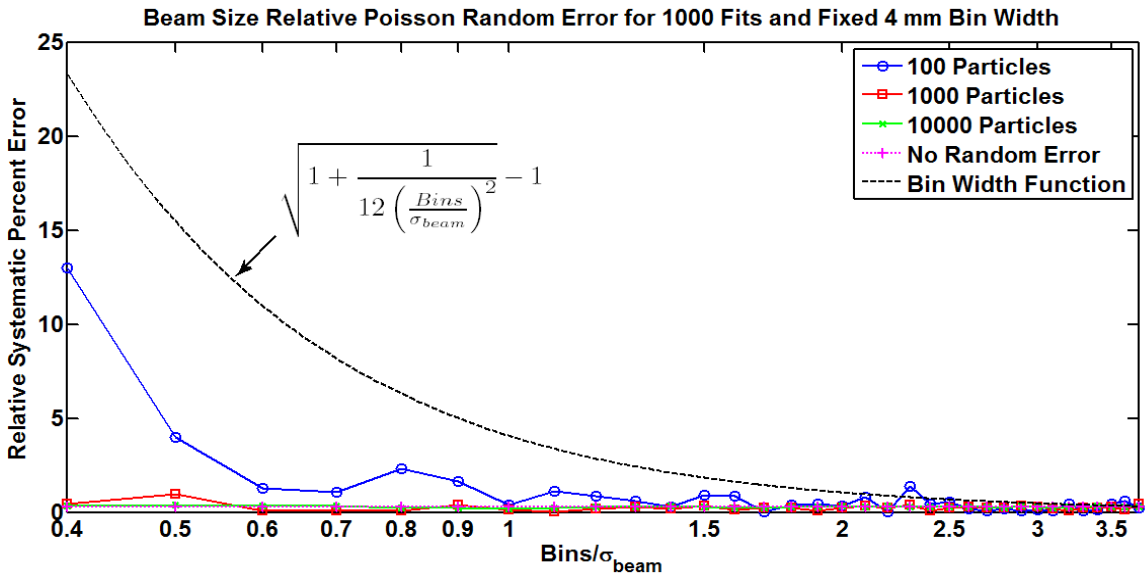

Figure 3.17 Systematic percent error shown for $Bins/\sigma_{beam}$ representing adjacent bins and variable bin size as the independent variable for the Bin Width Function and $Bins/\sigma_{beam}$ representing a fixed bin width and variable number of bins as the independent variable for Monte Carlo simulation of measured beam size.

Channeltron width equaling the bins size and a variable number of bins with gaps in between. Error distributions give $\sigma_\varepsilon = \sqrt{\overline{y}_i}$ due the applicability of the Poisson distribution to counting individual particles in a given time [148]. Figure 3.17 shows that the error in the beam size depends on the number of measured particles, as expected, as well as the number of bins used to make the measurement. The larger error due a low number of bins translates into a poorly constrained fit to the data.

For a large number of particles, the systematic error is equal to the error determined by the monitor resolution, as can be seen when the Bin Width Function is equal to the IPM fixed bin width for a sufficient number of bins to produce complete coverage. Furthermore, since the random error only introduces uncertainty in the ability of the fitting routine to replicate the distribution, the error due to the resolution is purely systematic. It exists sans

random error as shown by the No Random Error curve in figure 3.17.

Position Error

The IPM uses a Channeltron mounted to a linear actuator to drive the detector across the transverse direction of the beam. It is expected that there will be some error in the position at each desired location. It is possible to estimate the error in the measured beam size due to the positioning accuracy with a Monte Carlo simulation by using the $\overline{y}_i$ found from equation (3.33) with a random normal distribution having mean $\overline{x}_i$ and standard deviation equal to the positioning error. The *l* sets of *k* random position x_i with amplitudes $\overline{y}_i$ are used to generate profiles, where the initial particle number has been set to 10^6 to eliminate particle statistics error. The results are shown in figure 3.18 for 3 bin numbers, where 38 bins = 3.8 $Bins/\sigma_{beam}$, 25 bins = 2.5 $Bins/\sigma_{beam}$, and 15 bins = 1.5 $Bins/\sigma_{beam}$ for a fixed ctron size of 4 mm. Statistical error improves with an increased number of Channeltron locations. Beam size uncertainty can become 5% of the true beam size for position errors on the order of the detector width. However, for 0.5 mm position errors, which applies to actuators used for similar purposes at SNS, the error on the beam size is only ~1%.

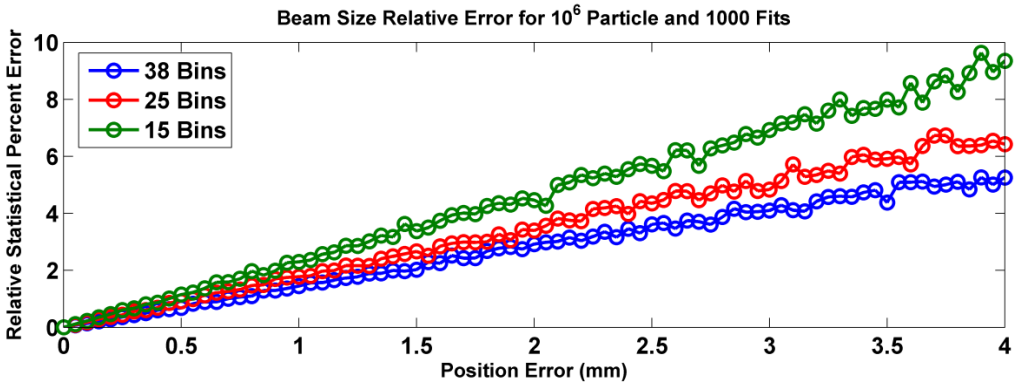

Figure 3.18 Beam size statistical error due to positioning errors on the Channeltron location.

Electronic Noise Error

Noise inherent in the electronics of the data acquisition chain will create an uncertainty in the data leading to an error in the measured beam size. There are a number of noise sources arising from the flow of electricity and the process of digitizing analog signals that are not dependent on the incoming particles and are represented by a constant σ_ε. Notationally it is prudent to characterize noise sources by their signal-to-noise ratio (SNR), which is defined to be the ratio of the measured signal power P_{signal} or amplitude A_{signal} to the noise power P_{noise} amplitude A_{noise} as

$$SNR = \frac{P_{signal}}{P_{noise}} = \left(\frac{A_{signal}}{A_{noise}}\right)^2 \tag{3.38}$$

or, expressed in the logarithmic[9] decibel scale, as

$$SNR(dB) = 10\log\left(\frac{P_{signal}}{P_{noise}}\right) = 20\log\left(\frac{A_{signal}}{A_{noise}}\right). \tag{3.39}$$

In the following simulations $A_{signal} = V_{signal}$ is taken to be the maximum of the input normal distribution representing the amplitude of the measured voltage, and the noise voltage $V_{noise} = A_{noise} = V_{signal}/\sqrt{SNR}$ is the error width σ_ε.

Thermal noise or Johnson-Nyquist noise is a measurable current present in electronic devices in the absence of an applied voltage irrespective of material and circuit geometry [168]. Arising from the random thermal agitation of charges in a conductor with temperature T and signal bandwidth Δf, the thermal noise voltage is [169]

$$V_{thermal} = \sqrt{4k_B TR\Delta f} \tag{3.40}$$

[9] In this text the base-10 logarithm will be denoted $\log_{10} x = \log x$ and the natural logarithm $\log_e x = \ln x$.

where R is the resistance across which the voltage is measured. For the IPM system, assuming a temperature 293 K, bandwidth of 17.5 MHz, and load resistor of 50 Ω, $V_{thermal}$ = 3.76x10^{-6} V. For a Channeltron with a 10^6 gain measuring electrons with an efficiency of 0.6 at the center of a typical first turn distribution after 100 accumulations results in a maximum first-turn profile signal of 0.306 mV. From equation (3.38) the signal-to-noise ratio is 6.6x10^3 or 38 dB due to thermal noise.

Quantization noise stems from round off errors as a result of digitization in an analog-to-digital converter (ADC). The quantization SNR (SQNR) is a function of the number of bits Q used to digitize the signal such that [170], [171]

$$SQNR = 10 \log 2^Q \approx 6.02Q \text{ dB}. \tag{3.41}$$

A 16-bit ADC gives SQNR = 96.3 dB, while SQNR = 84 dB for a 14-bit ADC. Thermal noise is expected to have a more significant effect on the measured data.

The results from Monte Carlo simulations based on the SNR are given in figure 3.19.

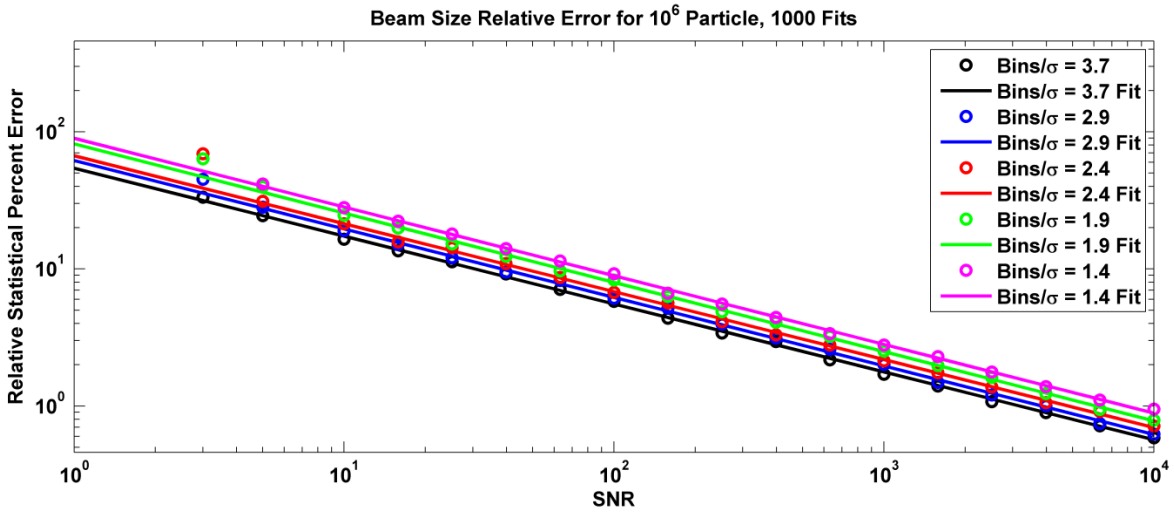

Figure 3.19 Statistical error due to constant noise sources characterized by the signal-to-noise ratio for a range of *Bins/*σ_{beam}.

Since the type of SNR is not specified it may be taken as the total SNR representing all sources of constant noise. The error due to noise can become quite large for signal-to-noise ratios less than 100. However, for the SNR due to thermal noise the percent error in the measured beam size is ~1% for the maximum $Bins/\sigma_{beam}$. It is interesting to note that the data for a particular $Bins/\sigma_{beam}$ is well parameterized by the line $\log \varepsilon_{rand} = -m \log SNR + \log K$ such that

$$\varepsilon_{rand} = \frac{K}{SNR^m} \tag{3.42}$$

except for signal-to-noise ratios < 5 where the error is large compared to the signal height, making profile fitting difficult.

Following an analysis shown in [53], it may be shown that, by plotting the *K* parameter from the fits for each $Bins/\sigma_{beam}$ data set, the fitting parameter *K* is

$$K = \frac{1.055}{\sqrt{Bins/\sigma_{beam}}}. \tag{3.43}$$

Equation (3.43) in conjunction with the fact that the fitted value of *m* in (3.42) is 1/2 yields an estimate for the statistical noise error for a SNR defined by (3.38) as

$$\varepsilon_{rand_{noise}} = \frac{1.055}{\sqrt{SNR \cdot Bins/\sigma_{beam}}} = \frac{1.055 V_{noise}}{V_{signal}\sqrt{Bins/\sigma_{beam}}}. \tag{3.44}$$

For a given detector resolution, if the noise and signal can be calculated or measured, the uncertainty on the measured beam size due to random noise may be found with equation (3.44).

In addition to constant sources of noise there is also the possibility of relative noise sources, such as nonlinearity in amplifier gain [164]. This effect is analyzed by simulating a Gaussian error that is the combination of individual errors ε_{abs} representing a constant noise

and a relative error giving the size of the noise as a fraction ε_{rel} of the input signal $\overline{y}_i$. In this case ε_{abs} is defined as a constant fraction of the maximum of the input profile and is related to the $SNR = 1/\varepsilon_{abs}^2$. By adding the individual errors in quadrature, the size of the error signal then becomes

$$\sigma_\varepsilon = \sqrt{\varepsilon_{abs}^2 + \left(\varepsilon_{rel}\overline{y}_i\right)^2}. \tag{3.45}$$

Stepping through values for relative and absolute noise gives the statistical error in the measured beam size as shown in figure 3.20 for the maximum $Bins/\sigma_{beam} = 3.7$. The relative noise component has only a small effect on the width error; increasing the percent error by just ~1% for a relative noise that is 10% of the input signal. In reality, nonlinear errors are expected to be small and, considering that they make only minor contributions to the beam size at large relative error percentages as seen in figure 3.20, beam size errors due to nonlinearities in the IPM electronics may be considered negligible.

3.2.3 Field Uniformity Induced Errors

Electric Field Uniformity

There is a potentially large source of measured profile distortion unrelated to beam space charge or random electronic noise. All previous analysis of particle trajectories have assumed perfectly uniform electric and magnetic fields, thereby eliminating any external field induced errors. In reality, the external electric fields will contain some component perpendicular to the ideal path, as can be seen in the multipole expansion of the electric potential $V(\vec{r})$ for a charge distribution $\rho(\vec{r})$

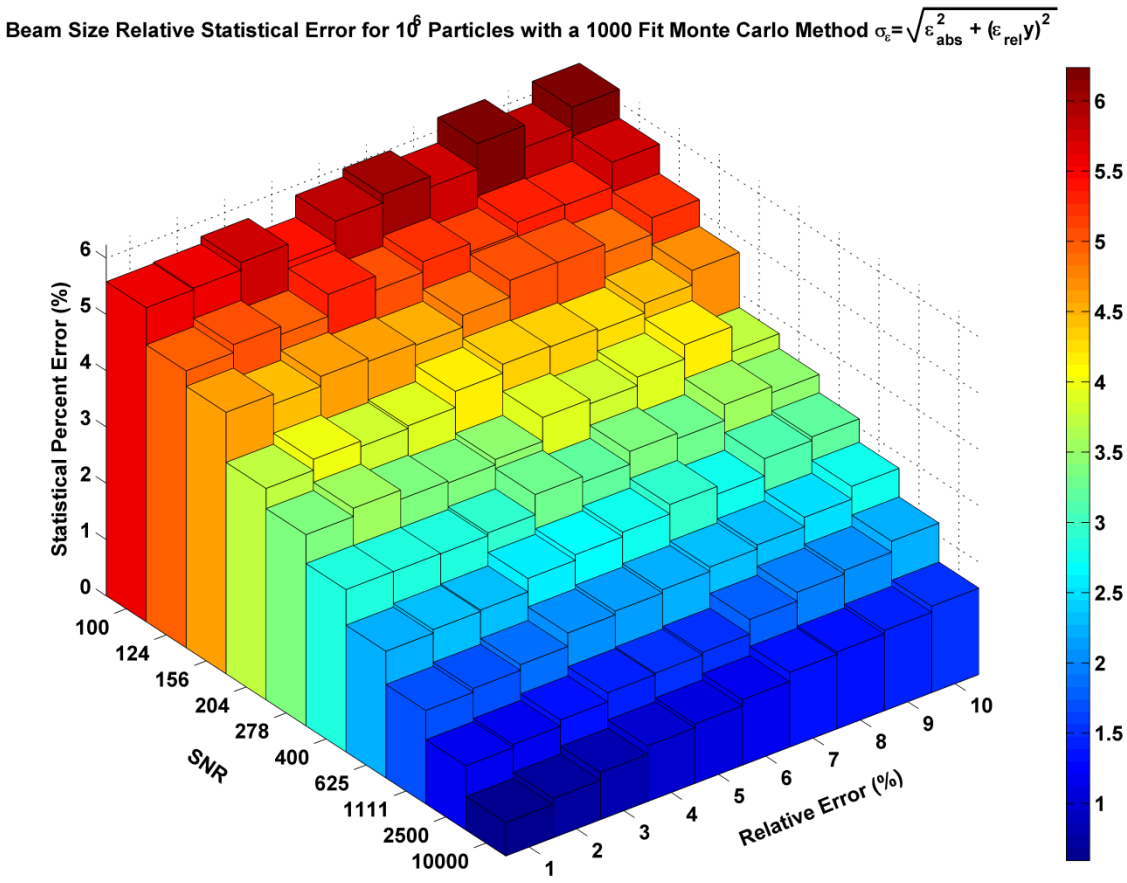

Figure 3.20 Statistical error due to the effects of constant and relative noise on the measured beam size for *Bins*/σ_{beam} = 3.7.

$$V(\vec{r}) = \frac{1}{4\pi\varepsilon_0}\left[\frac{1}{r}\int \rho(\vec{r}')dV' + \frac{1}{r^2}\int r'\cos\theta'\,\rho(\vec{r}')dV' + \frac{1}{r^3}\int (r')^2\left(\frac{3}{2}\cos^2\theta' - \frac{1}{2}\right)\rho(\vec{r}')dV' + \ldots\right]. \tag{3.46}$$

The expansion shows that as the distance from the charge distribution *r* increases, the monopole term dominates the potential. In the far-field limit, in the absence of boundary conditions to modify the potential, the potential of any distribution of charge resembles that of a point charge. This is clearly seen in figure 3.21 for the simulation of the electric potential of a flat plate with an applied voltage in a grounded box. The equipotential lines become increasingly circular further from the plate until boundary effects become important.

Horizontal electric field components due to the field non-uniformity produce a distortion in the measured profile. The distortion in a single particle trajectory is given by equation (3.7) with the average disturbing force due to space charge in eq. (3.7) replaced by the average horizontal component of the nonuniform bias field $\langle E_x \rangle$. In order for a particle to be distorted no more than half a Channeltron width of 2 mm over a distance of 13 cm from

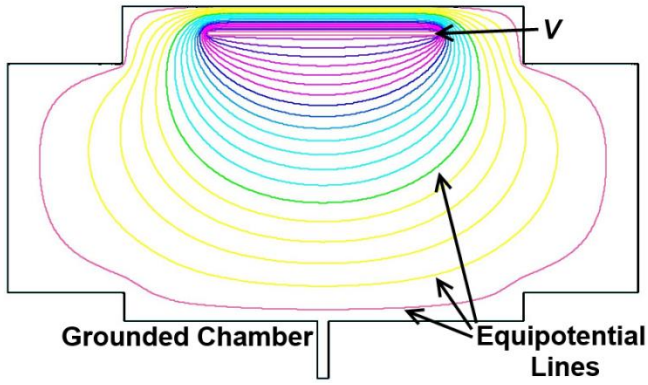

Figure 3.21 Finite element calculation of the potential of a flat electrode showing field non-uniformity.

the top the beam to the detector, the ratio of the average horizontal field component to the field magnitude must not exceed $\langle E_x \rangle / E$ = 1.5%. From the resolution study, a distortion of should add less than 0.5% error to the measured beam width. By manipulating the electrode geometry and size it possible to produce a uniform field over the region of the beam. The optimization of electrode geometry for field uniformity will be approached in a later chapter.

Magnetic field Uniformity

The magnetic field uniformity is simplified due to the symmetry and nature of the dipole magnet used. The charged particles are confined to spiral around the field lines, thus, nonlinearities in the magnetic field uniformity would produce distortions in the measured particle trajectories. It is important to choose a magnet design that yields the greatest field uniformity. It will be shown in a later section when the details and simulations of the magnet are discussed that the magnetic field produces a negligible error in the particle trajectories.

3.2.4 Secondary Particle Source Error

It was discussed in section 2.2.4 that beam-induced secondary electrons should contribute negligibly to a profile measurement. However, there are other forms of secondary particles that will contribute. In the case of electron collection there are two sources of secondary electrons in addition to beam-induced secondaries and field emission electrons.

Potential Electron Emission

An energetic ion striking a metallic surface interacts with electrons in the metal and may be neutralized through a process called Auger neutralization [172], [173]. This is the case in IPM electron collection when ions created during the beam passage are accelerated by the beam and strike the high voltage bias electrode of the detector. If the neutralization energy, or ionization energy, of the ion is twice the work function of the target, then an electron in

the valence band of the metal can quantum mechanically tunnel into the ion's potential well and fill a vacant state [174]. The energy released in this Auger type transition may then be transferred to liberate a second electron in a process that is often described as potential electron emission. A simple expression utilizing the ionization energy E_i, target work function w, and Fermi energy of the metal E_F may be used to define the secondary electron yield as [175]

$$\mathrm{SEY}_P = \frac{0.2(0.8E_i - 2w)}{E_F}. \tag{3.47}$$

For the case of an ionized water molecule with E_i = 12.6 eV incident on stainless steel, which has a work function of ~4.4 eV, and a Fermi energy (for iron) of ~11.1 eV, the number of secondary electrons per incident ion due to potential emission is 0.023.

Ion-Induced Secondary Electrons

Secondary electrons due to the transfer of energy through kinetic impact of beam particles with the accelerator chamber walls has been analyzed, but electrons from accelerated IPM ions may also be created through kinetic emission. Ions in the IPM will strike the electrode with energies on the order of 60 keV, which is well above the stainless steel work function. The process of secondary electron creation is the same for heavy charged particle energy transfer where the ion experiences hard and soft collisions that transfer energy to absorber electrons. Ion-induced secondary electron yields have been the focus of a number of studies due to their influence on particle detectors [176], [177].

An expression for SEY due to kinetic impact has been developed [178] as a function of the angle θ the incident particle makes with a direction normal to the target surface

$$\mathrm{SEY} = \frac{C\Lambda_M S_e}{\cos\theta}. \tag{3.48}$$

The specific yield Λ_M in equation (3.48) is a material-dependent parameter that defines the number of secondaries created per unit energy loss and has been found to have a value of 10.1 for protons normally incident on type 304 stainless steel [176]. S_e is the electronic stopping power and has been calculated for a 60 keV proton on 304 stainless steel with the program SRIM (The Stopping and Range of Ions in Matter) [179] to be 0.283 MeV · cm^2 · mg^{-1}. The constant *C* in equation (3.48) is a scaling factor that has been normalized to *C* = 1 for protons.

Given a specific yield of a proton on a given material, the SEY may be scaled for other ions impacting the same material. It has been shown [180] that heavy ions are less efficient at the production of secondary electrons and the scaling factor has an average value of 0.32 [181]. Lastly, due to the electromagnetic boundary condition that the electric field be perpendicular to an equipotential surface, in this case the electrode surface, the dominant bias field accelerating the ions is normal to the electrode meaning that most ions are incident at $\theta \approx 0$. The secondary emission yield is at a minimum due to the $1/\cos\theta$ behavior.

The IPM in electron collection mode would produce primarily 60 keV H_2O^+ molecules normally incident on the stainless steel electrode, producing 0.92 electrons per ion by equation (3.48). It is interesting to note that eq. (3.48) gives an SEY of 2.85 for 60 keV protons, which is approximately the same SEY quoted in section 2.2.4 for the electron-induced secondaries. As such the TiN coating used for electron cloud reduction reduces the electron induced secondaries to 1.5 and, since it is known [178] that ion induced secondaries only escape from a surface depth of ~10 nm, it is possible that the 100 nm TiN would

produce a similar reduction of the ion secondary emission yield. An ion SEY of 1.5 due to protons would have a heavy ion SEY scaled to 0.48. Two different studies [176], [182] give examples of ion-induced SEY in which normally incident 28 MeV protons on stainless steel give SEY= 0.14 and obliquely incident 5 keV argon ions on TiN coated stainless steel SEY = 0.57. Without exact data of incident ion secondary yields in the 60 keV range, it will be assumed that the IPM ion-induced SEY = 0.5.

Secondary Electron Error

The production of secondary electrons by ionization products will cause an error in measured beam profiles. The process, shown graphically in figure 3.22, by which secondary electrons contribute to a source of systematic error goes as follows: positive ions produced during beam-gas interactions are accelerated toward the bias electrode held at a negative potential V where they strike the electrode surface producing secondary electrons. These secondary electrons are then accelerated away from the electrode in a helical motion produced by the external magnetic field until they are collected in the Channeltron detector, indistinguishable from the true beam-produced electrons. The problem lies in the fact that the positive ions undergo trajectory distortions resulting in an unwanted secondary electron profile that is collected with the beam-electron profile.

As a limiting case, simulations for SEY = 1 are shown in figure 3.23 (a) for electrons created by gas ionization due to a nominal Gaussian beam with an rms beam size of 22 mm, for secondary electrons produced by the gas ions striking a negative electrode at 120 kV, and the combined distribution. The primary electron profile and combined measured distribution (with significant error) are shown in figure 3.23 (b). Errors in the measured electron distribution are a function of the secondary emission yield as illustrated in figure 3.24. The

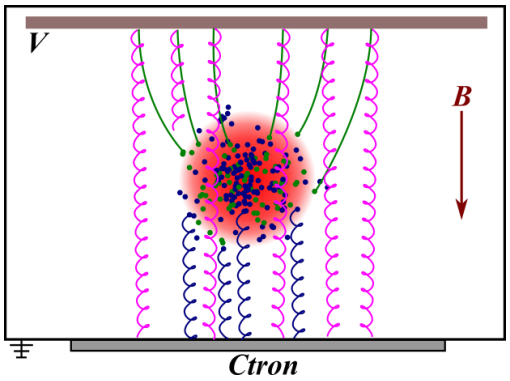

Figure 3.22 Graphical representation of the process by which ions produced in beam-gas interactions produce secondary electrons which are collected with original ionized electrons in the IPM electron collection mode.

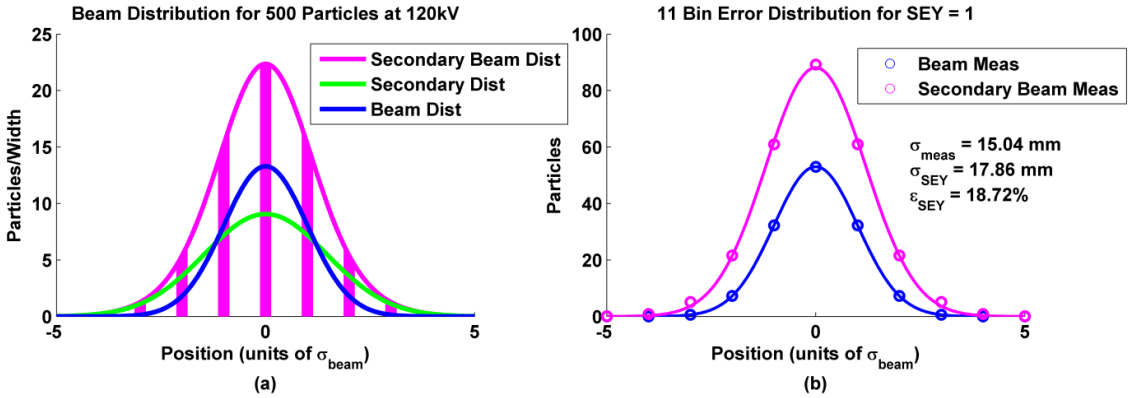

Figure 3.23 (a) Gaussian distributions for the nominal beam size, distribution of secondary electrons produced by ions in a 120 kV bias potential and SEY = 1, and combined secondary and initial distribution. (b) Measured beam and combined distributions.

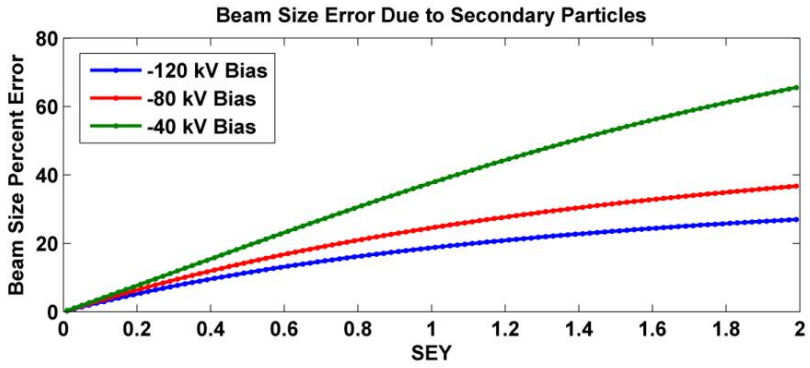

Figure 3.24 Percent error on the beam size due to ion-induced secondary electrons as a function SEY and electric bias potential.

error in the measured profile becomes large >10% at values of SEY larger than 0.4. Additionally, the secondary electron profile is related to the electric bias potential due to the ion profile spreading. This is shown for three different values of bias potential where the ion profile sizes determining the secondary electron contribution have been taken from figure 3.24. It is necessary to have a large bias potential for electron collection.

It can be seen from figure 3.24 that for the beam size error that ε_{SEY} = 12% for SEY = 0.5. This analysis reveals that a method of ion-induced secondary electron suppression must be included in the IPM design in order to produce electron profiles that meet the required accuracy. It should be noted that secondary electron errors are not an issue during ion collection since electrons produced at a positively biased electrode will not be accelerated to the detector.

3.2.5 Spatial Accuracy Estimation

It can be seen that there are a number of systematic and random errors that contribute to the measured profile accuracy and beam size. It is now possible to estimate the error of the final measured beam size due to the individual errors studied. Due to the independent and uncorrelated nature of each error the final error may considered to be the convolution of individual Gaussian beam error distributions. The errors may be added in quadrature, where the systematic component includes the resolution error ε_{res}, field uniformity error ε_{field}, secondary electron error ε_{SEY}, and space charge profile spreading ε_{SC}. The statistical error includes the error on the position ε_{pos}, absolute errors defined by the signal-to-noise ratio ε_{SNR}, encompassing thermal noise and quantization noise, relative errors from electronics nonlinearities ε_{rel}, and the uncertainty on the beam size due to the number of particles ε_{N}.

The overall relative error on the beam size for IPM electron collection takes the form

$$\varepsilon_{elec} = \sqrt{\varepsilon_{SC}^2 + \varepsilon_{res}^2 + \varepsilon_{field}^2 + \varepsilon_{SEY}^2} \pm \sqrt{\varepsilon_N^2 + \varepsilon_{pos}^2 + \varepsilon_{SNR}^2 + \varepsilon_{rel}^2}$$

$$= \sqrt{0.01^2 + 0.003^2 + 0.005^2 + 0.048^2} \pm \sqrt{0.01^2 + 0.01^2 + 0.02^2 + 0.01^2} \quad (3.49)$$

$$= 0.049 \pm 0.02 \Rightarrow 4.9\% \pm 2\%.$$

According to equation (3.49), an IPM electron signal will have an estimated measured beam size 4.9% larger than the true beam size with an uncertainty of 2%. Hence, the largest possible beam size error is 6.9% for the case of a 300 G magnetic field, 120 kV bias potential, and design parameters discussed in the previous sections. The secondary electron error ε_{SEY} provides the main contribution to electron profile measurement error and has been given as 4.8%, which will be justified in a later chapter discussing the final IPM design and in the next section analyzing electron collection times. While the ion-generated profiles do not suffer from secondary electron error the space charge error at 120 kV is 42%, making all other error sources negligible by comparison. It has been shown that the spatial accuracy of the IPM in electron collection mode will satisfy the 10% beam size error design goal.

3.3 Time Resolution

Two main factors determine the ability of the IPM to measure turn-by-turn signals; the time it takes to collect the ionization products and the ability of the system to resolve individual signals. The ability of the IPM to separate individual turn data is necessary to guarantee the fidelity of the profile assigned to each turn.

3.3.1 Collection Times

Ion Collection

Positively charged ions arising from beam-gas interactions are accelerated by the beam space charge and external electric bias field toward the Channeltron detector. Neglecting its initial thermal velocity, an ion will travel for a time *t* given by equation (3.6) which depends on the mass *m* and vertical electric field component E_y as $t \propto \sqrt{m/E_y}$. The collection time is larger for more massive ions, so that, as the beam passes through the IPM gas region and produces a variety of ions as outlined in section 2.2.1, the ions will arrive at the detector over a range of times.

Simulations done for a nominal fully accumulated beam calculated the time to collect all of the ions as a function of external bias voltage. The results, reported in figure 3.25, show the dependence of collection time on bias voltage for two different particle species. As expected, the collection time increases with particle mass. There is a 300 ns gap at the end of every beam pulse to allow for extraction from the ring. Particles created at the end of a beam pulse must be collected within the gap or they will be collected during a following turn, thereby mixing the turns and leading to errors and uncertainty in the final measurements. It can be seen from figure 3.25 that the primary ion signal from H_2O^+ will be collected within the 300 ns gap with a voltage of 120 kV.

The collection time limit determines the necessary minimum value of the electric potential chosen as the design parameter. Hydrogen ions are collected within the time allotted at the chosen potential. Figure 3.26 illustrates the effect of the delay in electrons created by ion-induced secondaries. They are delayed and spread in time due to the transverse ion distribution. The secondary electron distribution in figure 3.26 (a) is represented by a

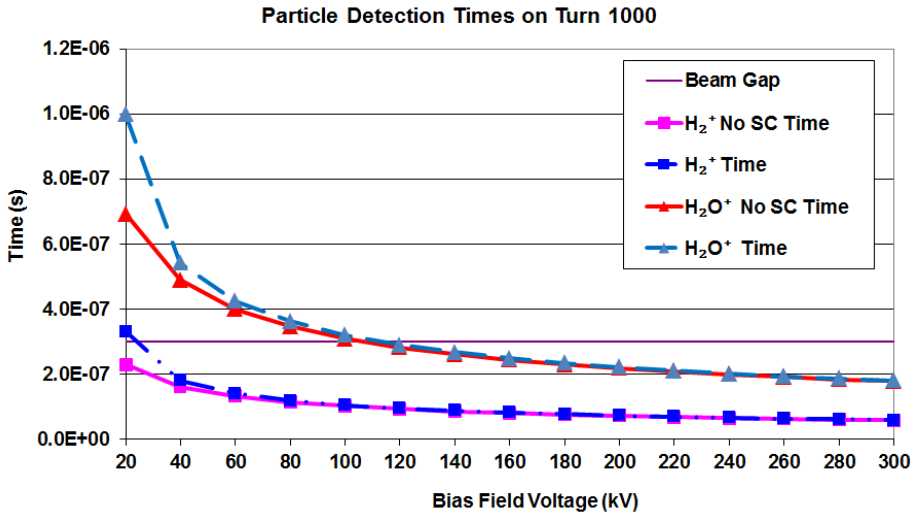

Figure 3.25 The time to collect all particles from a nominal beam distribution on the last turn as a function of external bias voltage for hydrogen and water ions.

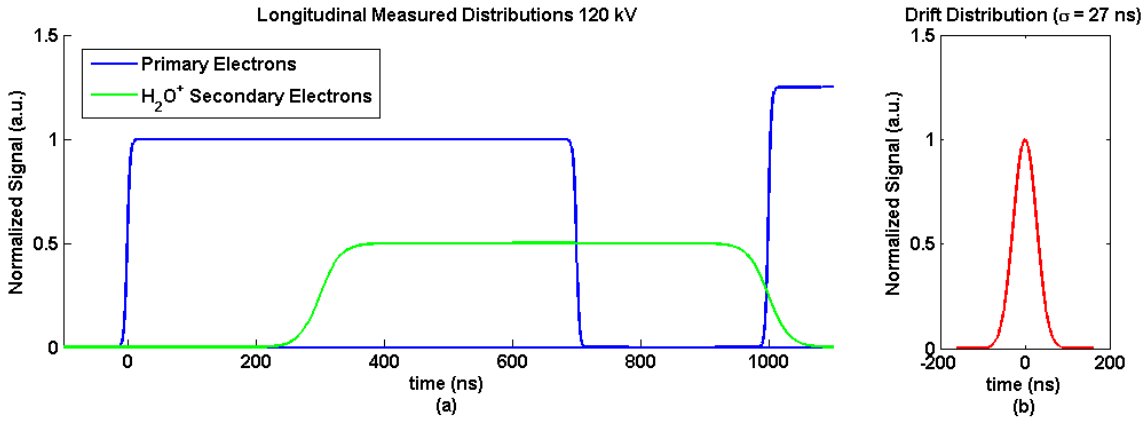

Figure 3.26 (a) Representative measured distributions from primary electrons and secondary electrons from H_2O^+ ions, where the secondary distribution has been convolved with the Gaussian distribution in (b) representing the spread in collection times due to the particle height distribution.

convolution of a Gaussian distribution (figure 3.26 (b)) of collection times with a standard deviation found from simulating H_2O^+ ions trajectories. The convolution smears out the primary distribution. The height is scaled so that the area under the secondary curve, or the integrated turn signal, is ½ the area under the primary curve, from assuming a secondary emission yield of 0.5 electrons per ion.

The small number of heavy ions created at the end of a pulse will not be collected within the turn and will contribute to the following pulse. Heavier ions than water constitute approximately 15% of the total ion signal and the heaviest ion, CO_2^+, will have a collection time that scales from water as $\sqrt{m_{CO_2}/m_{H_2O}}\, t_{H_2O}$. Heavy ions from the last 25% of the beam To pass through the detector region have the possibility of being collected in the next pulse. However, this represents <4% of total beam ions, and the effect of delinquent heavy ions will be considered negligible.

Electron Collection

Electron collection time considerations are more straightforward than those for ions. An electron at the top edge of the beam under the influence of a 0.47 MV/mm bias field, neglecting initial velocity, will take 2 ns to reach the detector. With ~1 ns spread in arrival times due to electrons arriving from different heights, the longest electron times are <10 ns, which is trivial compared to pulse length. Thus, there is no difficulty in collecting turn-by-turn electrons. While this holds true for primary ionized electrons, it does not hold true for those secondary electrons created through ion impact with the electrode.

Effects of Collection Time on Secondary Electrons

In electron collection mode, the primary ionized electrons are quickly accelerated toward the detector, while the ions take hundreds of nanoseconds to reach the electrode surface as

outlined earlier. As such, while the secondary electrons themselves make the transit from the electrode to the detector in 2.5 ns, the time scale of their measurement is based on the ions. This would cause a similar problem with turn-by-turn signal mixing as was described for ion collection. A solution is possible that simultaneously eliminates turn-by-turn mixing and reduces the error due to secondary electrons in the individual turn profiles.

By gating the Channeltron signal to omit signals during the beam gap the electrons due to secondary emission may be isolated from the primary electrons. The only electrons collected 20 ns after the end of beam pulse will be those created by ion-induced secondary electron emission. Ctron signal gating may be done most easily during data processing by matching the measured IPM signal with the SNS Ring timing signal to exclude IPM signal data during the gap. Considering a nominal 1 μs pulse with a 700 ns beam and 300 ns gap, a 41% reduction in secondary electron signal may be achieved. This partially justifies the secondary electron error quoted in the analysis of spatial resolution. Without beam gap secondary electron gating ε_{SEY} would be 7.2%.

3.3.2 Signal Processing

There are additional factors outside of particle collection times that contribute to the ability of the system to resolve turn-by-turn data. The Ctron signal passes through cables and amplifiers which all affect the final measurement. It is important to determine the effect of the signal path in order to guarantee that the measured signal is an accurate representation. The RF bunching structure of the beam will be ignored since the IPM sums the signal over each turn. Mini-pulses from a 1 ms long macro-pulse are injected in the ring at a frequency of 1.056 MHz, where the mini-pulses have been shaped by the LEBT and MEBT choppers. The LEBT chopper uses four electrostatic deflections to create 300 ns beam gaps while the

MEBT chopper uses a meander line traveling-wave structure to produce ~10 ns rise/fall times on each mini-pulse [183].

The final measured signal leading and trailing edges are characterized by the ability of the system to resolve quickly changing inputs as well as distortions induced by the cabling and electronics. The influence of such effects is depicted graphically in figure 3.27, which shows representations of signals from two turns with their respective distorted measured signals leading to mixing of turn data and subsequent amplitude error. Furthermore, the beam gap gating discussed in the previous section becomes less effective with significant signal distortion. The measured signal is a superposition of signals from primary electrons and ion-induced secondaries. With large distorted signals, the primary electron signal will extend further into the beam gap with the consequence that less of the gap can be used to remove the secondary electron signal.

The following sections will compose a study of the errors inherent in signal processing and the methods used for their mitigation. Requirements for IPM system electronics will also be given. Before continuing it is necessary to examine the relationship

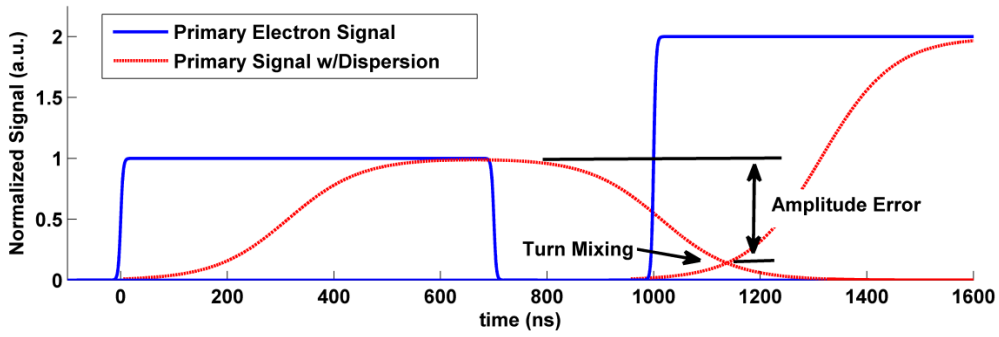

Figure 3.27 Graphical representation of the effects of dispersion and long rise times leading to turn mixing and amplitude errors.

between rise time and signal bandwidth.

Fourier Decomposition, Bandwidth, and Rise Time

Any periodic signal integrable over a period *T* may be considered as the superposition of sines and cosines given by the Fourier series [154]

$$f(x) = \frac{a_0}{2} + \sum_{n=1}^{\infty} a_n \cos(nx) + b_n \sin(nx) \tag{3.50}$$

$$a_n = \frac{1}{\pi} \int_{-\frac{T}{2}}^{\frac{T}{2}} f(x) \cos(nx) dx, \quad n \geq 0 \tag{3.51}$$

$$b_n = \frac{1}{\pi} \int_{-\frac{T}{2}}^{\frac{T}{2}} f(x) \sin(nx) dx \quad n \geq 1 \tag{3.52}$$

where a_n and b_n are the Fourier coefficients. A classic example is the Fourier series of a square wave, shown together with its first few harmonics in figure 3.28. The values of the coefficients are $a_0 = a_n = 0$, $x = 2\pi t/T$, and $b_n = 4/n\pi$ for odd values of *n*.

For the square wave example, defining $f_0 = 1/T$ as the fundamental frequency, the highest frequency $f_n = nf$ is used to represent the original signal bandwidth. In reality the bandwidth is the difference between the lowest used frequency and the highest. Signals that vary quickly in time require large numbers of frequencies or high bandwidths for accurate replication. The square wave, for example, would require an infinite bandwidth to reproduce the step function in the time domain. The bandwidth may then be related to the rise or fall time of a signal, which is defined as the time it takes the signal to change from a specified low value to a high value [184], as shown graphically in figure 3.29. For a low-pass RC filter it has been shown [185] that the impulse response rise time is

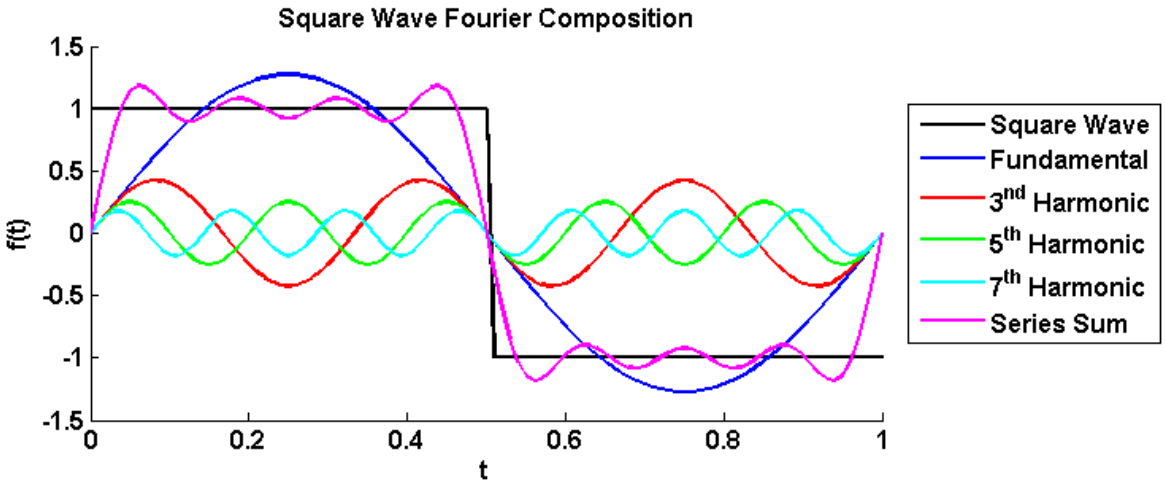

Figure 3.28 Fourier analysis of a square wave.

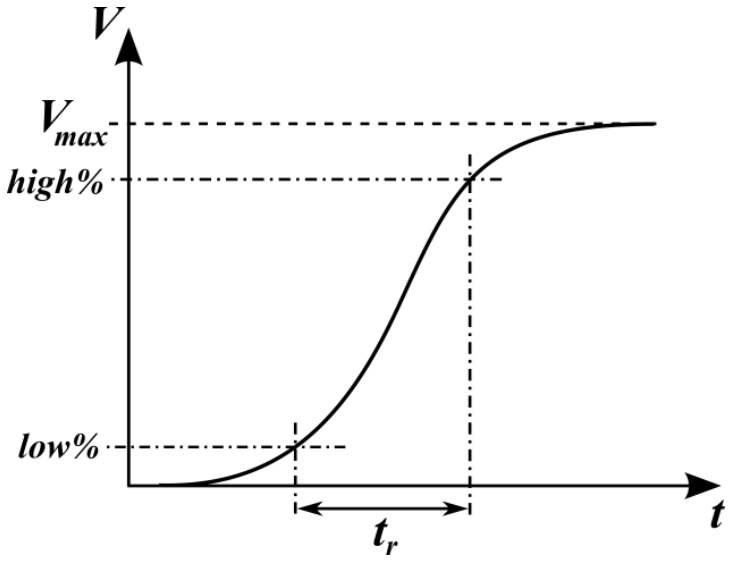

Figure 3.29 Representation of signal rise time.

$$t_r = \frac{0.35}{f_{3\text{dB}}} \tag{3.53}$$

where $f_{3\text{dB}}$ is the frequency at which the signal, in the frequency domain, has decreased by 3 dB and represents the bandwidth for a signal measured from 10% to 90% of the signal maximum in the time domain. Equation (3.53) is often used a rule-of thumb estimate for more complex signals, and for a 20 ns mini-pulse it gives a required bandwidth of 17.5 MHz. However, bandwidth definitions are rather arbitrary and a more useful definition will be use shortly.

Fourier Transform

While the Fourier series illustrates the principle of spectral decomposition, in practice it is only applicable for periodic signals. However, it may generalized to arbitrary non-periodic functions by using Euler's identity

$$e^{ix} = \cos x + i \sin x \tag{3.54}$$

to recast equation in (3.50) with $x \to t$ into a compact complex form [186]

$$\begin{aligned} f(t) &= \sum_{n=-\infty}^{\infty} c_n e^{in2\pi t/T} \\ c_n &= \frac{1}{T}\int_{-T/2}^{T/2} f(t) e^{-in2\pi t/T} dt. \end{aligned} \tag{3.55}$$

Non-periodic functions may be found as $T \to \infty$, which makes the fundamental angular frequency $\omega_0 = 2\pi/T$ become infinitesimally small. Correspondingly, $\omega_0 \xrightarrow{T\to\infty} d\omega$ making the combination $nd\omega \to \omega$ a continuous variable taking any value between $-\infty$ and ∞. With this limiting procedure, it can be shown [186] that the Fourier series (3.55) becomes the Fourier transform

$$\mathcal{F}(\omega) = \int_{-\infty}^{\infty} f(t) e^{-i\omega t} dt \tag{3.56}$$

and the inverse Fourier transform

$$f(t) = \frac{1}{2\pi} \int_{-\infty}^{\infty} \mathcal{F}(\omega) e^{i\omega t} d\omega. \tag{3.57}$$

The complex Fourier series and Fourier transform introduce negative frequencies which act to split the energy of the signal in the frequency domain over a positive set of frequencies and their negative frequency counterparts. The frequency domain of a signal has many useful properties that will be exploited shortly.

Transfer Function

A transfer function $H(t)$ relates the input of a system $X(t)$ to the output of a system $Y(t)$ in the time domain in such a way that the output maybe found through convolution

$$Y(t) = H(t) * X(t). \tag{3.58}$$

The benefit of equation (3.58) is that convolution in the time becomes multiplication in the frequency domain. Once the transfer function is known, the output may be found by taking the inverse Fourier transform of the frequency domain response

$$Y(\omega) = H(\omega) \cdot X(\omega). \tag{3.59}$$

For example an ideal cable would have an output signal identical to the input signal with a transfer function $H(\omega) = 1$, which is a Dirac delta function $\delta(t)$ in the time domain. Unfortunately no real cable has ideal characteristics and various distortions are introduced during the ~300 m of cable length from the IPM location to the signal processing chassis in the Ring Service Building (RSB).

3.3.3 Transmission Line Effects

A transmission line may be modeled using lumped circuit elements [187], as shown in figure 3.30 for a time varying voltage source $V(t)$, source impedance Z_S, characteristic transmission line impedance Z_0, and load impedance Z_L for a line length l. The impedance of the transmission line is a function of the conductor resistance per unit length R', inductance per length L', capacitance per length between the conductor and ground C', and conductance per unit length of the dielectric G'. For a differential length element ∂z of the transmission line in figure 3.30, the equations for the current and voltage from Kirchoff's laws are

$$\begin{aligned} \partial V(z,t) &= -R'\partial z I(z,t) - L'\partial z \frac{\partial I(z,t)}{\partial t} \\ \partial I(z,t) &= -G'\partial z V(z,t) - C'\partial z \frac{\partial V(z,t)}{\partial t}. \end{aligned} \tag{3.60}$$

Assuming a sinusoidally varying field in time with the for $V(z,t) = V(x)e^{i\omega t}$, equation (3.60) differentiated with respect to the line length ∂z and time yields

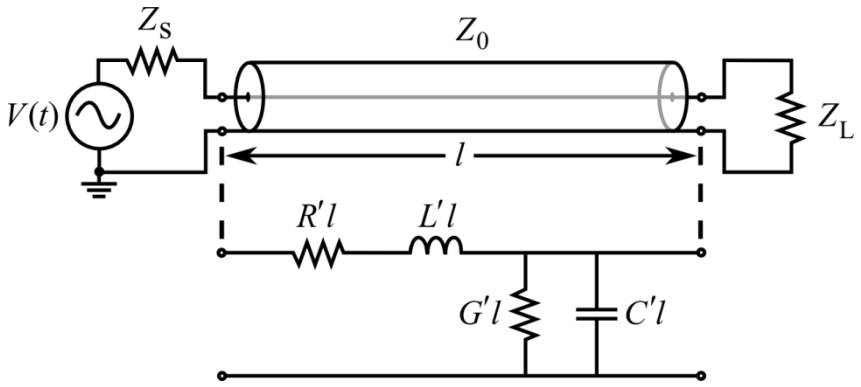

Figure 3.30 Lumped circuit element model of a transmission line of length *l* with characteristic impedance Z_0, source resistance Z_S, and load resistance Z_L. *R'*, *L'*, *G'*, and *C'* are resistance, inductance, conductance, and capacitance per unit length, respectively.

$$\frac{\partial^2 V}{\partial z^2} = \gamma^2 V(z)$$
$$\frac{\partial^2 I}{\partial z^2} = \gamma^2 I(z) \tag{3.61}$$

known as the telegrapher's equations, where $\gamma = \sqrt{(R' + i\omega L')(G' + i\omega C')}$ is the propagation constant.

Transmission Line Solutions

Solutions to the telegrapher's equations give the voltage and current in a transmission line. They are composed of traveling waves

$$V(z,t) = V^+ e^{-\alpha z + i(\omega t - \beta z)} + V^- e^{\alpha z + i(\omega t + \beta z)}$$
$$I(z,t) = \frac{V^+}{Z_0} e^{-\alpha z + i(\omega t - \beta z)} - \frac{V^-}{Z_0} e^{\alpha z + i(\omega t + \beta z)} \tag{3.62}$$

where V^+ and V^- terms represent the incident and reflected voltage waves, respectively, and

$$Z_0 = \sqrt{\frac{R' + i\omega L'}{G' + i\omega C'}} \tag{3.63}$$

is the characteristic impedance of the transmission line. The complex propagation constant is separated into its real and imaginary parts in equation (3.62) as $\gamma = \alpha + i\beta$, where α is an attenuation factor. It can be seen that if βz is the phase of the traveling wave, a phase advance of 2π occurs when β is multiplied by the wavelength λ. The factor $\beta = 2\pi/\lambda = \omega/v_p$ is the wave number which may be used to define the phase velocity of the transmission line, which is

$$v_p = \frac{\omega}{\mathrm{Im}\left\{\sqrt{(R' + i\omega L')(G' + i\omega C')}\right\}}. \tag{3.64}$$

From formula (3.64) is can be seen that the velocity is a function of the wave frequency ω.

This dependence on frequency is the source of dispersion and results in errors in the signal amplitude that affect the rise time and magnitude. These will be analyzed shortly.

Scattering Parameters

One more concept is needed before the effects of a transmission line can be studied. Since a transmission line may be characterized by incident and reflected waves, it may be represented by a two-port network, as depicted in figure 3.31, where the transfer function *S* for the network is known as the scattering or S-parameters, and is characterized by

$$\begin{bmatrix} V_1^- \\ V_2^+ \end{bmatrix} = \begin{bmatrix} S_{11} & S_{12} \\ S_{21} & S_{22} \end{bmatrix} \begin{bmatrix} V_1^+ \\ V_2^- \end{bmatrix}. \tag{3.65}$$

By terminating port 2 with a load identical to the characteristic impedance such that there is no reflected signal the transmission coefficient may be defined as

$$S_{21} = \left. \frac{V_2^+}{V_1^+} \right|_{V_2^- = 0} \tag{3.66}$$

with the reflection coefficient

$$S_{11} = \left. \frac{V_1^-}{V_1^+} \right|_{V_2^- = 0}. \tag{3.67}$$

By measuring the S-parameters of a system the effects of the system on any input signal may be discovered. A vector network analyzer (VNA) [188] is a diagnostic tool with two ports that, when connected to a system, sends signals over a range of frequencies and measures the

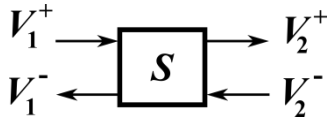

Figure 3.31 Two-port network transmission line representation.

response. As a way of illustrating the effects the cable on the actual signal, the scattering parameters were measured for a 70 m long RFS Cellflex SCF 14-50 coaxial cable. The results of the VNA measurement are reported in figure 3.32 where the magnitude of transmission parameter $|S_{21}|$ shown in the top trace and given in logarithmic units of dB, shows attenuation at higher frequencies.

The attenuation is a combination resistive loss by the copper, dielectric loses from the shielding, and loss of magnitude due to dispersion. The phase $\phi = \mathrm{Arg}(S_{21})$, shown in the bottom trace with units of degrees, has had the electrical delay of cable T_d removed in order to remove the phase changes introduced by varying the input frequency due to $\phi = \phi_{cable} + \omega T_d$, where the cable has $T_d = 280.13$ ns. While an ideal cable would have zero shift in phase for all frequencies, clearly the real cable introduces a shift, see figure 3.32, and this shift in phase is what results in phase dispersion.

Transmission Line Distortion

The measured S-parameters may be used to analyze the effect of a length of cable on signal with beam characteristics. A normalized Gaussian pulse centered at zero with a standard deviation chosen so that the 10% to 90% rise is equal to 10 ns is used as the input signal $X(t) = e^{-t^2/2\sigma^2}$. Its Fourier transform is also a Gaussian $X(\omega) = \sqrt{2\pi}\sigma e^{-\sigma^2\omega^2/2}$. The cable transfer function becomes

$$H(\omega) = |S_{21}|e^{i\phi} \tag{3.68}$$

and therefore allows the system response to be found through the application of equation (3.59), as illustrated in figure 3.33. The system response shows a number of important characteristics typical of transmission lines. The loss of magnitude is a result of attenuation and magnitude dispersion.

Figure 3.32 Network analyzer measurement of the forward transmission parameter for a 70 m long coaxial transmission line measured from 30 kHz to 1 GHz. (Top) Log magnitude of S_{21} in units of decibels (dB). (Bottom) Phase of S_{21} in units of degrees with 280.13 ns of electrical delay removed.

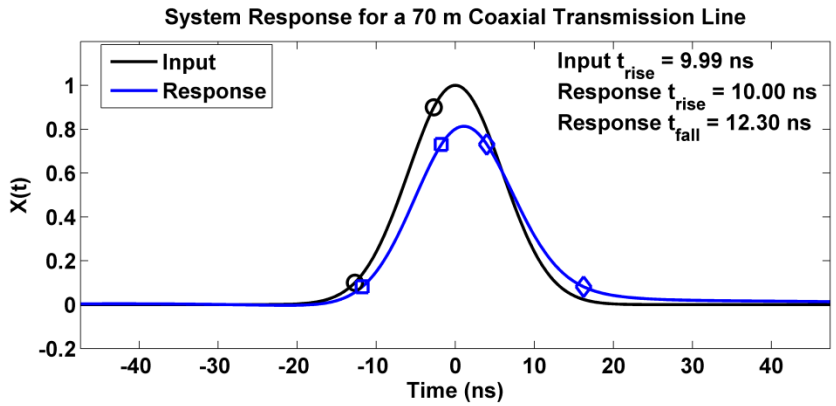

Figure 3.33 System response for a 70 m long coaxial cable with a Gaussian input signal showing attenuation, magnitude dispersion, and phase dispersion. Circle points show input rise time, squares output rise time, and diamonds output fall time.

Magnitude dispersion has the effect of spreading the pulse but does not result in loss of energy. Phase dispersion is responsible for the asymmetry of the measured signal in figure 3.33. While the signal fall time, or the rise time of the trailing edge of the signal in the example shown in figure 3.33, increases by a couple of nanoseconds, the actual cable used in the IPM would be at least four times longer, and thus have a much greater impact on the signal. It is useful at this point to introduce a more intuitive definition of signal bandwidth. Parseval's relation [189]

$$\int_{-\infty}^{\infty} |f(t)|^2 dt = \frac{1}{2\pi} \int_{-\infty}^{\infty} |\mathcal{F}(\omega)|^2 d\omega \tag{3.69}$$

relates the energy of a signal in the time domain to that in the frequency domain. Therefore a bandwidth may be defined such that 90% of a signal's energy E is contained within a width of frequencies f_E given by

$$\frac{1}{2\pi} \int_{-f_E}^{f_E} |\mathcal{F}(\omega)|^2 d\omega = 0.9 \int_{-\infty}^{\infty} |f(t)|^2 dt = 0.9E. \tag{3.70}$$

The Gaussian input signal in figure 3.33 has a bandwidth of 31.2 MHz, by equation (3.70),

for a 10 ns rise time, which is more signal-specific than formula (3.53).

Composite Rise Time

For the IPM system with an input signal rise time including a detector, cabling, and electronics, the final measured rise time [190] is

$$t_r = \sqrt{t_{pulse}^2 + t_{detector}^2 + t_{cable}^2 + t_{electronics}^2} \tag{3.71}$$

or in the frequency domain

$$f_{3dB} = \frac{1}{\sqrt{f_{pulse}^{-2} + f_{detector}^{-2} + f_{cable}^{-2} + f_{electronics}^{-2}}} \tag{3.72}$$

where the more conservative 3 dB bandwidth has been used. The amplifiers and electronics for the system will need to be chosen with sufficient bandwidth that the combined rise time is not more than 20 ns. For example, a pulse with a 10 ns rise time going through a Channeltron which has a 3-5 ns rise time followed by a 10 ns cable rise time and 13.2 ns of electronics rise time would have a resultant rise time of 20 ns.

Cable De-Embedding

It is possible to reduce the effect of the cable through digital signal processing techniques. If the transmission parameter S_{21} of a cable can be measured with a network analyzer, then once the signal has been digitized, a filter can be applied that reverses the effect of cable dispersion and returns the original signal. The process, described in detail in [191], applies a filter of the form

$$G(\omega) = \frac{W(\omega)}{S_{21} e^{i\omega T_d}} \tag{3.73}$$

where $W(\omega)$ is a windowing function chosen to take advantage of the full spectrum of

frequencies under consideration and T_d is the electrical time delay. By using the aforementioned technique, the distortions produced by the ~300 m cable length may be mitigated, allowing for better turn-by-turn resolution. Furthermore, de-embedding methods may be used on any linear circuit element.

Open Wire Effects

Another aspect of the signal path is the connection from the Ctron to the cable carrying the signal to the electronics. The Channeltron electron multiplication tube terminates in a metal cap with a wire to transport the charge. This wire is subject to capacitive coupling to the surrounding chamber as well as to dispersion due to self-inductance. Current in the wire generates a magnetic field according to Ampere's law. If the current is varying in time a voltage will be produced in the conductor according to Faraday's law, which acts according to Lenz's law to generate a current producing a magnetic field opposed to the original. A conductor's property to generate a self-imposed opposing magnetic field is known as self-inductance.

The self-inductance of an open straight wire of length *l* and diameter *d* in centimeters has been shown [192] to be

$$L_{low} = 2l\left[\ln\left(\frac{4l}{d}\right) - \frac{3}{4}\right] \tag{3.74}$$

given in units of nanohenries, and is valid for frequencies at which the skin effect is negligible. Formula (3.74) becomes

$$L_{high} = 2l\left[\ln\left(\frac{4l}{d}\right) - 1\right] \tag{3.75}$$

for higher frequency signals where there is no current in the interior of the conductor. The transmission parameter for the open wire may modeled with a simple inductor in series with

$R_0 = 50\ \Omega$ input and output impedance as

$$S_{21} = \frac{2R_0}{2R_0 + i\omega L}. \tag{3.76}$$

Equation (3.76) may then be used as the transfer function with a Gaussian input function to determine the system response, which is plotted in Figure 3.34. While there is some magnitude and phase dispersion introduced by an open wire due to self-inductance, the effect is only significant for long wire lengths. By keeping the wire to ~1 cm in length, any dispersive effect is almost entirely eliminated.

3.3.4 Electronics Effects

It has been shown in this section that it is possible to measure turn-by-turn profiles with the IPM system by using a variety of signal processing techniques. In addition to gating the beam gap signal to noisy particles, the dispersive and lossy effects of the signal path may be de-embedded from the signal, allowing for more accurate single turn separation. The performance of the electronics constitutes the last component necessary for signal integrity.

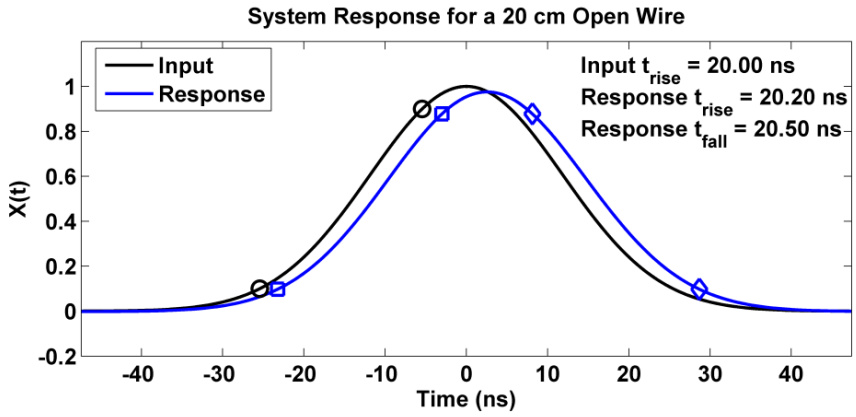

Figure 3.34 System response for a 20 cm long open wire with a 0.381 mm diameter.

Digitizer Condition

The bandwidth of the measured signal places a requirement on the digitizer used to convert the signal from analog to digital. By sampling the voltage or current of an analog signal at some frequency f_s a digital representation of the original signal may be made. However, if a signal, such as the solid curve sinusoid represented in figure 3.35, with frequency f is sampled a rate $f_s < 2f$ then the sampled wave will be an incorrect duplicate or *alias* of the original with frequency $f_{alias} = |f - Nf_s|$ for $N \in \mathbb{Z}$. The Nyquist theorem [193] states that the sampling rate must be at least twice the highest frequency or bandwidth in order to produce a non-aliased reproduction of the original signal. In fact, oversampling is beneficial in guaranteeing accurate signal reconstruction over the full bandwidth. The IPM needs a digitizer >70 MHz to prevent aliasing.

The bandwidth requirement extends to any amplifiers used in the system. Due to the small signal from the Channeltron, an amplifier is needed. An amplifier with 200 MHz bandwidth with a 35 MHz input signal would produce an output signal with a 35 MHz bandwidth by equation (3.72). With proper selection of electronics degradation of the time resolution due to the electrical components may be minimized. Coupled with the signal processing previously discussed, the IPM is capable of generating turn-by-turn profiles with

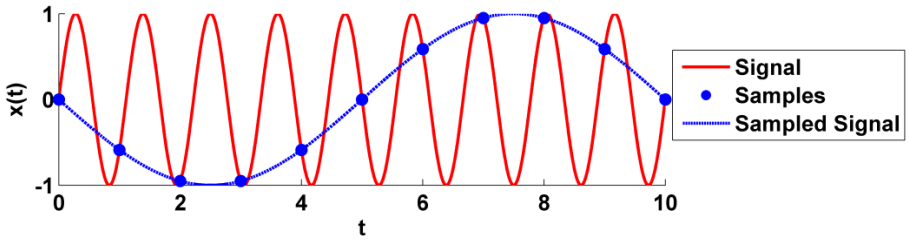

Figure 3.35 Pictorial representation of aliasing.

electrons.

3.4 Simulation Summary

A thorough study through simulation of various aspects IPM system, using the ORBIT IPM module to model track ionized particle trajectories, was performed. Based on fundamental principles, an IPM system is capable of delivering turn-by-turn profiles in the SNS ring with an accuracy of 10% on the rms beam size using electrons. Furthermore, it has been shown in this section that it is possible to measure profiles with sufficient time resolution by using a variety of signal processing techniques. In addition to gating the beam gap signal to noisy particles the dispersive and lossy effects of the signal path may be de-embedded from the signal, allowing for more accurate single turn separation.

Design Parameters

With the completion of the analysis of the system operation it is now possible to outline a list of design parameters with which to use in developing a physical system.

1) The beam pipe diameter in the IPM location is 25.4 cm but the effective diameter over which IPM fields need to be designed is 60 mm.
2) A 120 kV bias potential is required to reduce the profile spreading for ions and the errors from ion-induced secondary electrons, as well as to mitigate turn mixing due to ion collection times.
3) In electron collection mode a 300 G magnetic field is required to confine electrons to a Larmor radius such that the particle trajectory distortion is half of a Channeltron width.
4) Approximately 38 Channeltron measurement positions are needed across the IPM range in order to minimize systematic measurement errors.

5) The actuator driving the detector needs to have a position accuracy of ±0.5 mm.
6) Deviations in the ionized particle trajectory due to nonuniformity in the IPM electric bias and magnetic fields over the beam region must be less than or equal to half the Channeltron width.
7) Titanium nitride coating and secondary electron suppression must be included in the final design.
8) Care must be taken to minimize the Channeltron's open wire length to <1 cm.

With the outlined parameters it is possible to design an ionization profile monitor capable of measuring transverse profiles that meet the system requirements in table 1.2.

Chapter 4

Prototyping and Measurement

The theoretical basis and system analysis presented in the previous chapters provides an argument for the validity and ability of the IPM system to accurately measure beam profiles and outlines the necessary parameters a design would have to meet to do so. However, in order to guarantee the operational principles as well to determine unforeseen aspects of the accelerator environment, a prototype was needed before a final design could be established. Consequently, this chapter discusses the IPM test chamber that was built and installed along with the results of measurements and modifications that were added.

This chapter is composed of a description of the test chamber design and installation as well as considerations that went into the initial design. A summary of the progression of the test chamber is given along with modifications. Results of a study of the ion and electron signals are given followed by a summary of the design parameters derived from the test chamber data that are necessary to the final design.

4.1 IPM Test Chamber

4.1.1 Design Considerations

The IPM test chamber was conceived as a simple system that incorporated the main operational principles of the full-scale IPM but that could be built quickly and cheaply with minimal inconvenience to the accelerator's operation. As such, the primary focus of the test chamber was to show that a Channeltron-based system could measure turn-by-turn profiles. Since the only methods of Ctron profile measurement are either moving the detector with some form of actuator or having multiple Channeltrons requiring several power supplies, generating a full transverse profile was beyond the scope of the test chamber.

An IPM test chamber consisting of a single Channeltron fixed in the center of the transverse beam dimension with a high voltage electrode of arbitrary geometry located directly opposite the detector, to supply a bias voltage, was sufficient to test the basic IPM properties. A power supply was required to bias the Channeltron and a separate high voltage supply was required for the bias plate. An amplifier and oscilloscope were used to measure the Ctron current.

4.1.2 Test Chamber Design

Vacuum Chamber

It was desirable to use as many off-the-shelf components in the construction as possible in order to keep cost and construction time low. The IPM test chamber vacuum chamber is a 10 x 8 inch 304 stainless steel Conflat® 4-way cross with 0.062 inch thick walls. The 10 inch diameter cross pipe connects to the beam pipe and the 8 inch pipe is used for the detector and high voltage (HV) plate. Figure 4.1 shows the full setup of the test chamber. Conflat® flanges

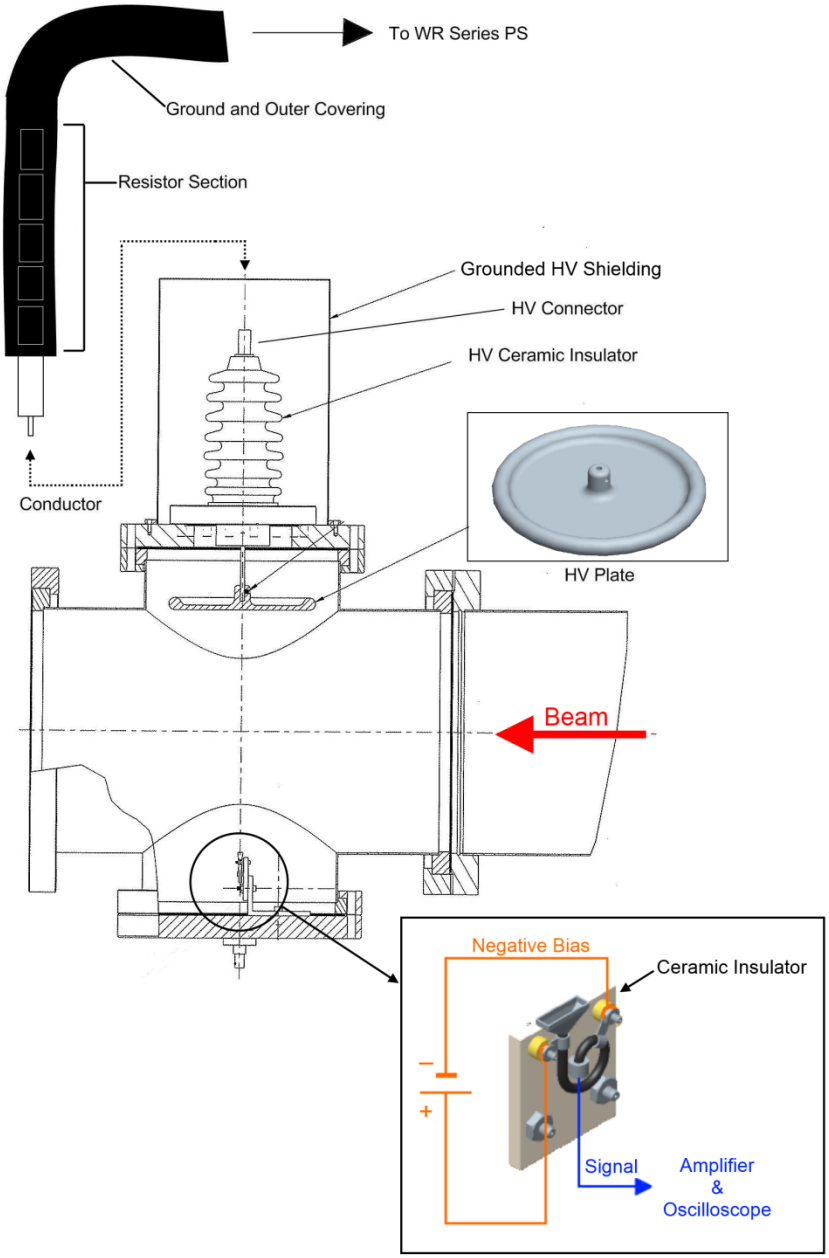

Figure 4.1 IPM test chamber setup and components consisting of chamber, high voltage bias plate, high voltage feedthrough, high voltage, power supply cable, and Channeltron assembly

with vacuum seal rings were used to mount to the main chamber.

High Voltage Bias

The high voltage bias plate is a 6 inch diameter circular disc mounted directly over top of the Channeltron where all the plate edges have a 0.25 in radius. An edge radius allows a high voltage to be applied without arcing inside the vacuum chamber (an in-depth arcing mitigation study will be presented in the next chapter). The bias plate is held in place by a set screw that tightens to the center conductor of a HV 70 kV vacuum feedthrough. The air side of the HV feedthrough has a 7 in diameter cylindrical grounded metal enclosure that provides personnel safety against high voltage and arcing dangers. The shielding enclosure also serves the purpose of supporting the end section of the HV cable connecting the power supply to the HV feedthrough. A chain of twelve 470 Ω, 5 W resistors imbedded into the end of the cable act as a load for power supply protection so, in the event of an arc, the surge of current will be dissipated across the resistor chain and not damage the supply. Unfortunately, this makes the last 3 feet of the HV cable very stiff and thus requires support. The shielding enclosure also has an access port so that the connection to the HV feedthrough may be made.

A Glassman WR Series 100 kV high voltage power supply with digital readouts and reversible polarity was used. By removing the outer cover of the unit and changing a module, the polarity of the potential supplied to the bias plate may be reversed; allowing for test chamber measurement of ions or electrons. The power supply was located in the ring service building basement.

Channeltron Assembly

The Channeltron assembly consists of an L-bracket to which was attached an electrically insulating Macor[10] [194] block. A single detector was mounted to the block in the center of the beam pipe such that its longest opening dimension was perpendicular to the beam direction. Two vacuum feedthroughs passed the Ctron biasing conductor and the signal wire. A Spellman 3 kV reversible polarity high voltage power supply was used to operate the Channeltron. In order to shield the Channeltron from the electric fields produced by the beam, a flat wire mesh disc approximately 3 inches in diameter was fixed to the Ctron mounting bracket and centered over the detector opening.

Installation

Upon acquisition and assembly of the components, the test chamber was leak tested to ensure compatibility with the SNS ring vacuum. Additionally, a high voltage test was performed before installation to verify the capabilities of the system. The setup for the high voltage test, performed with the vacuum chamber at 10^{-8} Torr, is shown in the left image of figure 4.2. The middle of figure 4.2 shows the shielding enclosure with the access panel removed to reveal the high voltage feedthrough for the bias plate with electrically insulating Kapton[11] [195] tape to reduce arcing. A bias plate voltage of 60 kV was achieved. A section of empty beam pipe was removed and the IPM test chamber was installed in the ring D straight, just upstream of the RF section and directly in front of the wall current monitor. The right image in figure 4.2 shows the final installation. The actual IPM will be located on the downstream side of the RF cavities.

[10] Macor is a registered trademark of Corning Inc.
[11] Kapton is a registered trademark of E.I. du Pont de Nemours and Company

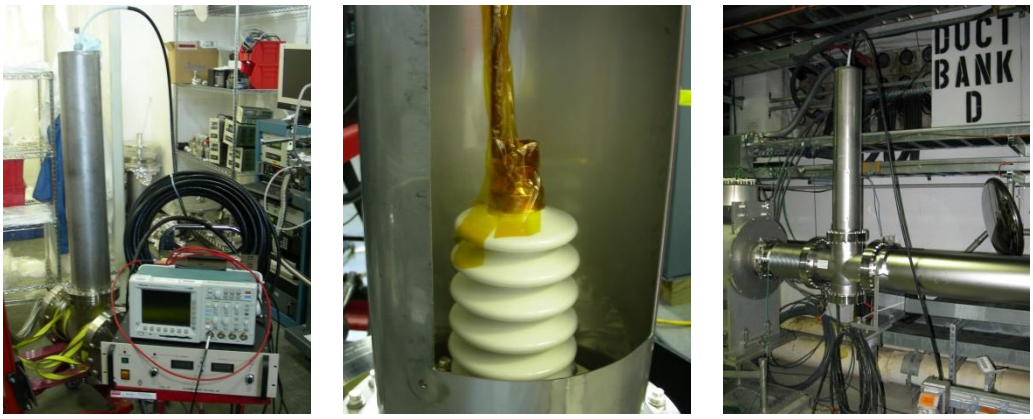

Figure 4.2 (Left) Experimental setup of high voltage test under UHV conditions. (Middle) Air side of the HV bias plate feedthrough with electrically insulating Kapton tape. (Right) Installed IPM test chamber.

4.2 Test Chamber Results and Modifications

Achieving the desired results in the IPM test chamber proved challenging and involved a process of trial and error. There were a number of unforeseen elements of the accelerator environment that had a significant effect on the measured signal. The final outcome was productive both in providing a proof-of-principle measurement as well as in elucidating a variety of issues that needed to be addressed in the final design. While the actual process of producing successful test chamber results was an iterative progression of measurement and chamber modification, the following section will summarize the measurements taken and the modifications made to address system problems.

Desired Test Chamber Result

A correct Ctron measurement of the beam in the ring should be characterized by DC current pulses with no AC behavior. Furthermore, since the Ctron functions as an electron source and the current direction is defined as opposite the flow of electrons, the voltage measured across the oscilloscope load resistor is negative. A measured test chamber signal on an oscilloscope

should consist of linearly decreasing voltage pulses with a 1 MHz frequency similar, except for signal polarity, to a beam current measurement taken by a ring beam current monitor (BCM). Shown in figure 4.3 is such a BCM measurement for a full beam ramp as well as a close up of the individual turns.

4.2.2 Test Chamber Measurements

The first measurement taken from the IPM test chamber, shown in figure 4.4, measured ions with a 60 kV bias potential while operating the Channeltron in analog mode with a 1 kV bias. The test chamber data in figure 4.4 shows essentially an AC signal. The passing beam produces image charges traveling in the accelerator pipe walls. These generate an AC signal when a load is placed across a gap in the accelerating structure. This beam-induced AC coupled signal dominates the test chamber measurement which is particularly visible in figure 4.5. This data was taken with no bias voltage and no Ctron bias so that, since no ionized products are being measured, all of the measured signal is from image current.

In an attempt to reduce the influence of the beam, a second cable was run alongside

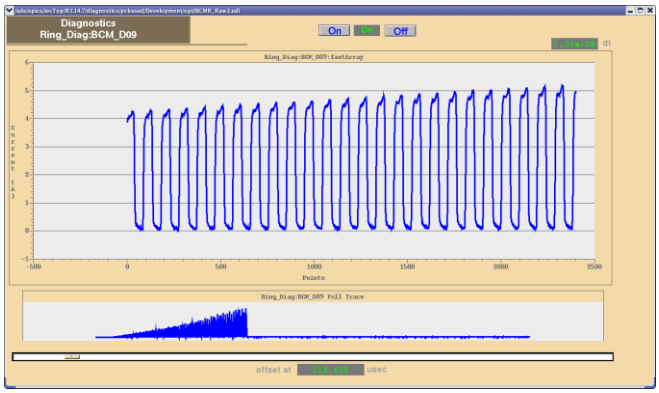

Figure 4.3 Screen shot of a ring beam current monitor measurement for a production beam, where the vertical axis is the BCM current in amps and the horizontal axis is time.

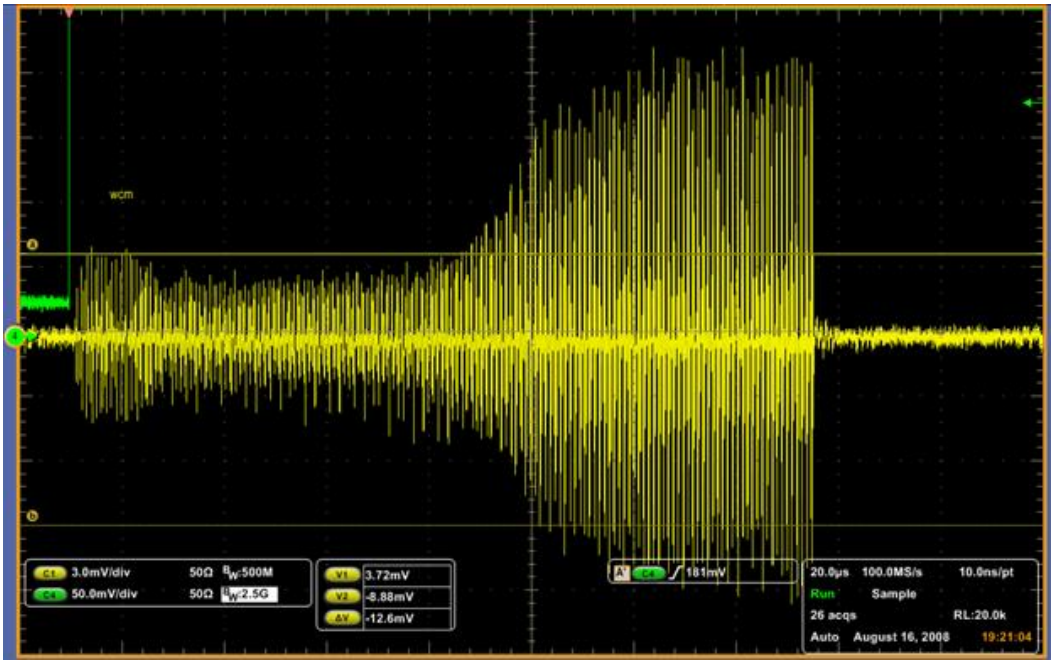

Figure 4.4 First IPM test chamber ion measurement with 60 kV bias and 1 kV Ctron voltage after initial beam line installation.

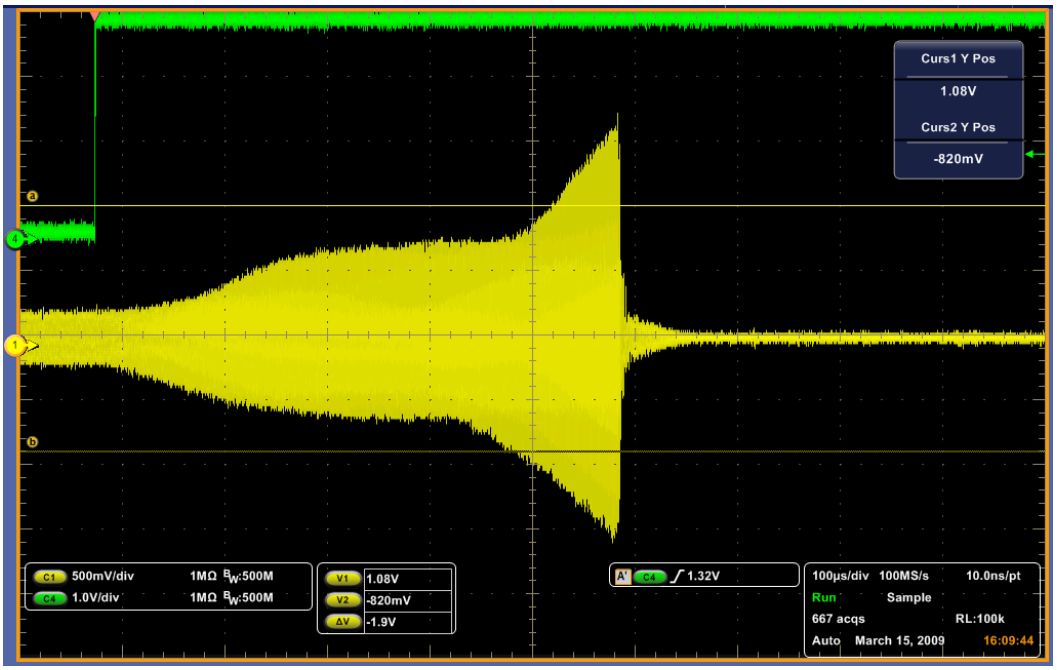

Figure 4.5 IPM test chamber ion measurement with 0 kV bias and 0 kV Ctron voltage from the installation version of the test chamber showing beam-induced signal.

the original cables and connected to the beam pipe in order to subtract the common mode from the Channeltron signal. This proved unsuccessful and the additional cable was left unterminated in tunnel. Furthermore, additional measurements revealed that the unterminated cable measured a significant amount of signal, suggesting that the tunnel environment was inducing parasitic noise through the cabling. A measurement using electrons was done by reversing the polarity of the bias plate potential. Results were also inconclusive due to the large AC signal.

4.2.3 Test Chamber Modifications

Vacuum Chamber and Cabling Modifications

Upon analysis of the original test chamber design, a number of design flaws became apparent. Figure 4.6 (a) shows an analysis of the initial test chamber. The Ctron signal coaxial cable was grounded to the beam pipe, which constituted a direct path for image current to enter the signal. Furthermore, much of the detector and wiring were exposed to the beam, allowing capacitive coupling by the beam into the measurement.

The test chamber was modified as explained in figure 4.6 (b) to include isolated feedthroughs that allowed the Ctron signal cable's ground to be floated from the beam pipe. A picture of the Channeltron with ground isolation wiring is shown at the left of figure 4.7, while the right side shows a cutaway drawing of the detector inside a grounded metal shielding can with an opening at the Ctron entrance to isolate the detector from the beam. Later, the shield enclosure was also modified to include a metal mesh over the detection opening to further reduce capacitive coupling. While the modifications did clean the IPM signal to some degree there is was still a significant contribution of environmental noise coupled into the actual

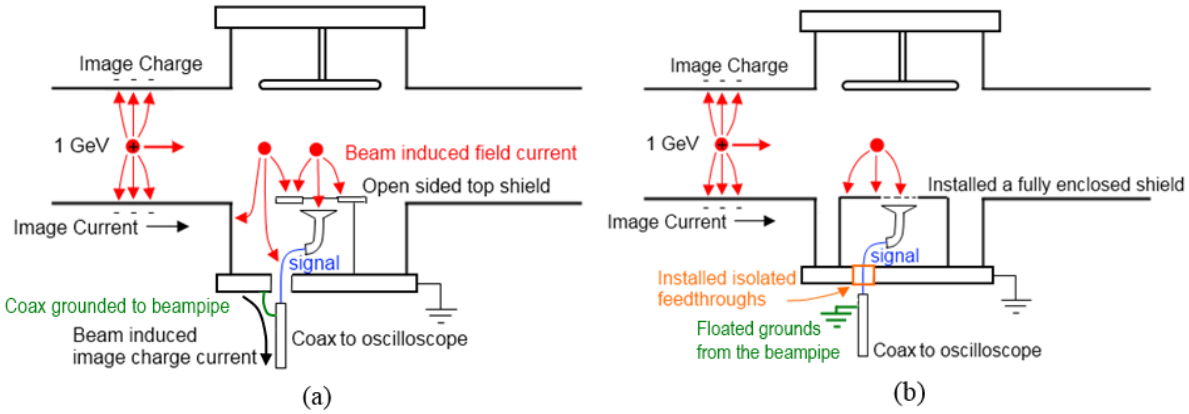

Figure 4.6 (a) Originally installed IPM test chamber layout showing beam-induced signal paths. (b) Modified chamber with image current isolation.

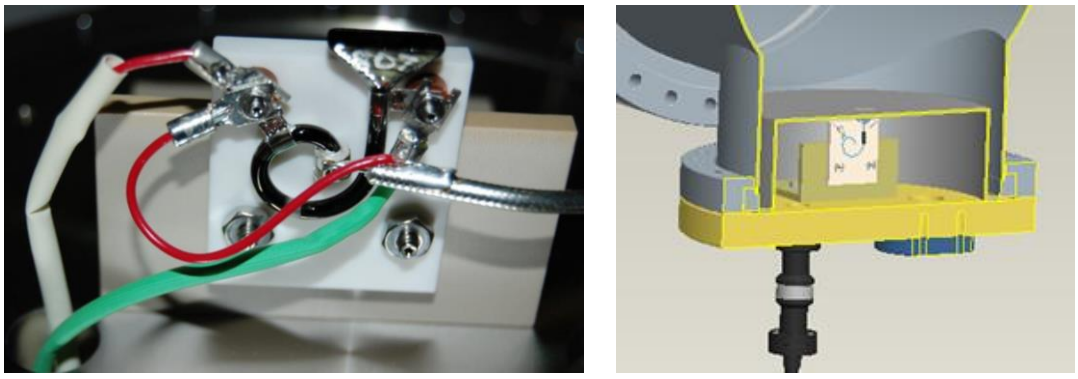

Figure 4.7 (Left) Channeltron wired for isolated feedthrough. (Right) Channeltron with grounded shield.

measurement.

Upon further examination it was determined that the cable being used for the Ctron signal was an unshielded cable which followed a path that ran next to the nearby RF cavities. New fully shielded cables were run, one for the Ctron signal and one for background subtraction, along a path away from the RF cavities. Also, a FEMTO DHCPA-100 high speed current amplifier was used in the RSB just before the oscilloscope to amplify the signal.

Modified Measurement Results

Measurements were taken for a production quality beam ~800 kW, figure 4.3. Test chamber results for ions and electrons are reported in figure 4.8 and figure 4.9. With the previously discussed test chamber modifications, a signal was finally measured that showed the beam ramping. Unfortunately the variable gain amplifier used only had a bandwidth of 1 MHz, which was insufficient to resolve turn-by-turn behavior

While this iteration of the test chamber proved successful in generating a measurement of the beam ramping by measuring ionization products, there was still excessive AC coupling. Since the amplifier was at the end of the signal path it was amplifying parasitic cable noise as well as the desired signal. By placing the amplifier in the tunnel immediately after the test chamber, it would be possible to greatly increase the signal to noise ratio.

The electron measurement in figure 4.9 exhibited behavior that resembled saturation due to the flattening of the data near the end of accumulation cycle. An unknown oscillation was also present at the beginning of the ramp. Results from a study of the electron signal peculiarities will be given shortly.

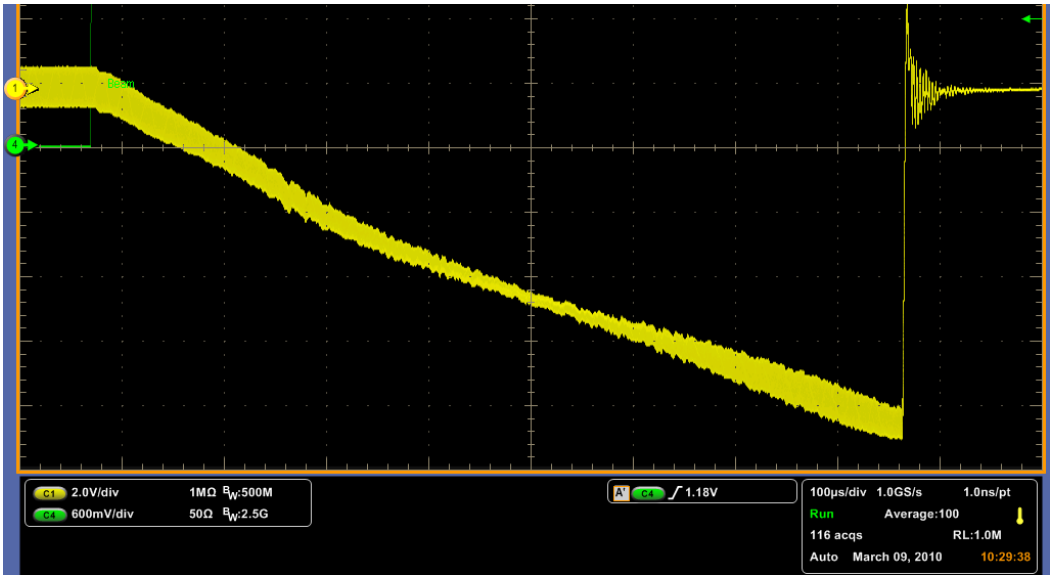

Figure 4.8 IPM test chamber ion measurement with a 1.33 kV Ctron bias and 30 kV electrode voltage with averaging for a modified test chamber including isolated feedthroughs, detector shielding can with opening mesh, and shielded cabling.

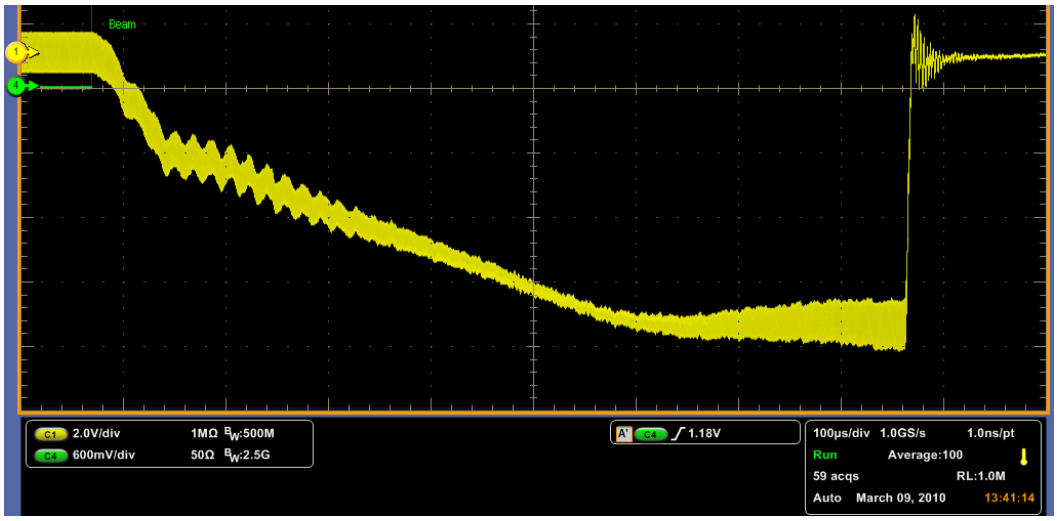

Figure 4.9 IPM test chamber electron measurement with a 1.26 kV Ctron bias and -20 kV electrode voltage with averaging for a modified test chamber including isolated feedthroughs, detector shielding can with opening mesh, and shielded cabling.

4.2.4 Test Chamber RF Noise

RF Interference Measurement Results

A FEMTO HCA-40M-100K-C current amplifier with a 40 MHz bandwidth and 10^5 gain was installed in the ring tunnel within a meter of the test chamber. However, initial measurements showed a considerable AC signal. Further study, presented in figure 4.11, revealed that, for the condition of no beam present, no electrode voltage, and the Channeltron turned off, there was an AC signal from the test chamber when the RF cavities were on (figure 4.10) and none when they were off (figure 4.11). By grounding the amplifier casing, the RF noise could be significantly reduced, as displayed in figure 4.12.

RF Mitigation

With a modified test chamber and grounded amplifier, the IPM test chamber was finally able to produce turn-by-turn beam measurements. Data from an ion measurement is shown in figure 4.13 with electron results in figure 4.14. In both measurements the background was subtracted by using a 0 kV Ctron bias measurement along with an inversion of the data to compare to BCM waveforms. Individual turns may be seen in the 5μs snapshot displayed in figure 4.15, which was taken from the figure 4.13 ion signal, which has a frequency of ~1.03 MHz.

4.3 Test Chamber Signal Study

4.3.1 Ion Signal

While the ion signal showed the best correlation with BCM measurements, it still exhibited undesirable behavior. In order to explore the signal, measurements were taken for a range of Channeltron biases to determine whether the effects where related to the detector or to a combination of the beam and residual gas. A 2000 point moving average was used to

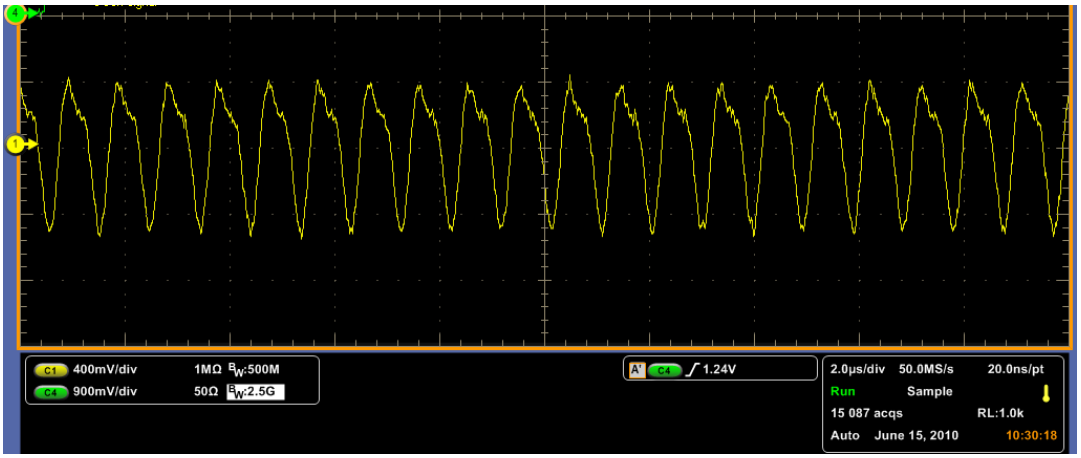

Figure 4.10 Test chamber measurement with no beam with RF cavities on.

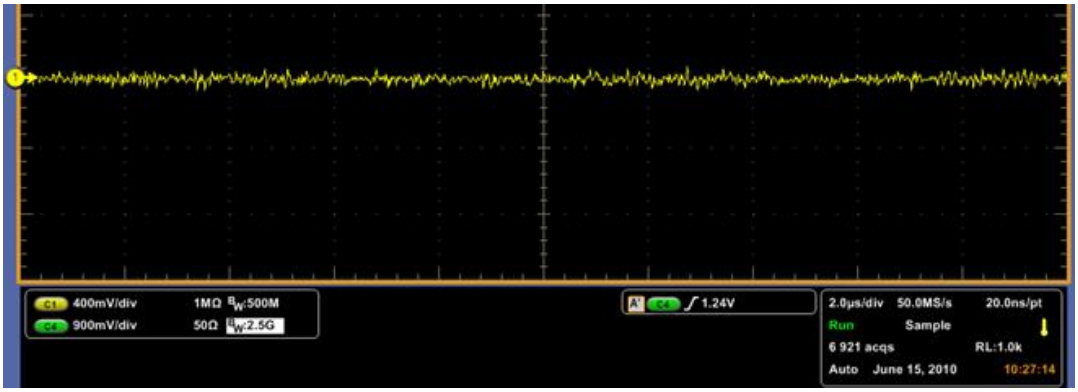

Figure 4.11 Test chamber measurement with no beam with RF cavities off.

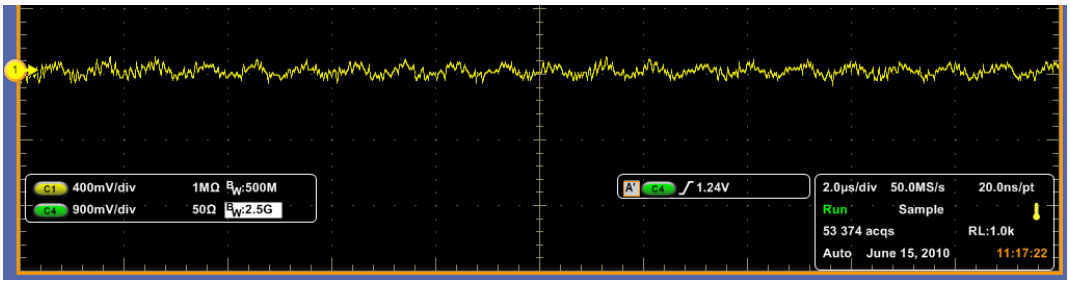

Figure 4.12 Test chamber measurement with no beam, RF cavities on, and grounded amplifier casing.

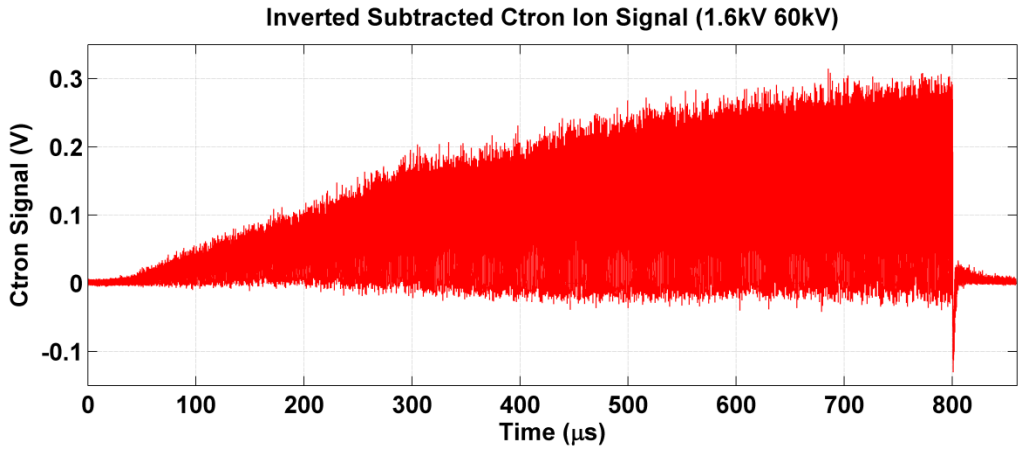

Figure 4.13 Test chamber ion signal after background subtraction and inversion for the fully modified test chamber with isolated feedthroughs, detector shield with opening, shielded cabling, high-bandwidth amplifier, and grounded amplifier casing.

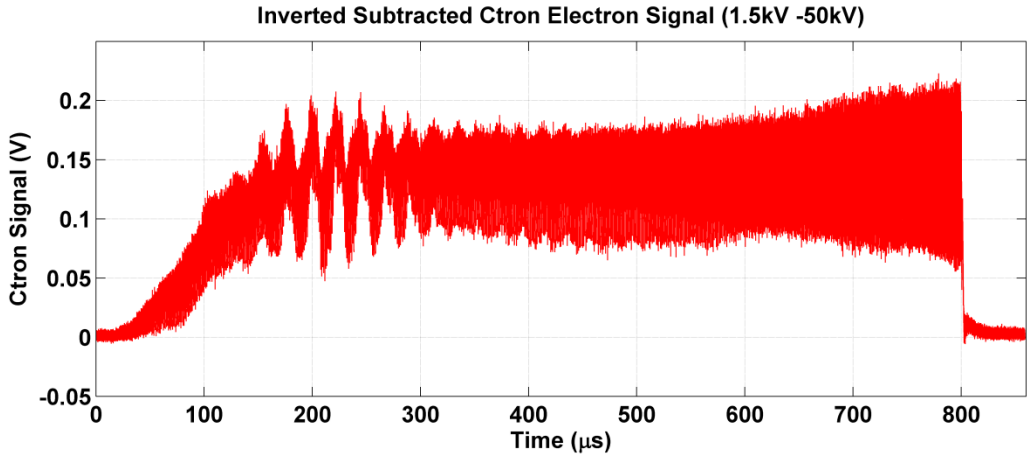

Figure 4.14 Test chamber electron signal after background subtraction and inversion for the fully modified test chamber with isolated feedthroughs, detector shield with opening, shielded cabling, high-bandwidth amplifier, and grounded amplifier casing.

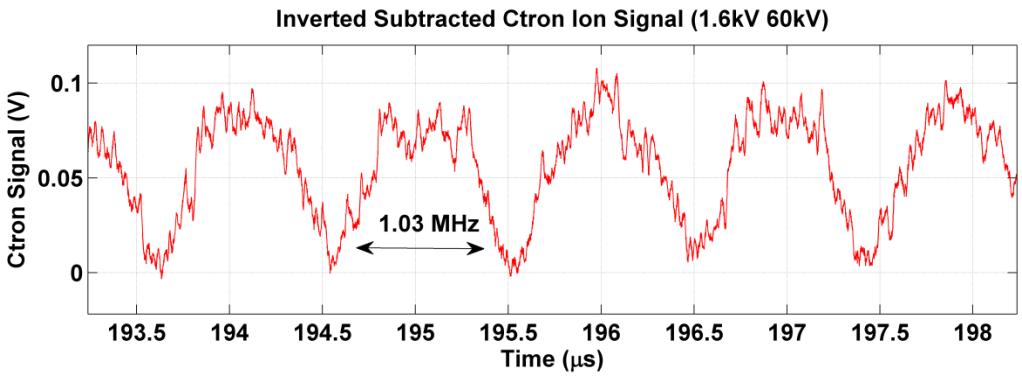

Figure 4.15 Individual turns in a 5 μs window of test chamber ion data for the fully modified test chamber with isolated feedthroughs, detector shield with opening, shielded cabling, high-bandwidth amplifier, and grounded amplifier casing.

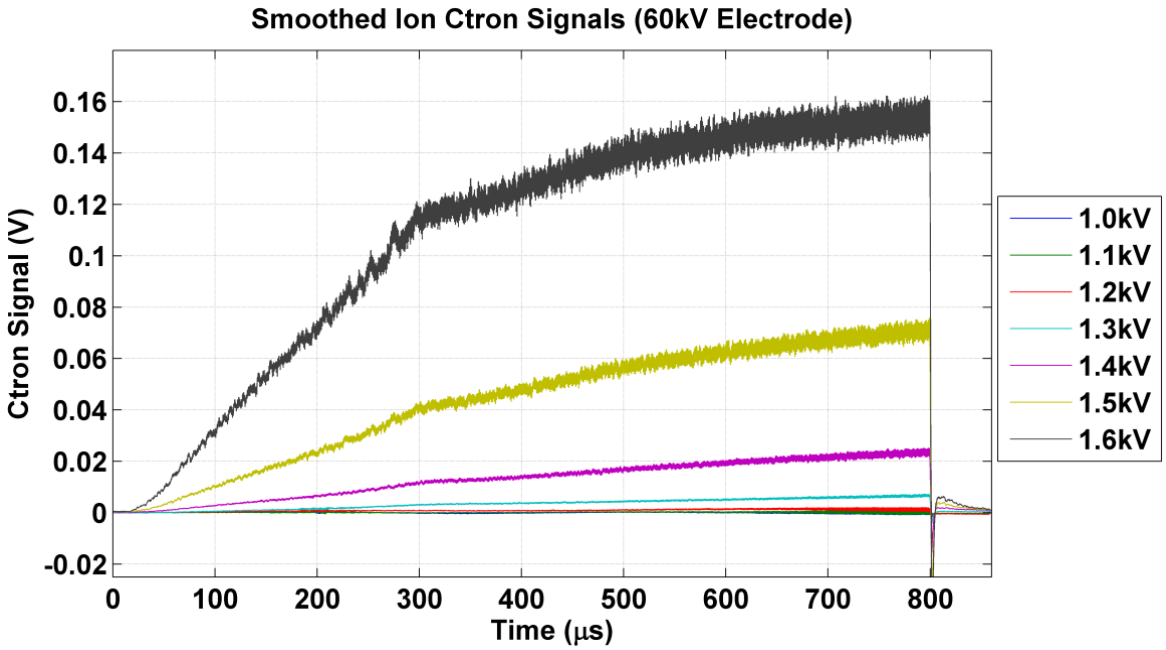

Figure 4.16 Smoothed ion signals as a function of Channeltron voltage from the fully modified test chamber.

smooth the data which eliminated the turn-by-turn resolution but allowed for a cleaner representation of the full accumulation.

Smoothed ion data for a production quality beam is given in figure 4.16 and figure 4.17 with an electrode potential of 60 kV. The ion data exhibits two artifacts, signal saturation beginning at the 300 μs mark and bump or knee at the same location. Differences between the different Ctron bias voltages are more visible in figure 4.17 which shows all the maximum signal amplitudes normalized to 1. All of the ion measurements were taken with a 60 kV electrode potential. Once the Ctron bias is high enough, ~1.3 kV, to operate in the analog mode, the saturation of the detector can be seen as the Ctron bias is increased. At 1.6 kV the signal flattens off at 300 μs. However, the knee is present at all analog Ctron biases regardless of later saturation.

Ion Knee

In order to explore the ion data knee a study was performed where the beam in the ring was accumulated to half intensity then stored for 200 μs, as shown in the BCM screenshot of figure 4.18 (a). It was postulated that the knee was an artifact of beam-induced residual gas pressure depletion and that by storing the beam the pressure effect would become more visible. However the results of the study shown in figure 4.18 (b) reveal no such pressure effect, as the Ctron signal remains constant throughout storage except for the highest detector bias. The saturation effect seen in the 1.6 kV signal of figure 4.18 (b) is likely caused by the inability of the Channeltron to sustain amplification at that bias voltage. It can be concluded that 1.6 kV is an upper limit for the Ctron bias and a reasonable operating range is around 1.3 kV. Raw data, background subtracted data, and averaged ion data are displayed in figure 4.19. It can be seen that there is still a significant source of AC signal, especially at the

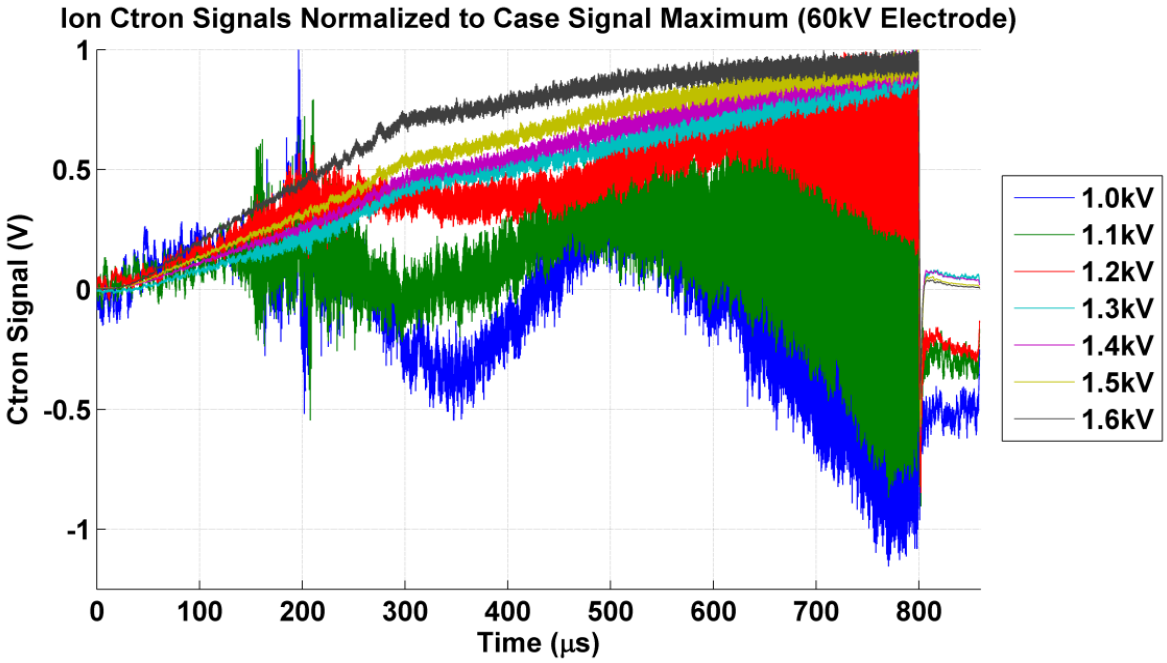

Figure 4.17 Fully modified test chamber smoothed ion signals as a function of Channeltron voltage, normalized to signal maximum.

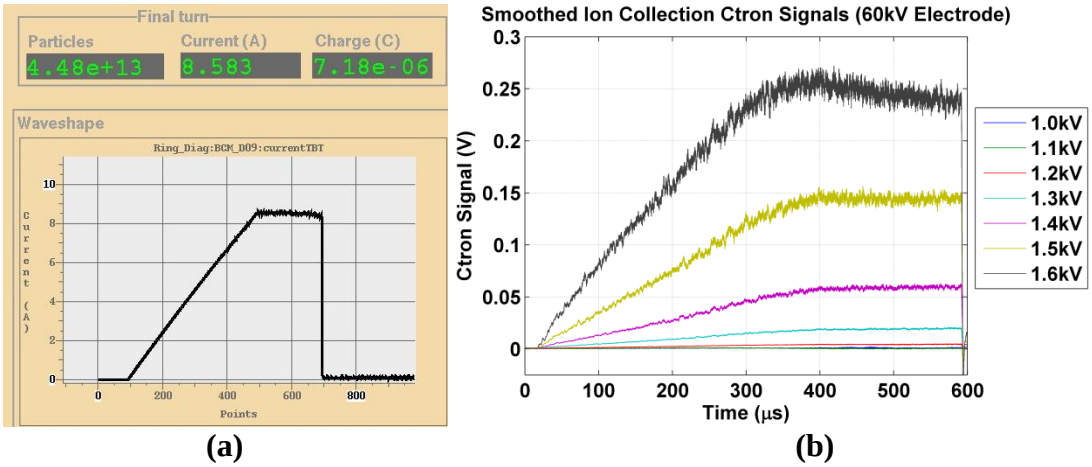

(a) **(b)**

Figure 4.18 (a) BCM screenshot for 100 μs of beam storage. (b) Test chamber smoothed ion signals as a function of Channeltron voltage for a stored beam.

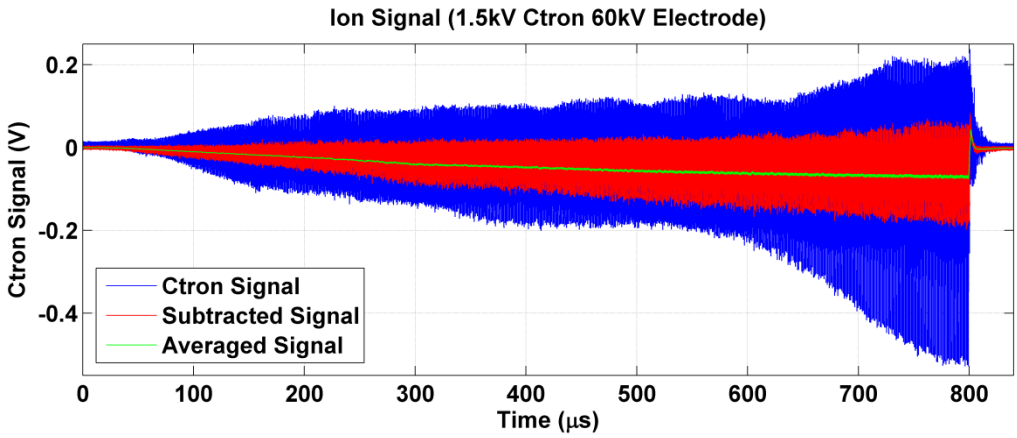

Figure 4.19 Raw fully modified IPM test chamber data along with background subtracted and averaged data for a 1.5 kV Ctron bias ion signal with a 60 kV electrode.

end of accumulation. A cleaner signal would facilitate a more accurate study of IPM signal behavior

4.3.2 Electron Signal

IPM test chamber electron signals collected for the same beam conditions as shown in figure 4.16 are shown in figure 4.20 and in the normalized version in figure 4.21. The electron data contains a number of peculiarities, such as a severe 45 kHz oscillation around 200 μs which damps out coincident with the expected saturation behavior, as seen more clearly in figure 4.21. Raw electron data for the 1.4 kV Ctron case in figure 4.22 shows a similarly AC coupled signal as with ions. The noise around 200 μs is also seen in many of the raw ion signals but disappears with background subtraction.

Electron Oscillation

In order to explore the origin of the electron signal oscillation, a study was done in which the beam was accumulated for 400 turns and then stored for 200. Then the beam intensity was reduced by half and the measurement repeated. By comparing the two beam conditions, the

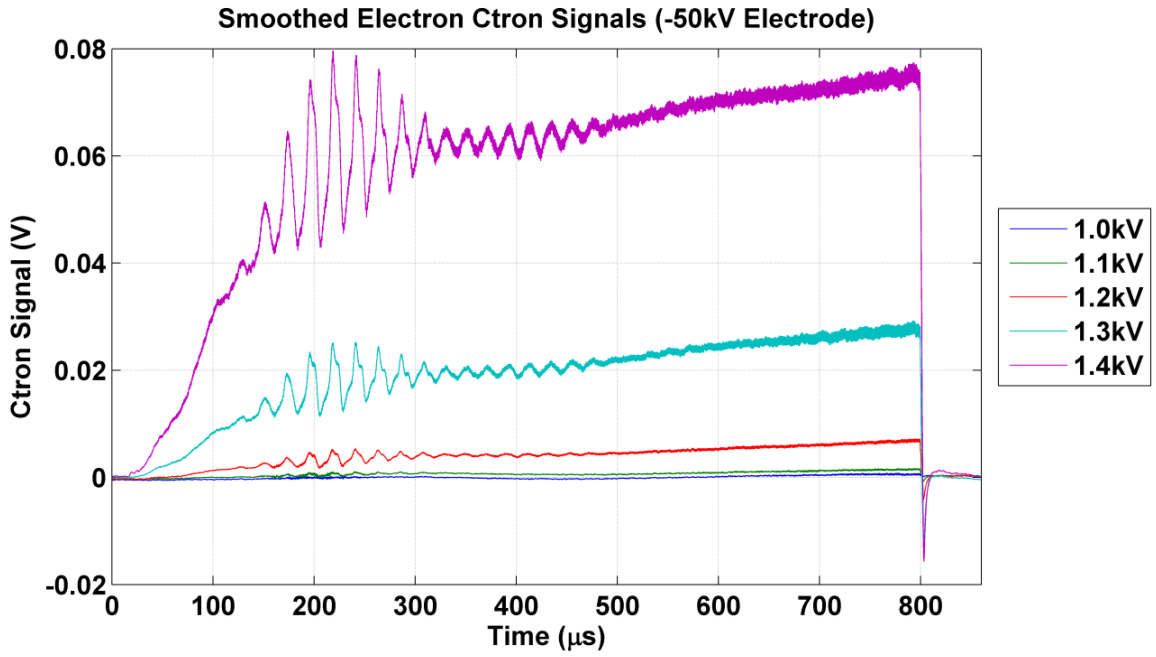

Figure 4.20 Fully modified test chamber smoothed electron signals as a function of Channeltron voltage.

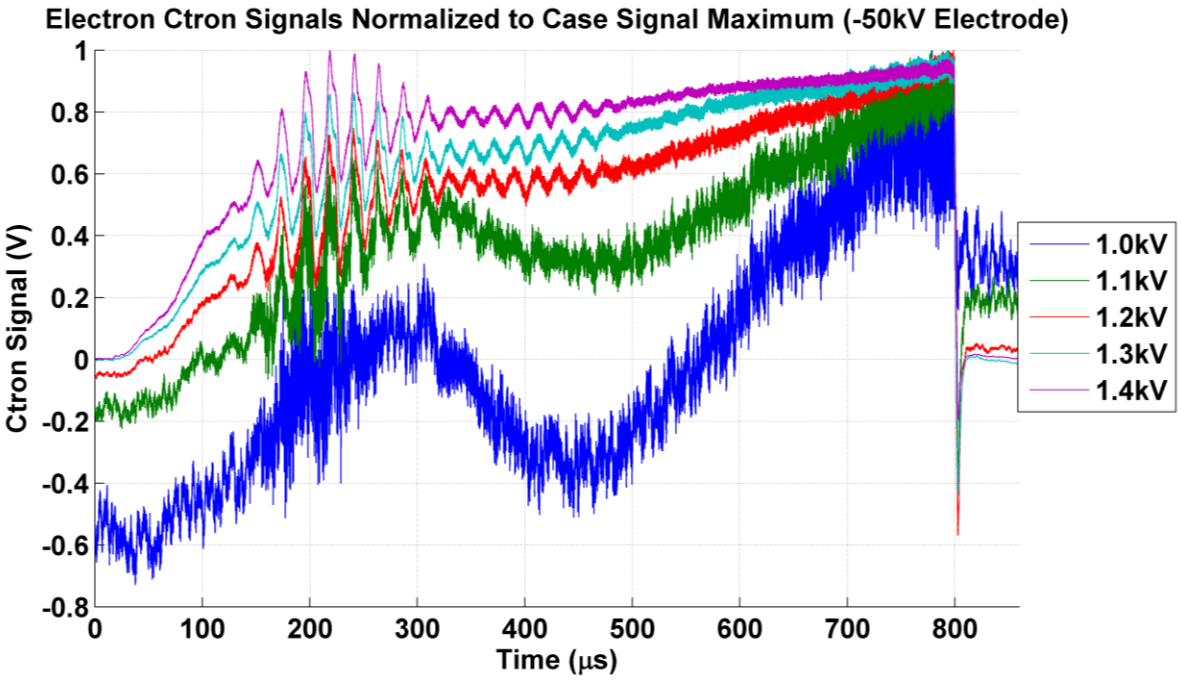

Figure 4.21 Fully modified Test chamber smoothed electron signals as a function of Channeltron voltage normalized to signal maximum.

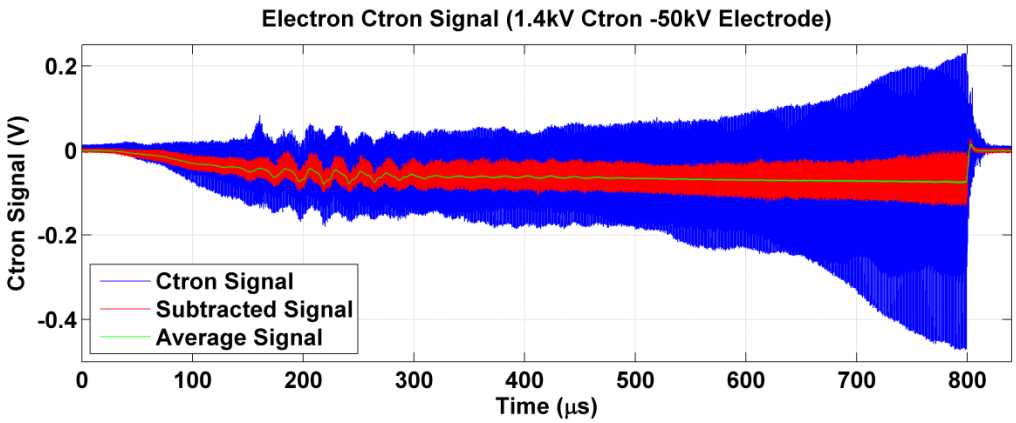

Figure 4.22 Raw fully modified test chamber electron data along with background subtracted and averaged data for a 1.4 kV Ctron bias with a -50 kV electrode.

effect of the beam on the electron signal may be seen. Results from the initially stored beam, figure 4.23 (a), are shown in figure 4.23 (b) and from the decimated beam, figure 4.24 (a), in figure 4.24 (b). It can be seen from figure 4.24 (b) that the oscillation is a function of the beam intensity. Beam decimation brings the stored intensity to that of the intensity where the oscillation occurs during the normal accumulation cycle. As such, since the oscillation is related to the beam intensity, it is plausible that the oscillation is due to actual measured electrons from multipacting, ion-induced secondary emission, or some form of beam instability. Due to the beam dependence it is unlikely that the electron oscillation is due to reflected signals within the test chamber electronics.

To further study the oscillation, another test was performed in which the electron signal from a fully accumulated beam was measured for a fixed 1.3 kV Ctron bias for various electrode potentials. The results are given in figure 4.25. First of all, the data shows the measured signal as a function of increased electrode potential. Also, trapping of electrons by the beam space charge potential well is seen in the loss of signal for the -10 kV case near the end of accumulation, when the space charge is strongest. Most importantly, the oscillation

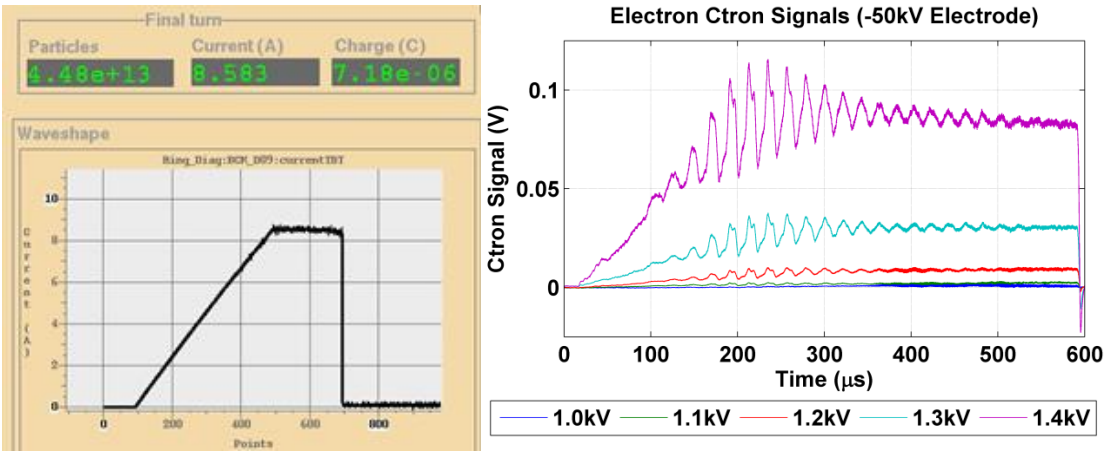

(a) **(b)**

Figure 4.23 (a) BCM screenshot for 100 μs of beam storage. (b) Test chamber smoothed electron signals as a function of Channeltron voltage for a stored beam.

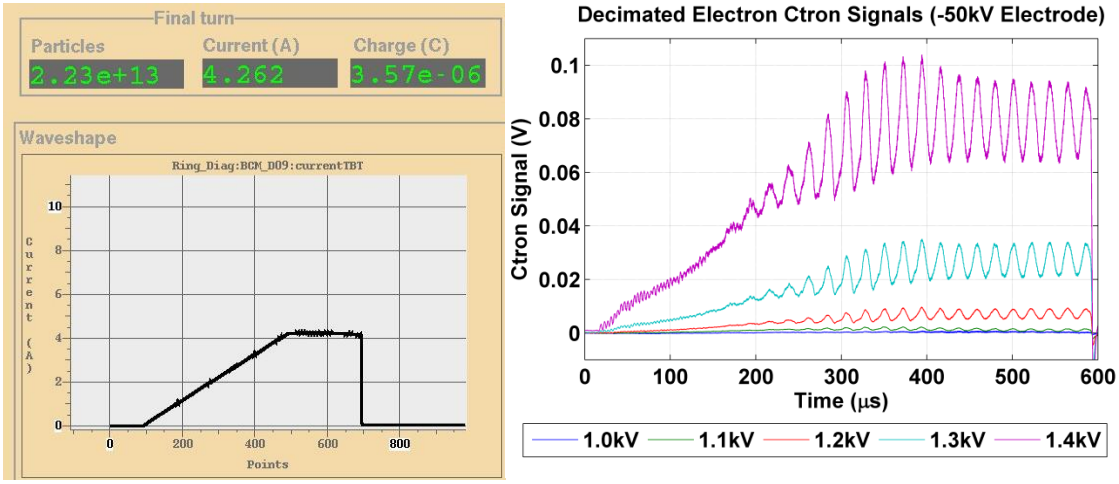

(a) **(b)**

Figure 4.24 (a) BCM screenshot for a decimated 100 μs of beam storage. (b) Test chamber smoothed electron signals as a function of Channeltron voltage for a decimated stored beam.

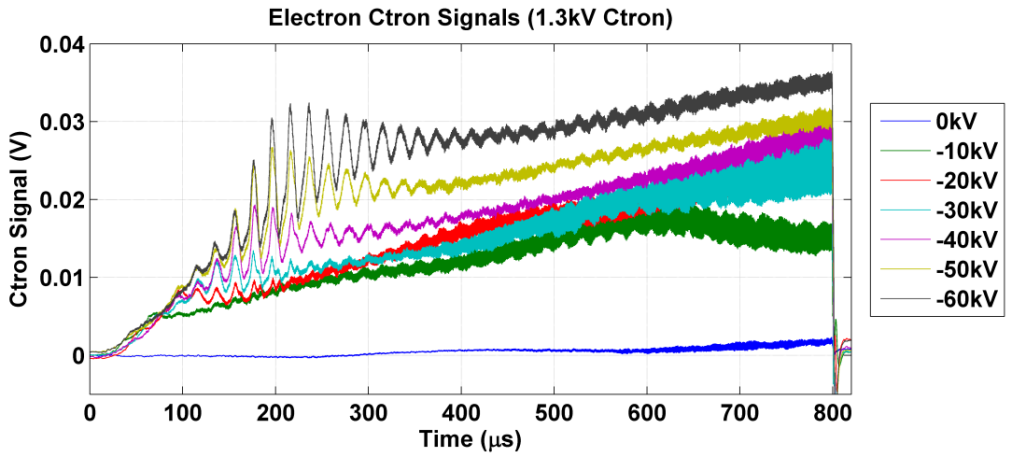

Figure 4.25 IPM test chamber electron data for a fixed Ctron bias as a function of electrode voltage.

strength significantly increases with the potential and the oscillation peak occurs at later times. This implies that the oscillation is an artifact of a beam-electron interaction and not due to an instability or multipacting.

It is possible that there is a more complex motion than previously anticipated caused by the superposition of forces due to the beam space charge and external bias field. The oscillation could be caused by forces that drive the electrons out of the beam until the beam potential is strong enough to damp the oscillation and achieve a steady state of ionized electron current. The exact mechanism causing the oscillation is unclear, as is the effect the external magnetic field in the full system would have.

4.4 IPM Test Chamber Conclusions

Noise Mitigation Parameters

IPM test chamber results are subject to a significant amount of beam and environmental noise. Knowledge gained from the test chamber design suggests additional design features to assure minimal signal noise.

1) In order to isolate the Channeltron from beam image current, isolated feedthroughs must be used and signal cable grounds must be floated from beam pipe.
2) Capacitive coupling from the beam directly to the detector hardware may be prevented by installing a fully encompassing grounded shield.
3) A method of background subtraction is necessary for accelerator environment noise.
4) Amplifiers installed in the ring tunnel must have grounded casings to reduce RF noise.
5) All cabling needs to shielded and cable paths chosen such that proximity to significant RF sources is reduced.

Signal Study Conclusions

Results from the final test chamber showed that the system is capable of measuring turn-by-turn signals. While the measurements taken do not fully explain the ion data knee, current postulations regard it as related to difficulty in differentiating between signal and noise. The electron oscillation is related to the beam intensity and electrode potential. Reduction of secondary electrons as well as the introduction of the electron collection magnet could have a significant effect on the electron signal. Further measurements with a complete IPM system will be necessary to characterize the electron behavior.

Chapter 5

IPM System Design

With the completion of an analysis of the fundamental principles for IPM operation, simulations to determine the design parameters, and experimental system verification with the test chamber, a final system can be designed. This chapter will describe the final design by major component such as the electrode, magnet, vacuum chamber, detector assembly, cabling, and high voltage feedthrough. Design considerations and methods will be presented for each component. Individual components will be related to the larger system framework culminating in a completed system.

5.1 Electrode Design

One of the components of the IPM system that nearly the entire system is built around is the bias electrode. Its size determines the vacuum chamber dimensions which in turn determines the magnet dimensions. The electrode was primarily designed with field uniformity in mind and then modified to accommodate additional aspects such as arcing mitigation and secondary electron reduction.

5.1.1 Field Uniformity Optimization

Transverse Field

The effects of a flat electrode, explored in section 3.2.3, showed the impact of the electrode size on the field uniformity. In theory, a flat plate, large when compared to the distance over which the field is considered, has a uniform field over the field region. However, simulations showed that the size of such an electrode would be physically unrealistic, forcing the dimensions of the vacuum chamber and magnet to be excessively large and driving up the cost.

An open-source 2D and 3D FEM partial differential equation solver, written in C++ and known as FreeFem++ [196], was initially used to determine the basic 2D electrode characteristics. By angling the ends of the electrode toward the beam the curvature in the potential lines may be reduced in the desired region. Described in figure 5.1, after the main electrode parameters such as the center width, wing length, wing angle, and chamber width were optimized for field flatness in FreeFem++, the commercial 3D FEM multiphysics solver

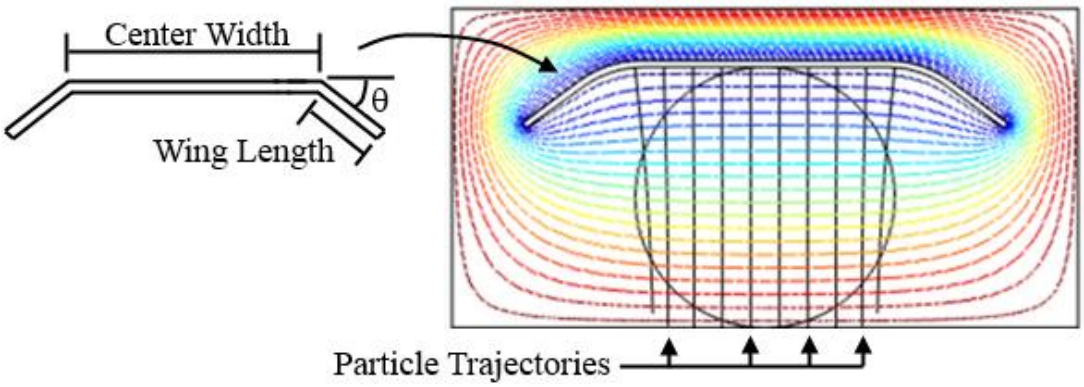

Figure 5.1 Graphical representation of the electrode optimization method and parameters.

COMSOL[12] [197] was used to simulate particle trajectories with the optimized electrode. Electrode optimization resulted in a 33.02 cm center width, 10.795 cm wing length, and 24 degree wing angle. Particle trajectory simulations for particles at three times the rms beam size above the beam, at beam center, and at three times the rms beam size below the beam are shown in the left portion of figure 5.2. The deviation is defined as the difference between the initial and final particle position and is displayed in the right of figure 5.2. The difference between the most extreme final particle positions at a particular transverse location is called the spread and is also shown in figure 5.2 (right).

The spread and deviations show that particles generated at a specified transverse position throughout the vertical beam range have an electrode field induced error of less than 2 mm. Therefore the electrode geometry satisfies the condition for field uniformity all the

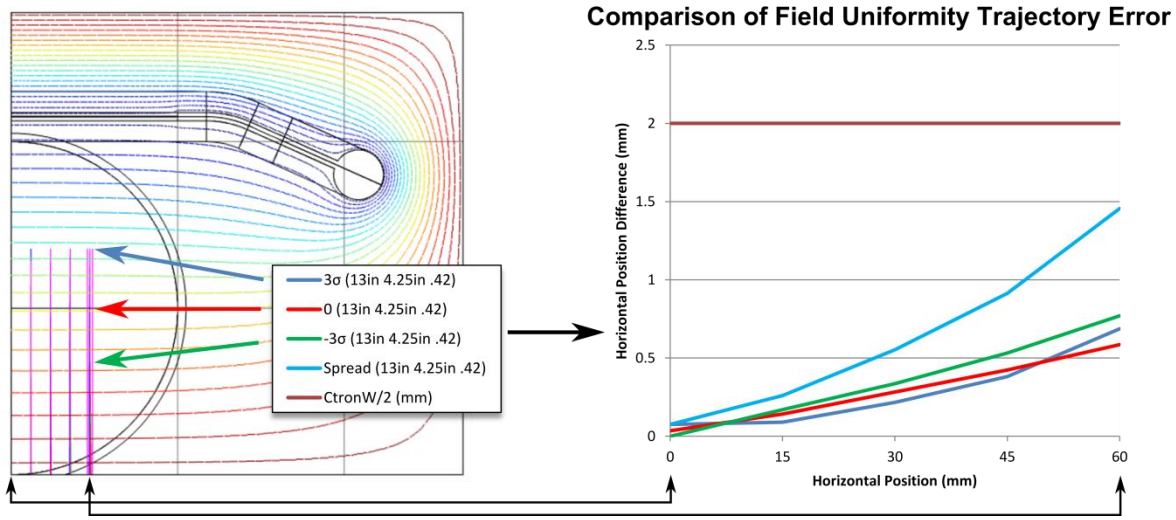

Figure 5.2 (Left) 2D particle trajectory setup. (Right) Comparison of the particle deviation due to field nonuniformity at different heights, along with particle spread.

[12] COMSOL is a registered trademark of COMSOL AB.

way out to 60 mm from the beam center.

Longitudinal Field

The longitudinal field distribution suffers from limitations in the flexibility of the electrode longitudinal geometry. Due to the condition that the electrode must not reduce the aperture of the beam pipe, longitudinal field shaping wings extending around the ionization region may not be used as they were for the transverse electrode dimension. Field uniformity is then only accomplished by electrode size. Limitations on the longitudinal length of the vacuum chamber due to the associated cost mean that a completely uniform longitudinal field is not possible.

A simulation of the longitudinal electrode potential and particle trajectories is given in figure 5.3 (a). Particles experience an outward force from the electrode centerline due to field nonuniformity. Depending on the height above the detector, particles created in the volume above the Channeltron will miss the detector opening. This lost signal contributes to profile errors as discussed in section 3.2. The number of particles collected is a function of the longitudinal electrode because larger longitudinal lengths yield flatter central fields. Particles from the top of the beam are most affected. Figure 5.3 (b) gives the percentage collected from the top of the beam as a function of electrode length. Due to spatial constraints, a longitudinal electrode length of 25.4 cm was chosen. From figure 5.3 (b), 42% of the top particles will be lost. To minimize profile errors from low-signal statistics, the number of collected accumulation cycles must be increased to compensate for longitudinal particle losses. The number of summed macro-pulses should be increased from 100, given in section 2.3.2, to 200 to guarantee sufficient signal, especially in the first few turns.

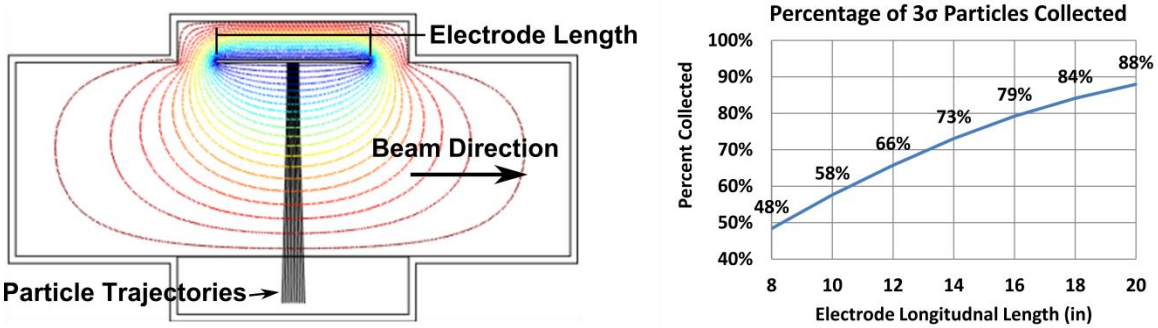

(a) **(b)**

Figure 5.3 (a) Longitudinal electrode particle trajectories. (b) Percentage of top beam particles collected due longitudinal field nonuniformity.

Alignment Tolerance

A 2D transverse simulation was performed in which the optimized electrode was rotated about its center to determine the effect of a misalignment inside the vacuum chamber. If the flat center part of the electrode is not parallel with detector plane, particles will receive a trajectory displacement. Results of the study showed that a maximum angle of 0.7 degree between the electrode center and detector plane could be tolerated before the particles were displaced more than 2 mm. This corresponds to a 6.3 mm tolerance in the difference between the bottom edges of the ends of the electrode and the plane of detection depicted in figure 5.4. Actual alignment errors are expected to less than a few millimeters, as specified in the design documents.

5.1.2 Vacuum Breakdown

Applying a high voltage across a gas filled gap can cause arcing between the electrode surfaces. The design of HV components to deal with such phenomena has been the subject of much study [134], [198], [199]. The voltage at which a gas will break down and sustain an

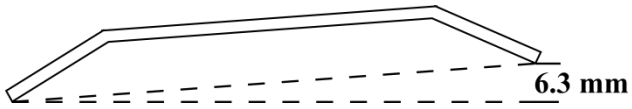

Figure 5.4 IPM bias electrode alignment tolerance illustration.

arcing current is a function of the gas pressure and the separation between electrode surfaces and is normally determined by the Paschen law [200], which is represented by a typical Paschen curve as shown in figure 5.5.

Breakdown Mechanism

In higher pressure gases, electrons emitted through field emission or thermionic emission gain enough energy in the electric field to ionize gas molecules causing an ionization cascade that supplies the necessary charged particles to form a current. The mechanism for vacuum breakdown and especially UHV breakdown differs from normal atmospheric breakdown because UHV electrons have a mean free path on the order of kilometers, precluding any form of charge avalanche. This means that the breakdown voltage is no longer a function of gas pressure.

There are a variety of theories on the initiation of UHV breakdown [201], i.e. the clump hypothesis [202], [203], but the exact mechanism is not completely known. A commonly used general explanation is that microscopic protuberances having enhanced electric fields, a phenomenon which will be explained shortly, will emit electrons through field emission. These particles, coupled with other free charged particles, are accelerated by the electric field to energies great enough to liberate charged particles upon impact, causing an arcing current to form. The bulk of UHV breakdown literature agrees that the breakdown voltage is a complex function of electrode geometry, material, and surface condition.

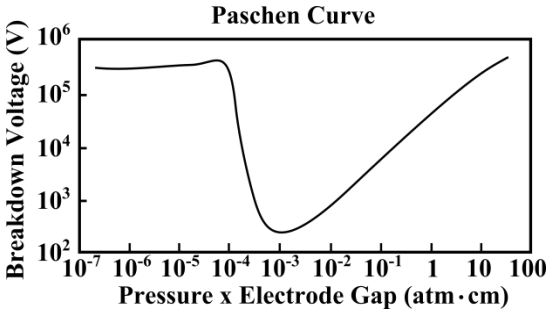

Figure 5.5 Typical Paschen curve.

Maximum UHV Field Limit

The IPM electrode poses a significant arcing hazard. An arcing event has the potential to permanently damage system components as well as to degrade the ring vacuum. Ensuring the electrode and chamber are designed well within an arcing limit is a high design priority. Much of high voltage design in the ultrahigh vacuum limit is based on experimental results for specific electrode materials and geometries.

A review of high voltage design literature shows that stainless steel in the 10^{-5} to 10^{-8} Torr range can sustain a maximum electric field of ~6 kV/mm before vacuum breakdown, for electrode gaps on the order of a few centimeters [201]. Other sources [134], [204] predict a maximum breakdown for clean, well-conditioned surfaces at a DC 120 kV potential of 6.7 kV/mm. In order to account for uncertainties attributed to the IPM electrode, a maximum field limit of 4.5 kV/mm was adopted. This includes a 32% safety margin.

Electrode Preparation

Further steps should be taken in the preparation and operation of the electrode to reduce possible arcing. A study [198] gave experimental evidence that polishing the electrode surface to remove imperfections can have a significant effect on arcing stability. Furthermore, surface preparation techniques discussed in [134] should be followed. These

include a 25 μm “mirror” polish and an ultrasonic bath of trichloroethylene, acetone, methanol and distilled water while keeping the electrode in as clean an environment as possible. It should be noted that isopropyl alcohol should be avoided as a cleaning agent on steel as it becomes trapped in the steel surface and constitutes a significant outgassing source [69]. Deinoized water may be used as a substitute. Conditioning is a process where, upon installation or chamber venting, the electrode voltage is slowly raised until an arc occurs and then held at that potential until the voltage is stable for ~1 minute. This allows the electric field to “burn off” small surface impurities leading to more stable operation at higher potentials. This technique was used successfully during installation and operation of the IPM test chamber.

5.1.3 Field Reduction

Parallel Plane Effect

Electrode arcing mitigation consists of identifying the electric field contributions, determining the controllable physical variables, and optimizing in accordance with the previously determined field limit. The first and simplest electrode field contribution is that of the fields produced by flat surfaces parallel to the flat chamber walls. These parallel planes separated by a distance *d* produce a uniform electric field given by

$$E_{Plane} = \frac{V}{d} \tag{5.1}$$

for a potential *V*. According to equation (5.1), the distance between flat electrodes for a 120 kV potential and 4.5 kV/mm field is $d_{min} = 27$ mm. This sets the minimum distance between the electrode and the chamber walls.

Edge Effect

The potential between two conducting planes meeting at a corner with angle β, as depicted in figure 5.6, and held at a potential V_0 is given by Laplace's equation in cylindrical coordinates

$$\nabla^2 V(r,\theta) = \frac{1}{r}\frac{\partial}{\partial r}\left(r\frac{\partial R}{\partial r}\Psi\right) + \frac{1}{r^2}\frac{\partial^2 \Psi}{\partial \theta^2}R = 0 \tag{5.2}$$

where the potential has been assumed to be separable $V(r,\theta) = R(r)\Psi(\theta)$. By separating the angular and radial variable in equation (5.2) it can be shown that

$$\frac{R}{r}\frac{\partial}{\partial r}\left(r\frac{\partial R}{\partial r}\right) = -\frac{1}{\Psi}\frac{\partial^2 \Psi}{\partial \theta^2} = \lambda^2 \tag{5.3}$$

with λ being an arbitrary constant. Superposition of homogeneous and nonhomogeneous solutions arising from the expression in (5.3) results in

$$V(r,\theta) = (A + B\ln r)(C + D\theta) + \left(Er^{\lambda} + Fr^{-\lambda}\right)(G\cos\lambda\theta + H\sin\lambda\theta) \tag{5.4}$$

where *A, B, C, D,E, F, G,* and *H* are determined by boundary conditions. The boundary condition at $\theta = 0$ such that the potential is a constant V_0 on the boundary implies $G = B = 0$, while the condition that the potential remains finite at $r = 0$ implies $F = 0$. The boundary condition $V(r,\beta) = V_0$ results in $D = 0$ and $\lambda = n\pi/\beta$ where *n* is a

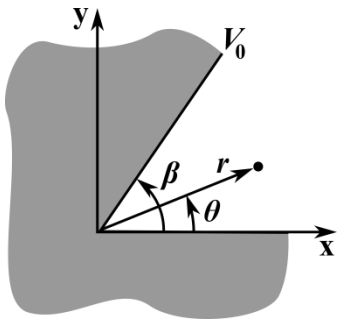

Figure 5.6 Corner charge calculation setup.

positive integer. *E* is determined by potentials far from the origin and can be ignored as it only affects magnitude of the potential [74]. With a change of notation $E \rightarrow a$, the general solution becomes

$$V(r,\theta) = V_0 + \sum_{n=1}^{\infty} a_n r^{\frac{n\pi}{\beta}} \sin\left(\frac{n\pi}{\beta}\theta\right). \tag{5.5}$$

For the purposes of examining the behavior close to the corner at small values of *r*, it is sufficient to only use the first term of equation (5.5), leading to

$$V(r,\theta) \cong V_0 + a_1 r^{\frac{\pi}{\beta}} \sin\left(\frac{\pi}{\beta}\theta\right). \tag{5.6}$$

The electric field may be found using $\vec{E} = -\vec{\nabla}V$ which may in turn be used to find the surface charge density σ by evaluating Gauss's law at the boundary

$$\sigma = \varepsilon_0 \vec{E}(r,0) = -\frac{\varepsilon_0 \pi a_1}{\beta} r^{\frac{\pi}{\beta}-1}. \tag{5.7}$$

Expression (5.7) reveals the nature of conductors with corners. An inside corner with $\beta = \pi/2$ makes the surface charge density $\propto r$. At $\beta = \pi$, or a flat surface, the expected uniform surface charge is obtained, while an outside corner $\beta = 3\pi/2$ makes $\sigma \propto r^{-1/3}$. Analysis of the surface charge shows that the surface charge goes to zero approaching an inside corner while it goes to infinity for an outside corner. From this it can be seen that sharp corners or objects greatly enhance the electric field and must be avoided.

Edge Radius

By rounding the edges of the electrode the sharp corners may be eliminated. The radius needed in order achieve the desired field may be estimated by considering the case of concentric infinitely long cylinders, where the inner cylinder with radius *a* held at a potential

V_0 represents the electrode edge and the outer grounded cylinder of radius *b* represents the chamber wall. Axial symmetry guarantees no angular dependence, and according to Gauss's law the electric field at a radial position *r* from the center is given by

$$\vec{E}_{cyl}(r) = \frac{V_0}{\ln\left(b/a\right)}\frac{1}{r}\hat{r}. \tag{5.8}$$

Using the fact the field is a maximum on the inner cylinder surface, equation (5.8) solved for the outer cylinder radius *b* is minimized when *a* = 27 mm. The gap between the inner and outer cylinder is then 45 mm. Instead of making a solid electrode of thickness 60 mm, which would be extremely heavy, or a hollow electrode which would be difficult to fabricate, a single solid stainless steel electrode of thickness 6.35 mm with cylindrical endcaps may be used, as illustrated in figure 5.7.

Corner Radius

The second source of field enhancement occurs at the four corners of the electrode. While rounding the edges generates curvature in a single plane, the corners must be rounded in two dimensions, which further increases the field and requires larger radii. Effects of corner radiusing may be initially estimated using concentric spheres with an inner sphere of radius *a* at potential V_0 and outer grounded sphere with radius *b*. The electric field at a distance *r* between the spheres is

$$\vec{E}_{sphere}(r) = \frac{V_0 ab}{b-a}\frac{1}{r^2}\hat{r}. \tag{5.9}$$

Setting $E_{sphere}(a) = E_{max}$ yields an inner radius a of 54 mm, corresponding to a minimum gap of 54 mm.

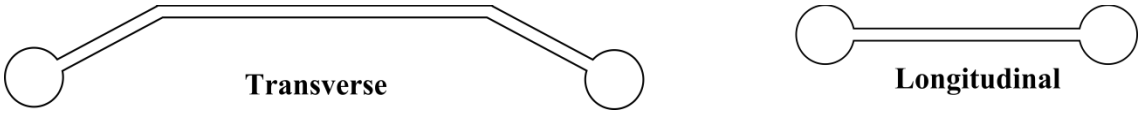

Figure 5.7 Transverse and longitudinal electrode profiles with field reduction caps.

Modeling and Optimization

Using the previous estimations, a 3D model was built in COMSOL, figure 5.8 (a), to simulate and optimize the electrode geometry based on the maximum field limit. In order to achieve simulation accuracy a fine mesh of tetrahedral elements was used for modeling the curved regions. Figure 5.8 (b) illustrates how finer meshing parameters were used on curves and in regions of two- plane curvature where the highest electric fields were expected. Optimal electrode geometry was achieved by adjusting parameters such as the edge and corner radii as well as the chamber dimensions.

The results of an electrostatic simulation of the electrode in the IPM chamber are presented in figure 5.9 showing surface electric field magnitude along with dimensions of the finalized electrode and vacuum chamber. A maximum field of 4.5 kV/mm occurs on the corner radius, which satisfies the UHV arcing limit. Further simulations showed that the chamber modifications as well as the addition of end caps produced no significant modifications to the particle trajectories.

5.1.4 Insulating Standoffs

Preceding analysis of the electrode has omitted any form of support structure. In order to hold it in place while maintaining electrical isolation, a dielectric insulating standoff must be used. Introduction of such an insulator adds new arcing paths that must be taken into consideration. Bulk breakdown occurs when the electric field in the volume of the dielectric

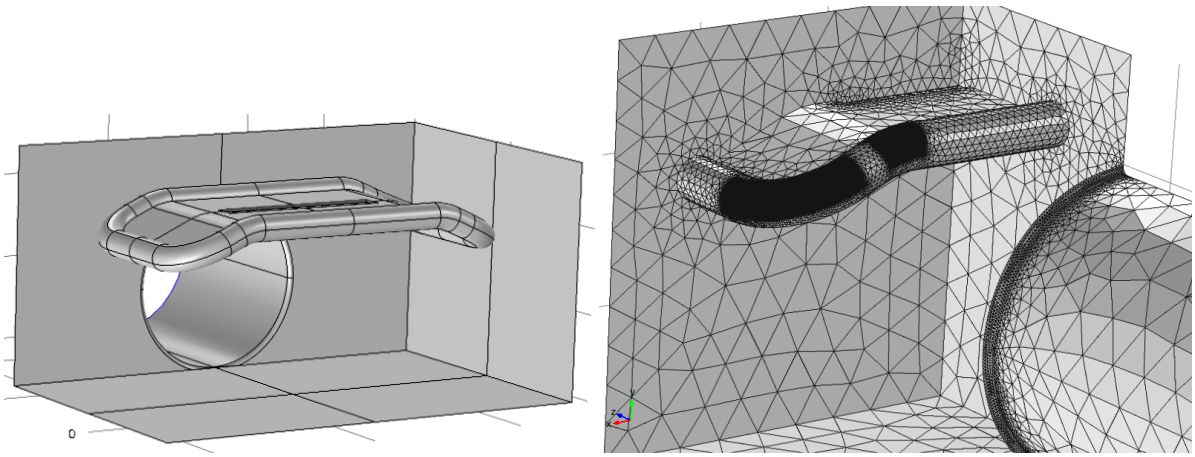

(a) **(b)**

Figure 5.8 (a) 3D electrode model. (b) Electrode optimization quarter model showing enhanced meshing in high field regions.

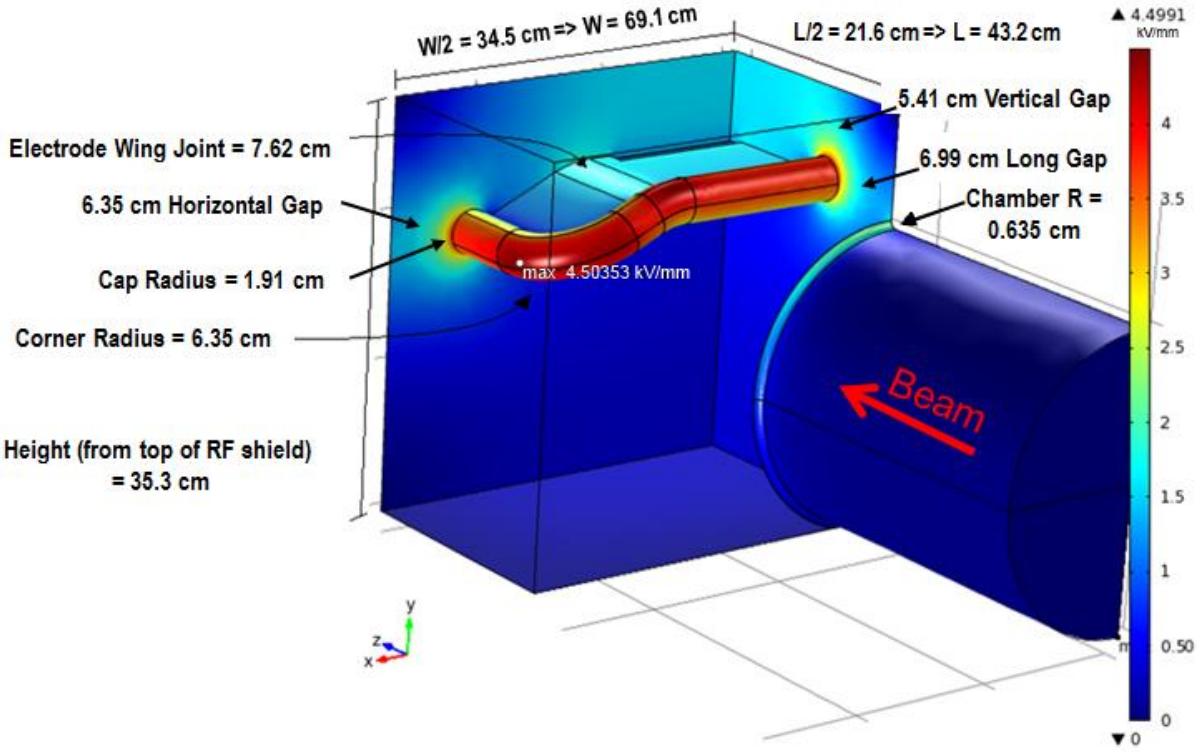

Figure 5.9 Quarter model of IPM chamber and electrode with electrostatic surface electric field simulation results for detailed optimized dimensions.

is large enough to cause a significant number of electrons to be excited into the material's conduction band, forming a current. When the dielectric begins to conduct the electrical breakdown current can permanently damaging the insulator.

Bulk electrical breakdown is represented by the material's dielectric strength, which is the maximum field tolerable. The dielectric strength has a value of 11 kV/mm for the insulators being considered here [205]. Insulator breakdown is of little concern in the IPM since the fields are guaranteed to be lower than 4.5 kV/mm and even less on the flat surfaces. A more significant source of insulator arcing exists that requires special design considerations.

Surface Flashover Mechanism

Surface flashover is a major source of insulator arcing and refers to an arcing path that develops along an insulator surface, often at electric fields lower than for bulk breakdown. While surface flashover has been the subject of much study [206–208], a complete theory has not been reached. Origination of surface flashover is generally attributed to electron emission by field or thermal emission from a triple point. A triple point is an interface where the insulator contacts the electrode and shares a boundary with a vacuum or gas. This point is subject to enhanced electric fields and will be discussed shortly.

Theories [206] for the formation stage of flashover are illustrated in figure 5.10, where the left model represents triple point emitted electrons striking the insulator surface, causing an avalanche of secondaries. The middle model represents bursts of electrons that form successive charged regions creating an avalanche mechanism. The right image of figure 5.10 illustrates theories not involving avalanches, such as gas discharge from the insulator surface by electron impact. It is generally agreed upon that the final stage of flashover occurs

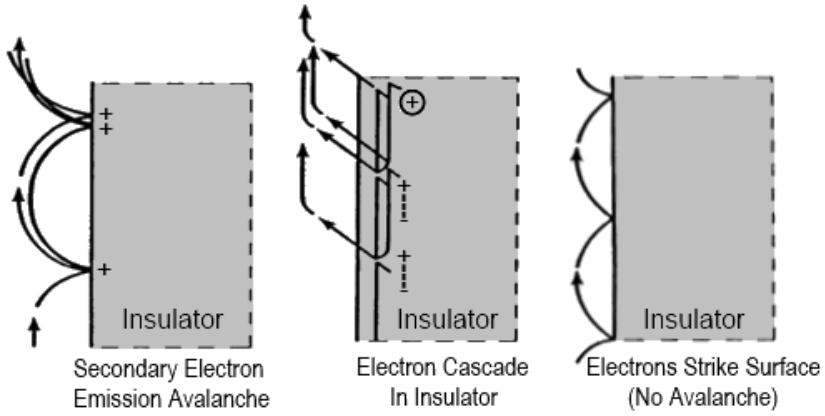

Figure 5.10 Three representative theories of the middle stage of surface flashover. [206]

when an arcing path forms in the gas desorbed from the insulator surface during the middle stage of the process.

Flashover Considerations

There are a number of design considerations affecting surface flashover voltages, as outlined in review studies such as [209]. A few such conclusions from the aforementioned study will be discussed in the following paragraphs and the references therein may be consulted for more in-depth treatment. It was experimentally verified that the technique of conditioning an electrode by slowly increasing applied potential is successful in producing a more stable operating voltage. This same technique has been shown to also be successful in flashover breakdown voltage reduction. Experimental data shows that the flashover voltage is independent of gas pressure below 10^{-6} Torr. Furthermore, studies report that there appears to be no significant effect on flashover voltage due to differences in electrode material such as stainless steel, copper, or aluminum [209].

Flashover voltages tend to decrease with increased dielectric diameter, due to the decreased surface charge density, and increased insulator contact area, up to a certain

saturation limit such as ~5 mm for a 2 mm long Macor ceramic insulator. Experimental evidence shows that the flashover voltage is also reduced with increased insulator length. An expression for calculating the flashover breakdown voltage is given in [209] for a solid insulator of length l in cm as

$$V_B = \sqrt{\frac{M_{cr} A_1 v_0 e l}{2\varepsilon_0 \gamma v_e (2A_0/(A_1 - A_0))^{1/2}}}. \quad (5.10)$$

In equation (5.10) the amount of desorbed gas considered critical just before flashover is M_{cr} in gas molecules per cm^2, A_1 given in eV is the electron impact energy, A_0 also in eV is the electron emission energy, v_0 is the desorbed gas molecule average velocity in cm per second, ε_0 is the free space permittivity, e is the electron charge, the molecules desorbed per electron is γ, and the average electron velocity is v_e = 5.94x10^7 $\sqrt{A_1}$ in cm/s.

Equation (5.10) may be used to solve for the minimum insulator length l for a given voltage. Using a breakdown voltage of V_B = 120 kV, with other parameters taken from [209],[210] for alumina such that M_{cr} = 1.5x10^{18} molecules/cm^2, A_1 = 20 eV, A_0 = 4.7 eV, v_0 = 1.5x10^5 cm/s, and γ = 4, an insulator length of 2.3 cm is found. This means that an insulator of at least 2.3 cm is required to prevent surface flashover for the voltage required by the IPM electrode. As it stands, satisfaction of the vacuum breakdown field requirement necessitates that the gap between top of the electrode and the top of vacuum chamber be at least 5.41 cm, which is over twice the length calculated.

Triple Point

As previously mentioned, the triple point conductor-dielectric-vacuum interface has been identified as a significant contributor to the formation of surface flashover. As such, it is necessary to explore methods of minimizing the triple point influence. A number of studies

[211–214] have explored the details of triple point field enhancement. In the case where the contact between the dielectric and the conductor is a right angle, as displayed in figure 5.11 (a), there is no field enhancement at the triple point [215]. Perfect contact between the insulator and conductor does not exist, due to microscopic or macroscopic irregularities in the dielectric edge as illustrated in figure 5.11 (b). These imperfections modify the electric field in the triple point region causing field enhancement.

It has been experimentally shown [216] that recessing the dielectric a distance *d,* shown in figure 5.11 (c), into the conductor lowers the flashover voltage by modifying the electric field such that the maximum occurs away from the triple point. Therefore, it has become common practice [134], [217] in high voltage design to recess the triple point. It is also common practice to keep external electrons away from the insulator surface as these can cause the same pre-flashover conditions as triple-point electrons.

Standoff Design

Based on the previous analysis of surface flashover, a set of cylindrical insulators have been selected to hold the electrode in place. Aluminum oxide Al_2O_3, commonly known as alumina, has been chosen as the insulator dielectric due to its electrical properties [205]. 99.8% pure alumina has a relative dielectric constant of 9.8. High purity alumina has been

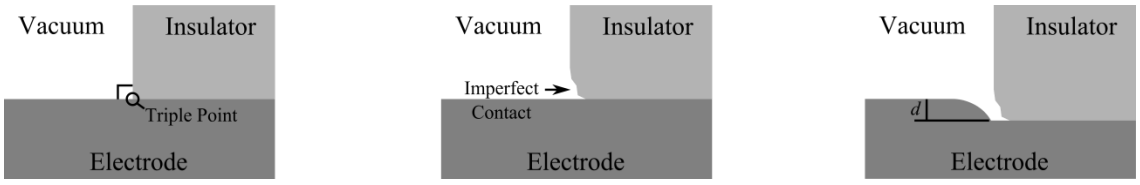

Figure 5.11 (a) Perfect contact triple point. (b) Imperfect contact triple point. (c) Recessed contact triple point.

successfully used in other areas of the SNS accelerator and is easily purchased off the shelf from a number of vendors. Four 1.27 cm diameter unglazed 99.5% alumina 6.35 cm long standoffs are fitted into 6.35 mm deep recessed holes with a 3.3 mm hole edge radius, as shown in figure 5.12. The insulators are on the opposite side of the electrode from the beam and the electrode produces strong electric field lines parallel to the standoff surface. Because of this, and the presence of the external magnetic field, electrons produced away from the insulator are not expected to be a source of flashover initiation.

The electrode has a mass of 19.1 kg giving it a weight of 187 N. With a tensile strength of 25,000 psi, four 1.27 cm diameter alumina standoffs could hold a force of 43 kN normal to the standoff endface, which is well above the electrode weight in the horizontal IPM system. Flexural strength describes the maximum bending force a material can withstand and is significant for the vertical IPM system, where the electrode is held in place by four alumina standoffs connected to the vacuum chamber sidewall.

A force perpendicular to the standoff cylindrical axis is applied by the weight of the electrode. A flexural strength of 49,000 psi is reported 99.5% alumina [205] for the same standoffs as in the horizontal system resulting in a supportable tangential weight of 171 kN, which is also well above the electrode weight. Furthermore, with a shear modulus G = 22×10^6 psi, length l = 6.35 cm, r = 6.35 mm radius, and a F_s = (187 N)/4 shear force, the

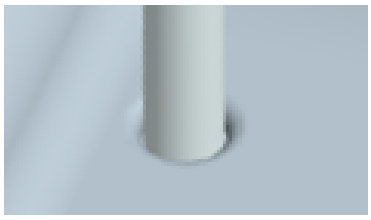

Figure 5.12 Electrode-standoff interface with recess.

vertical displacement due to the electrode weight in the vertical system is a trivial $\Delta x = F_s l/\pi r^2 G$ =0.2 μm. Further calculations [218] show that shear and tensile forces experienced by the flat head socket screw cap 10-32 stainless steel bolts and the threaded standoffs are able to support the electrode without failure.

5.1.5 Secondary Electron Suppression Mesh

The necessity of limiting sources of noise has been discussed at length in section 3.2, especially noise produced by secondary electrons generated when ions produced by electron generated profiles strike the electrode, as illustrated in the left image of figure 5.13. Presented here is a design modification to the electrode to reduce the flux of ion-generated secondary electrons. A wire mesh is installed in a rectangular cutout in the electrode center opposite the detector. The mesh allows a fraction of ions to pass through. These ions will then experience an equal but opposite force produced by the electrode, causing them to decelerate, reverse direction, and strike the mesh on the side away from the Channeltron. The right portion of figure 5.13 shows that electrons produced by ions striking the back side of

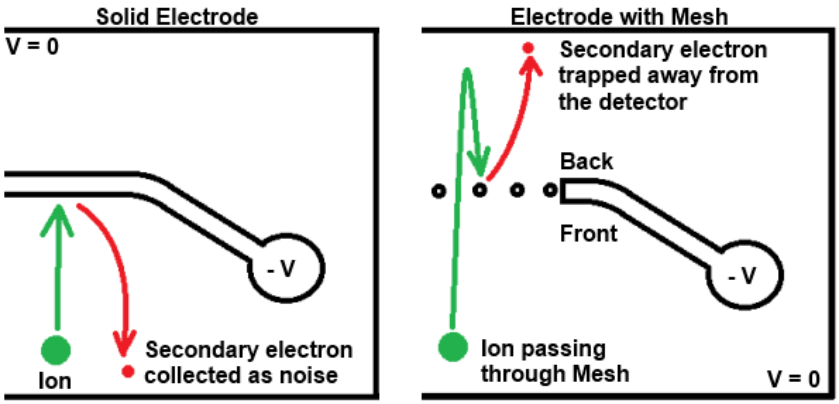

Figure 5.13 (Left) Representation of ion-induced secondary electron noise from a solid electrode. (Right) Secondary electron noise reduction with electrode mesh.

the mesh will be trapped away from the beam.

Effective SEY Estimation

A particular mesh is characterized by its open area fraction or percent f_{open}, defined as the open area divided by the total area. The density and size of the wires composing the mesh are contributing factors in defining the open fraction. The number of ions passing through the mesh is proportional to the open fraction. Likewise, the same fraction of ions will pass from the back of the mesh to the front and so on until all of the ions have been neutralized.

An effective secondary electron yield SEY_{eff} may be calculated based on the previous description. A model, given in figure 5.14, outlines the calculation in which a group of *N* ions pass through a mesh *n* times. Define N_n to be the number ions after each passage. N_{e_n} is the number of electrons produced on the detector side of the mesh by ions per traversal, and SEY_0 is the secondary electron yield of the mesh. Lateral motion of ions depicted in figure 5.14 is greatly exaggerated for illustrative purposes. Field uniformity prevents lateral ion motion except in the immediate vicinity of the wires, where the electric field terminates perpendicular to the conductor surface. The number of detector-side electrons created is the sum of electrons created per ion passage through the mesh

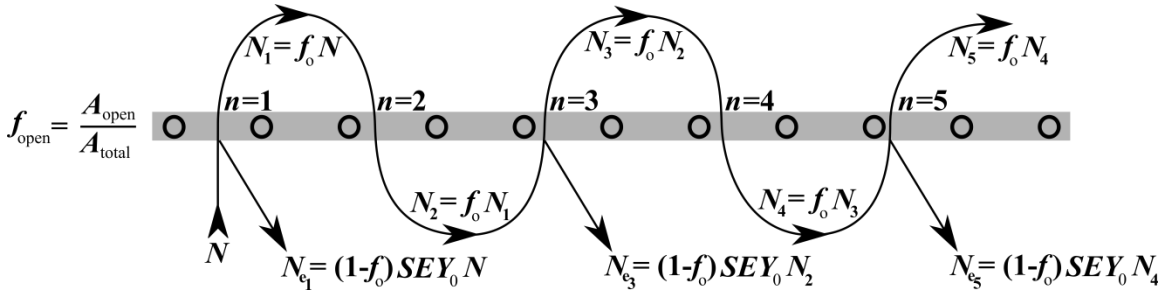

Figure 5.14 Model for effective secondary electron yield calculation.

$N_e = N_{e_1} + N_{e_3} + N_{e_5} + \cdots$. An expression for the effective secondary electron yield is then

$$SEY_{eff} = \frac{N_e}{N} = (1 - f_{open}) SEY_0 \sum_{n=0}^{\infty} f_{open}^{2n}. \quad (5.11)$$

The suppression mesh has the effect of lowering the SEY. For example, a mesh with a 50% open area results in $SEY_{eff} = 0.67 SEY_0$. Formula (5.11) shows that the higher the open fraction the lower the effective SEY. This is shown in figure 5.15, where equation (5.11) has been used to represent the SEY in the same type of profile resolution calculations as in section 3.2 with an $SEY_0 = 0.5$ and pulse gap gating has been used.

Mesh Determination

Two factors constrain the choice of suppression mesh; the electric field produced as a result of wire size and mesh opening size, and commercially available combinations of wire mesh parameters. High electric fields created by the small wire radius of the mesh are offset by the distance to the ground plane and density of the mesh. The maximum mesh field must obey the UHV field limit. Electrostatic COMSOL simulations where performed on an electrode with inset mesh, shown in figure 5.16, to determine the associated fields. Results from one such calculation are presented in figure 5.17 and show that, although the field lines terminate perpendicular to the conductor surface, they quickly become vertically uniform with a field maximum on the back side of the electrode closest to the chamber wall.

A range of commercially available meshes were simulated to find the optimal open mesh that was within the desired field limit. Based on the results of simulated meshes given in figure 5.18, a 304 woven stainless steel mesh with a wire diameter of 0.635 mm, mesh gap opening 1.91 mm, and open area percentage of 56% available from TWP Inc. [219] was chosen. This mesh satisfies the 4.5 kV/mm field limit and results in a spatial profile error of

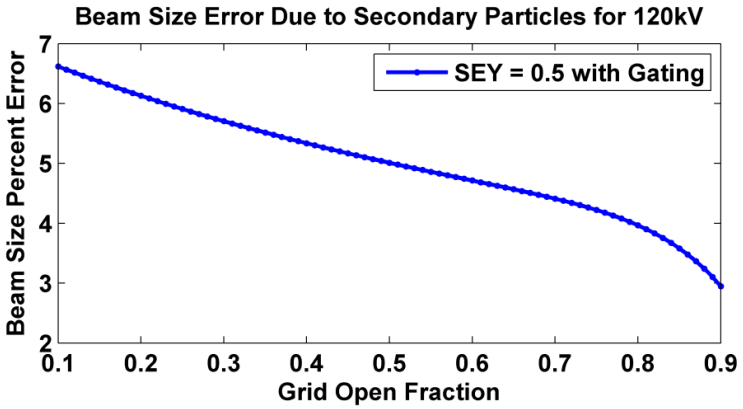

Figure 5.15 Electron profile spatial resolution as a factor of the mesh open fraction.

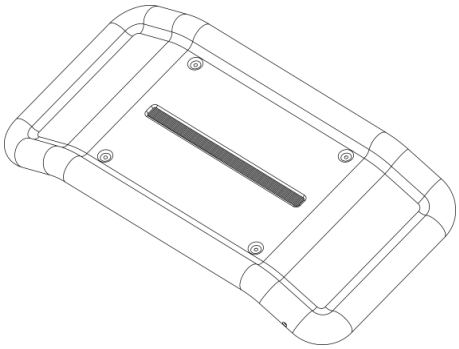

Figure 5.16 Optimized electrode with secondary electron suppression mesh.

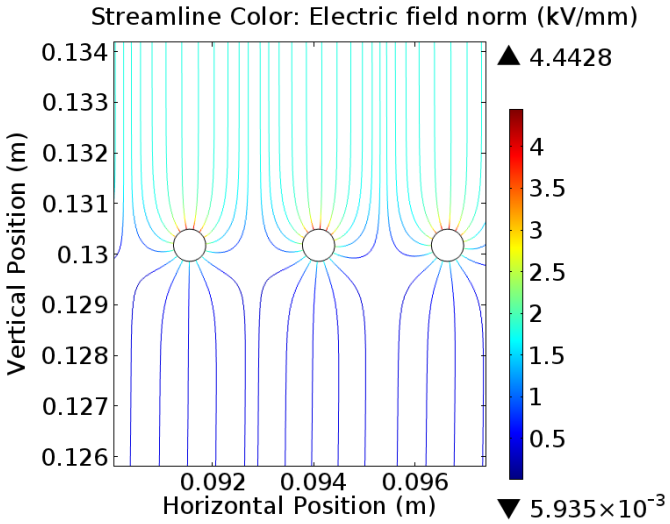

Figure 5.17 Close up of 2D FEM electrostatic calculation of mesh wires showing field lines whose color corresponds to electric field magnitude.

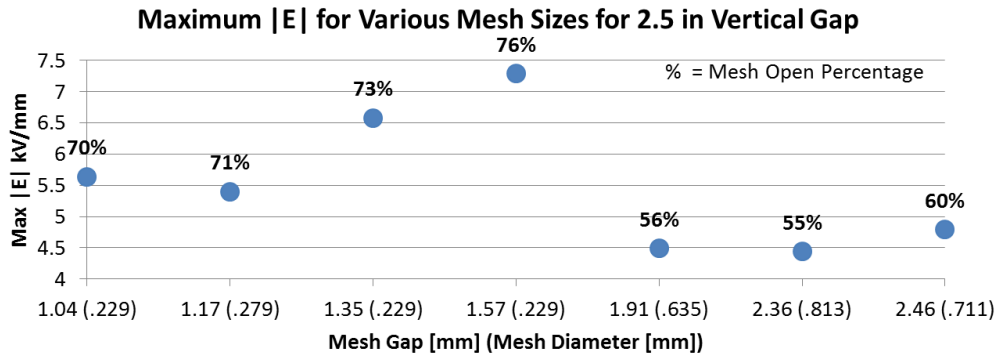

Figure 5.18 Maximum electric field simulation results for a selection of commercially available stainless steel woven meshes

4.8% from the analysis given in figure 5.15. Furthermore, simulations also showed that the mesh has a negligible effect on the particle trajectories.

5.1.6 Electrode Summary

An electrode has been designed and optimized for the SNS IPM to provide a uniform electric field for acceleration of ions or electrons with minimal trajectory error. Additionally, significant effort has been taken to analyze possible areas of vacuum breakdown and surface flashover. As a result, the electrode geometry has been modified to produce an electric field within the UHV field limit. Insulating alumina standoffs have also been chosen to hold the electrode in position with minimal arcing capacity. A method of secondary electron suppression using a mesh grid to trap secondary electrons away from the IPM detector has also been implemented with negligible influence on system operation.

Orthographic projections of the finalized electrode as well as an isometric view of the electrode and standoff s are shown in figure 5.19[13].

[13] Mechanical drawings were done by Kerry Ewald, a designer in the SNS research accelerator division.

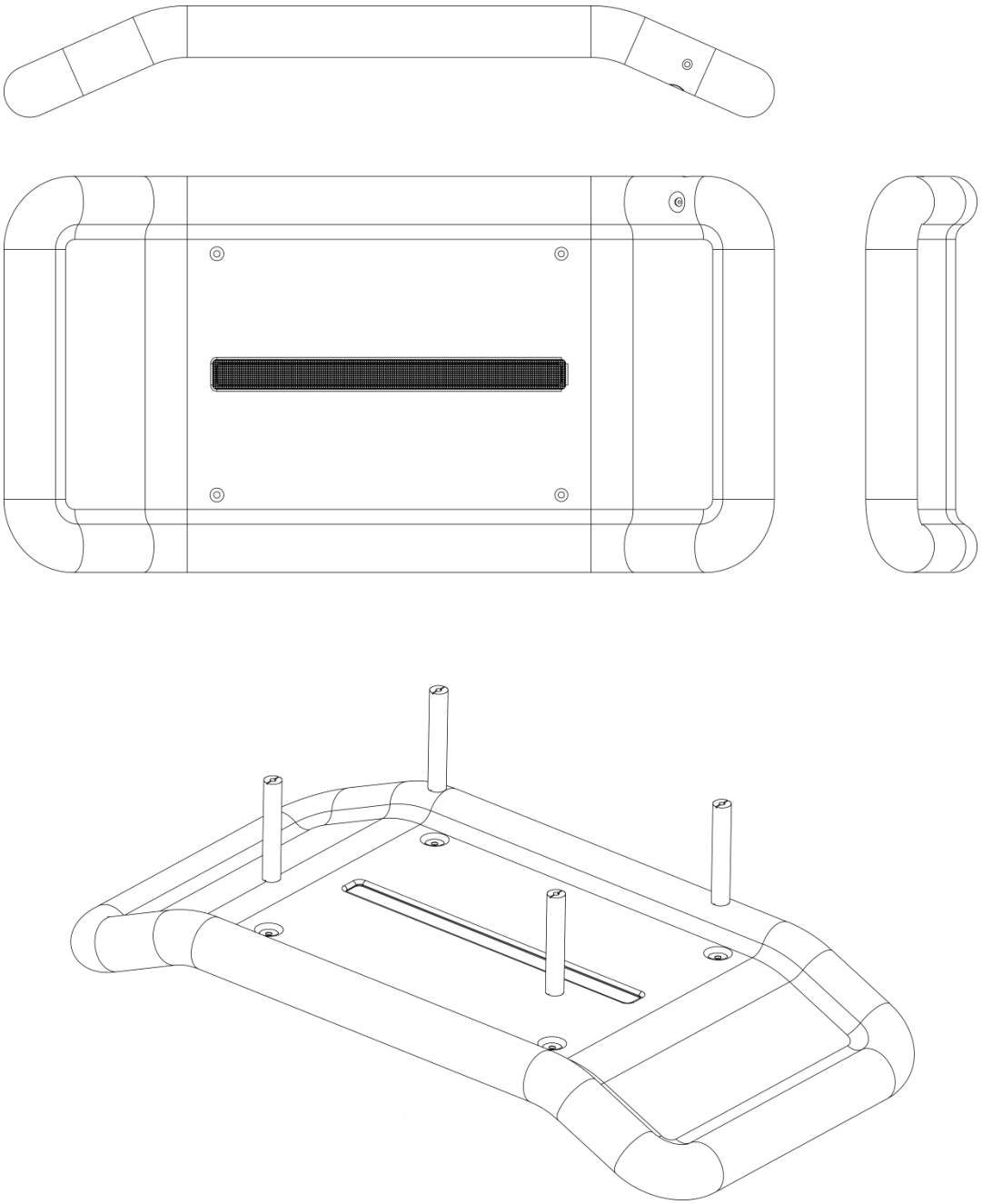

Figure 5.19 Orthographic projections of finalized electrode and isometric view of electrode and standoffs.

Electrode Beam Deflection

One of the IPM system requirements is that it has a negligible effect on the beam trajectory such that a 1 GeV proton is deflected ≤ 0.5 mrad. A deflection of this magnitude is correctable by downstream corrector magnets. The amount of deflection by the IPM electrode may be calculated for 1 GeV proton by assuming that the proton with a longitudinal momentum of 1.696 GeV/c experiences a force $qE = 1.602\text{x}10^{-19}$ C $\cdot$ 120 kV/25.4 cm = $7.57\text{x}10^{-14}$ N over a distance of 38.1 cm. At a velocity of $0.88c$, the impulse produced by the electrode imparts a 205 keV/c transverse momentum to the proton. The angle of deflection is then $\tan^{-1}$(205 keV/1.696 GeV) = 0.12 mrad which is within the deflection limit. Thus, no corrector system is required for the electrode deflection.

5.2 Magnet Design

As with the electrode, field uniformity will drive the IPM magnet design subject to the considerations of cost and size. An electromagnet will be used because the ability to adjust the field strength allows the influence of the IPM on beam dynamics to be completely removed if necessary. The magnet will be outside of the vacuum enclosure which allows for simpler operation and installation but increases the size. Also, the dipole moment must be analyzed to ascertain the need for a corrector magnet, and the higher order magnetic field multipole components must be $\leq$ 1% of the dipole moment to prevent more complex distortions of the particle orbit per the system design requirement.

5.2.1 Magnet Design Estimation

The basic magnet parameters may be estimated by using a simple C-magnet to represent an IPM magnet with gap for inserting the vacuum chamber. A diagram, given in figure 5.20,

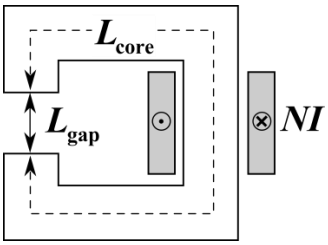

Figure 5.20 Magnet design calculation diagram.

shows a magnet with a core length L_{core}, permeability μ_{core}, gap length L_{gap} with a permeability of air μ_0, and cross section of a magnetic coil with *N* turns, each carrying a current *I*. A ferromagnetic material such as iron is assumed for the core and taken to be linear, isotropic, and homogenous such that μ_{core} is constant and $\mu_{core}/\mu_0 \gg 1$.

Stoke's theorem applied to Ampere's law allows the current in the coils to be related to the associated magnetic field *H* and flux density *B* as

$$\oint_C \vec{H} \cdot \overrightarrow{dl} = H_{core}L_{core} + H_{gap}L_{gap} = \frac{B_{core}}{\mu_{core}}L_{core} + \frac{B_{gap}}{\mu_0}L_{gap} = NI. \tag{5.12}$$

No flux leakage has been as been assumed for the core and the core-air boundary follows the magnetic boundary condition

$$\left(\vec{B}_{core} - \vec{B}_{gap}\right) \cdot \vec{n} = 0 \tag{5.13}$$

where $\vec{n}$ is a vector normal to the boundary leading to

$$\frac{B_{gap}}{\mu_0}L_{gap} = NI. \tag{5.14}$$

Assuming a 10% loss of magnetic field in the gap due to fringing effects such that $0.9B_{gap} =$ 300 G, equation (5.14) results in 13475 A $\cdot$ turns for a 50.8 cm gap. Depending on the number of coil turns chosen, the required current can be estimated, such as 13 A

for 1037 turns.

5.2.2 Design Simulation

Magnet Modeling

The IPM magnet design is based on the SNS HEBT corrector magnets [220], [221] which are window-frame magnets with racetrack style coils around the horizontal or vertical legs. These magnets produce a field of approximately 300 G using a 12 A current [222]. These magnets are air-cooled which greatly simplifies the design. Window-frame magnets are known to produce very homogenous fields without the addition of shims or complex geometries [223]. Based on the aforementioned magnet design and the dimensions of the IPM vacuum chamber dictated by the electrode design, a 3D simulation of the magnet, shown in figure 5.21, was performed to determine characteristics and realistic design parameters.

Inner dimensions of the dipole window are 76.2 cm horizontal width, 50.8 cm vertical height, and 25.4 cm longitudinal length. Simulations were performed with COMSOL using an ASTM A659 carbon steel core, which has a high magnetic permeability. Copper coils are

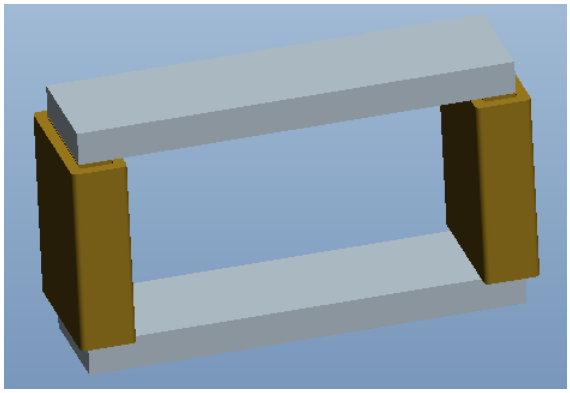

Figure 5.21 IPM dipole magnet representation.

represented by the brown regions in figure 5.21, where the number of windings and current was varied to achieve the desired field over the Channeltron region.

Longitudinal Field Results

Due to the short longitudinal pole length compared to the magnet aperture, much of the magnetic field is lost to edge fringing effects. A simulation, shown in figure 5.22, of the magnetic flux density outside the core of the IPM dipole magnet in a plane parallel to the longitudinal axis reveals the fringing effect of the magnet. As such, an increased number of turns was required to produce the 300 G central field. The final magnet design is comprised of two coils consisting 1008 turns of 8 AWG gauge coated copper wire with a 0.254 mm Kapton electrically insulating barrier between the coils and the steel core. A 13 A current allows the magnet to produce the required field while still allowing it to be air cooled.

Core Saturation

The thickness of the core was determined in order to prevent magnetic saturation of the steel. Steel has a magnetic saturation between 1.6-2.2 T [224]. With a thickness of 7.62 cm, the magnetic flux density in the bulk of the core is ~1 T, as seen in figure 5.23. The present design is well within the magnetic saturation limit coincident with production of the required central field.

5.2.3 Magnetic Field Evaluation

Transverse Field Error

It is important to evaluate the transverse field magnitude and uniformity. Transverse magnetic flux arrows with size and color determined by field magnitude are given in figure 5.24 along with black arrows showing the direction of the current in the coils. A more quantitative view the field uniformity is seen in figure 5.25, which shows that the magnitude

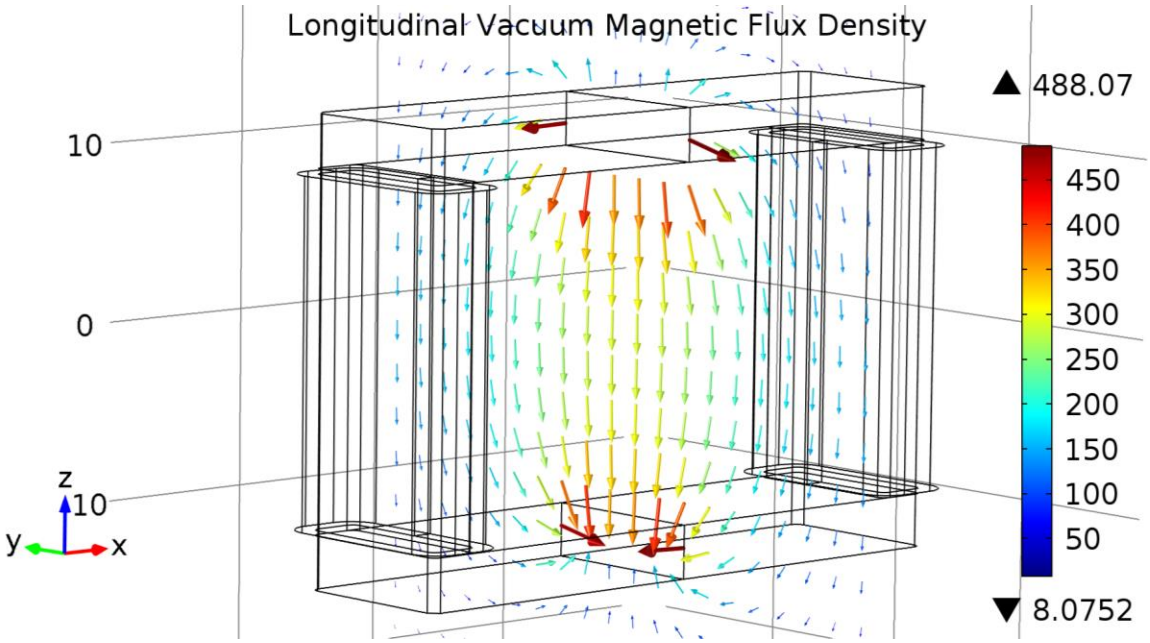

Figure 5.22 IPM dipole longitudinal magnetic flux density simulation with arrows showing field direction and arrow size and color representing field magnitude.

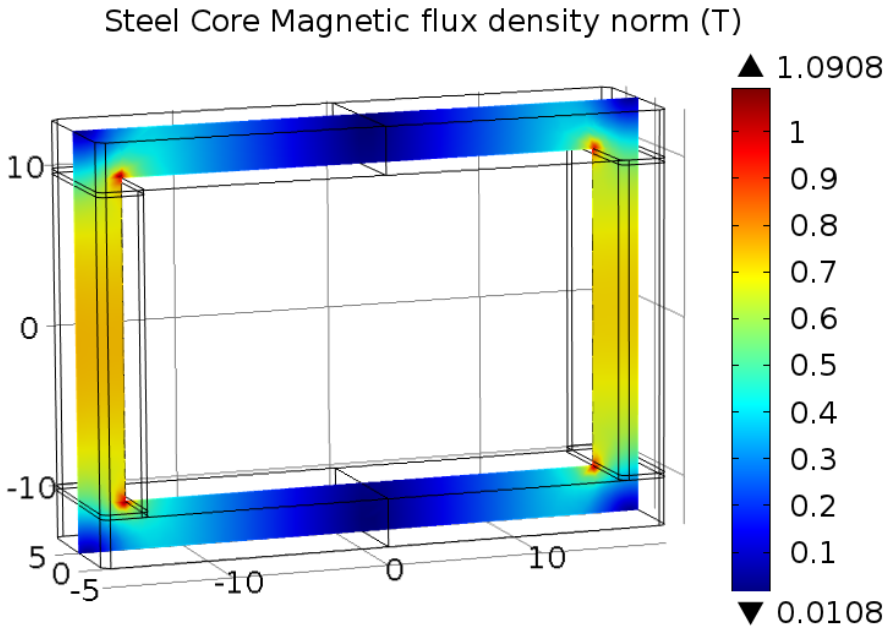

Figure 5.23 Transverse slice of the magnetic core showing flux density magnitude.

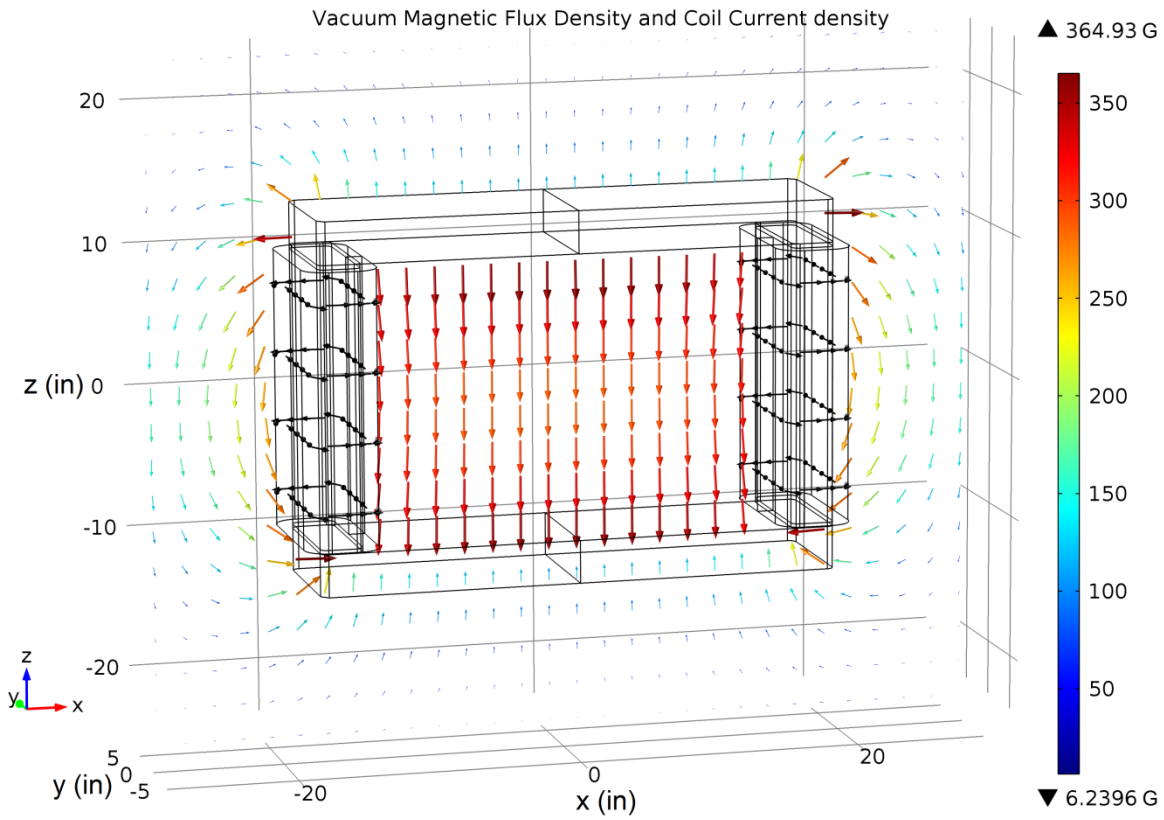

Figure 5.24 IPM dipole transverse magnetic flux density simulation. Arrows show the field direction and magnitude as well as the current direction in the coils.

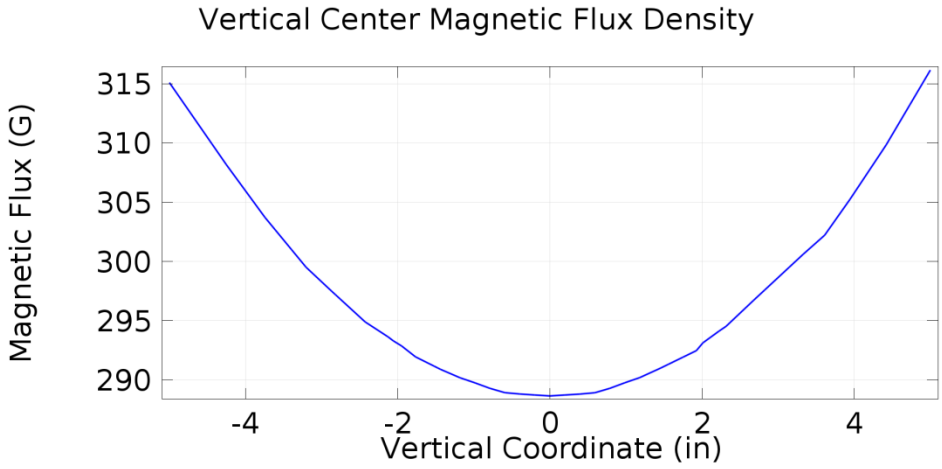

Figure 5.25 IPM magnetic flux along a vertical line in the horizontal center of the magnet.

of the magnetic field along a vertical line in the horizontal center of the magnet measured over a distance from the top of the beam pipe to the bottom has an average field value of 296 G. This is the average magnitude a particle will experience during its traversal from creation to detection. The horizontal field magnitude varies by 0.7% over the width of beam pipe.

A more conclusive evaluation of the magnets is provided by determining the effect of the simulated magnet on particle trajectories. A 100 eV electron, representing the upper limit of particle initial velocities, starting at the edge of the beam at the vertical center of the magnet was tracked in a uniform 394 kV/m electric field coupled with the simulated magnet field. The trajectories from the simulated field are compared to trajectories from the same particle in a perfectly uniform vertical magnetic field to show the effect of field errors. Results in figure 5.26 show the difference between the particle horizontal position and initial position throughout its trajectory for simulated and uniform magnetic fields. Less than a 0.2% increase in the Larmor radius is produced by the actual magnetic field and is considered to have a negligible effect on profile generation.

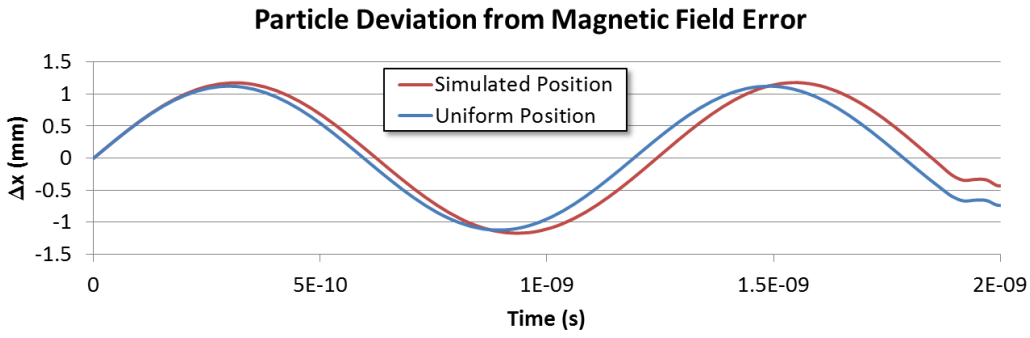

Figure 5.26 Horizontal particle deviation due to magnetic field errors for simulated and uniform magnetic fields

Magnet Multipole Analysis

The previous analysis has shown that the magnet will provide the field required to generate accurate profiles, but the effect of the magnet field on the beam motion is also critical. If the magnet were to introduce a large distortion in the proton trajectories, the downstream magnets would not be able to compensate, causing beam loss. There are two aspects of the IPM magnet that require compensation. The real magnetic field may be decomposed into a combination of "pure" multipole fields, which will be derived shortly, with the dipole field producing a uniform kick to all particles. Dipole field compensation will be addressed in a subsequent section. Higher order multipole fields produce more complex particle motion and are more easily corrected due to their small relative amplitude.

Consider a 2D magnetic field $\vec{B}(x,y) = B_x(x,y)\hat{x} + B_y(x,y)\hat{y}$. Maxwell's equations in a current free, static region give $\vec{\nabla} \cdot \vec{B} = 0$, leading to

$$\frac{\partial B_x}{\partial x} = -\frac{\partial B_y}{\partial y} \tag{5.15}$$

and $\vec{\nabla} \times \vec{B} = 0$, so that

$$\frac{\partial B_x}{\partial y} = \frac{\partial B_y}{\partial x}. \tag{5.16}$$

Equations (5.15) and (5.16) are known as the Cauchy-Reimann equations and form a set of conditions that guarantee that the two real-valued functions $B_x(x,y)$ and $B_y(x,y)$, defined on the real plane $\mathbb{R}^2$, may be represented together as an analytic function of one variable $z = x + iy$ on the complex plane $\mathbb{C}$ that is holomorphic or complex-analytic [189]. The complex function is

$$\vec{B}(x,y) \rightarrow B(z) = B_y + iB_x. \tag{5.17}$$

Because $B(z)$ is analytic it may be expanded in a power series [154]. Consequently, equation (5.17) may be expanded about the origin as

$$B_y + iB_x = \sum_{n=1}^{\infty} C_n(x+iy)^{n-1} \tag{5.18}$$

where the complex expansion coefficients are $C_n = B_n + iA_n$. The power series converges within a circle $|z| < r$ where, for a magnetic field, *r* is the largest radius inscribed in the magnet poles creating the field.

The right-hand side of equation (5.18) is a sum of individual multipole fields with each *n* representing a "pure" field. For the first few components, the multipoles have names, such as *n* = 1 dipole, *n* = 2 quadrupole, *n* = 3 sextupole, *n* = 4 octopole, and so forth. A magnet designed to create a particular multipole has 2*n* pole tips. In order to simplify the multipole component units, a reference radius R_{ref} is often employed [225] and along with a conversion to cylindrical coordinate, equation (5.18) becomes

$$B_\theta + iB_r = \sum_{n=1}^{\infty} C_n \left(\frac{r}{R_{ref}}\right)^{n-1} e^{in\theta} \tag{5.19}$$

where $r = \sqrt{x^2 + y^2}$ and $\tan\theta = y/x$.

By representing the complex expansion coefficients in the phasor form as $C_n = |C_n|e^{i\phi_n} = B_n + iA_n$, it can be seen that the phase ϕ_n simply determines the field orientation. As such, the pure multipole is defined as "normal" if $\phi_n = 0$ and "skew" if $\phi_n = \pi/2$. B_n corresponds to the normal multipole components and A_n the skew components. A normal dipole field, for example, is a purely vertical field while a skew dipole

is horizontal. As a matter of convention, multipole components are often normalized to 10^{-4} of magnitude of the main field component

$$c_n = \frac{C_n}{|C_{main}|} 10^4, \tag{5.20}$$

i.e. $C_{main} = C_1$ for a dipole magnet [226] with c_n expressed in "units".

It has been shown [225] that if *M* measurements of the radial and azimuthal components of a magnetic field are taken on a circle of radius r_0 at $\theta_m = 2\pi m/M$ for $m = 0, 1, 2, \ldots, M-1$ then the coefficients C_n may be found using the discrete Fourier transform

$$C_n = \frac{1}{M\left(r_0/R_{ref}\right)^{n-1}} \sum_{m=0}^{M-1} B_m e^{-in\theta_m}. \tag{5.21}$$

Here, $B_m = B_\theta + iB_r$ in equation (5.21) for the field components measured at each point θ_m. Furthermore, the previous analysis considered a two-dimensional field while the actual transverse field components also vary in the longitudinal direction z. This may be accounted for by solving for the integrated field components over the longitudinal pole distance *L*

$$\frac{1}{L}\int_L (B_\theta + iB_r)dz = \sum_{n=1}^{\infty} (B_n' + iA_n') \left(\frac{r}{R_{ref}}\right)^{n-1} e^{in\theta} \tag{5.22}$$

where B_n' and A_n' are the normal and skew integrated field components [227].

IPM Multipole Results

IPM magnet multipoles are calculated by finding the azimuthal and radial field components on the surface of a cylinder whose axis is coincident longitudinal dipole axis. The cylinder has a radius, also used as the reference radius, which is the maximum acceptance of the SNS ring $r_0 = R_{ref} = 12.78$ cm. Integrating the field components of the 25.4 cm longitudinal

cylinder length produces field components which are then used with equation (5.21) to produce integrated multipole components. An IPM magnet requirement that higher order multipole components must be <1% of the main field component comes from the SNS requirement for ring corrector magnets [4] and corresponds to 100 units by expression (5.20). Calculated higher order integrated multipole components from a simulated IPM dipole[14] are given in figure 5.27 and show that the normal integrated components are well below 100 units. Skew components are negligible for the horizontal profile magnet and are not reported in figure 5.27.

Magnetic Beam Deflection

The final property of the magnet to consider is the kick induced by the dipole multipole component. A dipole kick is measured by the angle in radians between the exiting particle trajectory and the unperturbed trajectory. For a proton with 1 GeV kinetic energy

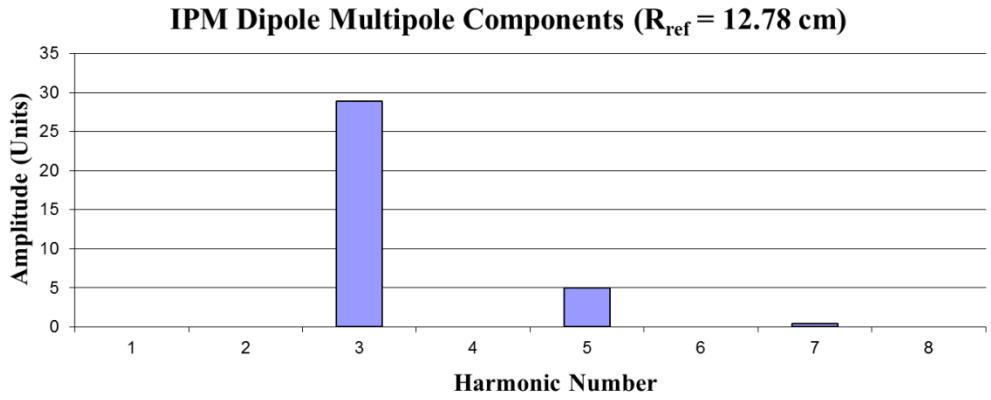

Figure 5.27 IPM dipole higher order integrated multipole components for a reference radius of 12.48 cm. [228]

[14] Due to computational resources, final IPM magnet multipole calculations were performed by SNS magnet designer Dr. J.G. Wang.

with momentum p and charge q, the Lorentz force describes the radial acceleration experienced by the proton traveling in the longitudinal z direction through a vertical magnetic field B_y for a length L. A transverse horizontal momentum is imparted to the proton such that the kick angle may be found by

$$\theta \cong \frac{\Delta p_x}{p} = \frac{q}{p}\int_0^L B_y(z)\,dz \tag{5.23}$$

where the small angle approximation has been used.

The integrated dipole strength along a longitudinal 25.4 cm line passing through the magnet center is 0.00709 T·m, as calculated from the magnet simulation. With a proton momentum of p = 1.684 GeV/c, expression (5.23) yields θ = 1.3 mrad, which is more than a factor of two times the 0.5 mrad limit. Compensating magnets will be required for both the vertical and horizontal IPM systems. Details of the corrector magnets are not discussed here but combined vertical-horizontal correctors are commonly used in SNS, as described in [229], and will be employed downstream of the IPM area.

5.2.4 Magnet Summary

A magnet for the IPM has been designed to provide a uniform magnetic field across the detection region for the production of accurate electron-based profiles. The final magnet design has a uniform transverse field that varies less than 1% across the beam pipe while using a low enough coil current as to not require water cooling. Furthermore, higher order integrated magnetic multipole components are well within the limits required for closed orbit transparency. Due to the integrated magnet strength, corrector magnets will be required for the horizontal and vertical IPM systems. The finalized magnet design is shown in figure 5.28.

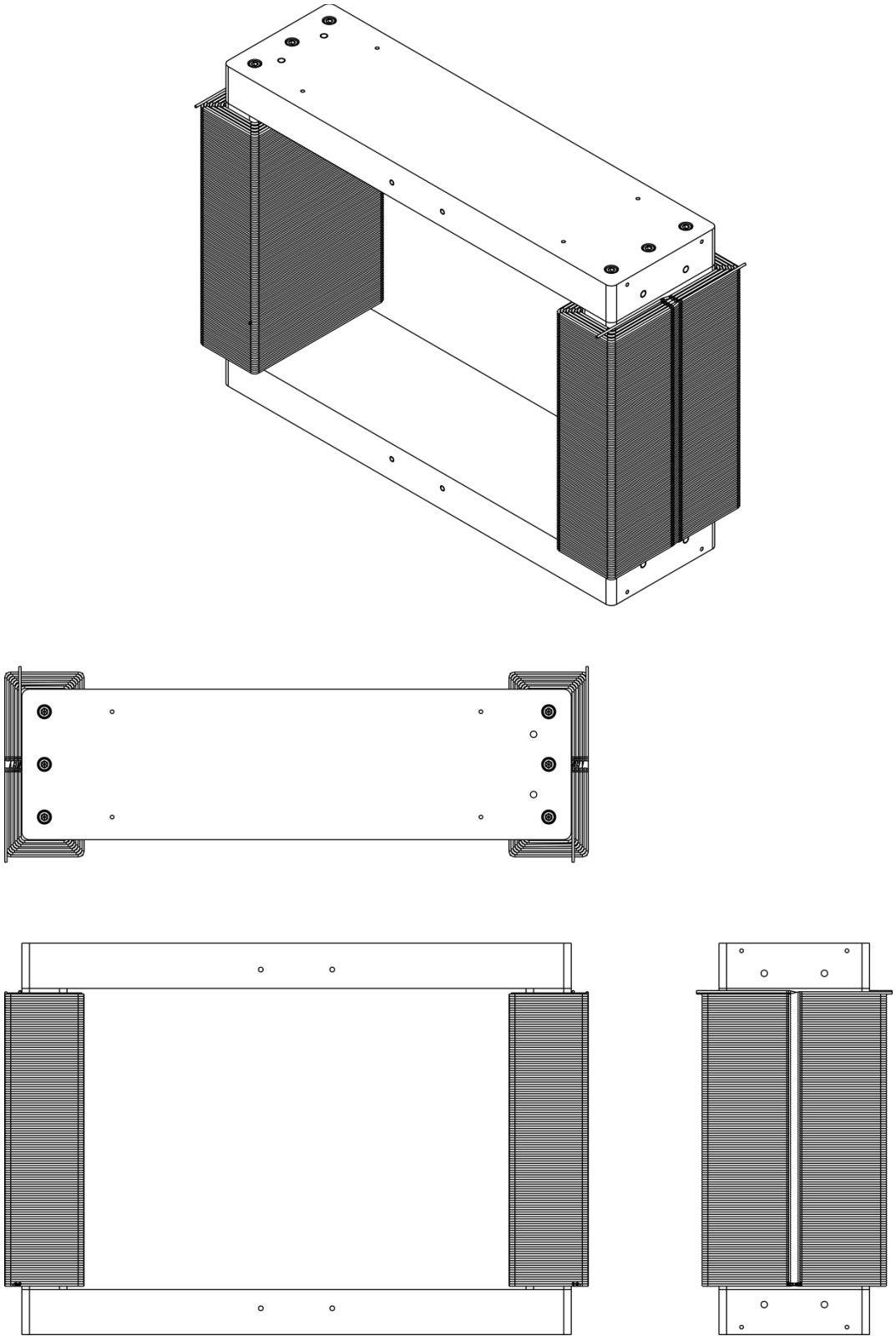

Figure 5.28 Orthographic, top, front, and side views of the finalized IPM magnet.

5.3 Detector Assembly

The detector assembly is comprised of a mechanism that drives the detector across the beam dimension to be measured as well as the housing that secures the Channeltron. This area of the design incorporates many isolation elements necessary to mitigate image current coupling. Furthermore, detector cabling inside the vacuum chamber, a possible source of beam induced noise, and efforts to shield and isolate the IPM signal from the accelerating environment will be discussed.

5.3.1 Channeltron Housing

As was found in the IPM test chamber, a significant amount of AC coupled beam signal is introduced into the measurement, and shielding is required to obtain a useful profile. An effort was made to ensure the Channeltron housing, or the portion of the detector assembly to which the detector is attached, was shielded as much as possible.

Channeltron Support

The Channeltron is held by a stainless steel support arm, the end of which is displayed in the left image of figure 5.29. Two detectors are mounted on the arm to allow for background subtraction and to act as spares in the event of a detector failure. Macor insulators are used to electrically isolate the Ctrons from the metal support. The support arm is attached at right angles to the actuator drive assembly, which is shown in the right of figure 5.29. A swivel mechanism has been incorporated into the support arm connection to the drive shaft that allows for a 90° rotation, making the entire assembly a linear unit for easy installation and removal.

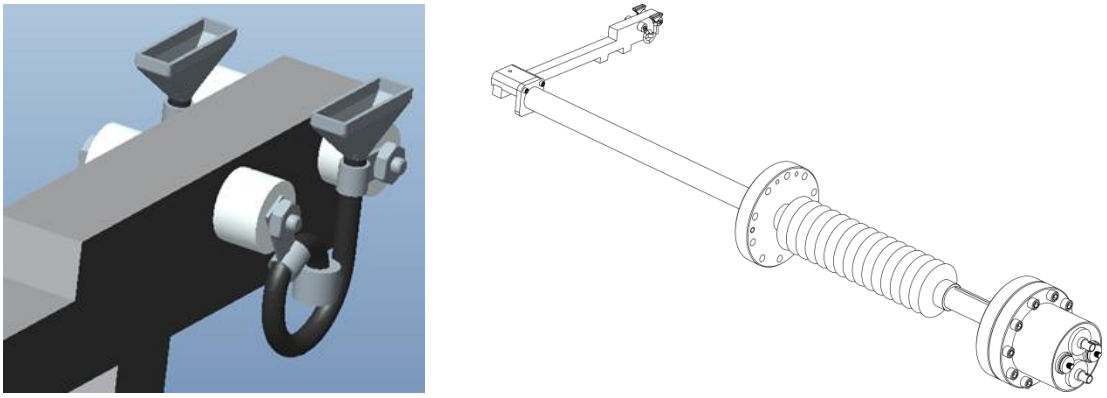

Figure 5.29 (Left) Close up of the end of the support arm holding the Channeltron detectors. (Right) Full Channeltron arm assembly with bellows.

Detector Shielding

To protect the immediate area of the detectors, a grounded metal shield encloses the Channeltrons and can be seen in figure 5.30. The 5-sided Ctron shielding box travels underneath a solid metal plate forming an inner floor within the IPM vacuum chamber. Depicted in figure 5.31, the vacuum chamber inner floor plate serves to shield the Ctron assembly as well as to provide a flat boundary for electric field uniformity. Collected particles pass through a rectangular slot in the inner floor and enter the detectors, whose openings travel coincidentally with the floor slot.

5.3.2 Detector Cabling and Feedthroughs

Cabling used in the vacuum chamber requires special considerations due to the ultrahigh vacuum. Each of the two Channeltrons requires a high voltage bias cable and a signal cable. Cables used in the IPM vacuum chamber will be 26 AWG, 50 Ω coaxial cable rated to $1x10^{-10}$ Torr with Accu-Fast™ floating connectors on the feedthrough end available off-the-shelf from Accu-Glass® [230]. Accu-Glass® also carries ultrahigh vacuum isolated feedthroughs which allow the ground conductor to be insulated from the surrounding

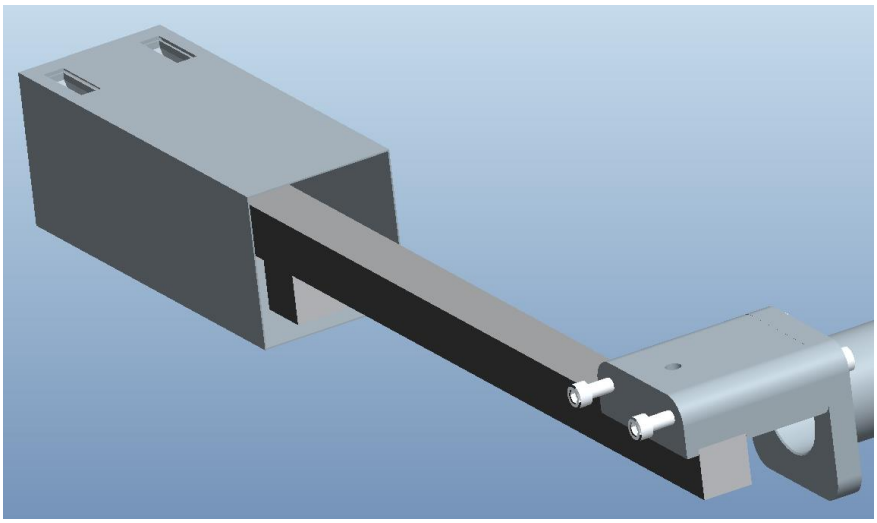

Figure 5.30 Channeltron assembly with 5-sided shielding block.

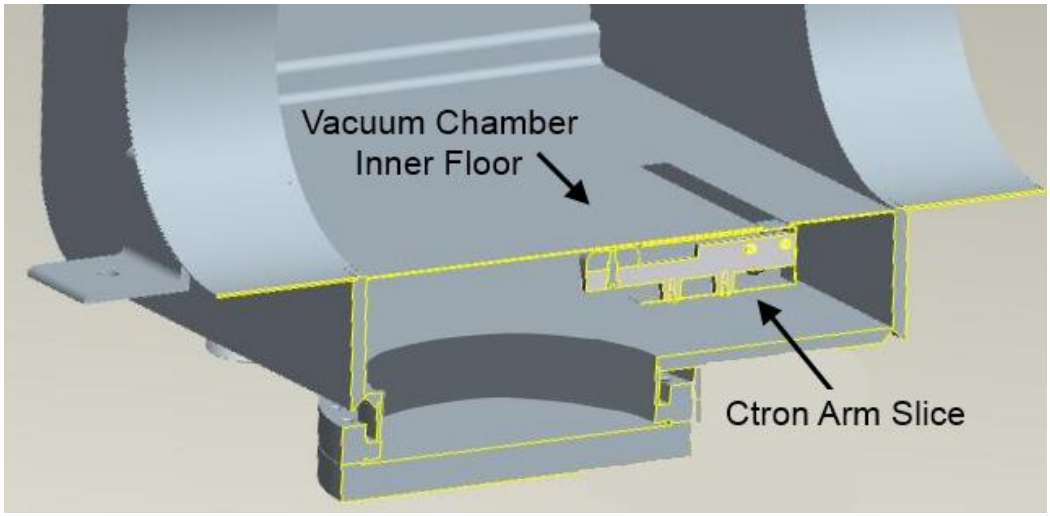

Figure 5.31 Cutaway of IPM vacuum chamber showing the inner floor plate.

structure. A 700 V DC feedthrough with an SMA connector on the air-side and a 5 KV DC, 5 Amp high voltage feedthrough with BNC air-side connector are set into a flange, illustrated in figure 5.32, for vacuum-to-air signal and bias voltage transfer. Signal cables on the air side the IPM to the Ring Service building will also be shielded from cables run away from the RF cavities.

5.3.3 Actuator

The final detector assembly component is the actuator used to drive the Channeltrons across the beam. By using an actuator similar to wirescanner actuators used elsewhere in the accelerator [231], the same drive electronics may be used for the IPM with slight modifications.The IPM actuator is a Parker® 404XE series linear actuator [232] which has been modified for radiation environments . With a positional accuracy of 90 µm and a bidirectional repeatability of ±20 µm, a maximum estimated position accuracy of 90 µm + 20 µm = 0.11 mm is obtained, which satisfies the condition for the profile error given in

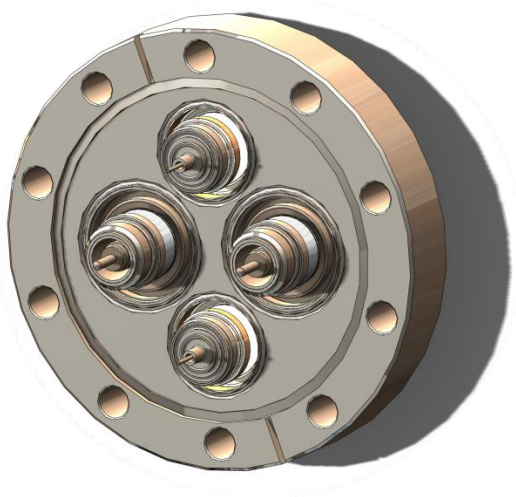

Figure 5.32 Vacuum side illustration of the vacuum feedthrough flange containing two sets of isolated signal and high voltage feedthroughs for Channeltron operation.

section 3.2.2 .

Measurement speed is a factor of actuator limitations, driver software, motor controllers, and vacuum load. Based on similar SNS systems a realistic speed of 5 mm/s will be assumed [233]. If it is assumed that 200 accumulation measurements are required at 30 measurement positions spaced 5 mm apart at a production rate of 60 Hz , the resulting approximate profile measurement time is $30\ measurements(200\ accumulations \cdot 1/60\ \text{Hz} + 1\ \text{s})$ = 2.2 minutes. The assumed measurement spacing will be justified later. While the final system measurement may differ, it should not exceed 5 minutes in the most extreme case.

5.4 Vacuum Chamber

5.4.1 Alignment and Installation

Included in the vacuum chamber support stand are alignment mechanisms that allow for vertical and horizontal alignment with the beam center. Furthermore, a positioning system has been designed into the magnet and chamber to permit alignment of the magnetic field. Other installation aspects have been considered such as a removable front face of the vacuum chamber that allows interior access for electrode installation. Also, a 7.62x17.48 cm port was added to the bottom of the chamber, underneath the detector slot, to grant easy access to the Channeltrons in the event that detector repair or replacement is needed. This also allows simplified removal of the entire detector assembly if needed. Finally, a 3.81 cm diameter port has been included that can be used for in-situ vacuum pressure measurements or residual gas analysis.

5.4.2 Wakefield Slats

Wakefield Production

A relativistic charged particle has longitudinal field components that are Lorentz contracted to form a disc perpendicular to the particle velocity, as derived in Appendix C. In a perfectly conducting accelerating pipe the particle's electromagnetic fields terminate on image charges which move synchronously with the moving particle. However, in reality, the finite conductivity of the accelerating structure causes the image charge to lag behind the beam particle, resulting in trailing electromagnetic fields known as wakefields [234].

Wakefields affect trailing beam particles and can lead to instabilities [235],[105]. Obstacles can also produce wakefields as beam energy is trapped in or behind accelerating structure aperture changes or cavities. This is illustrated in figure 5.33 which shows electric field lines for a Gaussian beam passing through an aperture in the left image and passing by a cavity in the right image. Wakefields can be seen forming in both cases. Efforts to reduce accelerating geometries that contribute to wakfield production were incorporated into the IPM vacuum chamber.

Detector Slot Image Current Modification

A discontinuity is introduced directly across the beam path by the detector slot in the IPM vacuum chamber inner floor plate. As such, a continuous path for beam image current was added across the slot in the form slats. The detector slot, depicted in figure 5.34, is formed with a row of 3.99 mm wide cutouts separated by 0.762 mm slats, parallel to the beam direction and crossing the detector opening. The effect on the profile is to reduce the number of measurement points by requiring nonadjacent Channeltron position. However, by the analysis of section 3.2.2, this reduces the number of $bins/\sigma_{beam}$ to 3.16 which, by

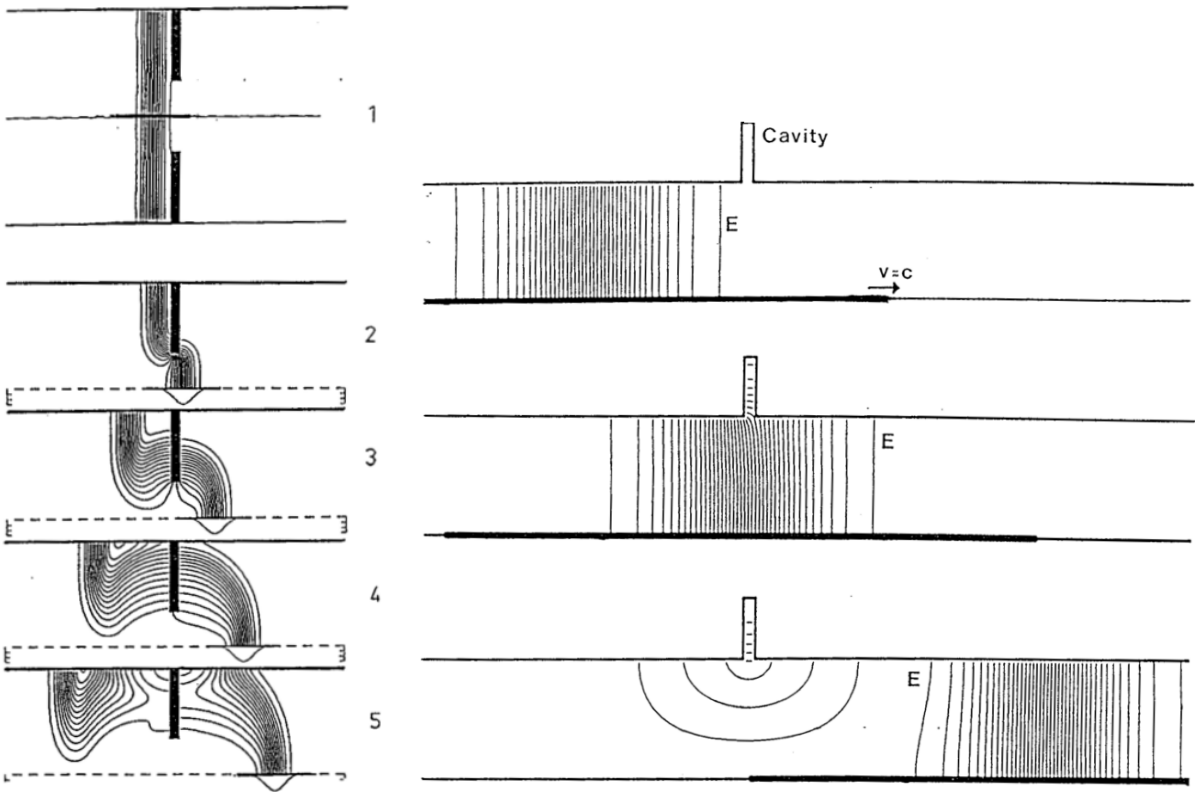

Figure 5.33 Successive steps showing wakefield production upon passage of a Gaussian beam (Left) through an aperture and (Right) by a cavity[15] [234]**.**

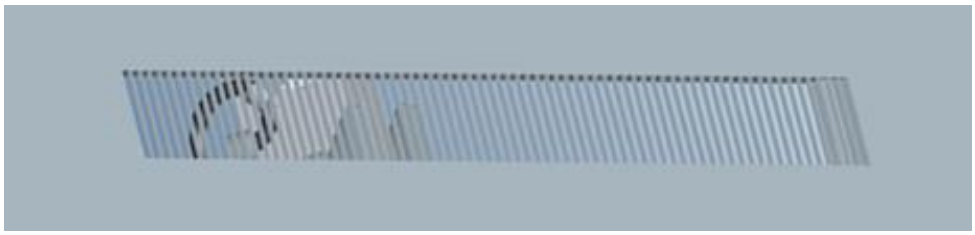

Figure 5.34 Vacuum chamber detector slot with image current path slats.

[15] Used with permission of Springer Publishing.

figure 3.17, has a negligible effect on profile error. Another benefit of the wakfield slats is to provide an additional measure of detector shielding from beam fields.

5.4.3 Detector-Beam Coupling Mitigation

Gap Field Attenuation

An additional method of beam coupling mitigation may be illustrated with the derivation of a 2D grounded well. Diagrammed in figure 5.35, an infinitely deep grounded well of width *w* is shown. The bottom side at *y* = 0 is electrically insulated from the walls and is held at a constant potential V_0, while the potential approaches to zero as *y* goes to infinity. The electric potential $V(x, y)$ inside the charge-free well is determined by Laplace's equation $\nabla^2 V = 0$. Laplace's equation, subject to the boundary conditions specified in figure 5.35, yields a solution of the form

$$V(x,y) = \sum_{n=1}^{\infty} D_n e^{-\frac{n\pi}{w}y} \sin\left(\frac{n\pi}{w}x\right) \tag{5.24}$$

where D_n are constant coefficients determined by the *y* = 0 grounded well boundary condition.

Multiplication of both sides of (5.24) by $\sin m\pi x/w$ and integration over the *x*

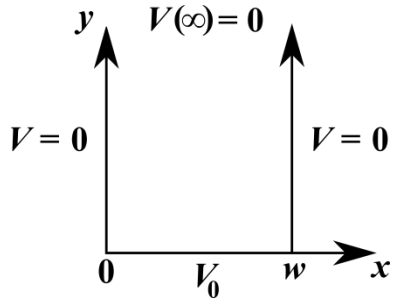

Figure 5.35 Diagram of grounded well boundary conditions.

dimension yields

$$\sum_{n=1}^{\infty} D_n \int_0^w \sin\left(\frac{n\pi}{w}x\right)\sin\left(\frac{m\pi}{w}x\right)dx = \int_0^w V_0 \sin\left(\frac{m\pi}{w}x\right)dx. \tag{5.25}$$

With two integrations by parts of the left side of expression (5.25), it can be shown that

$$\int_0^w \sin\left(\frac{n\pi}{w}x\right)\sin\left(\frac{m\pi}{w}x\right)dx = \begin{cases} w/2\,, & m = n \\ 0, & m \neq n \end{cases} \tag{5.26}$$

Therefore, since the right-hand side of equation (5.25) is only nonzero for *n* = *odd*,

$$D_n = \frac{4V_0}{n\pi} \qquad n = 1, 3, 5 \ldots \tag{5.27}$$

This allows the potential to be expressed as

$$V(x,y) = \frac{4V_0}{\pi}\sum_{n=odd}\frac{1}{n}e^{-\frac{n\pi}{w}y}\sin\left(\frac{n\pi}{w}x\right). \tag{5.28}$$

It can be seen from equation (5.28) that electric potential decays exponentially along the depth of the gap *y*. At a given gap depth *d*, an electric field present at the entrance of the gap will be attenuated at the gap exit. Furthermore, the degree of attenuation is determined by the depth *d* and width *w*, as can be seen from the ratio of the electric fields, found using $E = -\nabla V$, at the center of well

$$\frac{E\left(\frac{w}{2}, d\right)}{E\left(\frac{w}{2}, 0\right)} = \operatorname{sech}\pi\frac{d}{w}. \tag{5.29}$$

The attenuation is maximized for deeper and narrower wells.

EMI Honeycomb

The previous analysis reveals that a series of small grounded openings above the Channeltron will allow passage of passage of particles but attenuate electric fields entering the gap and thus prevent beam fields from terminating on the detector. COMSOL was used to simulate

this phenomenon for a 2D grounded opening in the floor of the IPM vacuum chamber shown in figure 5.36. It shows electric field lines entering the gap and terminating on the gap walls in accordance with the electric boundary condition, thus illustrating field attenuation in the gap.

Metallic honeycombs used to reduce electromagnetic interference, or EMI, displayed in figure 5.37 (left), are commercially available in a variety of sizes. By placing one just above the detector, as shown in figure 5.37 (Right), further beam isolation is achieved. Figure 5.38 shows results from simulations on a range of available gap width-depth combinations conducted to find the honeycomb parameters that optimize attenuation while minimizing the influence on the overall design, i.e. shorter gap depth. Due to availability, a gap opening of 3.175 mm was chosen and was found to have an attenuation of 89 dB with a depth of 3.2 mm. These honeycomb parameters reduce the electric field by four orders of magnitude and can be found in off-the-shelf laser welded panels [236]. These do not use adhesives to bond the mesh together, which is a high vacuum requirement.

5.5 High Voltage Feedthrough

In order to bring the electrode to the necessary potential for particle collection, a high voltage vacuum feedthrough (HVF) is required. Two aspects of the feedthrough necessitate consideration; both the air-side and the vacuum-side of feedthrough and the electrode connection must be analyzed for arcing hazards.

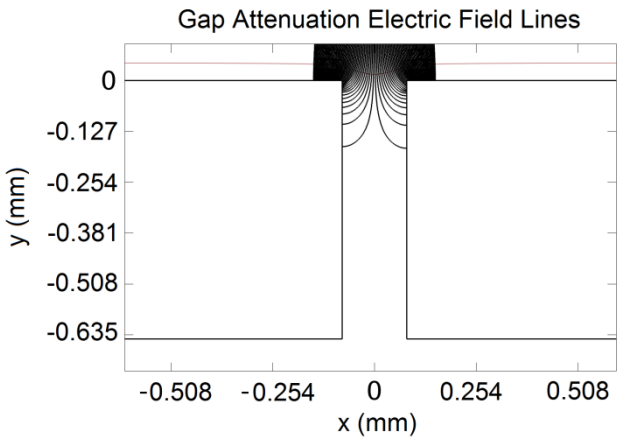

Figure 5.36 Electric field lines entering a grounded well showing attenuation.

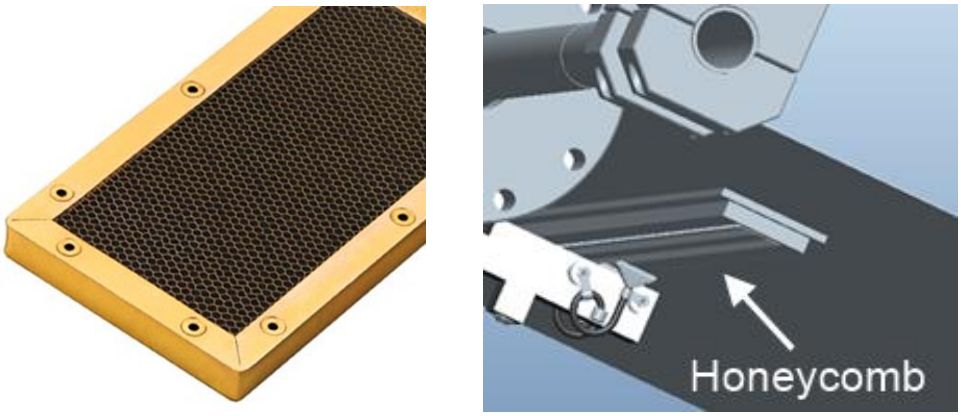

Figure 5.37 (Left) EMI honeycomb. [237] **(Right) Location of honeycomb above detectors.**

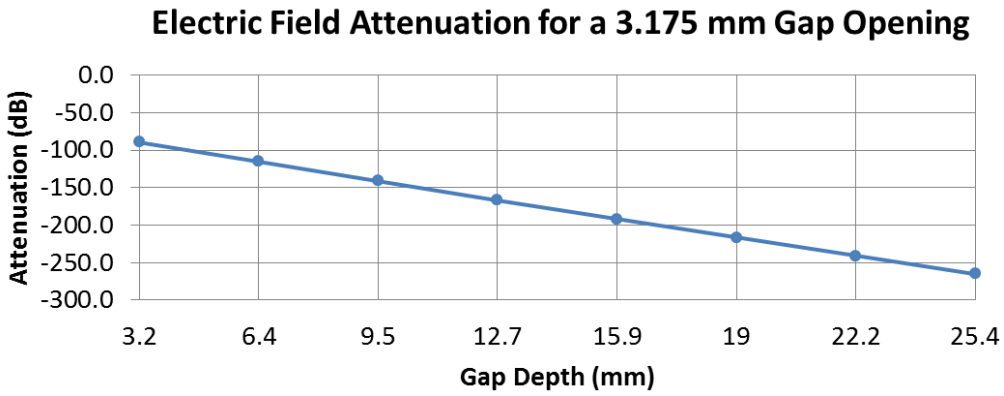

Figure 5.38 Simulated field attenuation for EMI honeycombs with 3.175 mm openings and varying depths.

5.5.1 HVF Air Side

Feedthrough and Air-Side Arcing Hazard

A 125kV high voltage feedthrough with 304 stainless steel housing, conductor and alumina ceramic insulator is affixed to the upper portion of the vacuum chamber in line with the electrode. Proximity to the surrounding accelerating structure introduces an arcing hazard. While the dielectric strength of atmospheric pressure air is 3 MV/m [238], the rule-of-thumb to prevent arcing in air is 2.54 cm of distance to ground per 10 kV. For a 120 kV potential, this would require a ~30 cm radius of clearance around the HVF. This is not realistically feasible.

Arcing Mitigation

The air-side HVF arcing solution comes in the form of a high dielectric strength potting material. Potting is accomplished by surrounding the HVF in a grounded metal enclosure, as illustrated in figure 5.39, then filling the enclosure with an epoxy resin. Araldite CW1312/HY1300 [239], for example, has a dielectric strength of 12 kV/mm. A minimum distance inside the HVF enclosure of 5.56 cm results in an electric field of 2.16 kV/mm, which is well below the epoxy breakdown limit. The enclosure, HVF, and short high voltage cable attaching to the HVF are potted together as a single unit which is then mounted to the vacuum chamber.

This modular design allows for simplified replacement or repair. Upon exiting the HVF enclosure the high voltage cable connects to a 125 kV rated, 15 kΩ, potted resistor box located in the tunnel close to the IPM location. This box receives the high voltage cable from the electrode power supply located in the RSB. As an additional measure of field reduction, figure 5.40 shows a cap designed to fit over the HVF connector threads to receive the high

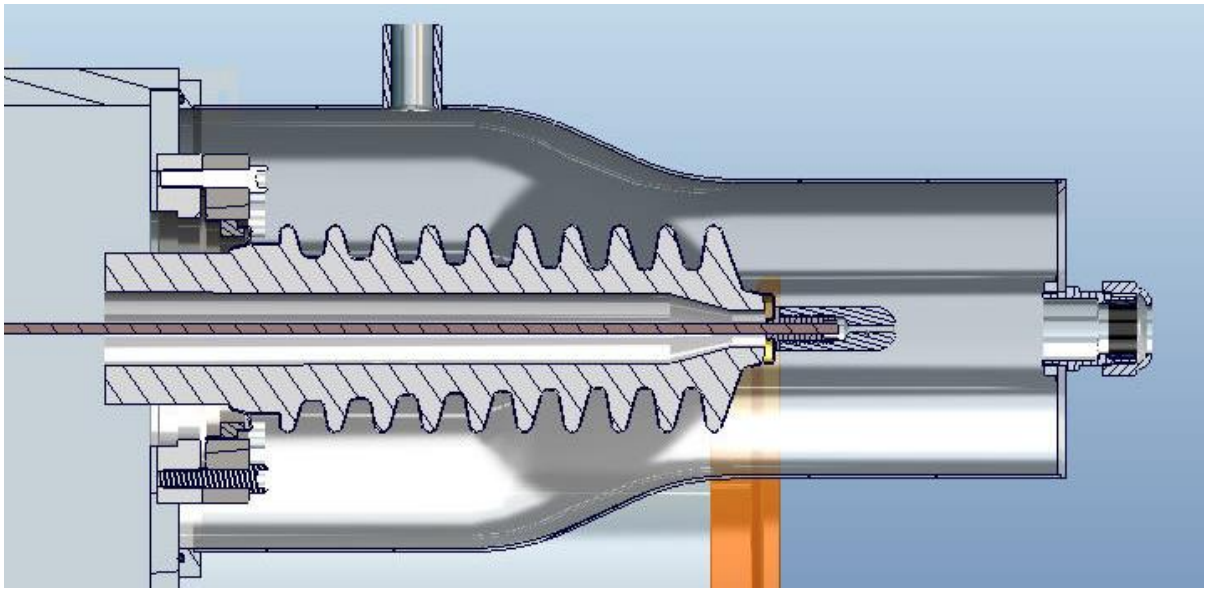

Figure 5.39 Cutaway view of air side of the high voltage feedthrough with protective enclosure.

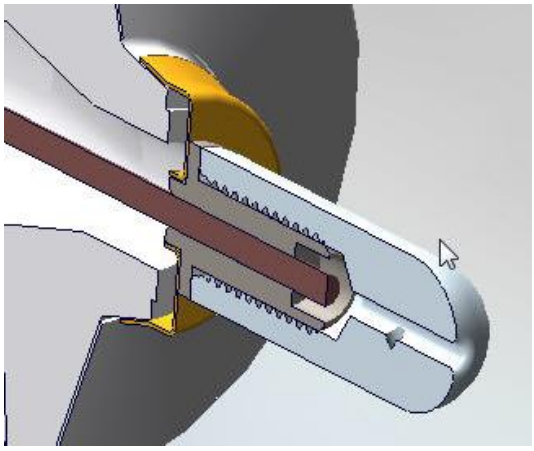

Figure 5.40 HVF electric field reducing screw cap.

voltage cable conductor, which reduces electric field enhancement by the thread edges.

5.5.2 HVF Vacuum Side

Vacuum-Side Arcing Hazard and Modeling

The vacuum side of the HVF presents a similar problem to that addressed in the electrode design. Shown in figure 5.41, the HVF center conductor passes the vacuum chamber wall, inserts into a hole in the electrode, and is held in place with a set screw. Using a concentric cylinder model described by equation (5.8), with a conductor diameter of 4 mm and nearest distance to the surrounding chamber wall of 9.86 cm, a 120 kV potential will induce an electric field of 15.4 kV/mm on the center conductor surface. This is considerably higher than the predicted UHV arcing limit.

A detailed COMSOL model of a HVF, presented in figure 5.42 (left), was built to simulate arcing mitigation solutions. By installing a custom made Macor sleeve over the exposed HVF center conductor, the electric field in the vacuum can be lowered to ~4 kV/mm as seen in the right portion of figure 5.42. This insulating sleeve allows the fields generated in vacuum by the HVF to be within the desired max field limit.

HVF Test Chamber

As a final method of verification, a HVF test chamber, displayed in figure 5.43, was built in order to test the HVF vacuum arcing limit. The chamber consists of a 43.6 cm long stainless steel cylinder with a 19.8 cm inner diameter. Due to availability, a 100 kV feedthrough was attached to the top where the bottom of the cylinder is attached to a vacuum pump. The 100 kV feedthrough has a 4 mm diameter center conductor. The chamber size was chosen to provide a grounded surface the same distance as the closest grounded surface in the real IPM configuration, thus resulting in similar electric field magnitudes. A 3.81 cm diameter metal

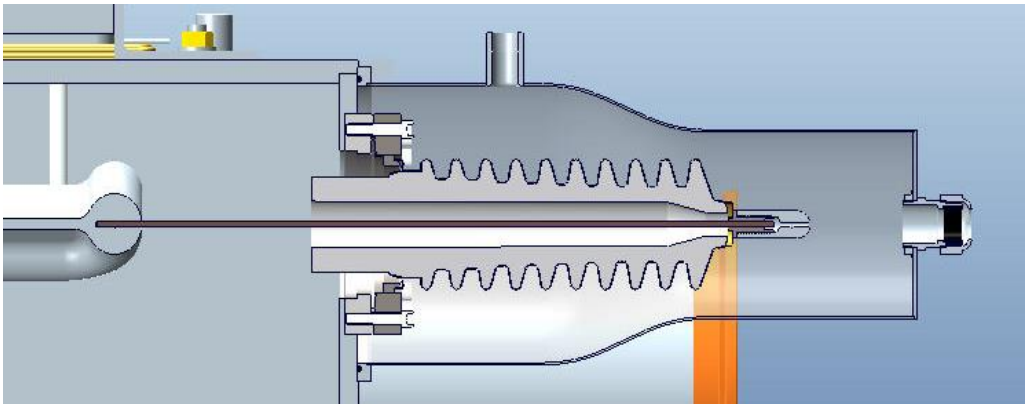

Figure 5.41 Complete HVF connection to the electrode.

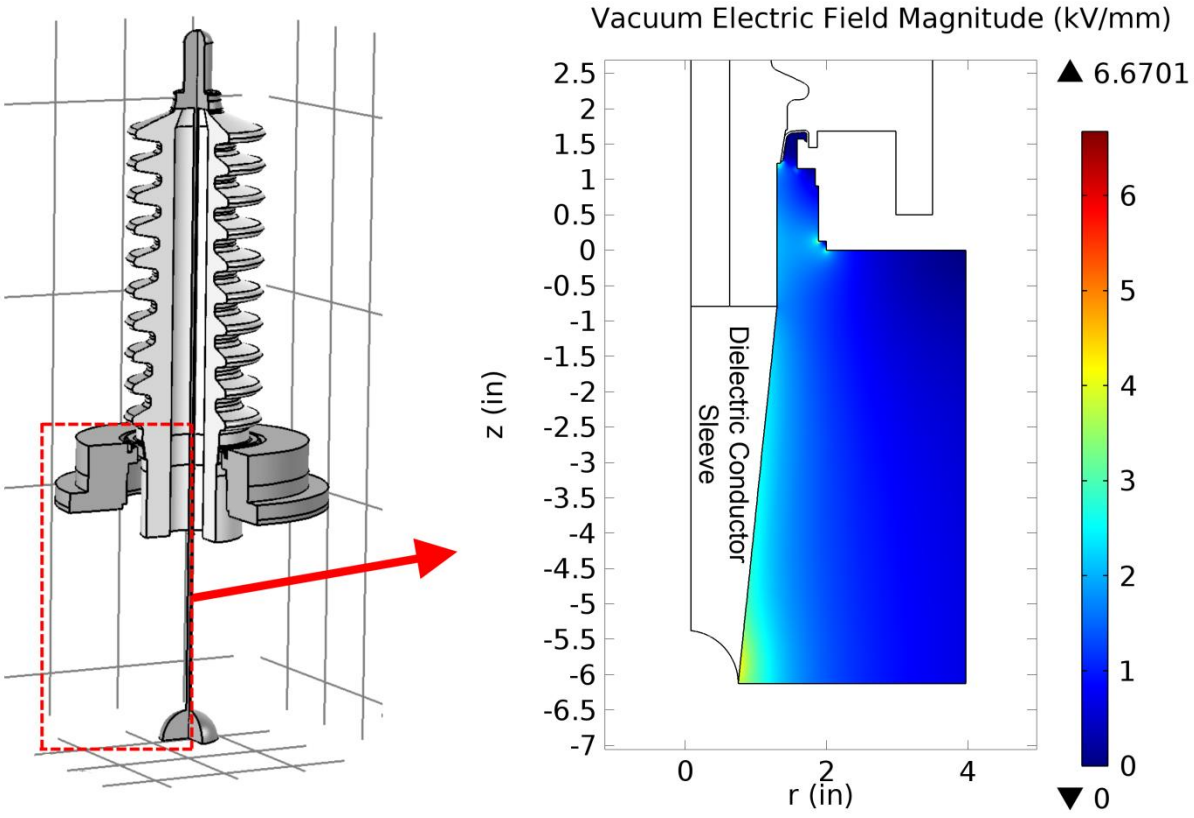

Figure 5.42 (Left) HVF COMSOL model with cutaway showing interior cross section. (Right) Simulation vacuum electric field magnitude results with insulating sleeve surrounding exposed conductor.

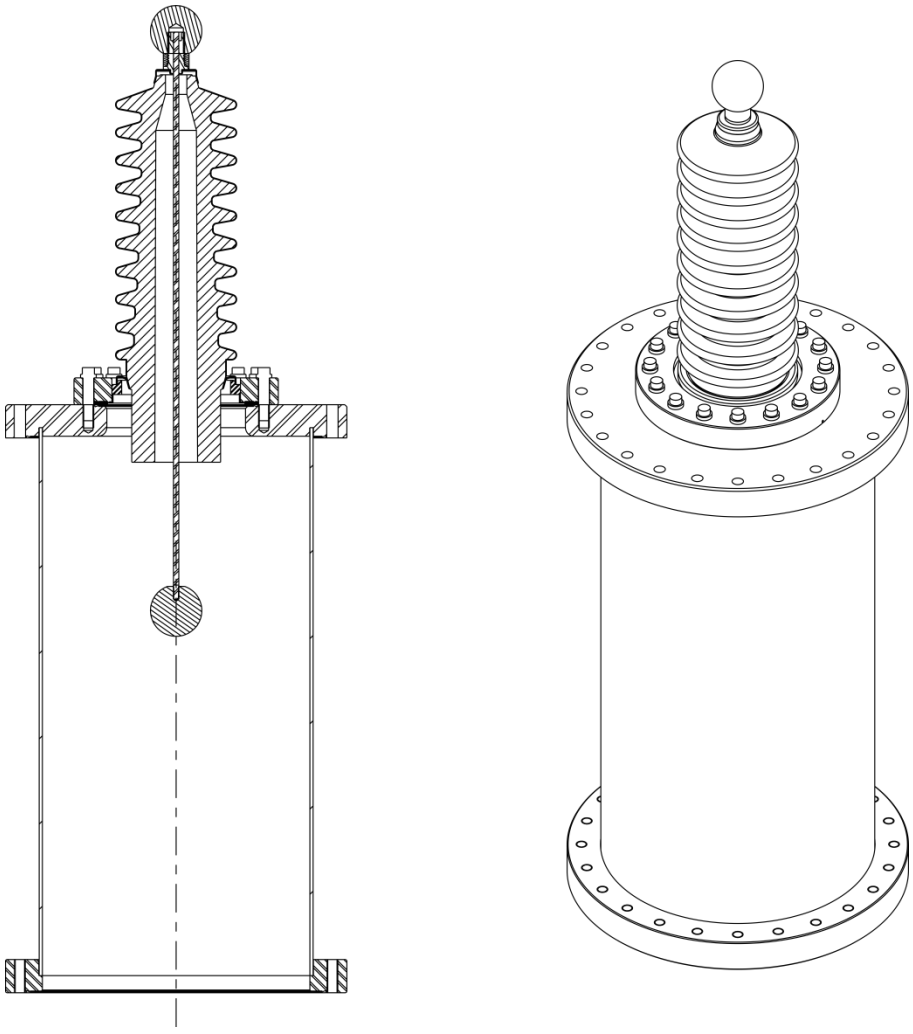

Figure 5.43 HVF test chamber with 4 mm center conductor diameter and 19.8 cm vacuum cylinder inner diameter.

sphere was attached to the end of the center conductor to ensure that the highest field was found on the center conductor surface.

After pumping to a vacuum of $4x10^{-8}$ Torr, the voltage to the HVF was raised, using the same power supply as for the IPM test chamber, until an arc occurred, the potential was raised slowly, which conditioned the test chamber, until a 100 kV potential was both achieved and stable. The test revealed that a conditioned feedthrough could maintain a maximum electric field of 12.8 kV/mm in a 10^{-8} Torr vacuum. While this is guaranteed for the HVF conductor geometry, it strongly supports the assumption that the electrode design should not arc during operation.

5.6 IPM Design Summary

A complete IPM system design has been finalized that has the ability to measure SNS ring beam profiles and meets all of the design specifications set out in table 1.2. The design takes into account vacuum breakdown and surface flashover with electrode edge radiusing and HVF conductor insulation. The electrode itself provides a uniform field over the measurement region and incorporates mechanisms for secondary electron suppression.

Furthermore, by taking into consideration beam induced noise with detector shielding, field attenuating honeycomb, isolated feedthroughs, and shielded cables, Channeltron signal fidelity is maximized. A fully assembled image of the vacuum chamber interior is given in figure 5.44. IPM beam influences due to the electrode and higher order magnet multiple components have been determined to be negligible and special consideration has been implemented for wakefield reduction. Corrector magnets are required for the IPM dipole moment beam deflection.

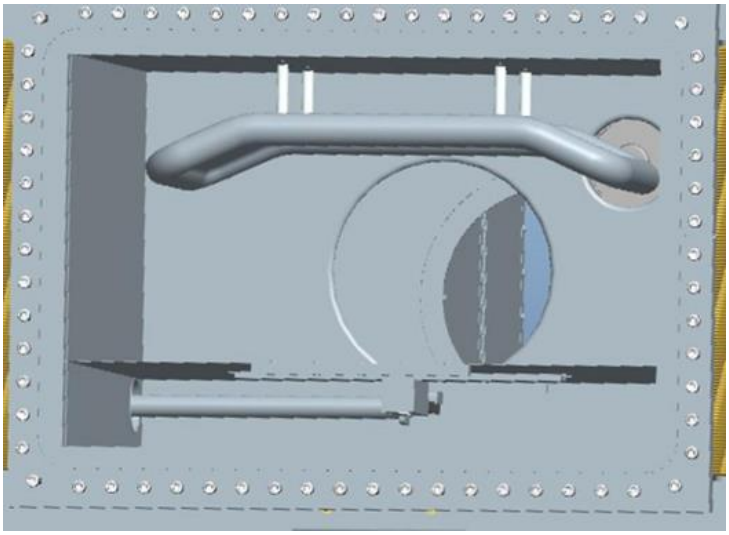

Figure 5.44 IPM vacuum chamber interior.

The full IPM system is composed of a horizontal profile measurement system followed by a vertical profile measurement system where the vertical system is identical to the horizontal excepted that it is rotated by an angle of 90°. With a longitudinal full-system length of 2.23 m and a height from the floor of 2.31 m, both vertical and horizontal profile measurement systems fit within the allotted space. Displayed in figure 5.45 is an exploded front view of the horizontal IPM chamber with electrode and removable front plate. Figure 5.46 shows the same chamber from the back with HVF, detector assembly, and magnet. Finally, given in figure 5.47 is the complete IPM system with horizontal and vertical profile monitor where the corrector magnets have not been included.

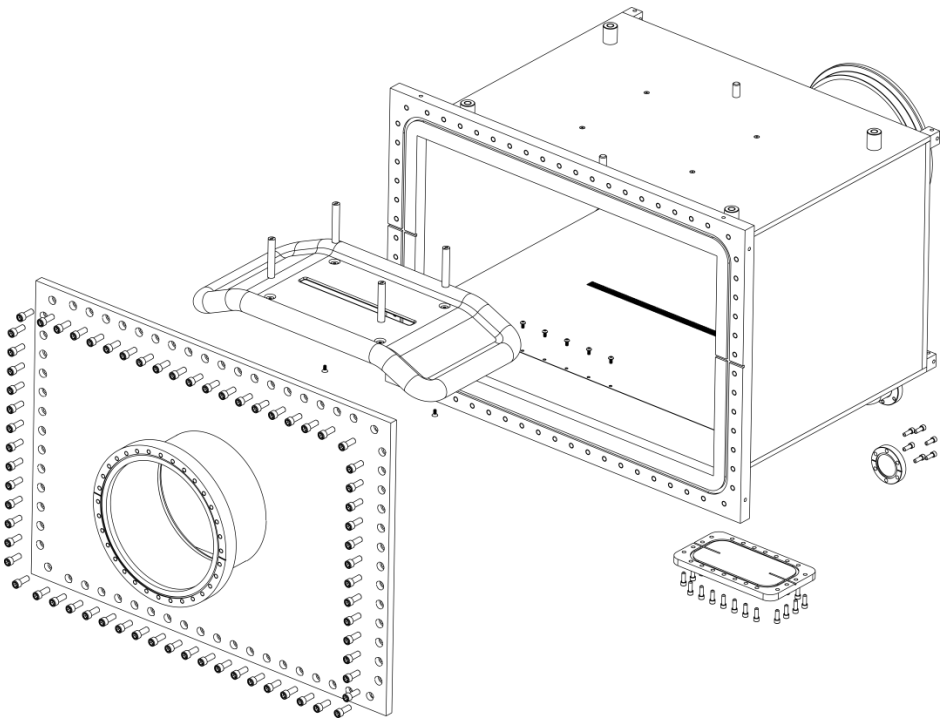

Figure 5.45 Horizontal IPM exploded front view.

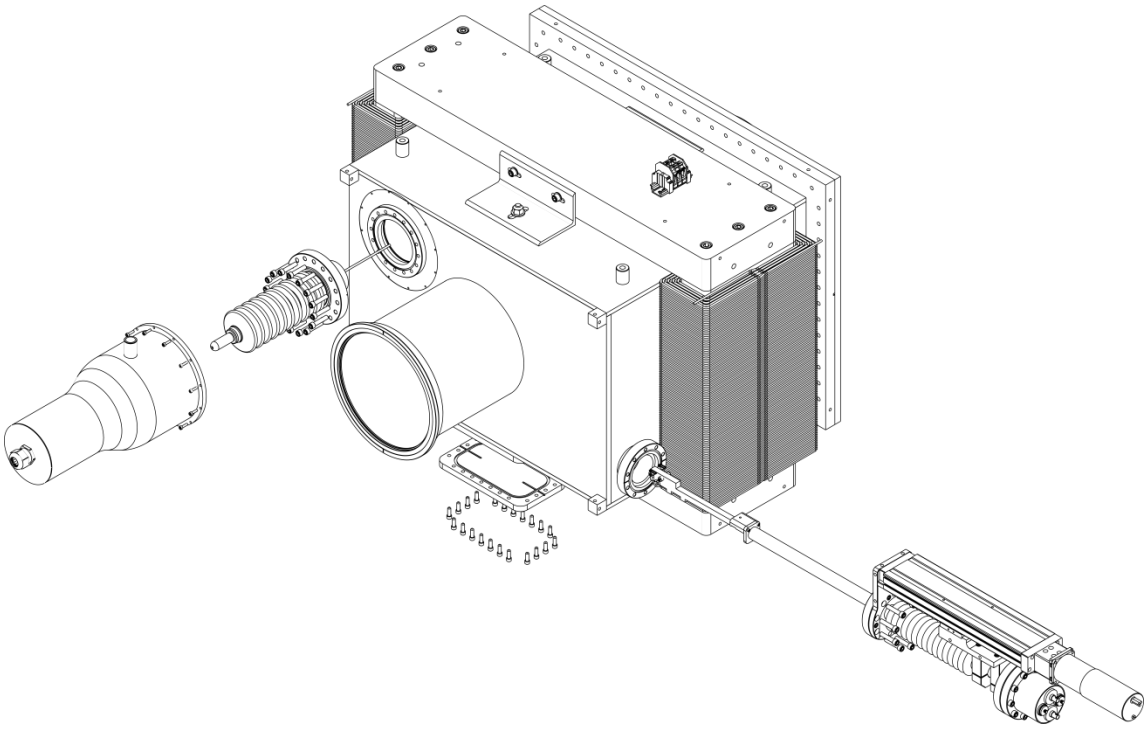

Figure 5.46 Horizontal IPM chamber exploded rear view.

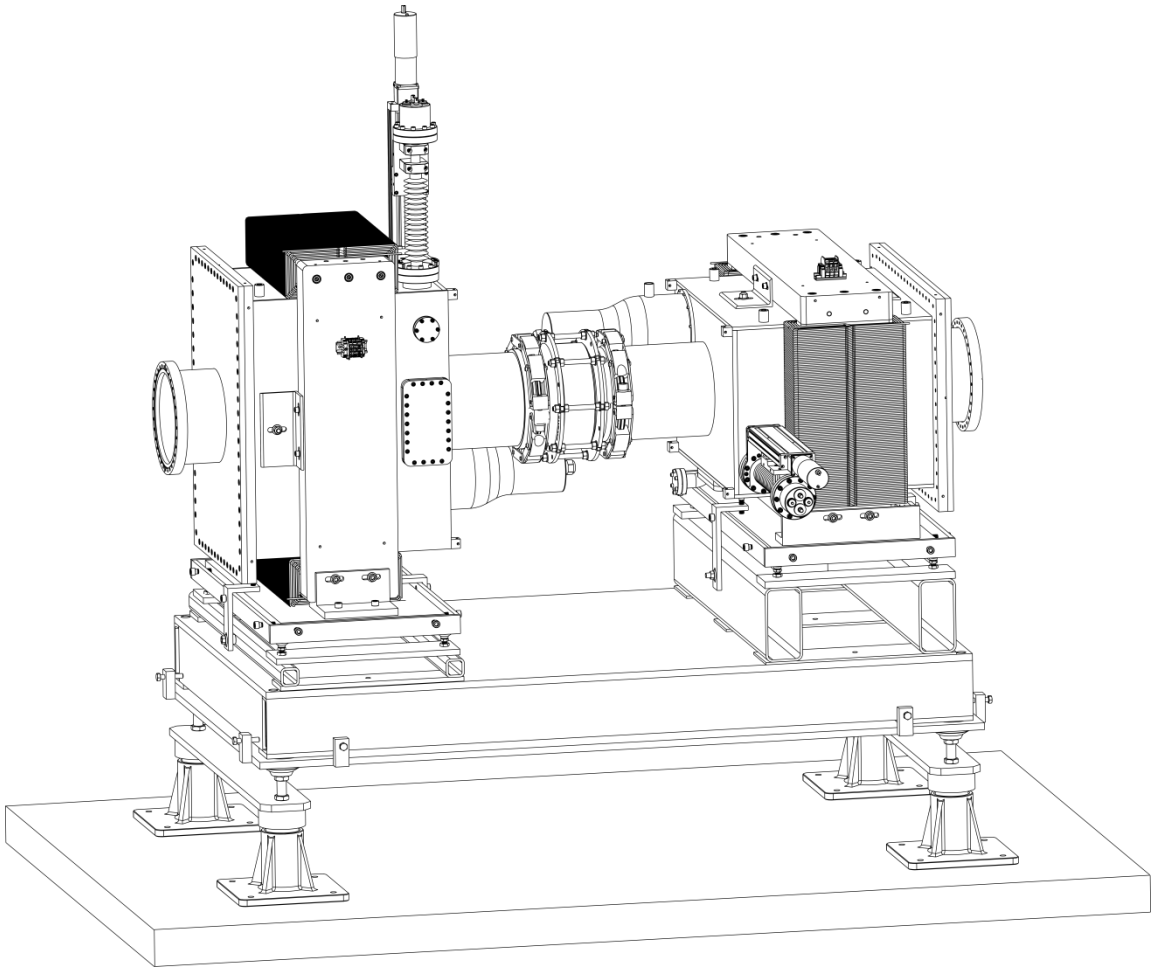

Figure 5.47 Complete IPM system with horizontal and vertical profile monitors.

Chapter 6

Summary

6.1 Overall Project Summary

This work presents the study, analysis, and design of an ionization profile monitor system for the SNS ring. A history of IPM development was presented that showed the technological development and current state of this type of beam diagnostic. A set of design parameters required to produce accurate turn-by-turn profiles for a production quality beam in SNS was then set forth. Based on first principles, the basic assumptions necessary to develop a theoretical framework for an IPM were proposed, which required the derivation of the theory of beam-gas interaction based on relativistic energy transfer. Beam energy loss leading to primary and secondary ionization was analyzed in order to determine pair production values for various gases. A detailed study of the residual gas at the IPM location through an RGA and pressure analysis allowed the estimation of ions and electrons created through ionization. Additionally, an analysis of the SNS electron cloud was performed to determine its influence on IPM profiles.

Once estimates for the expected signal had been determined, based on theoretical examination of measured gas data, a simulation study was reported that analyzed the IPM

operational parameters through particle trajectory tracking. The SNS ORBIT Runge-Kutta tracker was used as a building block to study longitudinal and transverse particle trajectory properties in a variety of electric and magnetic fields including beam space charge. Based on the trajectory study, design parameters and system limitations were established leading to profile measurement with electrons.

A detailed system accuracy study was performed based on a Monte Carlo method of profile generation subject to expected errors. The spatial accuracy was estimated and revealed further system constraints required in order to meet the design criteria. Likewise, investigation of the time resolution led to a data acquisition regime that preserves turn-by-turn resolution. The importance of secondary electron emission noise was identified as a major source of profile error.

An IPM test chamber was designed and built to test the basic IPM principles of turn-by-turn measurement with a Channeltron. The test chamber was vital in identifying unanticipated sources of beam and environmental signal noise. Results of the test chamber modifications gave rise to further design criteria necessary to obtain clean ionized particle measurements. Finally, each of the major IPM system design components was outlined in detail. Theoretical justification was given for many of the design decisions and all previously determined design criteria were implemented.

6.2 Future Work

While this work presents a detailed description and design of an SNS IPM system, a significant effort is required to bring the design to a physical and usable conclusion. Along with the design drawings, the majority of the components have been specified and quoted for

pricing. At the time of this writing, the cost for the complete IPM, composed of horizontal and vertical monitors, was ~$500,000 with an approximate lead time of 1 year for fabrication. Upon receipt of components, system assembly and lab testing in order to verify the system's ability to operate at the required voltage, measurement and verification of magnet multipole strengths, testing of Channeltron operation, and cable distortion need to be performed. Subsequently, upon assembly of the actuator and detector, Labview code needs to be developed for the system's data acquisition, signal processing, actuator control, and power supply management. Considering that the final goal is control room usability, the IPM software must be made user-friendly and compatible with the SNS accelerator control system.

Furthermore, SNS protocol requires the system to have built in safety features, such as a power supply shut off mechanism in the event of accelerator maintenance for the purpose of personnel protection. The IPM must also be tied into the larger accelerator protection system. Finally, commissioning of the IPM requires installation in the beamline and troubleshooting of unexpected system errors. Inevitably some measure of system modification will be required. Once the IPM profile accuracy has been compared with ORBIT simulations and the electron scanner profile monitor, the system may be turned over to accelerator operators as a verified ring profile diagnostic tool.

While it was determined the IPM would not be able to produce ion-based profiles with the required spatial accuracy, the system design supports ion collection. It was a goal of this project to design a system capable of measuring ion profiles that could eventually be used to study ion profile measurement methods. Determining a beam-based space-charge profile calibration would be a significant contribution to IPM technology and the system

proposed here has the capability to support such research

Upon successful installation and operation of the IPM, an upgrade to the system would involve replacing the movable single detector with an array of detectors. A row of contiguous detectors would eliminate the necessity for an actuator while greatly reducing measurement time. Such an upgrade would require a power supply control system for each detector as well as a method for in-situ detector calibration.

6.3 Final Remarks

An ionization profile monitor has been designed for the SNS ring that has the ability to measure turn-by-turn horizontal and transverse beam profiles for a full 60 Hz, production quality beam. With a measurement time of <5 minutes, the IPM system will have an estimated transverse measurement accuracy of 4.9% with a 2% uncertainty using ionized electrons. Signal processing and system design allows for 1 μs resolution with a rise time ≤20 ns or a 3 dB bandwidth ≥17.5 MHz. In order to sustain a 120 kV potential the IPM electrode has been designed to sustain a maximum 4.5 kV/mm electric field. Additionally, higher order magnet multipole components are <1% at a reference radius of 12.78 cm. While the electrode produces <0.5 mrad of beam deflection, the IPM magnets do not and therefore require corrector magnets. In conclusion, an IPM system design satisfying all of the required design criteria has been successfully completed for the Spallation Neutron Source accumulator ring.

Bibliography

[1] E. Rutherford, “Address of the President, Sir Ernest Rutherford, O.M., at the Anniversary Meeting, November 30, 1927,” *Proceedings of the Royal Society A: Mathematical, Physical and Engineering Sciences*, vol. 117, no. 777, pp. 300–316, Jan. 1928.

[2] C. R. Gould, G. L. Greene, F. Plasil, and W. M. Snow, “WORKSHOP SUMMARY: FUNDAMENTAL NEUTRON PHYSICS IN THE UNITED STATES: AN OPPORTUNITY IN NUCLEAR, PARTICLE, AND ASTROPHYSICS FOR THE NEXT DECADE,” in *Fundamental Physics with Pulsed Neutron Beams*, 2001, pp. 1–8.

[3] “Spallation Neutron Source,” 2012. [Online]. Available: http://neutrons.ornl.gov/facilities/SNS/. [Accessed: 02-Jun-2012].

[4] S. Henderson, “SNS Parameters List R13,” Spallation Neutron Source, Oak Ridge, Tennessee, 2005.

[5] M. P. Stockli, “The SNS Chopper System.” Spallation Neutron Source, Oak Ridge, Tennessee, p. 4, 2002.

[6] S. Assadi, “SNS Beam Instrumentations for High Power Operations,” in *The Eighteenth Meeting of the International Collaboration of Advanced Neutron Sources (ICANS)*, 2007, p. 4.

[7] C. Sibley, “MACHINE PROTECTION STRATEGIES FOR HIGH POWER ACCELERATORS *,” in *Particle Accelerator Conference*, 2003, pp. 607–611.

[8] R. E. Shafer, “Beam Position Monitoring,” in *AIP Conference Proceedings*, 1990, vol. 212, pp. 26–58.

[9] J. Galayda, “Beam Profile Measurements,” in *AIP Conference Proceedings 212: Accelerator Instrumentation*, E. R. Beadle and V. J. Castillo, Eds. Upton, New York: AIP, 1989, pp. 59–86.

[10] C. J. Liaw and P. R. Cameron, “CARBON WIRE HEATING DUE TO SCATTERING IN THE SNS,” in *Particle Accelerator Conference*, 2001, no. 2, pp. 2365–2367.

[11] M. A. Plum et al., “Beam Diagnostics in the SNS Linac,” in *Tenth Beam Instrumentation Workshop*, 2002, pp. 195–202.

[12] W. Blokland, S. Cousineau, D. Malyutin, and S. Starostenko, “ELECTRON SCANNER FOR SNS RING PROFILE MEASUREMENTS,” in *DIPAC 2009*, 2009, pp. 3–5.

[13] S. Payne, “Fast gas ionisation beam profile monitor for the ISIS Proton Synchrotron.” p. 42.

[14] P. Forck, “MINIMAL INVASIVE BEAM PROFILE MONITORS FOR HIGH INTENSE HADRON BEAMS,” in *International Particle Accelerator Conference*, 2010, pp. 1261–1265.

[15] V. Dudnikov, “Self-stamilization of e-p Instability and Accumulation of a Superintense Circulating Beam.” Upton, New York, p. 54, 2006.

[16] F. Hornstra and W. H. DeLuca, “NONDESTRUCTIVE BEAM PROFILE DETECTION SYSTEMS FOR THE ZERO GRADIENT SYNCHROTRON,” in *Sixth International Conference on High Energy Accelerators*, 1967, pp. 374–377.

[17] W. H. DeLuca, “Beam Detection Using Residual Gas Ionization,” *IEEE Transactions on Nuclear Science*, vol. 16, no. 3, pp. 813 – 822, 1969.

[18] E. W. McDaniel, *Collision Phenomena in Ionized Gases*. New York, Wiley, 1964.

[19] H. S. W. Massey and E. H. S. Burhop, *Electronic and Ionic Collision Impact Phenomena*. Oxford: Clarendon Press, 1952.

[20] W. H. Deluca and M. F. Shea, “A Nondestructive Linac Beam Density Profile Monitor,” in *Proton Linear Accelerator Conference*, 1968, pp. 190–197.

[21] C. D. Johnson and L. Thorndahl, “THE CPS GAS-IONIZATiON BEAM SCANNER,” in *Symposium on Beam Intensity Measurement*, 1968, pp. 909–913.

[22] A. Barlow et al., “Instrumentation and beam diagnostics in the ISR,” in *8th International Conference on High-energy Accelerators*, 1971, pp. 426–430.

[23] B. Vosicki and K. Zankel, “THE SODIUM CURTAIN BEAM PROFILE MONITOR OF THE ISR,” *IEEE Transactions on Nuclear Science*, vol. 22, no. 3, pp. 1475–1478, 1975.

[24] H. Ishimaru, Z. Igarashi, K. Muto, and S. Shibata, “Beam Profile Measurements for KEK 12 GeV Proton Synchrotron,” *IEEE Transactions on Nuclear Science*, vol. 24, no. 3, pp. 1821–1823, Jun. 1977.

[25] T. Hardek, W. Kells, and H. Lai, “Very Low Intensity Storage-Ring Profile Monitor,” *IEEE Transactions on Nuclear Science*, vol. NS-28, no. 3, pp. 2219–2221, 1981.

[26] J. R. Zagel, D. Chen, and J. Crisp, “Fermilab Booster Ion Profile Monitor System Using LabView,” in *Beam Instrumentation Workshop*, 1994, no. 4, pp. 384–390.

[27] J. R. Zagel, A. A. Hahn, J. L. Crisp, and C. Jensen, “IMPROVEMENTS TO THE FERMILAB IONIZATION PROFILE MONITOR SYSTEMS *,” in *Particle Accelerator Conference*, 1999, pp. 2164–2166.

[28] H. L. Weisberg, “Beam Profile Monitors for the AGS.” Upton, New York, pp. 1–9, 1981.

[29] H. Weisberg, E. Gill, P. Ingrassia, and E. Rodger, “An Ionization Profile Monitor for the Brookhaven AGS,” *IEEE Transactions on Nuclear Science*, vol. 30, no. 4, pp. 2179–2181, Aug. 1983.

[30] R. E. Thern, “Space Charge Distortion in the Brookhaven Ionization Profile Monitor,” in *PAC 1987*, 1987, pp. 646–648.

[31] M. R. Harold et al., “Diagnostics and Commissioning Progress on ISIS,” in *European Particle Accelerator Conference*, 1988, pp. 347–349.

[32] K. Wittenburg, “Experience with the Residual Gas Ionization Beam Profile Monitors at the DESY Proton Accelerators,” in *3rd European Particle Accelerator Conference*, 1992, pp. 1–5.

[33] J. Schwarz, “Beam measurement with rest-gas ionizations monitor in PETRA,” in *PcaPac 2000*, 2000.

[34] F. Hornstra, “RESIDUAL GAS IONIZATION BEAM PROFILE MONITORS FOR THE HERA PROTON MACHINES,” in *1st EPAC*, 1988, pp. 1160–1162.

[35] K. Wittenburg, “Transversal Emittance Measurement,” in *Harz-Seminar*, 1992.

[36] N. Ceci et al., “Preliminary Study for a Residual Gas Beam Profile Monitor,” in *5th European Particle Accelerator Conference*, 1996, pp. 1642–1644.

[37] V. Variale et al., “First test results for a residual gas beam profile monitor,” *Proceedings of the 1997 Particle Accelerator Conference*, vol. 2, pp. 2169–2170, 1998.

[38] M. Bellato, A. Dainelli, and M. Poggi, “Commissioning and Developments of the ALPI Diagnostics System,” in *4th European Particle Accelerator Conference*, 1994, pp. 1512–1514.

[39] B. Hochadel et al., “A residual-gas ionization beam profile monitor for the Heidelberg Test Storage Ring TSR,” *Nuclear Instruments and Methods in Physics Research Section A: Accelerators, Spectrometers, Detectors and Associated Equipment*, vol. 343, no. 2–3, pp. 401–414, Apr. 1994.

[40] J.-L. P. Vignet, R. M. Anne, Y. R. Georget, R. E. Hue, and C. H. Tribouillard, "Beam monitors based on residual gas ionization," in *7th Beam Instrumentation Workshop*, 1996.

[41] P. Cameron et al., "The RHIC Ionization Beam Profile Monitor," *Proceedings of the 1999 Particle Accelerator Conference*, vol. 3, pp. 2114–2116, 1999.

[42] W. C. Sellyey and J. D. Gilpatrick, "A compact residual gas ionization profile monitor (rgipm) system," in *Particle Accelerator Conference*, 1999, pp. 2152–2154.

[43] W. C. Sellyey, J. D. Gilpatrick, and R. Senior, "Bench test of a residual gas ionization profile monitor (RGIPM)," in *PAC 2001*, 2001, vol. 2, pp. 1318–1320.

[44] A. Jansson et al., "Tevatron Ionization Profile Monitor," Batavia, IL, 2003.

[45] A. Jansson et al., "An Ionization Profile Monitor for the Tevatron," in *2005 Particle Accelerator Conference*, 2005, pp. 2227–2229.

[46] A. Jansson et al., "TEVATRON IONIZATION PROFILE MONITORING," in *EPAC 2006*, 2006, pp. 159–167.

[47] Y. Sato et al., "Development of Residual Gas Ionization Profile Monitor for High Intensity Proton Beams," *IEEE Nuclear Science Symposium Conference Record, 2005*, vol. 2, pp. 1043–1046, 2005.

[48] S. Lee et al., "DESIGN STUDY OF A NONDESTRUCTIVE BEAM PROFILE AND HALOS MONITOR BASED ON RESIDUAL GAS IONIZATION FOR THE J-PARC RCS," in *The 14th Symposium on Accelerator Science and Technology*, 2003, no. November.

[49] K. Satou, N. Hayashi, S. Lee, and T. Toyama, "A PROTOTYPE OF RESIDUAL GAS IONIZATION PROFILE MONITOR FOR J-PARC RCS," in *EPAC 2006*, 2006, no. 1, pp. 1163–1165.

[50] K. Satou et al., "BEAM PROFILE MONITORING OF THE J-PARC 3 GeV RAPID CYCLING SYNCHROTRON," in *EPAC 2008*, 2008, pp. 1275–1277.

[51] R. Ishida, "R & D of Beam Monitors at J-PARC Neutrino Beamline," University of Tokyo, 2005.

[52] P. Forck, A. Bank, T. Giacomini, and A. Peters, "PROFILE MONITORS BASED ON RESIDUAL GAS INTERACTION," in *DIPAC*, 2005, no. 03, pp. 223–227.

[53] F. Roncarolo, "Accuracy of the Transverse Emittance Measurements of the CERN Large Hadron Collider," IPEP Institut de physique de l'energie et des particules, 2005.

[54] C. Bal, V. Prieto, R. Sautier, and G. Tranquille, “FIRST RESULTS FROM THE LEIR IONISATION PROFILE MONITORS,” in *Proceedings of DIPAC 2007*, 2007, pp. 120–122.

[55] E. Mahner, “Technical Design of the LEIR Vacuum System Technical Design of the LEIR Vacuum System,” Geneva, Switzerland, 2002.

[56] M. Sachwitz, A. Hofmann, S. Pauliuk, K. Tiedtke, and H. Wabnitz, “IONIZATION PROFILE MONITOR TO DETERMINE SPATIAL AND ANGULAR STABILITY OF FEL RADIATION OF FLASH,” in *EPAC 2008*, 2008, pp. 1266–1268.

[57] J. Egberts et al., “DETAILED EXPERIMENTAL CHARACTERIZATION OF AN IONIZATION PROFILE MONITOR,” in *DIPAC*, 2011, pp. 3–5.

[58] G. Ferioli, C. Fischer, J. Koopman, and F. Roncarolo, “BEAM STUDIES MADE WITH THE SPS IONIZATION PROFILE MONITOR,” in *DIPAC*, 2003, pp. 116–118.

[59] D. Liakin, V. Skachkov, P. Forck, and T. Giacomini, “Improving the Reliability of IPM,” in *DIPAC 2005*, 2005, vol. 29, no. 6, pp. 150–152.

[60] R. Connolly, R. Michnoff, and S. Tepikian, “Residual-Gas-Ionization Beam Profile Monitors in RHIC,” in *2005 Particle Accelerator Conference*, 2005, pp. 230–234.

[61] M. Poggi et al., “Activity of Diagnostics Laboratory,” *Africa*. pp. 1–2, 2006.

[62] M. Poggi et al., “TWO-DIMENSIONAL IONIZATION BEAM PROFILE MEASUREMENT,” in *DIPAC 2009*, 2009, pp. 384–386.

[63] B. G. Pine, C. M. Warsop, and S. J. Payne, “Modelling of Diagnostics for Space Charge Studies on the ISIS Synchrotron,” in *EPAC 2006*, 2006, vol. 3, pp. 1082–1084.

[64] S. J. Payne, P. G. Barnes, G. M. Cross, A. Pertica, and S. A. Whitehead, “A SELF CALIBRATING REAL TIME MULTI-CHANNEL PROFILE MONITOR FOR THE ISIS PROTON SYNCHROTRON,” in *DIPAC 2007*, 2007, pp. 364–366.

[65] R. E. Williamson, B. G. Pine, S. J. Payne, and C. M. Warsop, “ANALYSIS OF MEASUREMENT ERRORS IN RESIDUAL GAS IONISATION PROFILE MONITORS IN A HIGH INTENSITY PROTON BEAM,” in *EPAC 2008*, 2008, pp. 1317–1319.

[66] S. A. Whitehead, P. G. Barnes, G. M. Cross, S. J. Payne, and A. Pertica, “MULTI-CHANNELTRON BASED PROFILE MONITOR AT THE ISIS PROTON SYNCHROTRON,” in *BIW 2010*, 2010, pp. 1–5.

[67] J. Amundson, J. Lackey, P. Spentzouris, G. Jungman, and L. Spentzouris, “Calibration of the Fermilab Booster Ionization Profile Monitor,” *Physical Review Special Topics - Accelerators and Beams*, vol. 6, no. 10, pp. 1–15, Oct. 2003.

[68] J. Zagel, “Personal Communication.” .

[69] S. Payne, “Personal Communication.” .

[70] A. Kowalczyk, “Proton induced spallation reactions in the energy range 0 . 1 - 10 GeV,” Jagiellonian University, 2007.

[71] D. Filges and F. Goldenbaum, *Handbook of Spallation Research*. Weinheim, Germany: Wiley-VCH Verlag GmbH & Co. KGaA, 2009.

[72] S. Meroli, D. Passeri, and L. Servoli, “Energy loss measurement for charged particles in very thin silicon layers,” *Journal of Instrumentation*, vol. 6, no. 06, pp. P06013–P06013, Jun. 2011.

[73] L. D. Landau, “On the Energy Loss of Fast Particles by Ionisation,” in *Collected Papers of L. D. Landau*, First., D. Ter Haar, Ed. London, England: Gordon and Breach, Science Publishers, 1965, pp. 417–424.

[74] J. D. Jackson, *Classical Electrodynamics*, Third. Hoboken, NJ: Wiley, 1999, pp. 1–808.

[75] I. Hutchinson, “Chapter 6 Collisions of Charged Particles,” *MIT Open Courseware - Electromagnetic Interactions - Readings*, 2005. [Online]. Available: http://ocw.mit.edu/courses/nuclear-engineering/22-105-electromagnetic-interactions-fall-2005/readings/chap6.pdf.

[76] M. Inokuti and J. E. Turner, “MEAN EXCITATION ENERGIES FOR STOPPING POWER AS DERIVED FROM OSCILLATOR-STRENGTH DISTRIBUTIONS,” in *Sixth Symposium on Microdosimetry*, 1978, pp. 675–687.

[77] M. J. Berger and S. M. Seltzer, “Tables of Energy Losses and Ranges of Electrons and Positrons,” National Aeronautics and Space Administration, Washington, D.C., 1964.

[78] S. M. Seltzer and M. J. Berger, “Evaluation of the collision stopping power of elements and compounds for electrons and positrons,” *The International Journal of Applied Radiation and Isotopes*, vol. 33, no. 11, pp. 1189–1218, Nov. 1982.

[79] E. Segrè, *Nuclei and Particles: An Introduction to Nuclear and Subnuclear Physics*, Second. Reading, MA: Benjamin-Cummings Pub Co, 1977.

[80] W. H. Tait, *Radiation Detection*. London, UK: Butterworth Inc., 1980.

[81] G. F. Knoll, *Radiation Detection and Measurement*, Third. Chinchester, New York: Wiley, 2000.

[82] N. Bohr, "LX. On the decrease of velocity of swiftly moving electrified particles in passing through matter," *Philosophical Magazine Series 6*, vol. 30, no. 178, pp. 581–612, Oct. 1915.

[83] H. Bethe, "Zur Theorie des Durchgangs schneller Korpuskularstrahlen durch Materie," *Annalen der Physik*, vol. 397, no. 3, pp. 325–400, 1930.

[84] D. Groom, "Energy loss in matter by heavy particles," Particle Data Group, Note PDG-93-06, 1993.

[85] B. J. McParland, *Nuclear Medicine Radiation Dosimetry*. London: Springer London, 2010.

[86] K. Nakamura and (Particle Data Group), "Review of Particle Physics," *Journal of Physics G: Nuclear and Particle Physics*, vol. 37, no. 7A, p. 075021, Jul. 2010.

[87] J. Lindhard, "On the properties of a gas of charged particles," *Matematisk Fysiske Meddelelser - Kongelige Dankse Videnskabernes Selskab*, vol. 28, no. 8, 1954.

[88] D. I. Thwaites, "Bragg's Rule of Stopping Power Additivity: A Compilation and Summary of Results," *Radiation Research*, vol. 95, no. 3, pp. 495–518, 1983.

[89] B. Rossi, *High-energy Particles*. New York, NY: Prentice-Hall Incorporated, 1965.

[90] S. Sasaki, T. Sanami, K. Saito, K. Iijima, H. Tawara, and T. Murakami, "W-values for heavy ions in gases," in *2009 IEEE Nuclear Science Symposium Conference Record (NSS/MIC)*, 2009, pp. 702–705.

[91] U. Fano, "Ionization Yield of Radiations. II. The Fluctuations of the Number of Ions," *Physical Review*, vol. 72, no. 1, pp. 26–29, Jul. 1947.

[92] I. K. Bronic, "On a relation between the W value and the Fano factor," *Journal of Physics B: Atomic, Molecular and Optical Physics*, vol. 25, no. 8, pp. L215–L218, Apr. 1992.

[93] W. W. M. Allison and J. H. Cobb, "Relativistic Charged Particle Identification by Energy Loss," *Annual Review of Nuclear and Particle Science*, vol. 30, no. 1, pp. 253–298, Dec. 1980.

[94] I. B. Smirnov, "Modeling of ionization produced by fast charged particles in gases," *Nuclear Instruments and Methods in Physics Research Section A: Accelerators, Spectrometers, Detectors and Associated Equipment*, vol. 554, no. 1–3, pp. 474–493,

Dec. 2005.

[95] A. G. Mathewson and O. Gröbner, “Thermal Outgassing and Beam Induced Desorption,” in *Handbook of Accelerator Physics and Engineering*, A. W. Chao and M. Tigner, Eds. Singapore: World Scientific Publishing Co. Pte. Ltd., 1998, pp. 224–227.

[96] P. He, H. C. Hseuh, M. Maples, R. Todd, D. Weiss, and D. Wilson, “Hydrogen Outgassing and Surface Properties of TiN-Coated Stainless Steel Chambers,” in *First International Workshop on Materials and Vacuum*, 2003, vol. 671, pp. 292–299.

[97] J. Price and C. Stone, “Private Commincation.” .

[98] “Models RGA100 , Residual Gas Analyzer Operating Manual and Programming Reference,” vol. 8. Stanford Research Systems, Sunnyvale, CA, 2009.

[99] E. C. Montenegro, “Fragmentation of water by heavy ions,” *Journal of Physics: Conference Series*, vol. 194, no. 1, p. 012049, Nov. 2009.

[100] “Cracking Patterns,” *Hiden Analytical*, 2013. [Online]. Available: http://www.hidenanalytical.com/index.php/en/cracking-patterns. [Accessed: 10-May-2013].

[101] “Partial Pressures vs. Total Pressure for an Open Ion Source RGA,” *Leybold Inficon Tech Note*, 1991. [Online]. Available: http://www.inficon.com/download/en/Partial_pressures.pdf.

[102] K. Jousten, Ed., *Handbook of Vacuum Technology*. Weinheim, Germany: Wiley-VCH Verlag GmbH & Co. KGaA, 2008, pp. 646–647.

[103] H. C. Hseuh, C. J. Liaw, and M. Mapes, “DESIGN OF THE SNS ACCUMULATOR RING VACUUM SYSTEMS,” in *Particle Accelerator Conference*, 1999, pp. 1345–1347.

[104] A. G. Ruggiero and M. Blaskiewicz, “The Electron-Proton Effects in Intense Proton Bunches,” BNL/NSNS, Upton, New York, Tech. Note #8, 1997.

[105] A. W. Chao, *Physics of Collective Beam Instabilities in High Energy Accelerators*. New York, NY: Wiley-Interscience, 1993.

[106] Y. A. Cengel and M. Boles, *Thermodynamics: An Engineering Approach*, 4th ed. New York, NY: McGraw-Hill, 2001, pp. 152–153.

[107] N. Marquardt, “Introduction to the Principles of Vacuum Physics,” in *CERN Accelerator School: Vacuum Techonolgy*, 1999, pp. 1–24.

[108] S. Zheng, “Conductance Calculation - Molecular Flow, Long Tube of Circular Cross Section,” Fermilab, Batavia, IL, Tech. Rep. ssc-gem-tn-93-382, 1993.

[109] G. Guignard, “Selection of Formulae Concerning Proton Storage Rings,” CERN, Geneva, Switzerland, Yellow Report 10, 1977.

[110] K. M. Welch, “The pressure profile in a long outgassing vacuum tube,” *Vacuum*, vol. 23, no. 8, pp. 271–276, Aug. 1973.

[111] A. Aleksandrov, S. Assadi, S. Cousineau, V. Danilov, S. Henderson, and M. Plum, “FEASIBILITY STUDY OF USING AN ELECTRON BEAM FOR PROFILE MEASUREMENTS IN THE SNS ACCUMULATOR RING.,” in *PAC 2005*, 2005, vol. 2, no. 3, pp. 2586–2588.

[112] H. Hseuh et al., “DESIGN AND IMPLEMENTATION OF SNS RING VACUUM SYSTEM WITH SUPPRESSION OF ELECTRON CLOUD INSTABILITY,” in *31st Advanced ICFA Beam Dynamics Workshop on Electron-Cloud Effects*, 2004, pp. 119–122.

[113] O. Gröbner, “DYNAMIC OUTGASSING,” in *CAS-CERN Accelerator School*, 1999, no. 3, pp. 127–138.

[114] F. Rieke and W. Prepejchal, “Ionization Cross Sections of Gaseous Atoms and Molecules for High-Energy Electrons and Positrons,” *Physical Review A*, vol. 6, no. 4, pp. 1507–1519, Oct. 1972.

[115] M. Inokuti, “Inelastic Collisions of Fast Charged Particles with Atoms and Molecules—The Bethe Theory Revisited,” *Reviews of Modern Physics*, vol. 43, no. 3, pp. 297–347, Jul. 1971.

[116] Y. Baconnier, “Neutralization of Accelerator Beams by Ionization of the Residual Gas,” in *CAS - CERN Accelerator School: General Accelerator Physics*, 1985, pp. 267–297.

[117] J. de Segovia, “A review of electron stimulated desorption processes influencing the measurement of pressure or gas composition in ultra high vacuum systems,” *Vacuum*, vol. 47, no. 4, pp. 333–340, Apr. 1996.

[118] N. Hilleret, “Non-Thermal Outgassing,” in *CAS - CERN Accelerator School: Vacuum in Accelerators*, 2007, pp. 87–116.

[119] F. Sauli, “Principles of Operation of Multiwire Proportional and Drift Chambers,” Geneva, Switzerland, 1977.

[120] a. Muñoz et al., “Single electron tracks in water vapour for energies below 100eV,”

International Journal of Mass Spectrometry, vol. 277, no. 1–3, pp. 175–179, Nov. 2008.

[121] Y.-K. Kim et al., "Electron-Impact Cross Sections for Ionization and Excitation," in *NIST Chemistry WebBook, NIST Standard Reference Database Number 102*, P. J. Linstrom and W. G. Mallard, Eds. Gaithersburg, MD: National Institute of Standards and Technology. [Online]. Available: http://webbook.nist.gov. [Accessed: 23-Jan-2013].

[122] A. Edwards, R. Wood, A. Beard, and R. Ezell, "Single and double ionization of H2 by electrons and protons," *Physical Review A*, vol. 37, no. 10, pp. 3697–3701, May 1988.

[123] A. M. Sayler, E. Wells, K. D. Games, and I. Ben-Itzhak, "Velocity dependence of electron removal and fragmentation of water molecules caused by fast proton impact," *AIP Conference Proceedings*, vol. 576, no. 2001, pp. 33–35, 2001.

[124] M. Blaskiewicz, M. Furman, M. Pivi, and R. Macek, "Electron cloud instabilities in the Proton Storage Ring and Spallation Neutron Source," *Physical Review Special Topics - Accelerators and Beams*, vol. 6, no. 1, p. 014203, Jan. 2003.

[125] J. Wei and R. J. Macek, "ELECTRON-CLOUD EFFECTS IN HIGH-INTENSITY PROTON ACCELERATORS," in *ECLOUD '02 Workshop*, 2002.

[126] J. Wei et al., "ELECTRON-CLOUD MITIGATION IN THE SPALLATION NEUTRON SOURCE RING∗," in *PAC*, 2003, pp. 2598–2600.

[127] M. Furman and M. Pivi, "Probabilistic model for the simulation of secondary electron emission," *Physical Review Special Topics - Accelerators and Beams*, vol. 5, no. 12, pp. 1–31, Dec. 2002.

[128] M. Pivi and M. A. Furman, "MITIGATION OF THE ELECTRON-CLOUD EFFECT IN THE PSR AND SNS PROTON STORAGE RINGS BY TAILORING THE BUNCH PROFILE," in *20th Particle Accelerator Conference*, 2003, pp. 3222–3225.

[129] R. J. Macek et al., "ELECTRON PROTON TWO-STREAM INSTABILITY AT THE PSR," in *PAC 2001*, 2001.

[130] P. He et al., "SECONDARY ELECTRON EMISSION MEASUREMENTS FOR TIN COATING ON THE STAINLESS STEEL OF SNS ACCUMULATOR RING VACUUM CHAMBER," in *EPAC 2004*, 2004, pp. 5–8.

[131] R. Todd, P. He, H. C. Hseuh, and D. Weiss, "Summary on Titanium Nitride Coating of SNS Ring Vacuum Chambers," in *Proceedings of the 2005 Particle Accelerator Conference*, 2005, pp. 3088–3090.

[132] J. A. Holmes, “Private Communication.” .

[133] A. Shishlo, “Private Communication.” .

[134] R. V. Latham et al., *High Voltage Vacuum Insulation: Basic Concepts and Technological Practice*. San Diego, CA: Academic Press Limited, 1995.

[135] E. B. Podgorsak, “1 Introduction to Modern Physics,” in *Radiation Physics for Medical Physics*, Second., vol. 54, no. 1, Heidelberg, Germany: Springer, 2010, pp. 1–75.

[136] C. K. Sinclair, H. F. Dylla, T. L. Siggins, D. Manos, L. Wu, and T. J. Venhaus, “DRAMATIC REDUCTION OF DC FIELD EMISSION FROM LARGE AREA ELECTRODES BY PLASMA-SOURCE ION IMPLANTATION,” in *PAC 2001*, 2001, pp. 610–612.

[137] N. Tsoulfanidis, *Measurement and Detection of Radiation*, First. Washington, D.C.: Hemisphere Publising, 1983.

[138] R. F. Post, “Plasma Physics in the 20th Century,” in *Twentieth Century Physics*, Volume III., L. M. Brown, P. A, and B. Pippard, Eds. New York, NY: Bristol and American Institute of Physics Press, 1995.

[139] K. Miyamoto, “Fundamentals of Plasma Physics and Controlled Fusion,” National Institute for Fusion Science, Nagoya, Japan, NIFS-PROC-48, 2000.

[140] “CHANNELTRON HANDBOOK,” *Burle Industries*. [Online]. Available: http://www.photonisusa.com/.

[141] F. Cardarelli, *Materials Handbook: A Concise Desktop Reference*, 2nd ed. London, England: Springer-Verlag, 2008.

[142] L. Heroux and H. E. Hinteregger, “Resistance Strip Magnetic Photomultiplier for the Extreme Ultraviolet,” *Review of Scientific Instruments*, vol. 31, no. 3, p. 280, 1960.

[143] Y. B. Hahn, R. E. Hebner, D. R. Kastelein, and K. J. Nygaard, “Channeltron Gain in Magnetic Fields,” *Review of Scientific Instruments*, vol. 43, no. 4, p. 695, 1972.

[144] T. L. Chenevert and P. W. Zitzewitz, “Performance of a spiralled continuous electron multiplier in a magnetic field,” *Review of Scientific Instruments*, vol. 48, no. 12, pp. 1601–1602, 1977.

[145] R. H. Thomas, “Radiation Sources,” in *Handbook of Accelerator Physics and Engineering*, A. W. Chao and M. Tigner, Eds. Singapore: World Scientific Publishing Co. Pte. Ltd., 1998, pp. 598–605.

[146] J. G. Timothy and R. L. Bybee, “Effects of 1-MeV gamma radiation on a multi-anode microchannel array detector tube.,” *The Review of scientific instruments*, vol. 50, no. 6, p. 743, Jun. 1979.

[147] H. H. Refsum, B. Dehning, and J. Koopman, “SIMULATION OF AN ELECTRON SOURCE BASED CALIBRATING SYSTEM FOR AN IONISATION PROFILE MONITOR,” in *DIPAC 2005*, 2005, pp. 160–162.

[148] J. R. Taylor, *An Introduction to Error Analysis: The Study of Uncertainties in Physical Measurements*, Second. Sausalito, CA: University Science Books, 1997, pp. 297–298.

[149] H. J. de Blank, “Guiding Center Motion,” *Fusion Science and Technology*, vol. 49, no. 2T, pp. 59–66, 2006.

[150] J. Cary and A. Brizard, “Hamiltonian theory of guiding-center motion,” *Reviews of Modern Physics*, vol. 81, no. 2, pp. 693–738, May 2009.

[151] J. D. Galambos, J. A. Holmes, and D. K. Olsen, “ORBIT User Manual,” SNS-ORNL-AP Tech. Note 11, 1999.

[152] J. Galambos, S. Danilov, D. Jeon, J. Holmes, D. Olsen, and A. Luccio, “ORBIT – A RING INJECTION CODE WITH SPACE CHARGE,” IEEE, New York, New York, 1999.

[153] J. A. Holmes, J. D. Galambos, D. K. Olsen, J. H. Whealton, M. Blaskiewicz, and A. Luccio, “A PARTICLE-IN-CELL MODEL FOR SPACE CHARGE DYNAMICS IN RINGS,” in *EPAC*, 1998, pp. 1109–1111.

[154] S. Hassani, *Mathematical Physics: A Modern Introduction to Its Foundations*. New York, NY: Springer-Verlag, 1999, pp. 387–394.

[155] A. V. Fedotov, N. Malitsky, and J. Wei, “SPACE-CHARGE SIMULATIONS FOR THE SPALLATION NEUTRON SOURCE (SNS) RING USING UNIFIED ACCELERATOR LIBRARIES,” Brookhaven National Laboratory, Upton, New York, Tech. Note BNL/SNS No. 086, 2001.

[156] J. Beebe-Wang, Y. . Y. Lee, D. Raparia, and J. Wei, “Transverse Phase Space Painting for SNS Accumulator Ring Injection,” in *PAC 1999*, 1999, pp. 1743–1745.

[157] J. Beebe-Wang, Y. Y. Lee, D. Raparia, J. Wei, C. R. Prior, and S. Machida, “BEAM PROPERTIES IN THE SNS ACCUMULATOR RING DUE TO TRANSVERSE PHASE SPACE PAINTING,” in *EPAC 2000*, 2000, vol. 2, pp. 1465–1467.

[158] D. D. Wackerly, W. Mendenhall III, and R. L. Scheaffer, *Mathematical Statistics with Applications*, Sixth. Pacific Grove, CA: Duxbury Press, 2002, pp. 346–354.

[159] D. A. Edwards and M. J. Syphers, *An Introduction to the Physics of High Energy Accelerators*. Weinheim, Germany: Wiley-VCH Verlag GmbH, 1993.

[160] E. Kobetich and R. Katz, "Energy Deposition by Electron Beams and δ Rays," *Physical Review*, vol. 170, no. 2, pp. 391–396, Jun. 1968.

[161] E. W. Weisstein, "Sphere Point Picking," *MathWorld--A Wolfram Web Resource*. [Online]. Available: http://mathworld.wolfram.com/SpherePointPicking.html. [Accessed: 19-Apr-2013].

[162] K. Wittenburg, "Zum Auflösungsvermögen der Restgasionisations - Strahlprofilmonitore," PKTR, Note 70, 1991.

[163] T. He, C. Huang, B. M. Blum, J. A. Stankovic, and T. Abdelzaher, "JCGM 100:2008 Evaluation of measurement data — Guide to the expression of uncertainty in measurement," 2008. [Online]. Available: http://www.bipm.org/utils/common/documents/jcgm/JCGM_100_2008_E.pdf. [Accessed: 22-Apr-2012].

[164] M. Plum, "Error in beam width and beam position measured with SNS linac wire scanner system," Spallation Neutron Source, Oak Ridge, Tennessee, SNS-Note-Diag 75, 2002.

[165] G. A. F. Seber and C. J. Wild, *Nonlinear Regression*. Hoboken, NJ: Wiley-Interscience, 2003.

[166] D. W. Scott, "On optimal and data-based histograms," *Biometrika*, vol. 66, no. 3, pp. 605–610, 1979.

[167] D. W. Scott, "Multivariate Density Estimation and Visualization." Berlin, Germany, 2004.

[168] D. V Perepelitsa, "Johnson Noise and Shot Noise," no. 2. MIT Department of Physics, Cambridge, MA, 2006.

[169] C. D. Motchenbacher and J. A. Connelly, *Low-Noise Electronic System Design*. Wiley-Interscience, 1993.

[170] W. Kester, "Taking the Mystery out of the Infamous Formula,'SNR = 6.02N + 1.76dB,' and Why You Should Care," Analog Devices, Norwood, MA, MT-001, 2008.

[171] C. Man, "Quantization Noise: An Expanded Derivation of the Equation, SNR = 6.02 N + 1.76 dB," Analog Devices, Norwood, MA, MT-229, 2010.

[172] M. Cazalilla, N. Lorente, R. Muiño, J.-P. Gauyacq, D. Teillet-Billy, and P. Echenique, "Theory of Auger Neutralization of Ions at the Surface of a Diamond-Type Semiconductor," *Physical Review B*, vol. 122, no. 1, pp. 13991–14006, Nov. 1961.

[173] M. Kireeff Covo et al., "Beam energy scaling of ion-induced electron yield from K^{+} impact on stainless steel," *Physical Review Special Topics - Accelerators and Beams*, vol. 9, no. 6, p. 063201, Jun. 2006.

[174] H. Hagstrum, "Theory of Auger Ejection of Electrons from Metals by Ions," *Physical Review*, vol. 96, no. 2, pp. 336–365, Oct. 1954.

[175] L. M. Kishinevsky, "Estimation of electron potential emission yield dependence on metal and ion parameters," *Radiation Effects*, vol. 19, no. 1, pp. 23–27, Jan. 1973.

[176] P. Thieberger, A. L. Hanson, D. B. Steski, V. Zajic, S. Y. Zhang, and H. Ludewig, "Secondary Electron Yields and Their Dependence on the Angle of Incidence on Stainless Steel Surfaces for Three Energetic Ion Beams," Brookhaven National Laboratory, Upton, New York, BNL/SNS Tech. Note 064, 1999.

[177] T. A. Thornton and J. N. Anno, "Secondary electron emission from 0.5–2.5-MeV protons and deuterons," *Journal of Applied Physics*, vol. 48, no. 4, p. 1718, 1977.

[178] E. Sternglass, "Theory of Secondary Electron Emission by High-Speed Ions," *Physical Review*, vol. 108, no. 1, pp. 1–12, Oct. 1957.

[179] J. F. Ziegler, J. P. Biersack, and M. D. Ziegler, *SRIM - The Stopping and Range of Ions in Matter*, Second. Morrisville, NC: SRIM Co., 2009.

[180] D. Hasselkamp, *Particle Induced Electron Emission II*. New York, NY: Springer-Verlag, 1992.

[181] P. Stoltz, M. Furman, J.-L. Vay, A. Molvik, and R. Cohen, "Numerical simulation of the generation of secondary electrons in the High Current Experiment," *Physical Review Special Topics - Accelerators and Beams*, vol. 6, no. 5, p. 054701, May 2003.

[182] S. Kato and M. Nishiwaki, "Secondary Electron Emission from Metals and Graphites," in *Accelerator Technical Design Report for J-PARC*, Tsukuba, Japan: JAERI/KEK Accelerator Group, 2003, pp. 7–13. [Online]. Available: http://hadron.kek.jp/~accelerator/TDA/tdr2003/.

[183] S. Nath et al., "BEAM BEHAVIOR THROUGH THE SNS CHOPPER SYSTEM," in *LINAC2002*, 2002, pp. 2–4.

[184] W. S. Levine, Ed., *The Control Handbook*. Boca Raton, FL: CRC Press Inc., 1996, p. 158.

[185] T. J. Sobering, “Bandwidth and Risetime,” Kansas State University, Manhattan, KS, Technote 2, 2002.

[186] R. K. R. Yarlagadda, *Analog and Digital Signals and Systems*. Boston, MA: Springer US, 2010.

[187] G. Metzger and J. P. Vabre, *Transmission Lines with Pulse Excitation*. New York, NY: Academic Press Inc., 1969, p. 5.

[188] Agilent, “Network Analyzer Basics,” *Analysis*. pp. 1–94, 1998.

[189] G. B. Arfken and H. J. Weber, *Mathematical Methods for Physicists*, Sixth. Burlington, MA: Elsevier Academic Press, 2005, pp. 952–53.

[190] G. E. J. Valley and H. Wallman, Eds., *Vacuum Tube Amplifiers*. New York, NY: Dover Publications Inc., 1948, p. 77.

[191] A. Polisetti, C. Deibele, M. Schulte, and S. Assadi, “De-embedding a Cable Using FIR Signal Processing Techniques.” .

[192] E. B. Rosa, “The Self and Mutual Inductances of Linear Conductors,” *Bullietin of the Bureau of Standards*, vol. 4, no. 2, pp. 301–344, 1907.

[193] C. E. Shannon, “Communication In The Presence Of Noise,” *Proceedings of the IEEE*, vol. 86, no. 2, pp. 447–457, Feb. 1998.

[194] “Macor,” *Corning Inc.: Lighting & Materials*, 2009. [Online]. Available: http://psec.uchicago.edu/ceramics/MACOR Data Sheet.pdf.

[195] “Summary of Properties for Kapton Polyimide Films,” *Dupont*, 2012. [Online]. Available: http://www2.dupont.com/Kapton/en_US/assets/downloads/pdf/summaryofprop.pdf.

[196] F. Hecht, “FreeFem++ v3.23,” 2013. [Online]. Available: http://www.freefem.org/ff++/index.htm. [Accessed: 08-Dec-2013].

[197] “COMSOL,” 2013. [Online]. Available: http://www.comsol.com/. [Accessed: 08-Dec-2013].

[198] D. W. Williams and W. T. Williams, “Initiation of electrical breakdown in vacuum,” *Journal of Physics D: Applied Physics*, vol. 6, no. 6, pp. 734–743, Apr. 1973.

[199] G. Bacchin, F. Forlani, and N. Minnaja, “Electrical breakdown in ultrahigh vacuum,” *Il Nuovo Cimento B Series 10*, vol. 46, no. 1, pp. 128–131, Nov. 1966.

[200] F. Paschen, “Ueber die zum Funkenübergang in Luft, Wasserstoff und Kohlensäure bei verschiedenen Drucken erforderliche Potentialdifferenz,” *Annalen der Physik*, vol. 273, no. 5, pp. 69–96, 1889.

[201] D. Alpert, D. A. Lee, E. M. Lyman, and H. E. Tomaschke, “Initiation of Electrical Breakdown in Ultrahigh Vacuum,” *Journal of Vacuum Science and Technology*, vol. 1, no. 2, p. 35, Nov. 1964.

[202] L. Cranberg, “The Initiation of Electrical Breakdown in Vacuum,” *Journal of Applied Physics*, vol. 23, no. 5, pp. 518–522, 1952.

[203] V. A. Nevrovsky, “Clump Hypothesis and Mechanisms of Breakdown Initiation in Centimeter Vacuum Gaps,” in *2006 International Symposium on Discharges and Electrical Insulation in Vacuum*, 2006, pp. 45–47.

[204] S. Humpheries, “Electric field limits for vacuum breakdown,” *Field Precision Software Tips*, 2011. [Online]. Available: http://fieldp.com/myblog/2011/electric-field-limits-vacuum-breakdown/.

[205] “Properties, Alumina Material,” *Superior Technical Ceramics*, 2010. [Online]. Available: www.ceramics.net.

[206] H. C. Miller, “Surface Flashover of Insulators,” *IEEE Transactions on Electrical Insulation*, vol. 24, no. 5, pp. 765–786, 1989.

[207] H. C. Miller, “Flashover of insulators in vacuum: review of the phenomena and techniques to improved holdoff voltage,” *IEEE Transactions on Electrical Insulation*, vol. 28, no. 4, pp. 512–527, 1993.

[208] Tumiran, M. Maeyama, H. Imada, S. Kobayashi, and Y. Saito, “Flashover from surface charge distribution on alumina insulators in vacuum,” *IEEE Transactions on Dielectrics and Electrical Insulation*, vol. 4, no. 4, pp. 400–406, 1997.

[209] A. S. Pillai and R. Hackam, “Surface flashover of solid insulators in atmospheric air and in vacuum,” *Journal of Applied Physics*, vol. 58, no. 1, pp. 146–153, Oct. 1985.

[210] A. S. Pillai and R. Hackam, “Modification of electric field at the solid insulator–vacuum interface arising from surface charges on the solid insulator,” *Journal of Applied Physics*, vol. 54, no. 3, p. 1302, 1983.

[211] T. Takuma, “Field behaviour at a triple junction in composite dielectric arrangements,” *IEEE Transactions on Electrical Insulation*, vol. 26, no. 3, pp. 500–509, Jun. 1991.

[212] T. Kawamoto and T. Takuma, “Abnormality of electric field at a wedgelike edge of a

conductor or a dielectric interface and methods for its relaxation," *Electrical Engineering in Japan*, vol. 159, no. 1, pp. 1–8, Apr. 2007.

[213] T. Takuma and T. Kawamoto, "Field enhancement at a triple junction in arrangements consisting of three media," *IEEE Transactions on Dielectrics and Electrical Insulation*, vol. 14, no. 3, pp. 566–571, Jun. 2007.

[214] W. Stygar et al., "Flashover of a vacuum-insulator interface: A statistical model," *Physical Review Special Topics - Accelerators and Beams*, vol. 7, no. 7, pp. 1–21, Jul. 2004.

[215] M. S. Chung, B.-G. Yoon, P. H. Cutler, and N. M. Miskovsky, "Theoretical analysis of the enhanced electric field at the triple junction," *Journal of Vacuum Science & Technology B: Microelectronics and Nanometer Structures*, vol. 22, no. 3, p. 1240, 2004.

[216] A. S. Pillai and R. Hackam, "Influence of metal-insulator junction on surface flashover in vacuum," *Journal of Applied Physics*, vol. 61, no. 11. p. 4992, 1987.

[217] J. M. Wetzer and P. A. A. F. Wouters, "HV Design of Vacuum Components," in *IEEE Transactions on Dielectrics and Electrical Insulation*, 1995, vol. 2, no. 2, pp. 202–209.

[218] Y. Polsky, "Private Communication." .

[219] "Product Datasheet: 10 Mesh T304 Stainless . 025 " Wire Dia . 36 Inch Wide," *TWP Inc.*, 2013. [Online]. Available: http://www.twpinc.com/wire-mesh/TWPCAT_12/p_010X010S0250W36T.

[220] J. Tuozzolo, J. Brodowski, G. Danby, J. Jackson, and W. Meng, "Magnets for the National Spallation Neutron Source Accumulator Ring," in *Proceedings of the 1997 Particle Accelerator Conference (Cat. No.97CH36167)*, 1998, vol. 3, pp. 3233–3235.

[221] R. Thern, "BOOSTER RING CORRECTION MAGNETS," Brookhaven National Laboratory, Upton, New York, Tech. Note 224, 1994.

[222] T. Hunter, S. Heimsoth, D. LeBon, R. McBrien, and J. G. Wang, "Progress and Status in SNS Magnet Measurements at ORNL," in *Proceedings of the 2005 Particle Accelerator Conference*, 2005, pp. 609–611.

[223] T. Zickler, "Basic design and engineering of normal-conducting, iron-dominated electromagnets," in *CERN Accelerator School CAS 2009: Specialized Course on Magnets (CERN-2010-004)*, 2011, pp. 65–102.

[224] A. G. Clegg, P. Beckley, E. C. Snelling, and R. V. Major, "Magnetic Materials," in

Electrical Engineer's Reference Book, Sixteenth., M. A. Laughton and D. F. Warne, Eds. Burlington, MA: Elsevier Science, 2003.

[225] A. Wolski, "Maxwell's Equations for Magnets," in *CERN Accelerator School CAS 2009: Specialized Course on Magnets (CERN-2010-004)*, 2011, pp. 1–38.

[226] A. K. Jain and P. Wanderer, "Accelerator Magnets," in *Handbook of Accelerator Physics and Engineering*, A. W. Chao and M. Tigner, Eds. Singapore: World Scientific Publishing Co. Pte. Ltd., 1998, p. 406.

[227] K. Halbach, "Special Topics in Magnetics," in *Handbook of Accelerator Physics and Engineering*, A. W. Chao and M. Tigner, Eds. Singapore: World Scientific Publishing Co. Pte. Ltd., 1998, p. 446.

[228] J. G. Wang, "Private Communication." .

[229] S.-V. Badea, N. Tsoupas, J. Tuozzolo, and J. Alduino, "BUILDING A FAMILY OF CORRECTOR MAGNETS FOR SNS FACILITY," in *PAC 2003*, 2003, pp. 2138–2140.

[230] "Virtual Catalog," *Accu-Glass Products, Inc.*, 2013. [Online]. Available: http://accuglassproducts.com/virtual_catalog.php.

[231] M. A. Plum, W. Christensen, R. E. M. Sr, and C. R. Rose, "THE SNS LINAC WIRE SCANNER SYSTEM," in *Particle Accelerator Conference*, 2003, pp. 2485–2487.

[232] "404XE Catalog," *Parker Hannifin Corporation*, 2009. [Online]. Available: http://divapps.parker.com/divapps/emn/pdf/XE/404XE.pdf.

[233] C. Long, "Private Communication." .

[234] T. Weiland and R. Wanzenberg, "Wake Fields and Impedances," in *Joint US-CERN PAS*, 1990, pp. 1–54.

[235] F. Zhou, "Wakefield Induced Correlated Energy Spread and Emittance Growth at TTF FEL," DESY-MPY, Hamburg, Germany, TESLA FEL-Report 1999-05, 1999.

[236] "Honeycomb Ventilation Panels (3000 series)," *MAJR Products*, 2013. [Online]. Available: http://majr.com/emi-rfi-product/shielded-ventilation-panels-3000-series/honeycomb-ventilation-panels/.

[237] "Series 8000 Honeycomb Vents," *Tech-Etch*, 2011. [Online]. Available: http://www.tech-etch.com/shield/8000series.html.

[238] A. Hong, "Dielectric Strength of Air," *The Physics Factbook*, 2000. [Online].

Available: http://hypertextbook.com/facts/2000/AliceHong.shtml.

[239] "Araldite - CW1312/HY1300 - Encapsulant, Epoxy," *Farnell element 14*, 2013. [Online]. Available: http://uk.farnell.com/araldite/cw1312-hy1300/encapsulant-epoxy-1kg/dp/147590?Ntt=cw1312.

[240] H. D. Young and R. A. Freedman, *Sears and Zemansky's University Physics: with Modern Physics*, 11th ed. San Francisco, CA: Addison-Wesley, 2003.

[241] J. W. Rohlf, *Modern Physics from alpha to Z0*. Weinheim, Germany: John Wiley & Sons, 1994.

[242] C. R. Nave, "Mean Free Path, Molecular Collisions," 2010. [Online]. Available: http://hyperphysics.phy-astr.gsu.edu/hbase/kinetic/menfre.html#c2. [Accessed: 06-Apr-2012].

[243] M. Nič, J. Jirát, B. Košata, A. Jenkins, and A. McNaught, Eds., *IUPAC Compendium of Chemical Terminology*, 2nd ed. Research Triagle Park, NC: IUPAC, 2009.

[244] E. B. Podgorsak, *Radiation Physics for Medical Physicists*, Second. Heidelberg, Germany: Springer, 2010.

[245] S. T. Thornton and A. Rex, *Modern Physics for Scientists and Engineers*, Third. Boston, MA: Brooks/Cole, Cengage Learning, 2005.

[246] R. P. Feynman, R. B. Leighton, and M. Sands, *The Feynman Lectures on Physics: Volume II*, First. Reading, MA: Addison-Wesley, 1968, pp. 26–3.

[247] T. P. Wangler, *RF Linear Accelerators*. Weinheim, Germany: Wiley-VCH Verlag GmbH & Co. KGaA, 2008, pp. 203–205.

[248] R. Sternheimer, S. Seltzer, and M. Berger, "Density effect for the ionization loss of charged particles in various substances," *Physical Review B*, vol. 26, no. 11, pp. 6067–6076, Dec. 1982.

[249] D. K. Brice, "Stopping powers for electrons and positrons (ICRU report 37; International commission on radiation units and measurements, Bethesda, Maryland, USA, 1984)," *Nuclear Instruments and Methods in Physics Research Section B: Beam Interactions with Materials and Atoms*, vol. 12, no. 1, pp. 187–188, Aug. 1985.

[250] J. H. Miller, W. E. Wilson, S. T. Manson, and M. E. Rudd, "Differential cross sections for ionization of water vapor by high-velocity bare ions and electrons," *The Journal of Chemical Physics*, vol. 86, no. 1, p. 157, 1987.

[251] S. G. Lias, "Ionization Energy Evaluation," in *NIST Chemistry WebBook, NIST*

Standard Reference Database Number 69, P. J. Linstrom and W. G. Mallard, Eds. Gaithersburg, MD: National Institute of Standards and Technology. [Online]. Available: http://webbook.nist.gov. [Accessed: 12-Jul-2012].

[252] G. Choppin, J.-O. Liljenzin, and J. Rydberg, *Radiochemistry and Nuclear Chemistry*, 3rd ed. Woburn, MA: Butterworth-Heinemann, 2002.

[253] M. Jarrell and C. Ebner, "Chapter Thirteen: Charged Particle Collisions , Energy Loss , Scattering," 2001. [Online]. Available: http://www.phys.lsu.edu/~jarrell/COURSES/ELECTRODYNAMICS/Chap13/chap13.pdf. [Accessed: 18-Jul-2012].

[254] S. Y. Lee, *Accelerator Physics*, 2nd ed. Toh Tuck Link, Singapore: World Scientific Publishing Co. Pte. Ltd., 2004.

Appendices

Appendix A

Model Assumptions

Fundamental Interactions

Of the observable fundamental interactions, strong, weak, electromagnetic and gravity, the strong force, responsible for holding protons and neutrons together in the nucleus and quarks together to form hadrons, is the strongest. The relative strengths of these forces, e.g. weak and strong, may be compared through their dimensionless coupling constants that determine the strength of the force in an interaction. From observed data it has been found that the nuclear strong force coupling constant $\alpha_s \approx 1$ [240]. The electromagnetic force coupling constant is known as the "fine structure constant" and is defined as $= e^2/4\pi\varepsilon_0\hbar c = 1/137$. Thus, the strong force is two orders of magnitude stronger than the electromagnetic force.

The strengths of the weak and strong forces may be compared through decay times for separate processes governed by each that yield the same products. The result is that $\alpha_w/\alpha_s \approx 10^{-6}$ [241]. The ratio of the gravitational force to the electromagnetic force is found by dividing the force due to gravity between two particles by the force due to the electric field of those same two particles. Using the forces between an electron and a proton, since the orbital electrons are the primary interaction particle with the incident proton, this yields $\alpha_g/\alpha = F_{gravity}/F_{electric} = 4.4 \times 10^{-40}$ so $\alpha_g \approx 10^{-42}\alpha_s$. Because gravity and the weak force are orders of magnitude smaller than the strong and electromagnetic forces, they constitute negligible contributions to the interaction between a charged particle and an absorbing medium.

The electromagnetic interaction expressed by the Lorentz force,

$$\vec{F} = q\left(\vec{E} + \vec{v} \times \vec{B}\right), \tag{A.1}$$

has infinite range, as seen by the $1/r^2$ behavior of both the electric field contribution in Coulomb's law

$$\overrightarrow{E'} = \frac{1}{4\pi\varepsilon_0}\frac{q}{r^2}\hat{r} \tag{A.2}$$

where ε_0 is the permittivity of free space, and the magnetic field of a charge q moving with constant velocity $\vec{v}$,

$$\vec{B} = \frac{1}{c^2}\vec{v} \times \vec{E} = \frac{\mu_0}{4\pi} q \frac{\vec{v} \times \hat{r}}{r^2} \tag{A.3}$$

where r is the distance from the charge to the observation point and $\hat{r}$ is the unit vector in the direction of r. While the strong force is the strongest of the possible interactions, its range is on the order of a few femtometers. Therefore, the nuclear interaction cross-section is typically less than that for Coulomb interactions. This fact coupled with the low IPM gas density, makes the probability of nuclear reactions negligible.

The magnitude of the transverse component of the magnetic field of a relativistic charged particle with velocity $\beta_p c$ may be shown (see Appendix C for a derivation of relativistic charged particle fields) to be

$$|B_\perp| = \frac{\beta_p}{c}|E_\perp|. \tag{A.4}$$

The magnetic component of the Lorentz force (A.1) experienced by an orbital electron with charge q and velocity $\beta_e c$ due to a relativistic projectile is then

$$\vec{F}_B = q\vec{\beta}_e c \times \vec{B} \Rightarrow F_B = q\beta_e c B_\perp = q\beta_e\beta_p E_\perp = \beta_e\beta_p F_E \tag{A.5}$$

where $F_E = qE$ is the magnitude of the electric field portion of the Lorentz force. The orbital

velocity of a ground state electron is related to the speed of light and the fine structure constant as c/α, which is $0.007c$. Using this with the SNS proton velocity of $\beta_p = 0.86c$, we obtain a magnetic field component which is 0.6% that of the electric field. Therefore, the magnetic field may be considered as a negligible contribution to the ionizing force.

Coulomb interactions between high energy protons and residual gas molecules are the primary mechanism for the energy transfer required for ionization in the IPM. Elastic collisions are those in which energy is transferred from one particle to another but the total kinetic energy and momentum is conserved. Collisions in which a negligible fraction of kinetic energy is transferred to the target particle are also considered elastic. Coulomb scattering is the general term used to describe elastic Coulomb collisions, and most interactions can be characterized as elastic within certain limits. In inelastic collisions, kinetic energy is transformed into intrinsic energy such as nuclear excitation, atomic excitation, ionization, radiation, or charge exchange. However, in the IPM residual gas, it is not necessary to consider all electromagnetic energy transfer processes.

As with the case of nuclear interactions via the strong force, nuclear excitations to higher energy states due to Coulomb collisions with the nucleus are negligible. Bremsstrahlung is a form of electromagnetic radiation produced by the deceleration, or deflection, of an energetic charged particle by another. While it is possible to produce bremsstrahlen through inelastic Coulomb collisions of beam protons with the nucleus of a gas molecule, the process is negligible due to the mass dependence of the bremsstrahlung cross section and the high mass of baryons.

Charge exchange, the process by which a charge is transferred from a neutral atom or molecule to an ion, is normally the most important inelastic collision due to the relatively

small amount of energy required when to compared to other processes. However, for the case of 1 GeV protons, $v^2/u^2 \gg 1$, where *v* is the relative velocity and *u* is the atomic electron velocity. In this highly energetic region the charge exchange cross-section falls off very rapidly with increasing relative velocity *v*. For example, the cross-section falls off as v^{-12} for the transfer of a 1*s* neutral gas electron into a 1*s* state with the proton. Charge exchange may therefore be considered inconsequential when compared to ionization and excitation cross-sections that fall off as $v^{-2}\log \alpha v$ [19].

Coherent effects arise from the diffraction of the incoming particle wave with the target particle as well as interference produced by the superposition of incident and diffracted waves from several atoms at once. This type of scattering is primarily governed by the interatomic spacing given by the mean free path between particles $\ell = (n\sigma)^{-1}$ where *n* is the particle density and σ is the particle cross-section. The mean free path, defined as the average distance between collisions, in an ideal gas of identical particles having a Maxwellian distribution with temperature *T* and pressure *P*, can be shown [242] to be

$$\ell = \frac{k_B T}{\sqrt{2}\pi d^2 P} \tag{A.6}$$

where k_B is Boltzmann's constant and *d* is the diameter of the gas molecule. For a nominal IPM of pressure of 2.0×10^{-8} Torr and an average molecular diameter of 2.8 Å, the mean free path of the IPM gas prior to beam passage is 4.2 km. The de Broglie wavelength for a 1 GeV proton is 7.8×10^{-16} m. Because coherent scattering requires the wavelength of the incident particle be on the order of the interatomic distance between target particles, the proton wavelength $\lambda \ll \ell$ means that coherent scattering can be ignored.

Energetic heavy charged particles primarily lose energy through incoherent inelastic

Coulomb collisions with orbital electrons resulting in excitation and ionization. In excitation, atomic electrons absorb energy exactly equal to the energy between electronic excitation states. Due to the $1/r^2$ behavior of the Coulomb force and to screening by the inner electrons, the outermost electrons are most weakly bound to the nucleus and therefore require the least energy to remove. This energy is referred to as the ionization energy, while the term binding energy is used to refer to the energy required to remove all of the electrons from an atom [243]. When analyzing the energy transfer required for ionization, the complicated case of proton collisions with gaseous molecules can be simplified to collisions with the valence electron having the least ionization energy.

Point-Particle Assumption

Additional simplifications may be made. The 1 GeV proton de Broglie wavelength is small compared to the electron wavelength of ~10^{-9} m and to atomic dimensions of ~10^{-10} m. Therefore, diffraction effects with individual atoms or electrons are negligible and the proton can be regarded as a point particle, thus allowing collisions to be treated classically. The kinetic energy of gas molecules derived from kinetic theory and the ideal gas law allow for the calculation of the root-mean-squared velocity for ideal gas molecules with temperature *T* and mass *m* through the equation

$$v_{rms} = \sqrt{\frac{3k_B T}{m}}. \tag{A.7}$$

As seen in section 2.2.1, the lightest molecule in the IPM residual gas is the hydrogen molecule H_2 and thus characterizes the fastest gas particle. Using the hydrogen molecule mass and a temperature of 297 K, equation (A.7) gives an RMS velocity of 1914 m/s. The proton velocity is 5 orders of magnitude larger and the residual gas can be considered to be at

rest. Likewise, the velocity of a ground state electron is less than 1% the speed of light, and so the energetic protons collide with orbital electrons that are assumed to be at rest.

Appendix B

Cross Section & Rutherford Scattering

Center-of-Mass Frame

Elastic coulomb scattering, also known as Rutherford scattering after Earnest Rutherford whose experiments and derivations helped define the current atomic structure, can be derived classically by studying the kinematics of elastic collisions between charged particles interacting through the Coulomb force. The same result may be acquired with quantum mechanics as well and may be found in [244].

Consider a projectile particle of mass *m* and initial momentum $P_{P_i} = mv_0$ with initial position $\vec{r}_{P_i}$ incident on a target particle with mass *M*, initial $\vec{r}_{T_i}$ position, and momentum $P_{T_i} = 0$ in the Lab frame. The center-of-mass position vector and velocity vector, $\vec{R}_{CM}$ and $\vec{V}_{CM}$, are given by

$$\vec{R}_{CM} = \frac{m\vec{r}_P + M\vec{r}_T}{m + M} \tag{B.1}$$

$$\vec{V}_{CM} = \frac{m\vec{v}_P + M\vec{v}_T}{m + M} \tag{B.2}$$

$$m_r = \frac{mM}{m + M} \tag{B.3}$$

where $\vec{v}_P$ and $\vec{v}_T$ are the projectile and target velocities and m_r is the reduced mass. Figure B.1 shows a scattering diagram in the lab frame where the particles are separated by an impact parameter *b* defined as the perpendicular distance between the projectile velocity $\vec{v}_T$ and the target.

A collision is specified by scattering angles φ and ψ by representing the collision in

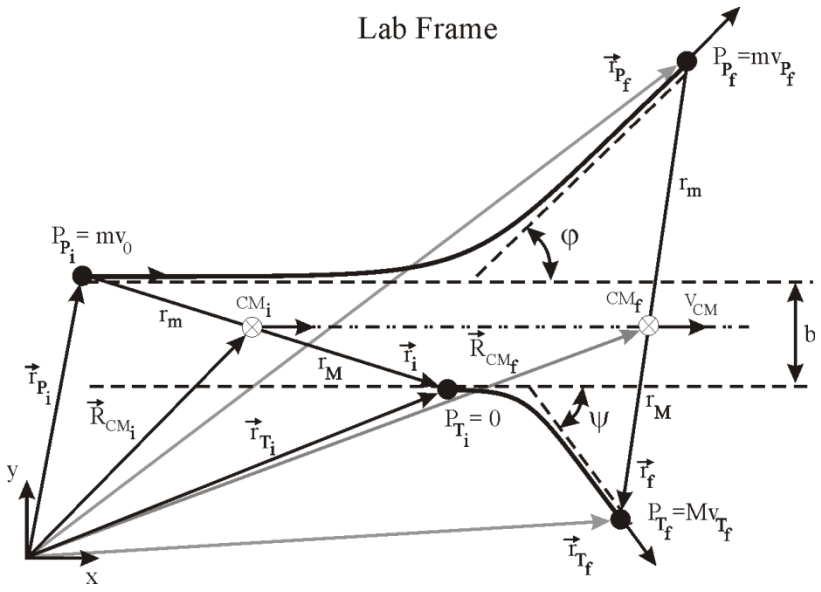

Figure B.1 Lab frame representation of scattering of projectile P by target T separated by impact parameter b where subscript i indicates initial values and subscript f denotes final values. r_m and r_M are the respective distances from the projectile and target particles to the center of mass at a particular time.

the center-of-mass frame as depicted in figure B.2 (a) where the origin is coincident with the center of mass. In the center-of-mass frame an elastic collision is defined as having the total momentum, energy, and angular momentum conserved throughout the interaction and may be described by a single scattering angle θ. It can be shown [244] that particles interacting through a 1/r potential such as the electromagnetic interaction will have trajectories given by hyperbolas with the hyperbolic line of symmetry passing through the center of mass in the center-of-mass frame, as shown in figure B.2 (a). The force equations of projectile and target position vectors $\vec{r}_P$ and $\vec{r}_T$, are given by Newton's second and third laws as

$$\vec{F}_P = m\frac{d^2\vec{r}_P}{dt^2} \tag{B.4}$$

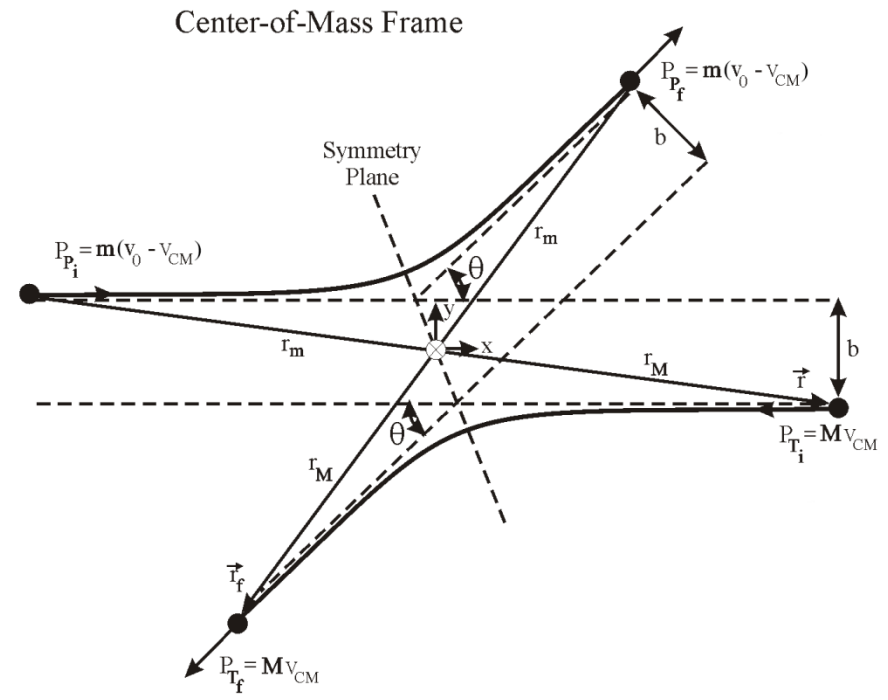

(a)

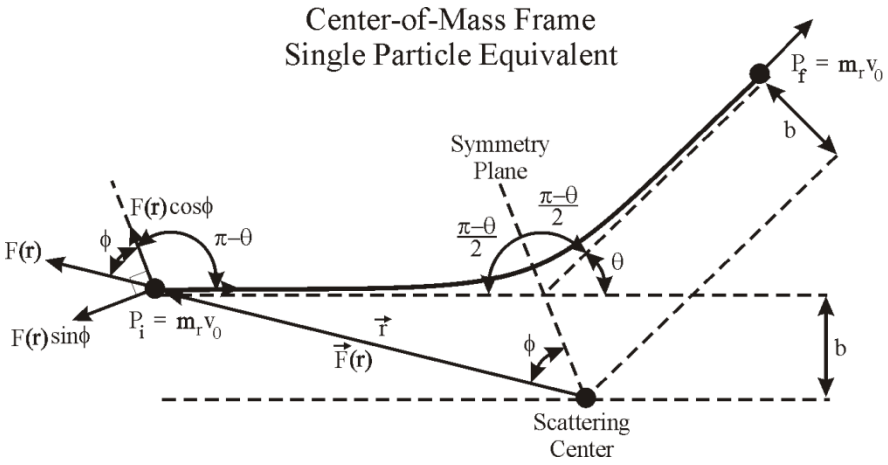

(b)

Figure B.2 (a) Two particle collision in the center of mass reference frame. (b) Single particle equivalent of two-particle collision via a radial force $\vec{F}(r)$.

$$\vec{F}_T = M\frac{d^2\vec{r}_T}{dt^2} = -\vec{F}_P \tag{B.5}$$

Multiplying equation (B.4) by *M* and (B.5) by *m* and subtracting (B.5) from (B.4) gives the force on the projectile

$$\vec{F}_P = m_r\frac{d^2}{dt^2}(\vec{r}_P - \vec{r}_T) \tag{B.6}$$

where $\vec{r} = \vec{r}_P - \vec{r}_T$ is the position vector from the target particle to the projectile. Equation (B.6) allows for the interaction between two particles to be replaced by an equivalent system of one particle in a central field with reduced mass m_r as shown in figure B.2 (b). A particle moving in a central repulsive field has a hyperbolic trajectory with the scattering center located at the hyperbola's outer focus, while for attractive fields, such as when the interacting particles have opposite charges, the scattering center is at the inner focus.

Impact Parameter

The change in momentum can be calculated using the impulse equation and Coulomb force. Due to the cancelation of the component of force perpendicular to the symmetry line in Figure B.2 (b), the change in momentum is along the symmetry. From the Coulomb force between the projectile with charge q_m and target q_M

$$\vec{F} = \frac{1}{4\pi\varepsilon_0}\frac{q_m q_M}{r^2}\hat{r}, \tag{B.7}$$

the change in momentum is found to be

$$I = \Delta P = \int_{-\infty}^{\infty} F\,dt = 2\int_0^{\infty} F\cos\phi\;dt = 2\frac{q_m q_M}{4\pi\varepsilon_0}\int_0^{\infty}\frac{\cos\phi}{r^2}\,dt \tag{B.8}$$

where ϕ is the angle between the line of symmetry and the projectile position vector. From the scattering geometry, shown in figure B.3, along with the elastic collision condition that

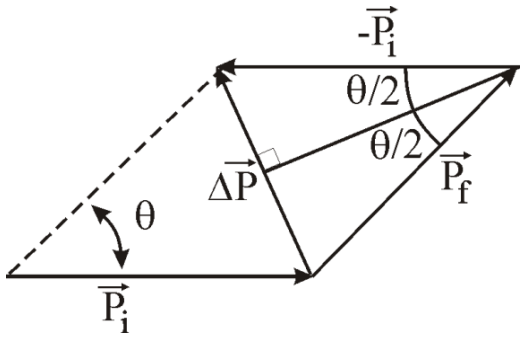

Figure B.3 Scattering geometry for an elastic collision giving the change in momentum as a function of initial momentum and scattering angle.

$\left|\vec{P}_i\right| = \left|\vec{P}_f\right|$ the change in momentum is found to be

$$\Delta P = 2m_r v_0 \sin\frac{\theta}{2}. \tag{B.9}$$

Since *b* is perpendicular to the momentum at all times

$$\vec{L} = \vec{r} \times \vec{P} \Rightarrow m_r v_0 b = m_r r^2 \frac{d\phi}{dt}. \tag{B.10}$$

Solving (B.10) for r^2 and substituting into (B.8), along with a change of limits to the angle between the symmetry line and the hyperbolic asymptotes, gives

$$2\frac{q_m q_M}{4\pi\varepsilon_0}\frac{1}{v_0 b}\int_0^{\frac{\pi-\theta}{2}} \cos\phi \; d\phi = 2m_r v_0 \sin\frac{\theta}{2}. \tag{B.11}$$

By integrating equation (B.11) and solving for the impact parameter *b* can be found to be related to the scattering angle through

$$b = \frac{q_m q_M}{4\pi\varepsilon_0 m_r {v_0}^2}\cot\frac{\theta}{2} = d\cot\frac{\theta}{2} \tag{B.12}$$

where

$$d = \frac{q_m q_M}{4\pi\varepsilon_0 m_r {v_0}^2} \tag{B.13}$$

is the distance of closest approach in a head-on collision when $b = 0$ and $\theta = \pi$.

Cross Section

When studying the interactions between energetic particles impinging on matter, the interaction cross-section concept is often used to express the probability of a particular process occurring. The basic concept is derived from the purely classical picture of point-like particles incident on an area A that encloses spherical volumes with cross-section σ centered on each target particle. The volumes are defined such that there is a 100% probability of interaction if the incident particle lands within the sphere and 0% if it does not.

The classical model can be extended to more accurate representations as seen in figure B.4 where the thickness of the target matter, dx, is small enough to ensure that no cross-sectional areas overlap and that the target area A includes n targets per unit volume, each with cross-section σ. The probability of an interaction P is then

$$P = \frac{interaction\ area}{total\ area} = \frac{n\sigma A\ dx}{A} = n\sigma\ dx \tag{B.14}$$

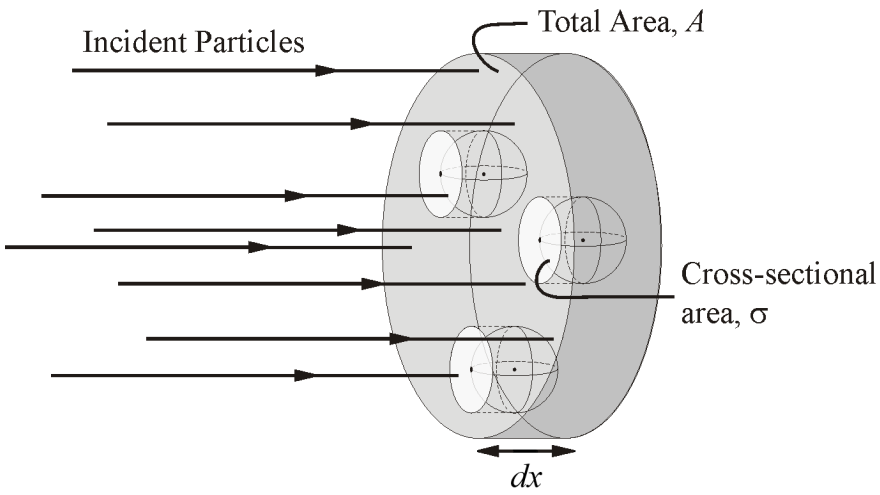

Figure B.4 Physical model of classical cross section.

where the cross-section, while still carrying the dimensions of area, is dependent on many factors. These include type of interaction, particle energy, as well as size and structure of the target, where σ is visualized more as a probability than a physical area. Not only can the cross-section have different values for the same target material depending on incident particle energy and type but different types of collision cross-sections for different physical processes, such as elastic, inelastic or nuclear scattering. These can vary as well and can be summed as

$$\sigma_{Total} = \sigma_{Elastic} + \sigma_{Inelastic} + \sigma_{Nuclear} \tag{B.15}$$

to give a total cross-section [80].

Differential Scattering Cross-Section

It is also useful to define cross-sections that give a measure of the spatial distribution of particles scattering off of matter. The principle is illustrated in figure B.5 where particles incident on a scattering center q will be scattered into a solid angle $d\Omega_s$ which is a two-dimensional angle whose vertex is coincident with the scattering center and describes a cone of observance defined by scattering angle between θ and $\theta + d\theta$. The differential cross-section is defined to be the scattered intensity I_s (the number of particles scattered into a solid angle $d\Omega$ at a given angle θ per unit of solid angle per time) divided by the incident intensity I_o (the number of incident particles per scattering center per area per time) as

$$\frac{d\sigma}{d\Omega} = \frac{I_s}{I_0} = \frac{Scattered\ Intensity}{Incident\ Intensity}. \tag{B.16}$$

The solid angle is subtended by an object projected on the surface of a sphere. In a similar way an arc is related to the angle it subtends, $s = r\theta$, the area of a cap on the surface of a sphere with radius r is $A = \Omega r^2$. The element of solid is defined in relation to the

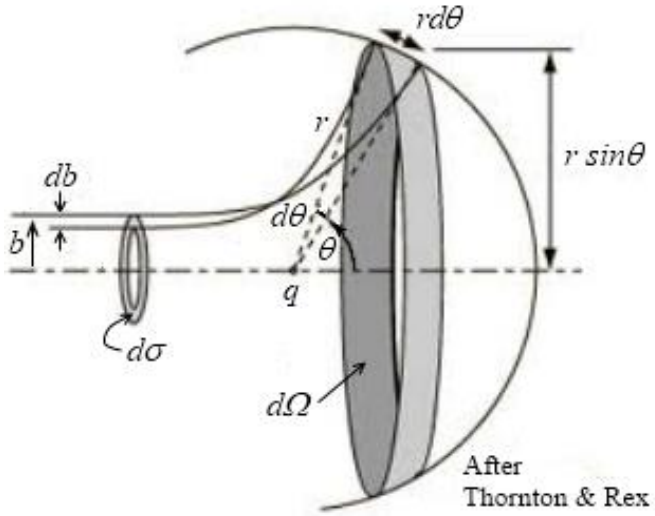

Figure B.5 Physical representation of the differential scattering cross-section[16] [245]**.**

spherical angles θ and ϕ for the unit circle as $d\Omega = sin\theta\ d\theta d\phi$. For the axial symmetric case shown in figure B.5,

$$d\Omega = \frac{dA}{r^2} = \frac{(rd\theta)\cdot(2\pi r\ sin\theta)}{r^2} = 2\pi\ sin\theta\ d\theta. \tag{B.17}$$

The probability of scattering into $d\Omega_s$ is then given by equation (B.16) where the total cross section is

$$\sigma = \int \frac{d\sigma}{d\Omega} d\Omega. \tag{B.18}$$

The number of particles scattered between the angles θ and $\theta + d\theta$ is equal to the number incident N_I with impact parameters between b and $b+db$ which traces an annulus with cross-sectional area $d\sigma$, as illustrated in Figure B.5. Given an incident intensity I_0,

[16] Modified from THORNTON/REX. Modern Physics for Scientists and Engineers, 2E. © 2000 Brooks/Cole, a part of CengageLearning, Inc. Reproduced by permission. www.cengage.com/permissions

$$N_I = I_0 d\sigma = I_0 2\pi b\, db = I_0 2\pi b \left|\frac{db}{d\theta}\right| d\theta \tag{B.19}$$

where the modulus of $db/d\theta$ must be taken in order to maintain a positive number of incident particles since the impact parameter decreases with increasing θ making the slope negative. The differential cross section may be obtained by using the equation for the impact parameter (B.13) and its derivative with respect to θ

$$\frac{db}{d\theta} = -\frac{d}{2}\frac{1}{\sin^2\frac{\theta}{2}} \tag{B.20}$$

along with the double angle formula $\sin 2x = 2\sin x \cos x$ and the definition of the element of unit solid angle (B.17),

$$I_0 d\sigma = I_0 2\pi\, d\cot\frac{\theta}{2}\,\frac{d}{2}\frac{1}{\sin^2\frac{\theta}{2}} = I_0\frac{d^2}{4}\frac{1}{\sin^4\frac{\theta}{2}}\,2\pi\sin\theta\, d\theta = I_0\frac{d^2}{4}\frac{1}{\sin^4\frac{\theta}{2}}d\Omega. \tag{2.21}$$

The resulting differential scattering cross section then becomes

$$\frac{d\sigma}{d\Omega} = \frac{d^2}{4}\frac{1}{\sin^4\frac{\theta}{2}} = \frac{1}{4}\left(\frac{Z_m Z_M e^2}{4\pi\varepsilon_0 pv}\right)^2 \frac{1}{\sin^4\frac{\theta}{2}} \tag{B.22}$$

where Z_m and Z_M are the projectile and target charge number, p and v are the momentum and velocity of the projectile. Equation (B.22) is the differential Rutherford scattering cross section for the case where $m \ll M$, while also neglecting target recoil. In the limit where the projectile mass is much smaller than the target mass, the reduced mass $m_r \cong m$. It is important to note that expression (B.22) is the same for like charges or opposite charge. It is also valid for relativistic particles with momentum $p = \gamma\beta mc$.

Appendix C

Relativistic Beam Characteristics

In order to gain a complete understanding of relativistic energy transfer leading to residual gas ionization, it is necessary to analyze the electromagnetic fields of moving charges. Beginning with Maxwell's equations in matter[17]

$$\vec{\nabla} \cdot \vec{D} = \rho_f \tag{C.1}$$

$$\vec{\nabla} \cdot \vec{B} = 0 \tag{C.2}$$

$$\vec{\nabla} \times \vec{E} = -\frac{\partial \vec{B}}{\partial t} \tag{C.3}$$

$$\vec{\nabla} \times \vec{H} = \vec{J}_f + \frac{\partial \vec{D}}{\partial t}. \tag{C.4}$$

where $\vec{D} = \varepsilon \vec{E}$ and $\vec{B} = \mu \vec{H}$ are the constitutive relations for a linear, homogeneous, isotropic medium in which ε is the permittivity and μ the permeability.

A particle moving with a velocity $\vec{v} = v\hat{y}$ can be considered at rest in a system *S'* moving with the same velocity relative to a stationary system *S* as illustrated in figure C.1. The particle with point charge *q* has a uniform radial electric field in *S'* given by Coulomb's law. At time $t = t' = 0$ the origins of *S* and *S'* are coincident and the particle passes a point *P* in system *S* with coordinates (0,0,*b*) and (0,-*vt'*,*b*) in *S'*. The Lorentz transformation for a boost along the $\hat{y}$ direction is given by

[17] $\vec{\nabla} = \hat{x}\frac{\partial}{\partial x} + \hat{y}\frac{\partial}{\partial y} + \hat{z}\frac{\partial}{\partial z}$ is the "del" operator in Cartesian coordinates with arrows $\vec{x}$ denoting vectors and carets $\hat{x}$ unit vectors.

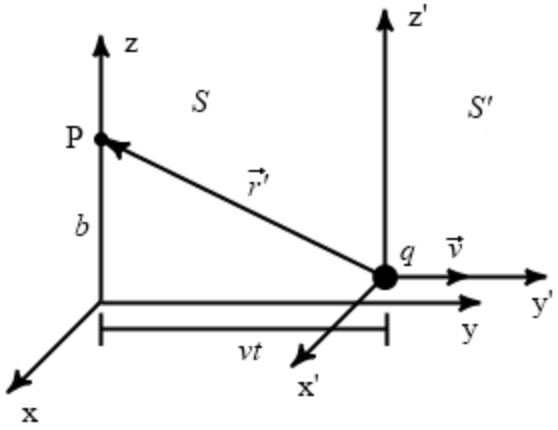

Figure C.1 Particle with charge q at rest in system S' moving with a velocity v relative to S and passing a point P with impact parameter b.

$$\begin{aligned} t' &= \gamma\left(t - \frac{v}{c^2}y\right) \\ x' &= x \\ y' &= \gamma(y - vt) \\ z' &= z. \end{aligned} \tag{C.5}$$

From the general Lorentz transformation of electromagnetic fields from a moving system *S'* with velocity $\vec{v}$ to *S* given in [74], the inverse Lorentz transformations in SI units can be found to be

$$\begin{aligned} \vec{E} &= \gamma\left(\overrightarrow{E'} - \vec{v} \times \overrightarrow{B'}\right) + (1-\gamma)\frac{\overrightarrow{E'} \cdot \vec{v}}{v^2}\vec{v} \\ \vec{B} &= \gamma\left(\overrightarrow{B'} + \frac{1}{c^2}\vec{v} \times \overrightarrow{E'}\right) + (1-\gamma)\frac{\overrightarrow{B'} \cdot \vec{v}}{v^2}\vec{v}. \end{aligned} \tag{C.6}$$

By using equations (C.6) to transform the electric field of a stationary charge with no magnetic field given by (A.1) in the moving system *S'* shown in figure C.1 and equations (C.5) to express the fields in a lab frame *S*, the fields of a relativistic charged particle are found to be

$$E_y = -\frac{q}{4\pi\varepsilon_0}\frac{\gamma v t}{(b^2+\gamma^2 v^2 t^2)^{3/2}}$$
$$E_z = \frac{q}{4\pi\varepsilon_0}\frac{\gamma b}{(b^2+\gamma^2 v^2 t^2)^{3/2}} \tag{C.7}$$
$$B_x = \frac{\beta}{c}E_z$$

and are shown graphically in figure C.2 (a) and (b). Equations (C.7) illustrate that, while the stationary particle has no magnetic component, a moving charge gains a magnetic field that becomes almost equal to E_z as $\beta \to 1$.

In figure C.2 (b) it can be seen that the integrated longitudinal force at *P* experienced by a test particle, as defined by the Lorentz force, equation (A.1) , cancels out as

$$F_z = \int_{-\infty}^{\infty} qE_z\, dt = 0 \tag{C.8}$$

and therefore an observer at *P* will experience only transverse fields. The time during which the transverse fields are appreciable decreases with increased velocity as $\Delta t \cong b/\gamma v$. This is further illustrated by the spatial representation of the electric field in figure C.2 (d) which shows a reduction in the direction of motion by a factor of γ^{-2} while the transverse field increases by a factor of γ. The net effect is that a residual gas particle in the beam pipe will only experience a very short pulse of force perpendicular to the beam direction, where the length of the pulse Δt will place a condition on the minimum energy transfer in an inelastic collision between a heavy charged particle and orbital electron.

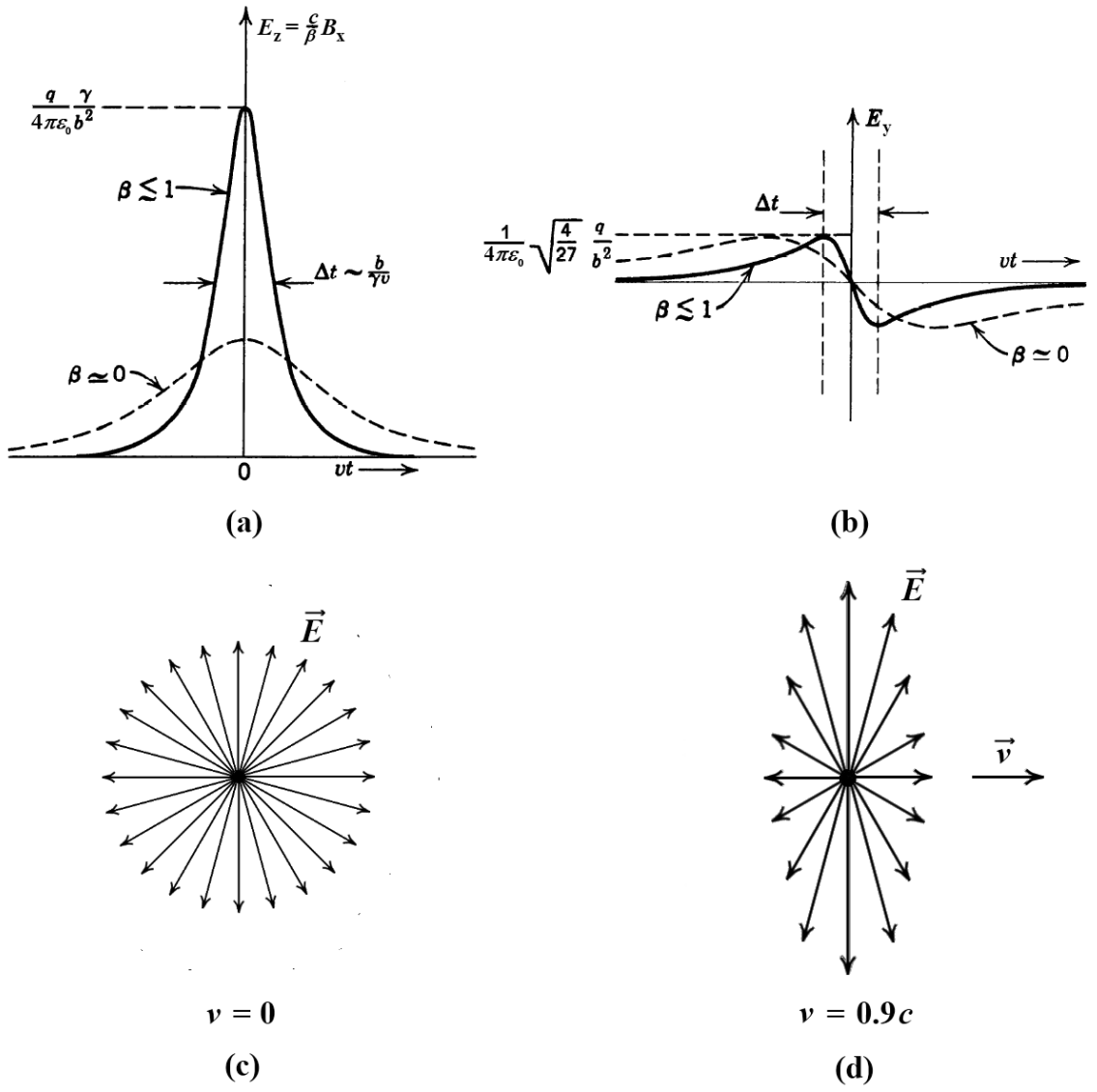

Figure C.2 Graphical representation of the fields of a uniformly moving charged particle. (a) & (b) Fields at point P in Figure C.1 as a function of time[18] [74]**. (c) & (d) Spatial representation of the electric field lines emanating from the position of a charge at rest and with velocity 90% the speed of light, respectively.** [246]

[18] This material is reproduced with permission of John Wiley & Sons, Inc.

Appendix D

Beam Envelope Parameters

Beam Coordinates

An accelerator utilizes electromagnetic fields in the form of the Lorentz force

$$\vec{F} = q\left(\vec{E} + \vec{v} \times \vec{B}\right) \tag{D.1}$$

to accelerate and guide a charged particle to its final destination. Since magnetic fields can do no work, longitudinal electric fields are used for acceleration while magnetic fields are used to manipulate the particle trajectory. There exists a reference or ideal trajectory that a particle would follow if it passed without error through all accelerator components. However, due to errors induced by accelerating fields in addition to the natural divergence of a beam of like-charged particles, individual particles follow paths that deviate from the reference path and without a form of focusing would quickly be lost.

A standard coordinate system used in accelerator applications is shown in figure D.1 which defines a longitudinal coordinate $\hat{s}$ that is tangential to the ideal trajectory and orthogonal unit vectors $\hat{x}$ and $\hat{y}$ defining the transverse plane whose origin is at location s along the ideal beam path. The local reference trajectory radius is $\rho(s)$.

Transverse Dynamics

For an accelerating structure composed mainly of linear focusing elements and for small displacements around the reference trajectory, the magnetic field, which by design has no longitudinal component, may be expanded to first order as

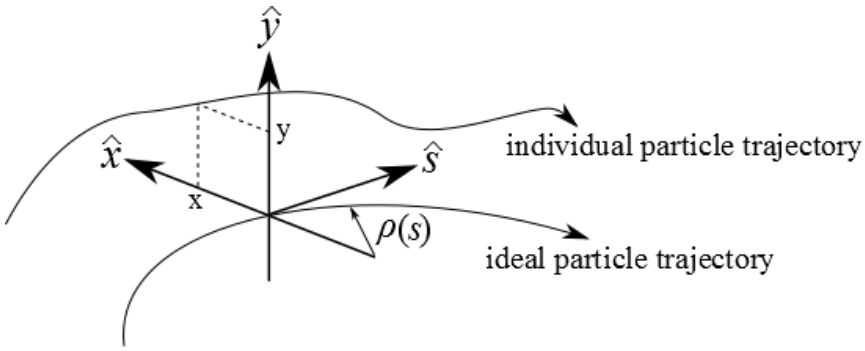

Figure D.1 Curvilinear beam particle coordinate system.

$$\vec{B} = \left(B_x(0,0) + \frac{\partial B_x}{\partial y}y + \frac{\partial B_x}{\partial x}x\right)\hat{x} + \left(B_y(0,0) + \frac{\partial B_y}{\partial x}x + \frac{\partial B_y}{\partial y}y\right)\hat{y}. \tag{D.2}$$

The first terms in the transverse components of (D.2) are uniform fields corresponding to dipole magnets which are primarily useful for trajectory bending. The second terms in equation (D.2) which describe the field of a quadrupole magnet, provide the necessary forces to focus the beam. In the current-free region of the magnetic aperture, Maxwell's equation $\vec{\nabla} \times \vec{B} = 0$ dictates that the transverse gradients be equal

$$\frac{\partial B_x}{\partial y} = \frac{\partial B_y}{\partial x}. \tag{D.3}$$

As such, the magnetic component of the Lorentz force $q\vec{v} \times \vec{B}$ produces a focusing force in one transverse dimension and a defocusing force in the other. A configuration of focusing and defocusing quadrupoles produces a net focusing effect [247] and causes a beam particle to oscillate about the ideal trajectory. These oscillation, known as betatron oscillations, are described by the solution to the transverse equation of motion[19] for a particle assuming no coupling between directions

[19] A complete derivation of equations of motion and transverse dynamics may be found in [159], [254]

$$\frac{d^2x}{ds^2} + K(s)x = 0$$
$$\frac{d^2y}{ds^2} + K(s)y = 0. \tag{D.4}$$

$K(s)$ acts as a position dependent restoring force and is proportional to the quadrupole field gradient during passage through a quadrupole magnet.

The solutions to equations (D.4), which is called Hill's equation, have the form of generalized harmonic oscillators [159]. The solution in the horizontal transverse dimension is

$$x(s) = \sqrt{\varepsilon\beta(s)}\cos(\psi(s) + \psi_0) \tag{D.5}$$

where $\psi(s)$ is the position dependent phase of the particle and ψ_0 the initial phase. $\beta(s)$ is called the beta function and describes the envelope inside which a particle oscillates about the reference trajectory as illustrated in figure D.2. The beta function is one of three parameters, known as Twiss or Courant-Snyder parameters characterizing the transverse motion. The remaining parameters are

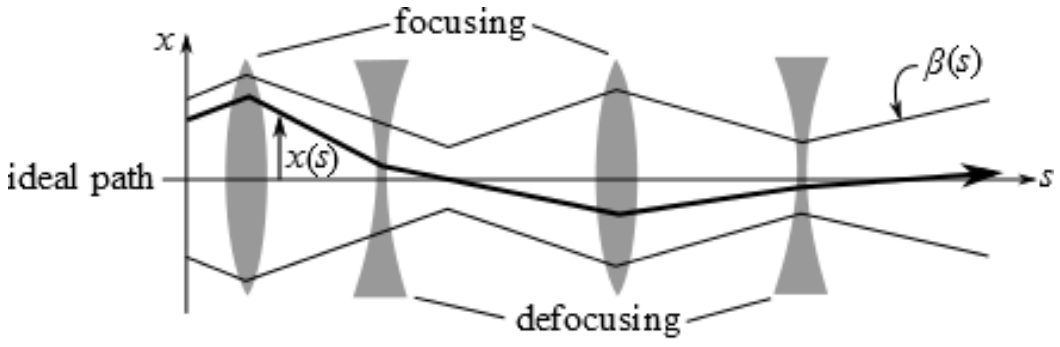

Figure D.2 Graphical representation of betatron oscillation about the ideal trajectory of a particle traversing focusing and defocusing quadrupoles. Quadrupole elements are represented with optical lenses.

$$\alpha(s) = -\frac{1}{2}\frac{d\beta(s)}{ds} \tag{D.6}$$

$$\gamma(s) = \frac{1+\alpha(s)^2}{\beta(s)}. \tag{D.7}$$

Beam Size

The equations of motion (D.6) and it's derivative with respect to *s*, x', satisfy the equation

$$\gamma(s)x^2 + 2\alpha(s)xx' + \beta(s)x'^2 = \varepsilon \tag{D.8}$$

where ε is termed the emittance and is the same quantity found in equation (D.5) . Equation (D.8) is the general equation of an ellipse in phase space[20] (x,x') with area

$$\int_{ellipse} dxdx' = \pi\varepsilon. \tag{4.9}$$

This phase space ellipse may change orientation and eccentricity depending on position in the accelerating structure, but the area remains the same. Each beam particle will be found somewhere on its respective ellipse with its position on the ellipse determined by $\psi(s)$, as illustrated in figure D.3 (a). Also shown in figure D.3 (a) are the physical dimensions of the phase space ellipse described through Twiss parameters.

A collection of beam particles may be described by a phase space ellipse encompassing a particular fraction of the beam particles. It has been shown [159] that for a Gaussian distribution of beam particles of width σ, the phase space ellipse with a fraction *F* of the total beam particles may be defined such that

[20] The velocity component of phase space $x' = \tan\theta$ where θ is the angle between the particles momentum *p* and longitudinal component p_s. Since, for beam particles, the transverse momentum $p_x << p$, the small angle approximation may be used $x' = \theta$ so that $p_x = px'$ where and x' is given in radians.

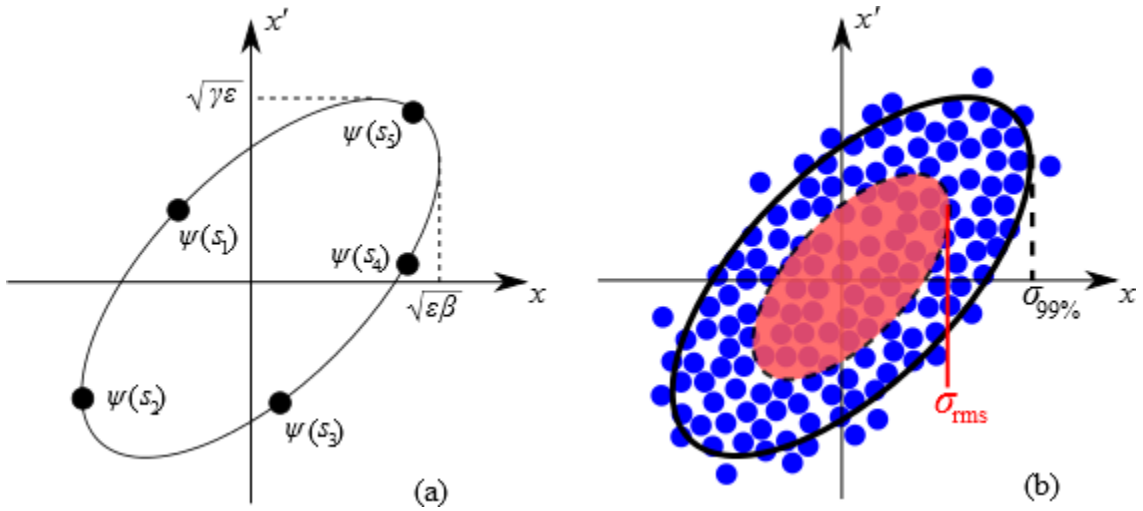

Figure D.3 (a) Phase space ellipse for a single particle showing the dimensions of the ellipse defined through Twiss parameters and individual particle locations in phase space as a function of different longitudinal locations s_n. (b) Phase space ellipses for an entire beam for different fractions of the encompassed beam.

$$\varepsilon = -\frac{2\pi\sigma^2}{\beta}\ln(1-F). \tag{4.10}$$

While there is no uniform definition in the accelerator community of the choice of F to define a standard emittance, a fraction of 39% is typically used to produce an RMS beam emittance of $\pi\sigma_{rms}^2/\beta$. A typical value use in SNS is the 99% emittance $\varepsilon_{99\%} = 10\varepsilon_{rms}$. The beam size[21] is defined by

$$\sigma = \sqrt{\varepsilon\beta}. \tag{4.11}$$

Figure D.3 (b) shows a representation of RMS and 99% phase space ellipses. The beam size may be defined for each transverse beam dimension and varies with the longitudinal position.

[21] The beam is more accurately defined as $\sigma_{rms} = \sqrt{\pi\varepsilon_{rms}\beta/\pi}$. However, it is standard practice to give the emittance in units of $\pi \cdot mm \cdot mrad$ and drop the value of π in the beam size calculation. This convention will be followed in this text.

Vita

Dirk Alan Bartkoski was born in Christiansburg, VA., on April 30, 1982. His father moved the family to Blacksburg, Co. to pursue a career in mine management. The Bartkoski family moved to Kentucky, where Dirk spent his childhood years being homeschooled. In 1996, he moved to Belmont, Ohio where he graduated high school through homeschooling and received his GED. After spending one year at the Ohio University Eastern Campus in a general engineering degree, he went to Oral Roberts University in Tulsa, OK. where he graduated with a B.S. in Engineering Physics and a minor in Math.

Dirk moved to Knoxville, TN in the fall of 2004 where he entered the Astronomy and Physics Department at the University of Tennessee. He began working with the Accelerator Physics group at the Spallation Neutron Source accelerator (SNS) located at the Oak Ridge National Laboratory in Oak Ridge, TN which is where he performed research that lead to his graduation in December of 2005 with a Master's degree in Physics from the University of Tennessee. After moving from the Physics group to the Beam Instrumentation Group at SNS he began work on his doctoral degree of which he is currently pursuing and plans on completing at the end of 2013. Upon graduation he plans on pursuing a post-doctoral position in accelerator physics and possibly writing fantasy and fiction.